Trinity College Dublin
Coláiste na Tríonóide, Baile Átha Cliath
The University of Dublin

High-Throughput Computational Investigation of Homogeneous and Heterogeneous Water Splitting Catalysts

by

Michael John Craig

A thesis submitted in partial fulfilment

of the requirements for the degree of

Doctor in Philosophy

at the

University of Dublin, Trinity College

2023

Declaration of Authorship

I declare that this thesis has not been submitted as an exercise for a degree at this or any other university and it is entirely my own work.

I agree to deposit this thesis in the University's open access institutional repository or allow the Library to do so on my behalf, subject to Irish copyright legislation and Trinity College Library conditions for use and acknowledgement.

I consent to the examiner retaining a copy of the thesis beyond the examining period, should they so wish (EU GDPR May 2018)

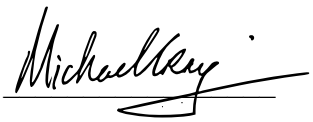

Michael John Craig

25 January 2023

Trinity College, The University of Dublin

Summary

One of the most effective ways to enable green hydrogen production is to improve water splitting technologies. A major source of inefficiency lies squarely with the oxygen evolution reaction (OER), with industrial-grade catalysts requiring precious metals which are not abundant enough to facilitate a hydrogen economy.

In this work, we study this reaction through density functional theory calculations and mining computational materials databases. Through computational modelling of the OER mechanism in 17 well-known molecular catalysts, we establish the universality of linear relationships between binding energies involved in this reaction. This linear relationship constrains a catalyst to have a minimum theoretical overpotential. However, crucially, in contrast to metal oxide catalysts, many molecular catalysts are known to undergo a one-electron oxidation prior to the formation of the crucial O–O bond. We extend the common water nucleophilic attack (WNA) mechanism by allowing for this oxidation and use it to rationalise the activity of state-of-the-art Ru-based molecular catalysts. This newfound understanding leads to the proposal of catalyst design principles which could identify novel catalysts for this reaction which are cheap and active. These principles are tested when we generate and calculate the WNA mechanism for a set of hundreds of hypothetical catalysts for this reaction, using ligands found in experimental water splitting complexes. We identify how certain catalysts can circumvent the constraint imposed by the linear relationship through the alignment of spin on oxygen atoms and explain the existence of metal-specific linear relationships using a spin-based heuristic.

Fe-based complexes are among the most promising molecular OER catalysts based on earth-abundant elements. We study mononuclear Fe complexes which have been shown to be active as well as inactive counterparts with the same ligand framework where Fe is replaced by Mn, Co, or Ni. The source of inactivity for Co and Ni is found to be their high

oxo wall, while for Mn it is reasoned to be a thermodynamic sink prior to the formation of a high-valent metal centre. The activity values of the Fe catalysts were then well captured by a simple thermodynamic descriptor which provides an impressive correlation with experimental turnover frequencies. Additionally, we provide evidence for the source of improved activity when functionalizing these complexes with electron withdrawing or electron donating groups. We study an internal C–H hydroxylation which recent experimental evidence has shown can turn off the catalyst and find that functionalization can switch the stability of topological isomers which are prone to this hydroxylation mechanism.

With a focus on heterogeneous OER catalysis, we develop a methodology to predict formation energies of binary oxides based on their oxidation states. Through tracking differences in metal-oxygen bond lengths between unary and binary oxides, we develop an understanding of common sources of stabilization across transition metal oxides. This leads to a simple scheme which appropriately weights parabolic equations fitted through unary oxide formation energies to predict formation energies for binary oxides $A_{1-z}B_zO_2$ – where z ranges from 0 to 1 – with a mean absolute error that compares well with state-of-the-art deep learning methods.

Using this scheme, we screen for mixtures of binary oxides which could be stable in acidic media and under the harsh oxidising potentials required for OER catalysis. We begin by developing an appropriate scheme which can identify recently reported alloys of iridium oxide which exhibit comparable stability in acid to the unary IrO_x, identifying a protocol that identifies 7 of 8. With this we screen for alloys of the stoichiometry $A_{1-z}B_zO_2$, finding 8 alloys based entirely on earth-abundant elements. Finally, we report the high-level implications of this model and outline how it constrains the search for stable oxide-based catalysts for this reaction.

Abstract

Understanding the sources of activity and stability in oxygen evolution reaction catalysts remains an open challenge. This thesis attempts to understand these factors by studying many catalysts for both homogeneous OER to glean high-level insights into the factors affording them high activity. First, we take 17 experimentally realized molecular catalysts and model the commonly assumed mechanism. Using principles derived from this work we attempt to screen for molecular catalysts with improved activity identifying Cr-based catalysts as a surprising potential option. We then focus specifically on Fe-based molecular catalysts and three inactive catalysts based on the same ligand framework but with Mn, Co, and Ni metal centres to understand the key differences which govern activity in these complexes. In heterogeneous catalysis, we focus on understanding how changes in metal oxidation state can influence stability in binary metal oxides. This leads to the development of a formation energy prediction scheme that is used to pre-screen mixtures of elements across the periodic table for active and acid-stable catalysts for the OER which are low-cost alternatives to the current catalysts based on precious metals.

Acknowledgements

Firstly I thank my supervisor, Professor Max García-Melchor, for all his support throughout four years of research, I am so very grateful for his giving me the opportunity to carry out this research. I would also like to thank Dr. Michal Bajdich for his support during my stay as a visiting researcher in Stanford University. All the work was part funded by the Provost's PhD fund and the Irish Research Council.

I estimate that over the past four years I have had about 100 burritos in the hallowed halls of Mama's Revenge Leinster St, and I am delighted to have shared them with everyone in the lab. Thank you for the fun, help and support; Eric, Kevin, Anna, Meriç, Manting, Marconi, Arantxa, Alex, Cian, and Felix.

The calculations which form a large part of this thesis would not have been possible without the work of the TCHPC and ICHEC staff maintaining compute clusters and provisioning hardware.

My heartfelt thanks go towards all my friends and family for their support and motivation throughout, without you I couldn't have kept the relative peace of mind that I did in the world outside of Trinity!

Publications

Publications related to the contents of this thesis

[1] Craig, M. J., Coulter, G., Dolan, E., Soriano-López, J., Mates-Torres, E., Schmitt, W., García-Melchor, M. Universal scaling relations for the rational design of molecular water oxidation catalysts with near-zero overpotential. *Nat. Commun*. **2019**, *10*, 4993.

[2] Craig, M. J., García-Melchor, M. Discerning Activity and Inactivity in Earth-Abundant Molecular Oxygen Evolution Catalysts. *ChemCatChem*. **2020**, *12*, 4775–4779.

[3] Craig, M. J., García-Melchor, M. High-throughput screening and rational design to drive discovery in molecular water oxidation catalysis. *Cell Rep. Phys. Sci.* **2021**, *2*, 100492.

Other publications

[4] Craig, M. J., García-Melchor, M. Faster hydrogen production in alkaline media. *Nat. Catal.* **2020**, *2*, 967–968.

[5] Craig, M. J., Barda-Chatain, R., García-Melchor, M. Fundamental insights and rational design of low-cost polyoxometalates for the oxygen evolution reaction. *J. Catal.* **2021**, *393*, 202–206.

[6] Craig, M. J., García-Melchor, M. Applying Active Learning to the Screening of Molecular Oxygen Evolution Catalysts. *Molecules* **2021**, *26*, 6362.

[7] Craig, M. J., García-Melchor, M. Reaction descriptors for the oxygen evolution reaction: Recent advances, challenges, and opportunities. *Curr. Opin. Electrocehm.* **2022**, *35*, 101044.

List of Abbreviations

AEM	Anion exchange membrane
ACM	Adsorbate cycling mechanism
BEP	Brønsted-Evans-Polanyi
BEEF	Bayesian error estimation framework
CAN	Cerium ammonium nitrate
CHE	Computational hydrogen electrode
COHP	Crystal orbital Hamiltonian population
DFT	Density functional theory
ECP	Effective core potential
EDG	Electron donating group
ESSI	Electrochemical step symmetry index
ET	Electron transfer
EWG	Electron withdrawing group
FEFOS	Formation energy from oxidation state
GGA	Generalised gradient approximation
GTO	Gaussian-type orbitals
HER	Hydrogen evolution reaction
HF	Hartree-Fock
HS	High spin
I2M	Interaction of two metal-oxo units
LCAO	Linear combination of atomic orbitals
LDA	Local-density approximation
LOM	Lattice oxygen-mediated mechanism
LS	Low spin
MAE	Mean absolute error
ML	Machine learning
MP	Materials Project
NHE	Normal hydrogen electrode
OER	Oxygen evolution reaction
OQMD	Open quantum materials database
PCET	Proton-coupled electron transfer
PDS	Potential-determining step
PEM	Proton exchange membrane
PES	Potential energy surface
PLS	Potential-limiting step
PT	Proton transfer
RDS	Rate-determining step
RHE	Reversible hydrogen electrode
ROOST	Representation learning from stoichiometry
SIE	Self-interaction error
SCF	Self-consistent field
SCRF	Self-consistent reaction field
SHE	Standard hydrogen electrode
TCO	Transparent conducting oxide
TOF	Turnover frequency
TON	Turnover number
TS	Transition state
UEG	Uniform electron gas
UV	Ultraviolet
VASP	Vienna ab initio simulation package
VDW	Van der Waals
WNA	Water nucleophilic attack

Table of Contents

Chapter 1 Introduction

Modern civilization owes much of its trappings to the practice of burning fossil fuels. Through combustion, carbon-carbon or carbon-hydrogen bonds contained in coal, oil and gas are converted into heat, then enabling the propulsion of mechanical prime movers such as turbines producing electricity or combustion engines transporting us. These devices enable modern life in rich nations: when US citizens were surveyed in 2006 about appliances they need, over 70% of respondents reported they needed a car, clothes washer, dryer or home air conditioning, and an increase over the previous decade was noted for every single appliance in the survey.[1] The utility of these things is undeniable, however, while powering lives using fossil fuels has brought leisure time and convenience, it is also fraught with unintended consequences. Carbon dioxide is an inherent by-product of these reactions. This gas can then reside in the troposphere and absorb and reemit infrared radiation emitted from the Earth's surface, while allowing radiation incident on the Earth from the sun to pass through.[2] As such, this molecule selectively traps radiation in the Earth's atmosphere. The United Nations' Intergovernmental Panel on Climate Change (IPCC) has noted that starting from 2018, only 1450 Gt of CO_2 emissions can be emitted to avoid a 2 °C increase in global temperatures above preindustrial levels with 50% probability, based on IPCC's Special Report 15, at the current rate of emissions, that would be depleted by 2058.[3] The implications of this temperature increase is a two-factor increase in the frequency of extreme weather events such as heatwaves and droughts relative to today.[3]

Regardless of the need to reduce CO_2 emissions into the atmosphere to tackle global warming, the finite nature of fossil-fuels necessitates a switch in the modes of human energy creation and use. It would therefore be desirable to design technologies to form

chemical bonds using renewable energy, and subsequently break these bonds to do useful work with no associated emissions. For example, storing energy in the form of hydrogen bonds and subsequently releasing that energy is one such technological scheme to address this challenge. The economic reconfiguration that this requires would entail the development of a new economic mode of production.

1.1 Hydrogen economy

The hydrogen economy is a term which is broadly defined as encompassing the vast array of technical components which would be required to facilitate the use of hydrogen molecules as a commercial product. Any product needs to be sourced or produced, packaged, transported, stored, and subsequently used. H_2 is no different, but this tiny molecule is thought essential to future efforts by governments to reach net zero targets by 2050.[4] Technological challenges to realizing this are abound. Hydrogen must be produced by electrolysis or chemical means, stored by compression or liquefication, and transported via ground transport or pipelines to an end-user where it can be converted to electricity by a fuel cell, whose only exhaust is water vapour. In this thesis, we concern ourselves with the generation of hydrogen via water electrolysis. All other applications of hydrogen, while essential, are effectively downstream of its generation.

One scenario where hydrogen could be produced economically involves excess, unwanted electricity from intermittent renewable energy sources supplies the voltage for Eqs. 1.1 and 1.2, thereby converting electrical energy to chemical energy. The associated half-reactions involved are the hydrogen evolution reaction (HER) and oxygen evolution reaction (OER):

$$HER: \quad 2H^+ + 2e^- \rightarrow H_2 \qquad E^0 = 0.00\, V_{SHE} \qquad (1.1)$$

$$OER: \quad 2H_2O \rightarrow O_2 + 4H^+ + 4e^- \qquad E^0 = 1.23\, V_{SHE} \qquad (1.2)$$

$$HER: \quad 2H_2O + 2e^- \rightarrow H_2 + 2OH^- \qquad E^0 = -0.83\, V_{SHE} \qquad (1.3)$$

$$OER: \quad 4OH^- \rightarrow O_2 + 2H_2O + 4e^- \qquad E^0 = 0.40\, V_{SHE} \qquad (1.4)$$

Where E^0 refers to the equilibrium half-cell potentials at 1 atm and 298.15 K against the standard hydrogen electrode (SHE). When occurring in acidic media the two half-reactions occur as shown in Eq. 1.1 and 1.2, and the half-reactions of electrolysis occurring in alkaline media are shown in Eq. 1.3 and 1.4. According to EirGrid, producer of electricity in Ireland, 1 TWh of wind energy, or 7.7% of total available wind energy was not captured due to the practice of voluntarily reducing energy output.[5] Utilising excess energy from intermittent renewable sources would be a promising way to produce hydrogen sustainably, leading to a renewable and green fuel while enhancing the economic viability of energy sources such as wind. A reason this approach has been overlooked is the lower round-trip efficiency of hydrogen energy storage from generation to end-use. However, the high energy density, coupled with long-term storability of hydrogen make it a particularly compelling long-term gird storage solution as compared with using the electricity to charge batteries. When accounting for these advantages, a comprehensive cost-benefit analysis which studied the energy stored per unit of investment over the lifespan of a given technology found that hydrogen energy storage via electrolysis is especially suited to handling overgeneration from wind turbines when compared to lithium-ion batteries.[6] Aside from the merits of using hydrogen to store energy, hydrogen produced by electrolysis holds great potential in decarbonizing industrial chemical processes such as fertilizer production[7] and steel manufacturing,[8] which cumulatively make up approximately 10% of global CO_2 emissions.

1.1.1 *Electrochemical hydrogen production*

Green electrochemical water-splitting uses electricity from renewable or low-carbon energy sources to drive the electrolysis of water. Nicholson and Carlisle first split water using electricity by filling a sealed tube with water, submerging a wire with Pt at either end, and connecting this wire to a zinc disc within a Voltaic pile. They had tried using wires

with different materials at the ends of the wire to no avail, which points us towards the critical components of an electrolyser, the catalysts at both the anode and cathode. While Pt remains the state-of-the-art HER catalyst,[9] anodic materials for the OER have improved since these experiments.

The anodic OER in acidic media involves the transfer of four electrons to the electrode and four protons into the electrolyte to facilitate the HER half-reaction, as seen in Figure 1.1a. In a selective proton-exchange membrane, (PEM) positively charged protons travel to the cathode while electrons are drawn to the anode. A schematic of the half-reactions of Eqs. 1.3 and 1.4 are occurring in an electrolyser in alkaline media is shown in Figure 1.1b, where water and hydroxyl ions are selectively exchange by an anion exchange membrane (AEM). Since we must produce hydrogen, our H_2 molecule addresses our energy challenge as an energy storage medium, as opposed to as source of energy such as carbon-based fuels.

The electrolyser setup is a determining factor in the correct choice of OER catalyst. PEM and AEM electrolysis are the two electrolyser setups which are the most technologically developed.[10] The PEMs are very efficient in comparison to the AEM in terms of product purity and achievable current densities, although, the electrocatalysts currently available are based on scarce and expensive raw materials, mainly Ir and Ru. AEM electrolysis use OER catalysts which are cheaper and more abundant, with Ni Raney being the commercial catalyst for this technology with NiFe and FeCo oxyhydroxides representing promising alternatives.[11–13]

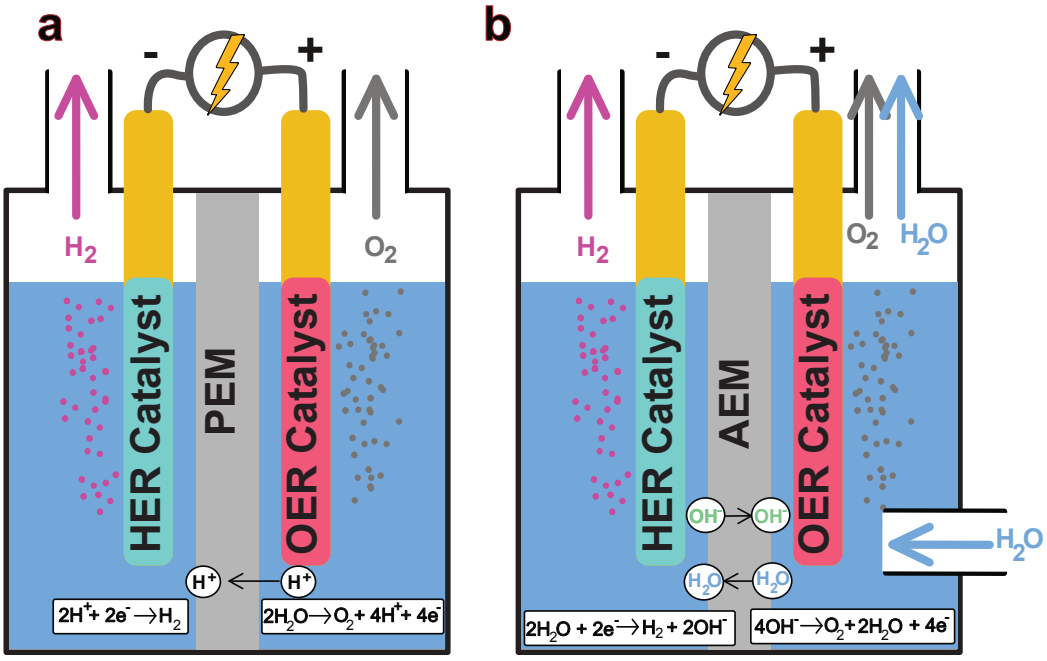

Figure 1.1. Schematic illustration of the HER and OER processes involved in the workings of an electrolyser in a) acidic media, known as a PEM electrolyser, and in b) alkaline media, using an AEM. The half-reactions associated with each are also shown.

To justify the vast technological shift towards hydrogen-based technologies, the way in which this hydrogen is produced must be cost-effective and carbon neutral. Unfortunately, due to the distinct drawbacks of PEM and AEM electrolysis, these requirements cannot be met in tandem as the costs associated with green electrochemical water splitting render it prohibitive in comparison to methane steam reforming, which currently dominates industrial hydrogen production.[14] Barring an increase in the cost of emitting carbon, the cost and efficiency associated with green water electrolysis must improve to compete with the dominant mode of production. Improving the OER represents one of the most promising route towards addressing this issue.[15] If we consider the overpotential – which denotes the difference between the potential at which a half-reaction is observed experimentally and the thermodynamic potential for the reaction, E^0 in Eq. 1.1–4 – we see that even the most active catalysts for OER have large overpotentials of *ca.* 0.3 V.[16]

While there are a multitude of factors which can influence the efficiency of these electrolyser setups including membrane type and conductivity,[17,18] device assembly technique,[19] and the electrolyte used[20] among others, we focus specifically on the variation in performance as a result of varying the OER catalyst. This thesis focuses on optimising catalysts for electrochemical OER by understanding sources of activity and stability to understand how we could enable the discovery of catalysts based on cheap and abundant materials to improve the sustainability and economic feasibility of the hydrogen economy. We will now outline the mechanisms proposed for the OER, as well as the different phases of OER catalysts.

1.2 Oxygen evolution reaction

The difficulty with the OER can be understood by acknowledging that it requires a total transfer of four electrons and four protons through the breaking of four O–H bonds. This process can be enabled by an electrocatalyst which lowers the activation barriers across these steps. To understand this reaction and the possible mechanisms and reaction barriers involved, first principles quantum chemical methods have proved valuable, and we use such tools to further develop our understanding of this reaction in this thesis.

1.2.1 *OER mechanisms*

Instead of modelling the entire water electrolysis process occurring in Figure 1.1, most *ab initio* methods focus on a specific half-reaction; in our case, the OER. Here, we focus on two mechanisms, namely the water nucleophilic attack (WNA) mechanism and the direct coupling of two metal-oxo units (I2M).[1] Each of the four constituent steps has an associated Gibbs energy change, ΔG, which is the thermodynamic potential that we use to discern the exergonicity of a given step in the reaction. In each case, the mechanism begins with a proton-coupled electron transfer (PCET) between the water molecule and the catalyst, thereby forming an adsorbed hydroxyl intermediate, which we will refer to as HO*

throughout this thesis. Subsequently, another PCET occurs as the O–H bond is broken to form an oxo intermediate O*. Then, the WNA mechanism continues via another water nucleophilic attack to form a hydroperoxo intermediate (HOO*) and subsequent O–H bond breakage to form O_2 gas and continue the cycle. This reaction can be represented thermodynamically as:

$$* + H_2O \rightarrow HO^* + H^+ + e^- \qquad \Delta G_1 = \Delta G_{HO^*} - eU + k_B T \ln a_{H^+} \qquad (1.5)$$

$$HO^* \rightarrow O^* + H^+ + e^- \qquad \Delta G_2 = \Delta G_{O^*} - \Delta G_{HO^*} - eU + k_B T \ln a_{H^+} \qquad (1.6)$$

$$O^* + H_2O \rightarrow HOO^* + H^+ + e^- \qquad \Delta G_3 = \Delta G_{HOO^*} - \Delta G_{O^*} - eU + k_B T \ln a_{H^+} \qquad (1.7)$$

$$HOO^* \rightarrow * + O_2 + H^+ + e^- \qquad \Delta G_4 = 4.92 - \Delta G_{HOO^*} - eU + k_B T \ln a_{H^+} \qquad (1.8)$$

where * denotes an active site, ΔG_{1-4} is the Gibbs energy change associated to each elementary step, ΔG_{i*} is the Gibbs binding energy of the OER intermediates, e is the electron charge, U the applied potential, a_{H^+} the activity of the protons in the electrolyte, while 4.92 is the negative of the experimental Gibbs energy of formation energy of two water.

The I2M shares the first two steps with the WNA before two metal-oxo units interact to form oxygen. In oxide-based catalysts, the evolved oxygen can come from the solvent water or from the lattice itself in what is called a lattice oxygen-mediated mechanism (LOM).[21,22]

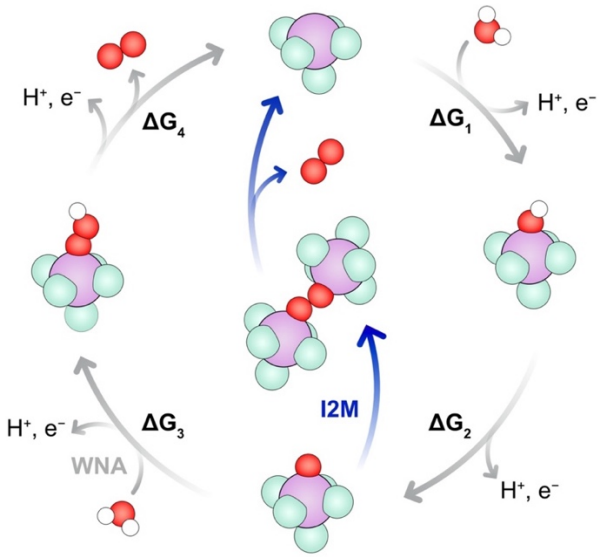

Figure 1.2. Illustration of the water nucleophilic attack mechanism highlighted along the grey paths with the associated proton coupled electrons transfers and the interaction of two metal-oxo units (I2M) mechanism shown in blue. The Gibbs energy changes ΔG_{1-4} are defined in Eqs. 1.5–8. The hypothetical active site is represented by a central purple and the oxygen and hydrogen atoms are red and white, respectively.

1.2.2 *Homogeneous OER*

Catalysts are called homogeneous if they exist in the same phase as the reagents, which is in solution in the case of water splitting. The most common type of homogeneous OER catalysts are inorganic complexes composed of a transition metal active site(s). The oxidation reactions at the metal site can be driven either by chemical oxidants, such as cerium ammonium nitrate (CAN), or electrochemically by an applied potential. The former method allows for rapid screening of potential catalysts activity,[23] but comes with an inherent limitation in the condition which can be applied since Ce^{IV} requires working at pH < 1.[24] Under these conditions, reactions last on the order of minutes, so a common metric to compare the efficiency of the complex is the turnover number (TON), defined as the ratio between the amount of product generated and initial catalyst over the span of the catalyst lifetime shown in Eq. 1.9. To compare catalytic activity, we use the initial turnover frequency (TOF), which is the TON per unit time.

$$TON = \frac{n_{O_2}}{n_{cat.}} \quad (1.9)$$

Llobet *et al.* synthesized a Ru-based catalyst with a TOF of 303 s^{-1} which they compared to the activity observed in photosystem II in the oxygen evolving complex contained in the chlorophyll of plants.[25] Molecular catalysts also have great tunability, as they can be functionalized through a multitude of electronic electron withdrawing groups (EWGs) and electron donating groups (EDGs) as well as steric groups which can be used to tailor their activities. In homogeneous OER catalysis, the Hammett parameter for a *para*-substituted pyridine in a mononuclear Fe-based complex has been correlated to the turnover frequency (TOF), with a NO_2 group leading to a two-fold increase in TOFs.[26] More recently, this analysis has been applied to a mononuclear Ru catalyst with a 10-fold increase in TOF upon functionalization with an ethoxy group, showing a volcano plot mapping TOF to the Hammett parameter.[27] The narrow range of this volcano with respect to the Hammett parameter provides a tantalizing prospect of tuning molecular complexes for the OER while also justifying the historic difficulty in finding highly active homogeneous catalysts. A unique factor in distinguishing molecular catalysts is their 3-dimensional nature and the fact that this can be exploited to selectively stabilize certain key intermediates to enhance the activity of a single site, which might not be possible with heterogeneous catalysts.[28]

This inherent tunability had meant that a oft-touted solution to improving the efficiency of the OER is to tether a tuneable homogeneous catalyst to a support to create a hybrid catalyst. Before we describe these we will outline the state-of-the-art in heterogeneous OER catalysis.

1.2.3 *Heterogeneous OER*

While homogeneous catalysts can exhibit TOF values which are orders of magnitude faster than those seen in heterogeneous systems, a primary drawback is that the most active

catalysts exhibit lifetimes less than 5 seconds long and are thus considered unstable.[25] Furthermore, these systems exhibit poor electron transport relative to heterogeneous catalysts which are in contact with a conductive support since the charge transfer process happens via the electrolyte-electrode interface. In industrial settings the OER is carried out with solid phase catalysts since they are more easily controllable and stable compared to homogeneous catalysts. As mentioned, IrO_2 is the industrial catalyst used for PEM electrolysis and $Ni_{1-x}Fe_xOOH$ for AEM electrolysis.[29] Choosing a figure of merit for these types of catalysts is difficult since the effective electrochemical surface area, electrode geometry and chemical environment can have differing, competing influences on the activity.[30] However, a commonly used metric is the overpotential at a current density of 10 mA/cm^2, a value chosen since it roughly matches the current density expected in an solar-driven water splitting device which is 10% efficient under 1 kW/m^2 of solar radiation.[31–33] McCrory et al. benchmarked the performance of many catalysts in alkaline and acidic media using this metric, finding that every tested catalyst could reach this metric over the range of 0.35–0.43 V of overpotential in alkaline media, while only IrO_x was stable under oxidizing conditions in acidic media. The stability was tested by measuring the overpotential when the catalyst first reached 10 mA/cm^2 and then measuring the overpotential required to reach the same current density two hours later. While IrO_x was far more stable than the other tested oxides ($NiFeO_x$, $CoFeO_x$, $NiCoO_x$, CoO_x, $NiLaO_x$, $NiCuO_x$, NiO_x, $NiCeO_x$) it still exhibited a 10% increase in the required overpotential over the course of two hours.

For alkaline media, the catalyst for AEM which is thought most appealing and exhibits the lowest overpotentials are Ni-based oxyhydroxides or Fe-doped modifications of the same which were described by Corrigan in the late 1980s.[29] Sargent *et al.* improved over the state-of-the-art AEM catalyst by doping W^{6+} into FeCo oxyhydroxides using a sol-gel

synthesis, observing an overpotential of 191 mV at 10mA/cm^2.[11] A general principle appeared to emerge then, with reports of high valent dopants with charge +5 and +6 improving the activity of both $Ni_{1-x}Fe_xOOH$ and $Co_{1-x}Fe_xOOH$,[13] with a 10-fold enhancement in TOF observed against the commercial Raney Ni catalyst. Given these catalysts are based on cheap, abundant elements, and given the low overpotentials achievable using these technologies, work in AEM is beginning to focus on membrane and device setup to further efficiency.[34]

Conversely, PEM electrolysis still relies on Ir. To illustrate the problem with this reliance, a recent technoeconomic analysis has shown that unless the Ir content of PEM electrolyser catalysts are significantly reduced and 90% of the used Ir is recycled, then the supply of this metal will not meet demand.[35] Efforts to reduce the iridium content of PEM catalysts have included nano structuring to improve efficiency, alloying with other elements or housing Ir in an acid stable matrix such as WO_3 to improve stability. Lewis and co-workers have worked on developing precious metal free antimonates such $Ni_{0.5}Mn_{0.5}Sb_{1.7}O_x$ for the OER in acid,[36] although their overpotentials were large at ca. 700 mV at 10 mA/cm^2. In this vein, Nocera *et al.* have developed a protocol to develop template-stabilized catalysts which are stable in acid,[37,38] tackling the problem highlighted by the benchmarking from McCrory, wherein they dope a highly acid stable, conductive, yet inactive host material in PbO_x, converging on a $Co_{0.14}Fe_{0.03}Pb_{0.85}O_x$ mixture.[37] In the introduction of Chapter 8 we provide further details on PEM catalysts which operate in acidic media, as we pre-screen binary oxides for stability, the focus on this deriving from the fact that there are no acid stable catalysts which approach the activity of Ir and Ru-based OER catalysts in acid.

Another proposed route to avoid this element involves the use of hybrid catalysts which involves the anchoring of an earth-abundant homogeneous catalyst, which have seen per-metal TOF values which are orders of magnitude higher than those seen in heterogeneous

catalysts,[39] on a support to combine the advantages of heterogenous and homogeneous catalysis.

1.2.4 *Hybrid OER*

The promise of hybrid OER is that if an appropriate pairing of molecular catalyst, heterogeneous catalyst and anchoring strategy are found, an optimal catalyst would be possible. This prospect is illustrated in Figure 1.3.

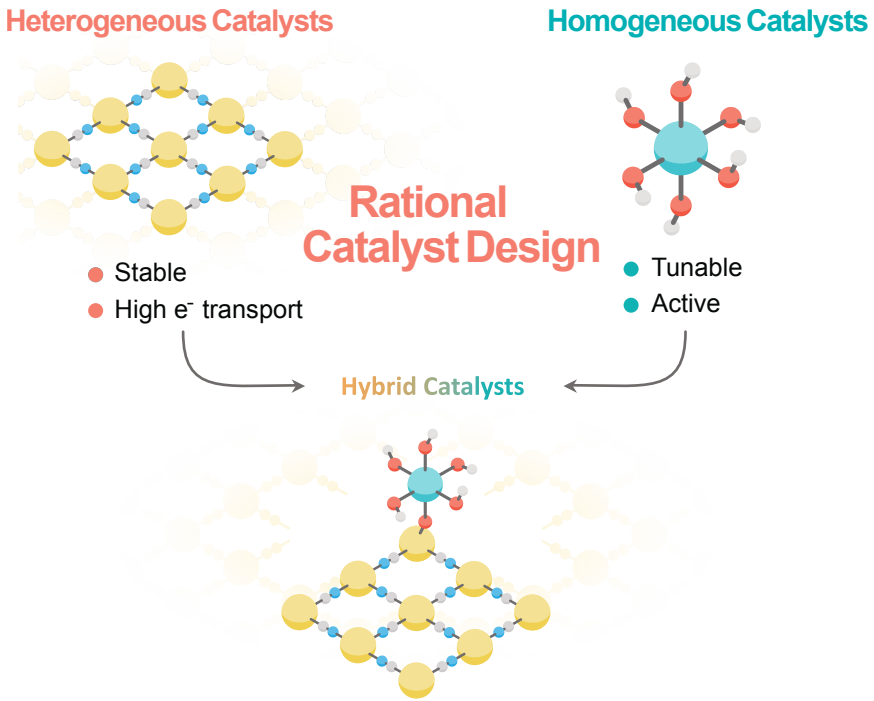

Figure 1.3. Motivation for the development of hybrid catalysis which combine the strengths of heterogeneous and homogeneous catalysis.

There are a myriad of potential methods to anchor a molecular catalyst onto a solid support through covalent linkers,[40] or π-π interactions between molecular catalyst ligands and carbon nanotubes.[41] Indeed Llobet and co-workers successfully anchored a Ru molecular catalyst on multiwalled carbon nanotubes by functionalising the axial ligands with oligomers which facilitate the C–H π-interactions between the molecular complex and the graphitic surface to catalyse the OER in neutral pH with high current densities of ca. 200 mA/cm^2.[41]

To enable the rational design of hybrid catalysts, we need to understand the factors constraining water-splitting technologies. When catalytic activity can be described through an energy-based descriptor, the optimisation of catalysts for this reaction becomes amenable to computational screening by simply modelling the relevant thermodynamics. Correlating activity and descriptors in this way has become a powerful means to understand fundamental facets of the OER, guide future experimental investigations, and enable high-throughput computational screening of hypothetical catalysts. Over the course of this thesis we will analyse and develop activity descriptors for homogeneous catalysis and develop stability descriptors in heterogeneous catalysis, thus enabling hybrid catalysts by taking a two-pronged approach. In the following section we detail well-known OER descriptors.

1.3 OER catalyst descriptors

1.3.1 *Activity descriptors*

The seminal foundation for the use of descriptors in OER catalysis was laid down when Trassati described how the heat of formation for oxides, ΔH_f, related to the reaction overpotential in the shape of a volcano (see Figure 1.4a). This allowed for the beginnings of a rationalization for the source of the overpotential on the surface of oxygen-evolving electrocatalysts.[42,43]

Theory caught up with the spirit of this experimental descriptor decades later when Nørskov *et al.*[44] modelled the OER on oxidized metal surfaces assuming a WNA mechanism – as outlined by Eqs. 1.5–8, which we will derive in Chapter 2 – and described the concept of theoretical overpotential, (η_{theor}) defined as the applied potential at which all elementary steps become downhill.[45] This figure of merit for predicting OER activity can be determined by subtracting the thermodynamic redox potential of water oxidation from the maximum of ΔG_{1-4}, according to Eq. 1.10.

$$\eta_{theor.} = \max \frac{(\Delta G_{1-4})}{e} - 1.23\ V_{RHE} \quad (1.10)$$

In doing this analysis for perovskites and metal oxides, Nørskov and co-workers found that η_{theor} correlates with experimental activity, leading to a volcano-shaped view of the relationship between OER activity and the difference between the binding energy of the O* and HO* intermediates, $\Delta G_{O^*} - \Delta G_{HO^*}$,[45,46] as seen in Figure 1.4b. Notably, this descriptor is more intuitive compared to ΔH_f as it relates to the transfer of protons and electrons on the surface of the catalyst. The same authors and Koper[8] further described that, since two of the thermodynamic quantities, ΔG_{HOO^*} and ΔG_{HO^*} are linearly correlated, with a fixed difference of 3.2 eV, and since this is larger than the thermodynamically ideal 2.46 eV (2×1.23 eV), we can justify the inactivity of OER catalysts from first principles. This can be seen from Figure 1.4 where both the experimental and theoretical overpotentials appear to have a minimum threshold. Another implication is that the energy change of the step occurring before the HOO* intermediate formation is a strong determinant of the predicted overpotential since the predicted potential determining step is likely to be either the formation of O* from HO* or HOO* from O*. We see in Figure 1.4b some of the most active catalysts at the peak of the volcano including RuO_2, IrO_2 and Co_3O_4, which comports with experiment as these materials are some of the most active for PEM electrolysis.[16,48] Of these, IrO_2 is most commercially viable as a PEM electrocatalyst due to its durability. The correspondence between the most active catalysts and those found at the peak by Man *et al.* established the $\Delta G_{O^*} - \Delta G_{HO^*}$ descriptor in subsequent analyses as the most prominently calculation used to justify OER activity.

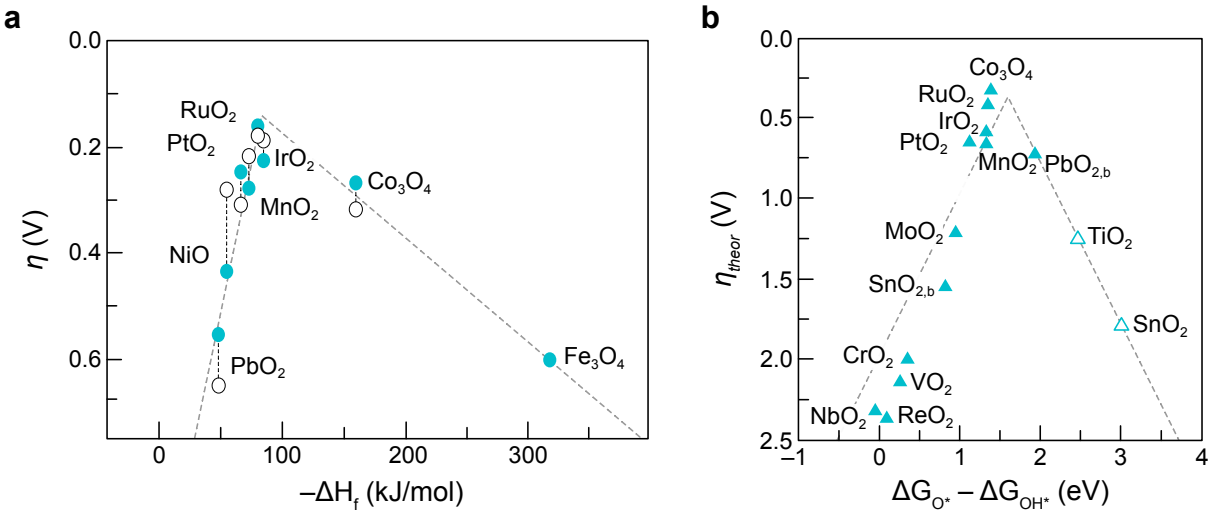

Figure 1.4. Overview of thermodynamic activity descriptors applied to OER catalysts. a) Experimental relationship between oxide heat of formation, ΔH_f, and overpotential, blue (white) circles denote that experiments were carried out in acidic (alkaline) media.[42,43] b) Volcano relationship demonstrating the utility of the OER descriptor $\Delta G_{O^*} - \Delta G_{HO^*}$, blue (white) triangles denote high (low) surface coverages.[46]

While this descriptor has enabled the identification of likely active sites and promising oxyhydroxides,[11,49,50] and oxides,[46,51–53] as catalysts, recent investigations have at tackling the shortcomings of this approach. For instance, PCETs are not always potential determining and there is no treatment of the kinetics which ultimately determine reaction rate, we instead implicitly assume by the Brønsted-Evans-Polanyi (BEP) principle that the kinetic barrier is correlated with the thermodynamic potential energy difference.[54] Another issue with an overreliance on $\Delta G_{O^*} - \Delta G_{HO^*}$ lies in the fact that the potential-determining step, which governs η_{theor}, may not coincide with the rate-determining step.[55] This has been addressed by Calle-Vallejo and co-workers, where they showed that reducing $\Delta G_{HOO^*} - \Delta G_{HO^*}$ does not necessarily correlate with improved activity.[56] To mitigate this, they introduced the electrochemical step symmetry index (ESSI), which measures the average of those steps with $\Delta G_{1-4} > 1.23$ eV. While the advent of the $\Delta G_{O^*} - \Delta G_{HO^*}$ descriptor and electronic descriptors has allowed for first principles investigation of OER catalyst activity, we will extend our understanding of this descriptor for molecular catalysts

by considering non PCET mechanisms. Furthermore, relying only on activity descriptors overlooks a crucial determinant of the practical realization of catalysts: their stability. Even the state-of-the-art acidic OER catalysts based on iridium or ruthenium are unstable, with daily overpotential increases observed for both.[57,58] We now outline the descriptors which have been used to study this.

1.3.2 *Stability descriptors*

The stability of a material is essentially a function of the difference between its ground state energy and other competing phases, a concept we outline in further detail in Section 2.7. Typically, the phases considered only includes solid phases, which precludes modelling the species observed in OER catalysis. To address this, the scope of considered phases was extended by Persson *et al.*[59] to include aqueous phases which may exist in solution, allowing for computational stability measurements more suited to test for durable OER catalysts which are tested in solution and at varying pH.[60] We describe this methodology further in Section 2.7.3, but in effect, it allows for a quantitative measure of stability in aqueous environments for pH and applied potentials of interest. Denoted as ΔG_{pbx} it is understood that a value of 0 eV/atom means that a material is stable with respect to competing phases for a given set of conditions, but heuristic investigation of metastable materials in aqueous environments set a threshold of 0.5 eV/atom.[61] By comparing the energetics of adsorbate cycling mechanisms (ACMs) such as the WNA against mechanisms involving the catalyst such as the LOM, where the evolved oxygen is sourced from the catalyst itself, Kolpak *et al.* showed, similar to the aforementioned work on activity descriptors, that the nominal number of outer electrons 3d perovskites (i.e. the number of d-electrons in the B cation) correlates with an energetic descriptor determining whether the AEM or LOM dominates.[62]

In this thesis we will focus on developing a general theory to predict oxide stability based on data from open-source materials databases and use this theory to screen for acid stable OER catalysts. Repositories of computational materials simulation results have become prominent as a source of both material and descriptor discovery, which we now outline.

1.4 Open-source materials databases

In 2011, the Materials Genome Initiative was announced by the National Science and Technology Council, an executive branch of the United States Government. This initiative led to hundreds of millions of dollars of research and development investment into the accelerating materials discovery through combining insights from experiment, theory, and computation.[63,64] Impressive databases of computational materials simulation results have sprung out of this, including the Materials Project (MP),[65] the Open Quantum Materials Database (OQMD),[66] and AFLOW.[67] We note here that due to the high computational demands required by such large computational materials databases, the simulation quality of this data is not as high as possible. In any case, these impressive efforts to increase the amount of available materials data are very valuable; they provide a foundation from which researchers can validate or test hypotheses, enable materials screening efforts which have enabled discovery,[68] and handle the increase in the rate of scientific research output which doubles roughly every 15 years.[69] There is a need to synthesize this information computationally as it becomes less and less tractable for humans to parse all this information, and as the dataset of considered materials grows, the potential for statistics and machine learning-based predictive algorithms becomes greater. The time required to take a material from lab-derived discovery to commercial realization is approximately 10–20 years from inception to use.[70] Furthermore, the rate of scientific research output is growing year on year at a rate of 4% leading to a doubling rate roughly every 15 years.[69] With such a spate of data, machine learning algorithms tackle this by attempting to ‘learn’

materials descriptors based on available training data. The state-of-the-art in this area is a method which uses deep learning to allow for structure-agnostic prediction of materials formation energies. An in-depth description behind the mechanics of this algorithm is beyond the scope of this thesis, but it essentially represents any material with any composition as a weighted graph where nodes in the graph are weighted by composition. This approach is referred to as **R**epresentati**o**n Learning fr**o**m **St**oichiometry (or *Roost*) and achieved a MAE of 0.03 eV/atom on a test set of formation energies. In Chapter 7 of this thesis, we will compare results from this methodology to a predictive theory we develop which has specific application to binary oxides, a subset of materials which are especially relevant for heterogeneous OER.

1.4.1 *Materials data for OER catalyst discovery*

A recent development in computational OER research involves combining activity and stability descriptors to screen for potential catalysts which are active and stable in acidic conditions to identify cheaper alternatives to IrO_2 in PEM electrolysis. These studies tend to employ the MP database to query for aqueous stability descriptors for entries hosted on the site. One such study filtered out candidate materials predicted to be unstable by calculation of ΔG_{pbx} at pH = 0 and a range of applied potentials relevant for the OER, reducing the search space drastically from 47,814 to 68, and then tested the remaining catalysts for surface reactivity and conductivity, leaving 15 remaining.[71] This approach was also applied to 2D materials gathered from C2DB,[72] MaterialsCloud[73] and 2Dmatpedia,[74] computational materials databases tailored to 2D materials, finding that the acidic stability filter reduced the search space from 11,000 to 35.[75] Without a thorough benchmarking of every material it is not possible to test the true positive and true negative rates of such a filter, but the power of such a filter lies in how discriminative it is by confining a search towards materials which we have evidence for being acid stable. Other works have applied

the filter to newly generated calculations of stability at pH = 0 and an applied potential of 1.23 V_{SHE} for equimolar polymorphs of binary oxides of the form $A_{0.5}B_{0.5}O_2$ and $A_{0.5}B_{0.5}O_3$.[76] Recent work has also hypothesized an intimate relationship between activity and stability by considering all catalysts stability along with their *ab initio* calculated reactivity from open-source repository Catalysis-Hub.[77] In doing so they noted that the most active catalysts appear to require some lower limit of instability with values for ΔG_{pbx} of approximately 0.2 eV/atom .[78] They reason that this is related to the difference in the number of d-electrons between the catalyst and the most stable aqueous species;[78] if this difference is 0, the catalyst is stable yet inactive, if this difference is very high, the catalyst is too unstable, They therefore propose there is a goldilocks region which the likes of IrO_2 inhabit, with this rutile oxide being just stable enough with respect to the most stable $IrO_4^{[2-]}(aq)$ species.

1.5 Thesis outline

A common thread running through this thesis is a focus on the *throughput* of water splitting which we model computationally. The motivation for this emphasis arises from a desire to draw high-level and general trends from data, trends which would not be possible to glean by studying single catalysts independently, but at higher detail. To accelerate the discovery of hybrid OER catalysts we take a two-pronged approach by developing descriptors in homogeneous and heterogeneous catalysis to enable future research with the tools to perform faster analyses using our descriptors. In homogeneous catalysis we focus on testing the existence of scaling relations for molecular systems, and then apply the derived knowledge to develop descriptors for screening. We also test the discriminative power of computation in distinguishing active catalysts from inactive ones. In heterogeneous catalysis we tackle the issue of catalyst stability by developing a general methodology to predict material formation energies of binary oxides with stoichiometry $A_{1-z}B_zO_2$, enabled

by data ingested from MP and OQMD which we use to forecast stability and screen for stable catalysts in the acidic regime and under the harsh, oxidising environments of PEM electrolysers. A general overview of the structure of the thesis is shown in Figure 1.5, depicting how the homogeneous and heterogeneous chapters are delineated, and which chapters focus on descriptors and method development and which ones focus on applying those descriptors and methods for screening.

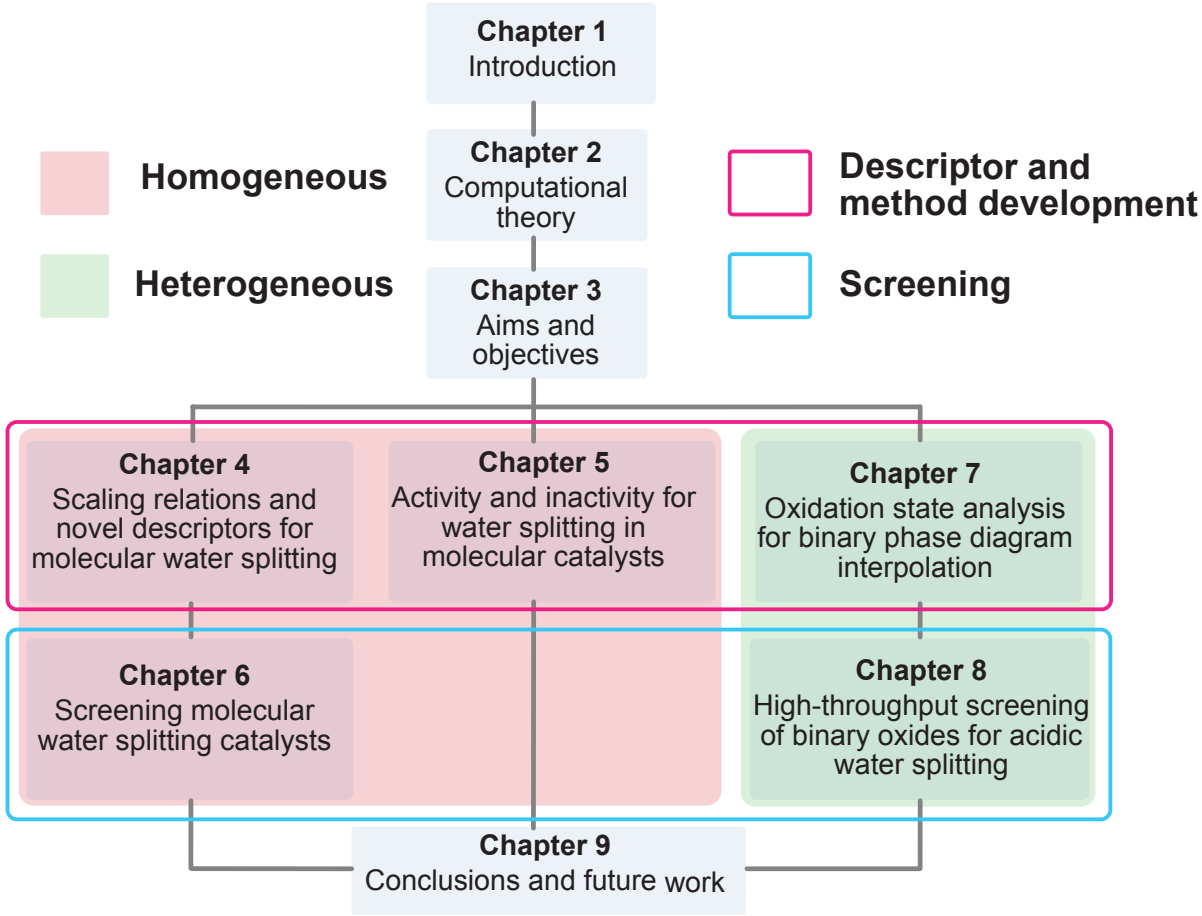

Figure 1.5. Graphical outline of the contents contained in this thesis.

Chapter 2 Computational Theory

2.1 Schrödinger equation

An essential equation in the foundation of theoretical chemistry is the non-relativistic Schrödinger equation, shown in Eq. 2.1, which describes the energy of a general chemical system.

$$\left(-\sum_i \frac{\hbar^2}{2m_e}\nabla_i^2 - \sum_k \frac{\hbar^2}{2m_N}\nabla_k^2 - \sum_i\sum_k \frac{e^2 Z_k}{r_{ik}} + \sum_{i<j}\frac{e^2}{r_{ij}} + \sum_{k<l}\frac{e^2 Z_k Z_l}{r_{kl}}\right)\Psi = H\Psi = E\Psi \quad (2.1)$$

The indices i and j run over electrons, k and l over nuclei, and Z denotes the nuclear atomic number, with Ψ the wavefunction. The action of the operator within the brackets on the left-hand side of Eq. 2.1 is known as the Hamiltonian, H, and returns the system eigenvalue, E. From left to right, the terms denote the electronic kinetic energy, the nuclear kinetic energy, electron-nuclear interaction, electron-electron interaction, and nuclear-nuclear interactions. Throughout this thesis we apply the Born-Oppenheimer approximation,[79] which considers the nuclear positions to be fixed, an approximation that is justified in circumstances where the nuclei move far slower than electrons. This approximation allows for the nuclear kinetic energy to be neglected, and the nuclear-nuclear interaction can be considered constant. Then, Eq. 2.1 simplifies as shown in Eq. 2.2.

$$\left(-\sum_i \frac{\hbar^2}{2m_e}\nabla_i^2 - \sum_i\sum_k \frac{e^2 Z_k}{r_{ik}} + \sum_{i<j}\frac{e^2}{r_{ij}}\right)\Psi = E\Psi \quad (2.2)$$

Equation 2.2 is extremely difficult to solve analytically for all but the simplest cases, so it is tackled numerically when applied to more interesting physical and chemical phenomena. A primary prescription we have for improving the wavefunction in this way – assuming it is well described, which we will outline in later sections of this chapter – is the variational

principle, shown in Eq. 2.3 and derived by imposing the orthonormality of the wavefunction. This principle sets out how to arrive at a ground state energy E_0 from the wavefunction Ψ. We take wavefunction which leads to the minimum possible energy, which we denote the ground state energy, E_0.

$$\frac{\int \Psi^* H \Psi \, dr}{\int \Psi^* \Psi} \geq E_0 \tag{2.3}$$

This recasts the problem in Eq. 2.2 as an optimisation problem, since the lower the eigenvalue found for a given choice of Ψ, the better our description of the ground state. Furthermore, we construct using single electron Hamiltonians, for $h(i)$ electron i, leading to:

$$H = \sum_{i}^{N} h(i) \tag{2.4}$$

This results in spin orbitals satisfying the equation

$$h(i)\psi_j(x_i) = \varepsilon_j \psi_j(x_i) \tag{2.5}$$

with electron i occupying an orbital ψ_j with energy ε_j. In order to satisfy the Pauli exclusion principle so that the sign of Ψ is inverted upon swapping electrons, we use a Slater determinant to avoid violations of the Pauli exclusion principle so for an N electron wavefunction:

$$\Psi = |\psi_i(x_1)\psi_j(x_2) \dots \psi_\eta(x_N)| \tag{2.6}$$

where we assume the application of a normalisation constant such that $\int \Psi^* \Psi = 1$. Wavefunction theory has progressed by continually improving prescriptions for creating Ψ. However, owing to its simplicity and computational efficiency, density functional theory (DFT) has seen more widespread use in describing chemical systems of interest.[80,81] In the following, we will describe the theoretical basis for DFT, as well as the methods adopted for our studies of molecular OER catalysts.

2.2 Density functional theory

We can only obtain physically meaningful properties from the wavefunction using quantum mechanical operators, and the electronic wavefunction depends on $3N$ variables for each spin. This motivates the question: can we construct a Hamiltonian from another physical value which also depends on less variables? One sensible physical observable to use would be the electron density, ρ, which is equal to N when integrated over all space and depends on just three spatial coordinates for a given point in space.

Early approaches to solve Eq. 2.2 by optimising the electron density, assumed non-interacting electrons and an infinite uniform electron gas.[82–84] This led to the Thomas-Fermi model, with an energy functional as shown in Eq. 2.7.

$$E[\rho(r)] = \frac{3}{10}(3\pi^2)^{\frac{2}{3}}\int \rho(r)^{\frac{5}{3}}dr - \sum_k \int \frac{Z_k}{|r - R_k|}\rho(r)dr + \frac{1}{2}\iint \frac{\rho(r_1)\rho(r_2)}{r_{12}}dr_1 dr_2 \quad (2.7)$$

Note that in the above equation we have switched to atomic units for notational simplicity. Such early density functional theories varied in the description of the kinetic energy density functional, the first term, and showed poor performance for realistic chemical systems. This is because they do not account for electron exchange and correlation. The biggest source of error from this approach comes from the kinetic energy.

Ultimately, this method predated the theoretical basis for modern DFT methods, which we will now describe.

2.2.1. Hohenberg-Kohn theorems and Kohn-Sham DFT

The first foundational theorem of DFT from Hohenberg and Kohn proves that a nondegenerate ground state density of a system is uniquely determined by a specific external potential.[85] The proof is carried out via *reductio ad absurdum* by showing that if different external potentials can describe the same ground state density, a contradictory

inequality is derived between the same expressions. The second theorem used this proof along with Eq. 2.3 to show that energy functionals of the density, $E[\rho(r)]$, can also obey the variational principle.

Kohn and Sham then provided a key insight to consider a fictitious system of non-interacting electrons with the same density as a real system of interest which does contain interacting electrons.[86] The functional which describes this treatment is shown in Eq. 2.8 where we approximate the kinetic energy using Slater determinants composed from ψ_i as in Eq. 2.5 to describe a system of non-interacting electrons with the same density as the exact electronic wave function.

$$E[\rho(r)] = -\frac{1}{2}\sum_i \int \psi_i^*(r)\nabla^2\psi_i(r)dr - \sum_k \int \frac{Z_k}{|r-R_k|}\rho(r)dr + \frac{1}{2}\iint \frac{\rho(r_1)\rho(r_2)}{r_{12}}dr_1dr_2 + E_{xc}[\rho(r)] \quad (2.8)$$

The only unknown term in this expression is the exchange-correlation functional, $E_{xc}[\rho(\boldsymbol{r})]$, which contains the difference in kinetic energy between the interacting and non-interacting systems as well as the non-classical electron-electron interactions. The action of one-electron operators are assumed separable, so the one-electron Kohn-Sham Hamiltonian, h_i^{KS}, for electron i can be applied to monoelectronic wavefunctions ψ, which minimise E.

$$h_i^{KS}\psi_i = \left(-\frac{1}{2}\nabla_i^2 - \sum_k \frac{Z_k}{|r_i - R_k|} + \int \frac{\rho(r')dr'}{|r_i - r'|} + \frac{\delta E_{xc}}{\delta\rho}\right)\psi_i = \varepsilon_i\psi_i \quad (2.9)$$

We do not know the form of the wavefunction without applying h_i^{KS}, yet this in turn depends on the wavefunction. Therefore, we must apply Eq. 2.9 self-consistently[87] by initially guessing $\rho(r)$, constructing and solving Eq. 2.9 to form better coefficients for the

orbital coefficients, and then applying $\rho(r) = \sum_i^N |\psi_i(r)|^2$ where N is the number of electrons. This scheme is performed iteratively until a convergence criterion is met.

A primary issue with this approach is that $E_{xc}[\rho(r)]$ is unknown, and there is no prescription for how it should be described, although if it were to be discovered, we could solve Eq. 2.9 exactly. In the following, we outline how this exchange-correlation functional is approximated, and how it varies across the functionals applied within this thesis.

2.2.1 *Electronic exchange and correlation*

In this section we use the common notation to construct an exchange-correlation energy functional, ε_{xc}, which is comprised of the sum of individual components of exchange and correlation functionals, E_x and E_c, respectively, where E_x is defined in Eq. 2.10.

$$E_x[\rho(r)] = \int \rho\,(r)\varepsilon_x dr \tag{2.10}$$

The simplest approach to construct ε_x is to assume that it depends only on the value of ρ at a given position. If we assume a uniform electron gas (UEG), as Dirac and Slater did prior to the Kohn-Sham theorems,[83,84] we can derive the exchange energy in Eq. 2.11.

$$E_x^{UEG}[\rho(r)] = \int \rho\,(r)\varepsilon_x^{UEG} dr = -\frac{3}{4}\left(\frac{3}{\pi}\right)^{\frac{1}{3}} \int \rho\,(r)^{\frac{4}{3}} dr \tag{2.11}$$

This leads to an exchange-correlation functional known as the local density approximation (LDA) because it depends only on the local density at a given position. The use of these LDA-type functionals is only justified in cases where the electron density varies slowly, and improved results in molecular reaction energies are found when ε_{xc} includes higher-order derivatives of the electron density.[88–90]

2.2.2 *Generalised gradient approximation (GGA)*

Including both the density and the spatial derivative of the density in ε_{xc} leads to functionals known as generalised gradient approximation functionals, or GGAs. These are typically constructed by appending another term or series of terms to the integral in Eq. 2.11, which

are functions of the dimensionless quantity, $x = |\nabla\rho|/\rho^{4/3}$. As an example, one popular GGA is the Perdew-Burke-Ernzerhof (PBE) functional,[91] shown in Eq. 2.12

$$E_x^{PBE} = \int \rho\,(r)\varepsilon_x^{UEG}(1 + \frac{c_x\gamma x^2}{1+\gamma x^2})dr \qquad (2.12)$$

with values for non-linear parameters γ and c_x derived by restricting the form of E_x^{PBE} in low and high-density limits, and low- and high-density varying limits. The correlation energy is a parametrised function which is also subject to mathematically inspired constraints.

In this thesis, we have employed a GGA functional known as Bayesian error estimation framework with van der Waals corrections, or BEEF-vdW.[92] This functional has seen widespread use due to the impressive performance shown for adsorption energies and transition state barriers on transition metal surfaces.[93,94] Unlike PBE, this GGA functional uses a systematic empiricist approach to arrive at E_{xc}, while also allowing for the quantification of DFT uncertainty. In the following, we briefly describe how this is achieved.

To describe the exchange energy, ε_{xc} is expanded in a power series of the reduced density gradient using Legendre polynomials. Correlation energy is then described using local LDA, E^{LDA-c}, semi-local PBE correlation, E^{PBE-c}, along with vdW-DF2 nonlocal correlation,[95] E^{nl-c}, to account for non-covalent interactions, which we describe later in this chapter.

$$E_{xc}^{BEEF-vdW} = \sum_{m=0}^{29} a_m E_m^{GGA-x} + \alpha_c E^{LDA-c} + (1-\alpha_c)E^{PBE-c} + E^{nl-c} \qquad (2.13)$$

By inspection of the above equation, we can see that this functional is dependent on 31 coefficients. The cost function which defines how these coefficients are updated is regularised to reduce overfitting. Datasets of molecular formation and reaction energies,

transition state energy barriers, non-covalent interactions, and solid-state properties were used to arrive at the optimum parameters for Eq. 2.13 with α_c=0.6001664769 and the series of α_m values shown in Table 2.1.

Table 2.1. Coefficients for the Legendre polynomial expansion in Eq. 2.13.

m	α_m	m	α_m
0	$1.516501714 \times 10^{0}$	15	$-8.018718848\times10^{-4}$
1	$4.413532099 \times 10^{-1}$	16	$-6.688078723\times10^{-4}$
2	$-9.182135241\times10^{-2}$	17	1.030936331×10^{-3}
3	$-2.352754331\times10^{-2}$	18	$-3.673838660\times10^{-4}$
4	3.418828455×10^{-2}	19	$-4.213635394\times10^{-4}$
5	2.411870076×10^{-3}	20	5.761607992×10^{-4}
6	$-1.416381352\times10^{-2}$	21	$-8.346503735\times10^{-5}$
7	6.975895581×10^{-4}	22	$-4.458447585\times10^{-4}$
8	9.859205137×10^{-3}	23	4.601290092×10^{-4}
9	$-6.737855051\times10^{-3}$	24	$-5.231775398\times10^{-6}$
10	$-1.573330824\times10^{-3}$	25	$-4.239570471\times10^{-4}$
11	5.036146253×10^{-3}	26	3.750190679×10^{-4}
12	$-2.569472453\times10^{-3}$	27	2.114938125×10^{-5}
13	$-9.874953976\times10^{-4}$	28	$-1.904911565\times10^{-4}$
14	2.033722895×10^{-3}	29	7.384362421×10^{-5}

A further family of functionals include the second derivative of the electron density in the description of the exchange-correlation functional, as detailed in the next section.

2.2.3 *Meta GGAs*

Meta-GGA functionals or mGGAs include the second derivative of the electron density in the description of the exchange-correlation energy density. Due to issues with numerical instability, the kinetic energy density, τ, is normally used to describe this second derivative instead of the Laplacian of the density, which is related to the second derivative of the density,[96] as seen in Eq. 2.14.

$$\tau(r) = \sum_{i}^{occ.} \frac{1}{2} |\nabla \psi_i(r)|^2 = \frac{\nabla^2 \rho}{2} - \sum_{i}^{occ.} \psi_i^*(r) \nabla^2 \psi_i(r) \qquad (2.14)$$

The kinetic energy density is then included in ε_{xc} along with ρ and $\nabla\rho$ in distinct ways, depending on the functional. In this thesis we have used the M06-L functional,[97] which has seen success in describing reaction barriers for transition metal complexes.[81,98,99] A further example mGGA developed by Perdew *et al.* is the TPSS functional,[100] derived by imposing mathematical constraints on the form of ε_{xc}^{mGGA} in the limits of high and low varying density.

In this thesis, we have used the TPSSh functional, a hybrid mGGA density functional derived from TPSS. We describe this group of functionals in the next section.

2.2.4 *Hybrid meta GGAs*

Density functional theories which mix the exact exchange of non-interacting electrons derived from Hartree-Fock[87,101,102] theory with exchange-correlation functionals derived from DFT are known as hybrid mGGAs or hybrid functionals. These functionals aid in the cancellation of the spurious self-interaction error (SIE) of electrons, inherent in DFT which arises from the Coulomb term in Eq. 2.8, $\frac{\rho(r_1)\rho(r_2)}{r_{12}} dr_1 dr_2$ which allows for the interaction of an electron with itself. For an exact exchange functional, this would not be possible, and this problem is magnified in cases where we wish to model systems with localized orbitals, as the electrons tend to delocalize to minimize the SIE.

In our case, to calculate ground state energies, we have applied the TPSSh hybrid mGGA functional,[103] which includes a 10% of HF exchange, derived by an empirical fit. The expression of this exchange-correlation functional is shown in Eq. 2.15.

$$E_{xc}^{TPSSh} = 0.9E_x^{TPSS} + 0.1E_x^{HF} + E_c^{TPSS} \tag{2.15}$$

This functional has been shown to give good results across reaction energy calculations,[80] hyperfine structure,[104] biochemistry,[105] and transition metal chemistry.[81] In addition, we have used the B3LYP functional,[106] which liberally mixes Hartree-Fock (HF) exchange through local and semi-local DFT exchange while the correlation energy is comprised of LDA and a different and semi-local DFT functionals.

2.2.5 *GGA+U*

Another way to tackle the SIE is the DFT+U approach which applies an energy penalty to partially occupied orbitals in the construction of the functional. Dudarev[107] described the introduction of a Hubbard term U on valence states for the Coulomb interactions and exchange parameter J. We then define an effective Hubbard parameter, $U_{eff} = U - J$, and apply the penalty as in Eq. 2.16

$$E_{GGA+U} = E_{GGA} + \frac{U_{eff}}{2} \sum_{I,\sigma} \sum_{i} \lambda_i^{I,\sigma} (1 - \lambda_i^{I,\sigma}) \tag{2.16}$$

Where $\lambda_i^{I,\sigma}$ is the occupation of orbital i on atom I. By construction, this correction is non-existent if the orbital is either fully occupied or fully unoccupied. The appropriate U_{eff} must be chosen carefully since it may be necessary to use different values for different applications. In our case, we use GGA+U-derived energies which are used by the Materials Project database.[65,108]

All functionals described thus far assume that only local information about the electron density is sufficient to describe E_{xc}, neglecting long-range, dynamic correlation. These adverse effects can be addressed by considering non-covalent interactions.

2.2.6 *Dispersion corrections*

There are many approaches to including the effects of non-covalent interactions, which are a result of long-range electron correlation. One approach involves including an energy functional into the one-electron Hamiltonian, as is carried out in the vdW-DF2 method.[95] In this thesis, we have accounted for dispersion using another well-established approach, Grimme-D3 dispersion corrections,[109] which adds a correction term, E_{disp}, to the energy calculated by DFT according to the following expression:

$$E_{disp} = -\sum_{AB}\sum_{n=6,8} s_n \frac{C_n^{AB}}{r_{AB}^n} f_{d,n}(r_{AB}) \tag{2.17}$$

where AB denotes an atom-atom pair within a molecule, s_n is a density functional-dependent scaling factors, r_{AB}^n the interatomic distance, C_n^{AB} an atom-atom specific, fitted coefficient and $f_{d,n}$ a damping function to determine the range of the dispersion correction. The incorporation of long-range interactions has seen success in reducing the errors of dispersion-bound alkane dimers.[80]

2.3 Linear combination of atomic orbitals

To represent the wavefunction Ψ in Eq. 2.6, we must represent the orbitals, ψ_i, from which they are constructed sensibly. This is achieved with mathematical basis sets which are simply linear combinations of atomic orbitals (LCAO) which we call a molecular orbital.

$$\psi_i = \sum_a C_a^i \varphi_a \tag{2.18}$$

where C_a^i represents the coefficient for atomic orbital φ_a within the molecular orbital ψ_i. We can use these coefficients to obtain the wavefunction with the lowest energy, allowing for the application of the variational principle.

The following sections briefly outline how basis functions which are applied in this thesis are constructed.

2.3.1 *Gaussian basis sets*

The use of Gaussian functions to represent wavefunctions was first introduced by Boys,[110] enabling *ab initio* wavefunction evaluations to be realised. Their essential advantage is that multiplication and addition of two Gaussians leads to another Gaussian, aiding computational efficiency and integral evaluations. The form of Gaussian type orbitals (GTOs) is shown in Eq. 2.19

$$\gamma(x, y, z; \alpha, i, j, k) = N x^i y^j z^k e^{-\alpha(x^2+y^2+z^2)} \tag{2.19}$$

where N is a normalisation constant, x, y and z represent cartesian coordinates and i, j and k are integers, with s-type orbitals for $i = j = k = 0$, p-type for $i + j + k = 1$ and d-type for $i + j + k = 2$. The use of Gaussian basis sets to describe wavefunctions seems curious, as the qualitative shape of individual Gaussians do not resemble $1s$ orbitals, which exhibit a cusp at the nucleus where Gaussians do not, and decay much slower than GTOs. This is resolved through the linear combination of GTOs, first determined for a selection of atoms by Pople *et al.*,[111] defining basis functions such as φ

$$\varphi = \sum_i^M d_i \gamma(x, y, z; \alpha, i, j, k) \tag{2.20}$$

with coefficients d_i chosen to represent the atomic orbital correctly. These coefficients d_i are held fixed while the α coefficients in the exponent are free to vary. This basis set is known as STO–MG with M the number of GTOs used to make up φ, which represents atomic orbitals.

Basis functions as shown in Eq. 2.19 are not sufficient to describe changes in valence orbitals, as they do not allow for the electron density to adjust in response to the surrounding atoms. Therefore, multiple functions with different exponents and coefficients are used to describe valence orbitals, allowing for greater flexibility. This approach is known as split-valence, where 'tight' functions with high α values and 'loose' functions with low α values

are combined to describe valence orbitals. We will describe the common notation of split-valence basis sets through an example. The 6-31G[112,113] basis set uses $M = 6$ gaussian functions for core orbitals, while valence orbitals are described through a linear combination of 3 inner valence or 'tight' and 1 outer valence or 'loose' function of the form of φ; the letter G only indicates that Gaussian functions are used.

Polarisation functions must also be added to our basis set for improved molecular descriptions. This is typically addressed by adding further GTOs with higher quantum numbers of angular momentum. If we were to add a single polarisation function, s-type orbitals would be additionally represented by p-type polarisation functions and p-type orbitals by d-type polarisation functions. The nomenclature for such a basis set would be 6-31G(d,p), the first letter denoting atoms heavier than He and the second letter H and He atoms.

Finally, diffuse functions are often added to allow for electrons to lie far from the nucleus; their use is signalled through a '+' sign. In this thesis, we have applied the 6-31+G(d,p), meaning atoms heavier than He have been described by an additional one s and one set of p-functions with small α.

In our study of molecular OER catalysts, we have used a 6-31G(p) basis set for C and H atoms and a 6-31+G(d,p) for the more electronegative N, O, F and Cl atoms. The choice of this basis is founded upon previous studies which found that, when using DFT, this basis set size has produced good results in organometallic reactions.[114,115]

In the next section we outline how we described the metal centres of the molecular catalysts, which are of utmost importance.

2.3.2 *Effective core potentials*

In the case of transition metals, the large number of electrons associated with such atoms and the relativistic speeds of core electrons make describing an appropriate GTO difficult.

Therefore, analytic functions, called effective core potentials (ECPs) are often used to describe the core electrons of these heavier elements. In our case, we have applied the LANL2DZ[116] ECP for transition metals, where the DZ denotes a double-zeta or synonymously split-valence description of the valence electrons. In tandem with this ECP and basis set, we have used the optimised coefficients for the accompanying f-type polarisation functions.[117]

2.3.3 *Mulliken population analysis*

To assess the number of unpaired electrons in the system we have used the Mulliken charge scheme,[118–121] which uses the concept of LCAOs. We outline the algorithm using an example for a diatomic molecule with a normalised MO, ψ_i which can be written in terms of their respective spin orbitals, χ_α and χ_β

$$\psi_i = c_{i\alpha}\chi_\alpha + c_{i\beta}\chi_\beta \tag{2.21}$$

we then describe the charge distribution by squaring this wavefunction

$$\psi_i^2 = c_{i\alpha}^2\chi_\alpha^2 + c_{i\beta}^2\chi_\beta^2 + 2c_{i\alpha}c_{i\beta}\chi_\alpha\chi_\beta \tag{2.22}$$

integrating over all electronic coordinates, and using the fact that the spin orbitals and MOs are normalized

$$1 = c_{i\alpha}^2 + c_{i\beta}^2 + 2c_{i\alpha}c_{i\beta}S_{\alpha\beta} \tag{2.23}$$

where $S_{\alpha\beta}$ denotes an overlap integral. In the Mulliken interpretation, one electron in the MO contributes $c_{i\alpha}^2$ to spin orbital χ_α and $c_{i\beta}^2$ to spin orbital χ_β. For open shell systems with unpaired electrons, we take the difference between spin up and spin down Mulliken charges, and take this to be the spin density on a given atom. This is a simple scheme to calculate charge populations, however, it suffers from method-dependence since it is sensitive to the representation applied for a given problem such as the method or the type of basis set.[122]

2.3.4 *Plane wave basis sets*

We use plane wave basis sets as a brief proof of concept that scaling relations derived from localized basis sets are also seen for other types of basis sets. Therefore, we provide only a brief overview of the theory behind plane wave basis sets. If we consider the system for which we solve the Kohn-Sham equations to be periodic so it can be defined as an infinite, regular lattice, we can make use of Bloch's theorem.[123] This theorem determines that eigenfunctions, $\psi(r)$, of a periodic Hamiltonian can be written as a product of $e^{ik\cdot r}$ – with wavevector k in the first Brillouin zone – and a function, $u(r)$ with the same period as the lattice. The Brillouin zone defines the unit cell which contains all points in reciprocal space and are closer to the origin than to any other point of the reciprocal lattice. We can respect the periodicity of u by setting it proportional to $e^{iK\cdot r}$, with K the lattice vector in reciprocal space. This leads to plane waves of the form,

$$\psi_k^n(r) = \sum_K c_K^{n,k} e^{i(k+K)\cdot r} \tag{2.24}$$

with n labelling which Brillouin zone the eigenfunction represents. Since working with infinite basis sets is impractical, we must restrict the summation in Eq. 2.24 by setting a maximum K_{max} while taking considerations for the appropriate form of the wavefunction. Concretely, K_{max} must be large enough to describe changes of the wavefunction over small regions of real space. We will refer to K_{max} through the energy cut-off, E_{cut} shown in Eq. 2.25.

$$E_{cut} = \frac{\hbar^2 K_{max}^2}{2m_e} \tag{2.25}$$

For core electrons, plane waves are impractical since their wavefunctions vary over a very short distance, so pseudopotentials must be used to represent wavefunctions for those electrons. In this report, we have employed the widely used projected augmented-wave pseudopotentials.[124,125]

2.4 Potential energy surface

To apply these sophisticated mathematical treatments to real-world experimental data we need to introduce a way of considering all possible arrangements a molecule can take up. To do this we introduce the concept of a potential energy surface (PES) represents the potential energy of a set of atoms over their possible configurations. This is a $3N-6$ dimensional surface where $N \geq 3$ and denotes the number of atoms. The points which represent the ground state on these surfaces are the local minima, where all first order derivatives are zero, and second order derivatives over the potential energy surface are positive. In practice, quantum chemical codes require that the derivatives are below a certain user-defined threshold and are confirmed as true stationary points by performing frequency calculations which determine the curvature at a point in the PES by calculating the curvature along cartesian nuclear coordinates. Another interesting concept which we use in this thesis is the saddle point of a PES where all but one coordinate – the reaction coordinate – with a negative second derivative along that coordinate and with all first order derivatives are zero. This saddle point in the PES then defines the geometry of the transition state along that reaction coordinate, a coordinate which we define as a specific bond distance throughout this thesis, though this could in principle be any coordinate. To calculate the activation energy, we calculate the difference in energy between this saddle point and the global minim preceding it.

2.5 Modelling the solvent

Catalytic reactions of relevance to the OER are carried out in solution, not in vacuum conditions as we assume in calculations, and moving from the gas phase to the solvent phase can greatly impact a chemical reaction. The energy of solvation can completely alter the PES with respect to the gas phase.[126] Water is of particular relevance to the OER and can play a non-innocent role in chemical reactivity and can participate in oxygen

evolution.[127] We could account for this effect by adding water molecules explicitly, so as to enclose molecular OER catalysts within a layer of solvation. However, this approach quickly runs into problems. In particular, the first solvation shell can require hundreds of waters; we also do not have an unbiased method of choosing the correct number of water molecules to solvate arbitrary molecules the same way and sampling all possible energy minima is intractable with current computational resources.

This difficulty has led to the development of computationally efficient schemes of treating the effect of the solvent by means of continuum models. We perform this by representing the charge distribution of the solvent as a continuum with a dielectric constant. As such, these implicit solvation models account for electrostatic and non-electrostatic interactions between solute and solvent without considering explicit solvent molecules. These models define a solvation energy ΔG_S^o which is broken down into three contributions as in Eq. 2.26

$$\Delta G_S^o = \Delta G_{ENP} + G_{CDS} + \Delta G_{conc}^o \tag{2.26}$$

where the ΔG_{ENP} term denotes the difference between the gas phase and liquid phase structure in electronic (E), nuclear (N) and polarization (P) components of the free energy. The G_{CDS} term relates to the solvation energy change arising from solvent cavitation, (C) dispersion (D) and changes in the structure of the solvent (S). The ΔG_{conc}^o term then is a result of the concentration change between gas and liquid-phase standard states.

A linear isotropic nonhomogeneous medium to form cavities is then defined as[128]

$$\nabla \cdot (\varepsilon \nabla \Phi) = -4\pi\rho_f \tag{2.27}$$

where ε is the dielectric constant, Φ is the electrostatic potential and ρ_f is the charge density of the solute, where each value is set on the points of a discretized grid. Since the solution of Eq. 2.27 depends on the solute charge density, it must be solved iteratively, in a procedure known as the self-consistent reaction field (SCRF) scheme.[129,130]

In our studies, we have used the SMD solvent model,[131] which, like most implicit solvation models also accounts for solute-solvent interactions which are not electrostatic in nature. This is performed by considering the amount of solvent-accessible surface area to be linearly related to solvation energy interaction, a reasonable assumption based on experimental investigations of solvation energy.[132] This area is found by considering atomic van der Waals radii of the solvent molecule. The area where a given atom meets the solvent is included in a parametrized function which also contains values representing atom specific parameters, pairwise atomic parameters as well as solvent specific parameters such as its refractive index. Through the use of linear regression, this function is fit to 2,821 experimental solvation energy datapoints.[131]

As well as the solvent effects, we must also consider the conditions within electrochemical environments, as outlined in the next section.

2.6 Modelling electrocatalysis

The working condition of an electrochemical cell is dynamic, with an applied bias, electrical double layer, electrolyte-electrolyte and electrode-electrolyte interactions. How can we use DFT calculations to account for this? In the following we will describe the theoretical background justifying our use of the thermodynamic potentials used throughout this thesis.

2.6.1 *Thermochemistry*

The spontaneity of a reaction can be determined by calculating the Gibbs energy difference, ΔG, between reactants and products. We calculate the electronic energy from KS-DFT (E), and use statistical thermodynamics to determine the zero-point vibrational energy, ZPE and the entropic contributions, S, to arrive at G as in Eq. 2.28

$$G = E + ZPE + PV - TS \tag{2.28}$$

for a given temperature T. For molecular systems, the common practice is to consider the translational, rotational, vibrational and electronic contributions to the entropy.[133] We often treat ΔV term as negligible, and as such approximate the energy as the enthalpy. The common approach in computational surface catalysis is to only account for the vibrational and electronic contributions of the adsorbate. This can be introduced, for example, via the thermochemistry package in the Atomic Simulation Environment.[134]

2.6.2 *Computational hydrogen electrode model*

In this thesis, we have applied the computational hydrogen electrode[135] (CHE) model to the problem of attempting to describe the environments under which electrochemistry occurs. Setting the reference potential to the standard hydrogen electrode (SHE), the CHE model equates the Gibbs energy of one half the hydrogen molecule to that of a proton and electron pair because these species are taken to be in equilibrium at 0 V. Thus, we assume the solvated protons and electrons are in equilibrium with gas phase hydrogen

$$H^+(aq) + e^- \rightleftharpoons \frac{1}{2}H_2(g) \tag{2.29}$$

Expressed in terms of chemical potentials:

$$\mu_{H^+(aq)} + \mu_{e^-} = \frac{1}{2}\mu_{H_2(g)} \tag{2.30}$$

We can express these chemical potentials of these species in terms of the activity of the protons, a_{H^+}, which relates to pH, Boltzmann's constant k_B and the shift in electron energy assumed when a potential $U$is applied and the partial pressure of hydrogen in the system $p_{H_2(g)}$ as:

$$\mu_{H^+(aq)} = \mu^0_{H^+(aq)} + k_B T ln a_{H^+} \tag{2.31}$$

$$\mu_{e^-} = \mu^0_{e^-} - eU \tag{2.32}$$

$$\mu_{H_2(g)} = \mu^0_{H_2(g)} + k_B T ln p_{H_2(g)} \tag{2.33}$$

Where the $\mu^0_{H^+(aq)}$, $\mu^0_{e^-}$, and $\mu^0_{H_2(g)}$ values denote the chemical potentials at standard conditions, *i.e.* ($p_{H_2(g)} = 1\,bar,\ a_{H^+} = 1,\ T = 298.15\,K$). At these conditions the standard state chemical potentials are equal, and therefore, we can calculate the chemical potential of hydrogen in the gas phase using DFT.

To model water in the liquid phase, which is relevant for OER, we make an approximation by calculating the internal energy of water in the gas phase using DFT but calculating the chemical potential at $T = 298.15$ and 0.035 bar, conditions at which gas and liquid water are in equilibrium.

$$\mu_{H_2O(l)} = \mu_{H_2O(g)} \tag{2.34}$$

Finally, the effect of the electric field imposed by the double layer can be neglected when the dipole moment of the adsorbate considered is sufficiently small.[135,136] This method, therefore, allows for approximate calculation of the PCET steps involved in an electrochemical reaction through DFT calculations.[137]

2.6.3 *Modelling the oxygen evolution reaction*

Through application of the CHE model and the calculation of the Gibbs energies, we can evaluate the elementary steps of the OER process. For example, take the first PCET which involves the formation of an HO* intermediate, we can obtain the Gibbs reaction energy for this step as:

$$H_2O + * \rightarrow HO^* + H^+ + e^-$$
$$\Delta G_1 = G_{HO^*} + \mu_{H^+(aq)} + \mu_{e^-} - G_* - \mu_{H_2O(l)} \tag{2.35}$$

Where G_{HO^*} and G_* represent the Gibbs energies of an active site with and without HO* respectively. Using Eqs. 2.31, 2.32 and 2.34:

$$\Delta G_1 = G_{HO^*} + \mu^0_{H^+(aq)} + k_B T ln a_{H^+} + \mu^0_{e^-} - eU - G_* - \mu_{H_2O(g)} \tag{2.36}$$

Then, using Eq. 2.30 and the fact that we can express the chemical potentials of hydrogen and water in the gas phase using their DFT-calculated energies, $E_{H_2O(g)}$ and $E_{H_2(g)}$

$$\Delta G_1 = E_{HO^*} - E_* - \left(E_{H_2O(g)} - \frac{1}{2}E_{H_2(g)}\right) + \Delta ZPE - T\Delta S + k_B T ln a_{H^+} - eU \quad (2.37)$$

Where we have collected the entropic and zero-point energies from each of the four species into ΔZPE and $-T\Delta S$. We then gather the calculated terms on the right-hand side of the equation and denote them as $\Delta G_{HO^*} = G_{HO^*} - G_*$

$$H_2O + * \rightarrow HO^* + H^+ + e^-$$
$$\Delta G_1 = \Delta G_{HO^*} + k_B T \ln a_{H^+} - eU \quad (2.38)$$

The subsequent step in the OER is the PCET involved in the oxidation of the HO* species to O*, and by applying the same logic as in Eq. 2.34 we arrive at the following equation:

$$HO^* \rightarrow O^* + H^+ + e^-$$
$$\Delta G_2 = E_{O^*} - E_{HO^*} + \frac{1}{2}E_{H_2(g)} + \Delta ZPE - T\Delta S + k_B T ln a_{H^+} - eU \quad (2.39)$$

Once more we collect the terms and use the fact that the G_* terms in the binding energies of ΔG_{O^*} and ΔG_{HO^*} cancel, and to derive Eqs. 2.40–2.42 we appropriately balance $E_{H_2O(g)}$ and $E_{H_2(g)}$ depending on the reactants and products involved:

$$HO^* \rightarrow O^* + H^+ - e^-$$
$$\Delta G_2 = \Delta G_{O^*} - \Delta G_{HO^*} + k_B T \ln a_{H^+} - eU \quad (2.40)$$

$$O^* + H_2O \rightarrow HOO^* + H^+ - e^-$$
$$\Delta G_3 = \Delta G_{HOO^*} - \Delta G_{O^*} + k_B T \ln a_{H^+} - eU \quad (2.41)$$

$$HOO^* \rightarrow O_2 + H^+ + e^-$$
$$\Delta G_4 = G_{O_2} - \Delta G_{HOO^*} + k_B T \ln a_{H^+} = 4.92 \text{ eV} - \Delta G_{HOO^*} - eU + k_B T \ln a_{H^+} - eU \quad (2.42)$$

where ΔG_{HO^*}, ΔG_{O^*} and ΔG_{HOO^*} are the binding energies of each OER intermediate, and G_{O_2} is replaced by the experimental Gibbs reaction energy of 4.92 eV due to known issues in describing the triplet ground state of molecular oxygen with DFT.[138] This simplification is further justified since the dissociation of the oxygen molecule is rarely limiting. We use $T = 298.15\ K, pH = 0, P = 1\ bar$ and U is potential against the normal hydrogen electrode.

The theoretical overpotential, $\eta_{theor.}$, is then found through Eq. 2.43 where 1.23 V is the thermodynamic potential of the OER versus the reversible hydrogen electrode (RHE).

$$\eta_{theor.} = \frac{max(\Delta G_{1-4})}{e} - 1.23\ [V] \tag{2.43}$$

we have V in square brackets to denote the application of $U = 1.23\ V_{RHE}$. To model the Gibbs energy change associated with a molecular one-electron oxidation, we have used Eq. 2.44, where we denote the oxidized species as $G_{(+)^*}$.

$$\Delta G_{ox} = G_{(+)^*} - G_* + eE^*_{abs} \tag{2.44}$$

In Eq. 2.44 E^*_{abs} is the value assigned to the normal hydrogen electrode potential in water referenced in vacuum, for which we used a previously calculated value of $-4.28\ V$.[139] The method applied to arrive at this value uses the absolute solvation Gibbs energy of the proton calculated using the cluster pair approximation method. Enthalpy and entropy corrections are then added by numerically solving equations from Fermi–Dirac statistics.[140] This method showed appreciable agreement with previous studies of iron-based molecular water oxidation catalysts.[141]

Since activation barriers are not calculated in this thermodynamic analysis, $\eta_{theor.}$ represents a lower bound for the expected onset potential of OER, since the kinetics determine the overpotential. However, provided BEP relations[54] between reaction and activation energies hold, this analysis indirectly highlights where the highest transition state energy is expected to be.[55] Furthermore, the activation energies of the $HO^* \rightarrow O^*$ have been found to correlate to the reaction binding energies in a study of transition metals[142] and these barriers have also been shown to be on the order of 0.2 eV in a study of the electrochemical oxygen reduction reaction over a Pt(111) surface.[143] For these reasons, we neglected investigations into these activation barriers because such calculations require the modelling of explicit solvent and are computationally-intensive. As such, including these

calculations would not be amenable to high-level analyses of trends across molecular OER catalysis.

2.7 Thermodynamic stability of inorganic solids

An inorganic solid is defined by its structure and composition. Given these, we can use DFT to calculate a ground state energy, which is defined by that energy associated to the most stable arrangement of atoms for a given composition.

The stability of a structure A_aB_b in its ground state can then be forecast using its formation energy, ΔE_f, defined as the energy difference between the structure and the separated constituent parts

$$\Delta E_{f(A_aB_b)} = E_{A_aB_b} - aE_a - bE_b \tag{2.45}$$

This value is less than zero if A_aB_b does not segregate into phases A and B, and greater than zero if it does. This quantity is not enough to determine whether a material is thermodynamically stable, for this we need to consider all possible linear combinations of ground state formations energies of A and B phases, as well as any material in the $A-B$ chemical space. Creating a phase diagram in some quantity x, where this is often the molar concentration of a given element, we can create what is known as the convex hull which is formed from the lower envelope joining all datapoints across this chemical space, as shown in Figure 2.1. This lower envelope defines the boundary region of thermodynamic stability, with ΔE_{hull} representing the distance to the lower hull at a given point in the phase diagram. For instance, the MnO_3 datapoint shown in Figure 2.1 is an example of a material which is above this lower envelope and thereby unstable, while Mn_2O_3 is an example of a material which is on this lower envelope and stable; it is said to be on the hull.

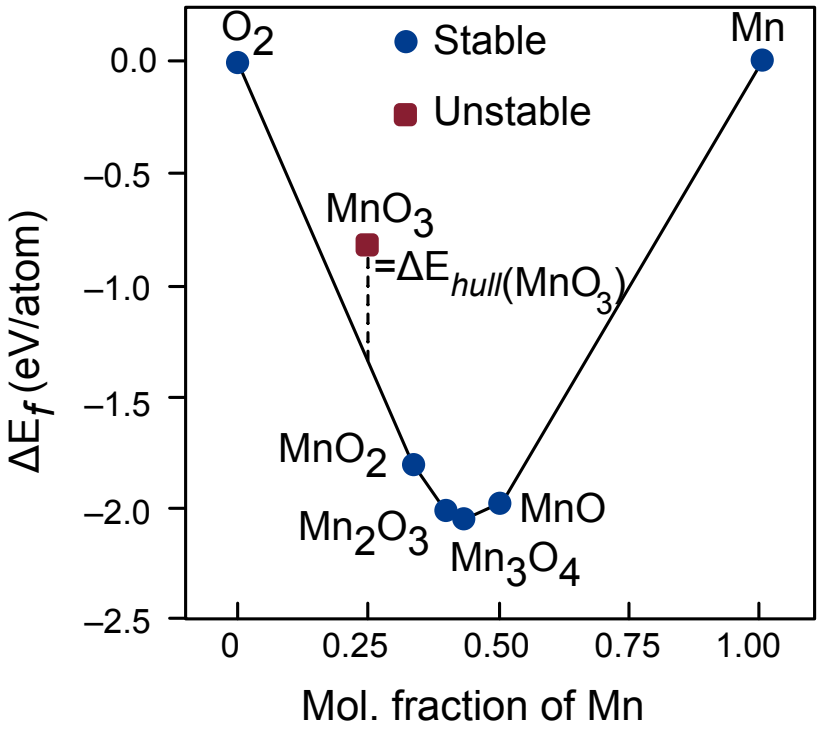

Figure 2.1. Convex hull phase diagram for the Mn–O system, with ΔE_f values calculated as in Eq. 2.45, and the convex hull connecting the points with $\Delta E_{hull} = 0$. A material with formula MnO_3 predicted to be above the convex hull is also shown to illustrate ΔE_{hull} qualitatively. Data is taken from the Materials Project database.[65] Blue/red points represent materials that are predicted to be stable/unstable with respect to phase segregation on the basis of the convex hull diagram formulation.

A material is predicted to be stable, then, if $\Delta E_{hull} = 0$, meaning there is no linear combination below that material on the convex hull and is said to be on the hull. We note here that there are many known materials with values of $\Delta E_{hull} > 0$ which are denoted metastable.[144] The scale of acceptable measures of metastability differ across chemistries. Some known, stable oxides exhibit calculated values of ΔE_{hull} on the order of 50 meV/atom, this is reasoned to be because known metastable materials are the result of syntheses processes which allowed a given material to be the lowest Gibbs energy phase at some point in the synthesis.[144]

DFT considers systems in vacuum at 0 K, so formation energies calculated from it can be mapped to formation enthalpies, ΔH_f, by including zero-point energy corrections and

integrating the heat capacity at constant volume up to the appropriate temperature. To model the Gibbs energy, we also need to consider entropy contributions, with vibrational entropy being the primary source of this contribution in most cases.[145] The internal energy E, H and G are related as:

$$G = H - TS = E + PV - TS \tag{2.46}$$

where P, T, V and S represent the pressure, temperature, volume, and entropy of the system, respectively. When considering the relative stability of condensed phases at standard pressure, the PV term is small and often neglected, and at 0 K we see that G then simplifies to E, which we can calculate with DFT. This analysis applies to closed systems, but we can extend this formalism such that it can treat varying compositions as a function of chemical potential under the grand chemical potential phase diagrams.

2.7.1 *Grand chemical potential phase diagram*

By modelling E and determining ΔE_{hull} values we can determine phase equilibria at a given controlled composition, often the environments of interest are controlled by a specific synthesis parameter such as the chemical potential of oxygen, μ_O. This parameter can, for instance, be varied by temperature or changes in oxygen environments such as N_2 or Ar atmosphere or, as is relevant to OER catalysts, by varying the applied potential. To introduce μ_{O_2} into a different thermodynamic potential than Eq. 2.45 we first need to incorporate the compositions of the constituent elements. The relevant thermodynamic potential to consider competing phases with respect to an oxidizing or reducing environment is the oxygen grand chemical potential, φ, developed by Ceder *et al.*[146] and defined as

$$\varphi\left(T, P, N_A, N_B, \mu_{O_2}\right) = G\left(T, P, N_A, N_B, \mu_{O_2}\right) - \mu_{O_2} N_{O_2}\left(T, P, N_A, N_B, \mu_{O_2}\right) \tag{2.47}$$

for a hypothetical $A - B - O$ system, where we use $N_{A/B} = x_{A/B}/(N_A + N_B + N_O)$ where $x_{A/B} = N_{A/B}/(N_A + N_B)$ to normalize with respect to number of particles in the system

using With these terms can normalize with respect to $A-B$ composition, and neglect the PV term to:

$$\bar{\varphi}\left(T,P,x_A,x_B,\mu_{O_2}\right) \approx \frac{E-TS-\mu_{O_2}N_{O_2}}{N_A+N_B} \tag{2.48}$$

To handle the entropic term, we assume that phase equilibria will occur through absorption or loss of oxygen gas, so that the entropy of this gas is taken to be the primary contribution, whose effect can be captured by the oxygen chemical potential:

$$\mu_{O_2}\left(T,p_{O_2}\right) = \mu_{O_2}(T,p_0) + kTln\frac{p_{O_2}}{p_0} \approx h_{O_2}(T,p_0) - T(s_{O_2}(T,p_0) - kln\frac{p_{O_2}}{p_0}) \tag{2.49}$$

With p_{O_2} the partial pressure of oxygen, p_0 a reference oxygen partial pressure, $\mu_{O_2}(T,p_0)$, $h_{O_2}(T,p_0)$, and $s_{O_2}(T,p_0)$ are the chemical potential of oxygen, enthalpy and entropy per molecule at a given temperature and at the reference oxygen partial pressure. The expression in Eq. 2.50 then simplifies to

$$\bar{\varphi}(T,P,x_A,x_B,\mu_O) \approx \frac{E-\mu_O N_O}{N_A+N_B} \tag{2.50}$$

Using Eq. 2.50, the effect of outside influences such as temperature and oxygen partial pressure on a multicomponent phase diagram can be captured by a single variable: μ_O. This approach was developed to study $Li-Fe-P-O$ phase equilibria,[146] which is highly technologically relevant for battery applications. Just as in Figure 2.1, we can calculate grand chemical potential formation energies $\bar{\varphi}_f$ within a chemical system, for varying values of μ_O, from which we can a convex hull analyses and calculate $\bar{\varphi}_{hull}$ within varying potential spaces. This approach has seen extensive use in screening for applications in Li-ion battery technology.[147,148]

2.7.2 *Pourbaix energy*

Marcel Pourbaix reported an atlas of data for almost every element in the periodic table, wherein it showed the species present for a given pH and redox potential in aqueous

solutions;[149] such diagrams are widely known as Pourbaix diagrams. To extend the analyses in the preceding section, which only consider solid-solid equilibrium, and to plot such Pourbaix diagrams, we require the Gibbs energy of potential redox reactions, $\Delta_r G^0$, for a binary $A-B$ system in aqueous media, which can be generally represented as

$$aA(s) + bB(s) + cH_2O(l) \rightarrow [A_aB_bO_cH_d]^m(aq) + (2c-d)H^+ + (2c-d+m)e^- \quad (2.51)$$

where a, b, c and d represent stoichiometric coefficients for A, B and O and m is the charge of the formed aqueous species $[A_aB_bO_cH_d]^m$. Using the Nernst equation, we can then relate the reaction Gibbs energy change to the charge transferred as:

$$-(2c-d+m)FE^0 = \Delta_r G^0 + RTlnQ \quad (2.52)$$

Where Q is the ratio of the activity of the reaction product and reaction reactants, at chemical equilibrium this is equal to the equilibrium constant of the electrochemical half-reaction, writing this explicitly:

$$= \Delta_r G^0 + RTln\left[\frac{(a_{[A_aB_bO_cH_d]^m})(a_{H^+})^{2c-d}}{(a_{A(s)})^a(a_{B(s)})^b(a_{H_2O})^c}\right] \quad (2.53)$$

then, expanding the a_{H^+} term using the nature of logarithms we arrive at:

$$= \Delta_r G^0 + RTln\left[\frac{(a_{[A_aB_bO_cH_d]^m})}{(a_{A(s)})^a(a_{B(s)})^b(a_{H_2O})^c}\right] - 2.303(2c-d)RTpH \quad (2.54)$$

Where F is the Faraday constant, E^0 is the cell potential, R the ideal gas constant $pH = -log[pH^+]$, and a_i denote the activities of the respective reactants and products in Eq. 2.52. In practice, identifying the redox reaction for which the difference between the expressions on the left and right in Eq. 2.52 is minimized identifies the range of potentials and pH at which a certain aqueous species or solid phase is stable. Using this insight, Persson et al. developed a method which uses experimental redox reaction energies in the atlas from Marcel Pourbaix to correct DFT-calculated redox reactions involving aqueous species. Then, they combined these corrected energies with DFT calculations for solid phases to correct $\Delta_r G^0$ and create computationally-derived Pourbaix diagrams.[59]

To consider metastable materials,[61] we introduce the term Pourbaix hull energy ΔG_{pbx} as:

$$\Delta G_{pbx} = \Delta_r G^0 + RTlnQ + (2c - d + m)FE^0 \quad (2.55)$$

which is taken as a measure of instability at a specified pH and applied potential. Hence, a large ΔG_{pbx} value indicates there is a higher driving force towards whatever redox reaction is on the hull formed by the formation energies of the solid and aqueous phases. This method has been used to identify novel materials[150] and screen for OER electrocatalysts.[71,76]

2.8 Materials Project data

In Chapters 7 and 8, we use data and tools provided by the Materials Project. In this section, we describe how this information is calculated. Firstly, we note that any large-scale computational materials database needs to tackle the issue of defining a uniform calculation scheme. In the case of the Materials Project, it contains millions of calculations using the Vienna Ab Initio Simulation Package (VASP) implementation of the computationally amenable GGA-PBE functional, and applies the rotationally invariant approach of Dudarev[107] to GGA+U for cases where localized d or f-states should be considered. In particular, the energies are calculated using the PBE+U level of theory for V, Cr, Mn, Fe, Co, Ni, Mo, and W-containing oxides, while all other materials are calculated with PBE. To define the U value the formation energies of unary oxides were calculated over a range of U and the value which minimized the discrepancy between experiment and computation was taken.[108] Issues with this approach have been outlined previously, since the DFT+U approach is motivated by correctly localizing electrons, not reproducing energies, so fitting the Hubbard U such that it reproduces experimentally observed localized electronic structures of defects is more appropriate.[151] In any case, the MP primarily concerned with thermodynamic energetics, so their scheme may be more appropriate for their use case, and we provide the values they use in Table 2.2.

Table 2.2. Values for DFT+U used in the calculations of MO_x oxides in the Materials Project.[108]

m	$+U$	m	$+U$
Co	3.32	Cr	3.7
Fe	5.3	Mn	3.9
Mo	4.38	Ni	6.2
V	3.25	W	6.2

The kinetic energy cutoff – E_{max} in Eq. 2.25 – for calculations in MP is set by multiplying by 1.3 the highest cutoff recommended by the pseudopotentials used for the set of elements being simulated. Their force convergence criteria are found by taking the product of the number of atoms in the cell and 0.0005, for units in eV/atom. To mix PBE energies with those calculated with PBE+U, a per metal correction scheme is applied in Materials Project for any reaction which mixes these two methods such that the error in binary formation reactions energies is minimized.[152] Finally, an adjustment of –0.687 eV per O atom is included to correct for issues with correlation and the systematic underestimation of oxidation enthalpies in the GGA+U framework, as noted by Wang *et al.*[108]

For further details on specific heuristics used by MP, which at the time of writing, could be found at:

https://docs.materialsproject.org/methodology/materials-methodology/calculation-details.

Chapter 3 Objectives

The overarching thread binding this thesis is the use of DFT and data-driven techniques to understand fundamental thermodynamic constraints which limit both molecular and heterogenous OER catalysts. In each of the following subsections, we briefly summarize the aims of the research presented in this next chapters while outlining the rationale for their being studied.

3.1 Scaling Relations and Novel Descriptors for Molecular Water Splitting

Molecular catalysts for the OER are the most active catalysts in terms of activity (*i.e.* turnover frequency, TOF), but they suffer from poor stability and electron transport. Most computational studies focus on heterogeneous OER catalysis, with few reports focusing on their homogeneous counterparts. Thus, we began our studies by modelling a set on experimentally realized molecular catalysts and applying methods commonly used in heterogeneous catalysis to:

- Determine whether linear scaling relationships between binding energies can be derived for homogeneous catalysts and compared with heterogeneous systems.
- Rationalize the exceptional activity of the most active Ru-based molecular catalysts.
- Develop design principles to enable the search for complexes which can catalyse the OER efficiently.

3.2 Activity and inactivity towards water splitting in molecular complexes

Based on our study of experimental catalysts, we noted that we had been predicting one well-known Fe-based catalyst to be very inactive. To understand and correct this we carry out a more in-depth analysis of this family of complexes by considering more than one active site. In doing so, we aim to rationalize:

- The source of inactivity among Mn, Co, and Ni-based catalysts with the same ligands.
- The source of activity among Fe-based catalysts with different ligands.
- The source of instability due to off-cycle reactions which are the source of instability for the molecular catalyst.

3.3 Screening molecular water splitting catalysts

Using the design principles described upon completing our study of experimentally known molecular catalysts described in section 3.1, we set out to generate hypothetical complexes generated through combining different ligands arranged in different geometries which were then tested for their ability to catalyse the OER at low overpotentials via the 'extra oxidation mechanism'. As a result of this, we aimed to:

- Study whether linear relationships between binding energies across different DFT methods.
- Identify efficient catalysts for experimental testing.
- Rationalize metal-specific scaling relations between specific binding energies.

3.4 Oxidation state analysis for binary oxide stability prediction

Turning our attention to heterogeneous catalysts, we focused on using materials databases to develop a predictive theory of oxidation state changes as a source of stability in binary oxides. We chose to use pre-existing data instead of studying specific systems due to the vast swathes of investigations already available on heterogeneous OER catalysts. Furthermore, most studies of oxides for OER focus on reactivity while ignoring materials stability, which is a more discriminative property for acidic oxygen evolution. With this in mind, we set out to do the following:

- Understand the stabilising influence of oxidation state changes in binary oxides.
- Develop a model to represent this influence and allow for formation energy predictions.

- Validate the model against pre-existing data in the computational materials databases, namely the Materials Project.

3.5 High-throughput screening of binary oxides for acid stable water splitting

Discovering a catalyst which exhibits activity comparable to platinum group metals for acidic oxygen evolution, while also retaining material stability, would be of exceptional value due to the improved efficiency of PEM electrolysers.[153,154] This motivates an application of our oxide stability predictor to forecast which elements represent the most promising candidates to reduce or eliminate precious metal content for acidic oxygen evolution. To do this, we define two clear goals:

- Define a scheme to determine whether to classify a material as acid stable for the OER and determine where our model can and cannot identify known acid stable oxygen evolution reaction catalysts.
- Gather cross-periodic table statistics for material stability under acidic conditions and high applied potential.

Chapter 4 Scaling Relations and Novel Descriptors for Molecular Water Splitting

4.1 Introduction

Molecular catalysts for the oxygen evolution reaction exhibit the highest turnover frequencies amongst all catalysts.[28] This motivated a study of a representative snapshot within molecular OER catalysts to compare against commonly applied methodologies used for heterogeneous catalysts. With this aim, we curated the literature for molecular OER catalysts for seminal works reporting discovered molecular catalysts which were significant advances, while also respecting our desire to represent as much chemical diversity as possible. With these objectives in mind, we will enumerate a brief history of molecular catalysts via the catalysts which are studied in this chapter. Each of the subsequently mentioned complexes are labelled **M-I**, with M denoting the metal and I a labelling number which will be denoted in Arabic numerals, where we have grouped catalysts by metal, and shown in Figure 4.1.

The first reported molecular catalyst for OER was the so-called 'blue dimer'[155] from Meyer (cis,cis-$[(bpy)_2(H_2O)Ru(III)ORu(III)(H_2O)(bpy)_2]^{4+}$; bpy=bipyridine) and co-workers in 1982, which consisted of two octahedrally-coordinated Ru atoms connected through a bridging oxygen, we refer to this complex as **Ru-1**. The redox flexibility of this system in having two Ru sites to oxidize was used to justify the observation of the impressive activity of RuO_2, a highly active heterogeneous catalyst for the OER. Another dimeric catalyst based on Mn $[(terpy)(H_2O)Mn(III)(O)_2Mn(IV)(H_2O)(terpy)](NO_3)_3$; terpy=2,2′:6,2″-terpyridine) was reported in 2001 by Brudvig *et al*;[156] this complex, which we denote as

Mn-10, draws similarities with the oxygen evolving complex found in chlorophyll and is composed of dimeric Mn centres in a Mn_4CaO_5 unit. One of the first synthesized mononuclear catalysts was reported in the group of Thummel, where again the catalyst was ruthenium-based, and we denote as **Ru-2**. Dimer formation drove the O–O bond formation in Ru-2, and no report of a reaction catalysed through a single site mechanism was reported until 2008 when Meyer and co-workers used $[Ru(tpy)(bpm)(H_2O)]^{2+}$ and $[Ru(tpy)(bpz)(H_2O)]^{2+}$ (tpy is 2,2′:6′,2″-terpyridine; bpm is 2,2′-bipyrimidine; bpz is 2,2′-bipyrazine) and noted the existence of Ru(V)=O-enabled mechanism.[157] In 2011, exceptional activity was observed by the groups of Sun and Llobet[25,158] within a family of Ru-complexes with a common tetradentate equatorial ligand (2,2′-bipyridine-6,6′-dicarboxylic acid) with varying axial ligands exhibiting TOF values up to 300 s^{-1} prior to deactivation. This group of catalysts are denoted **Ru-4**, **Ru-5** and **Ru-6** in Figure 4.1. Then, ligand-mediated water oxidation was proposed to occur for another Ru-based catalyst with two benzimidazole-based tridentate ligands, which we denote as **Ru-7** and **Ru-8**,[159] and displayed TOF and TON values similar to those reported by Llobet and co-workers.[1] Further improvements in TOF were observed, again by Llobet and co-workers, by using a similar tetradentate ligand as in **Ru-4**, **Ru-5** and **Ru-6**, with a key difference in that there was a dangling carboxylate arm, thought to facilitate O–O bond formaition.[160]

Mononuclear Mn-based catalysts bearing pentadentate anionic ligands were developed by Brudvig *et al.*[161] which could stabilize high valent Mn up to Mn(V); we refer to the two complexes reported in that work as **Mn-11** and **Mn-12**. Iron-based catalysts consisting of a single metal centre began to be discovered as a tetraamido macrocyclic ligand coordinating iron commonly referred to Fe-TAML and denoted as **Fe-13** in this chapter.[162] This catalyst exhibited a TOF of $1.3s^{-1}$, although it degraded within minutes under relevant reaction conditions.[162] Lloret-Fillol, and co-workers then reported a family of Fe-based

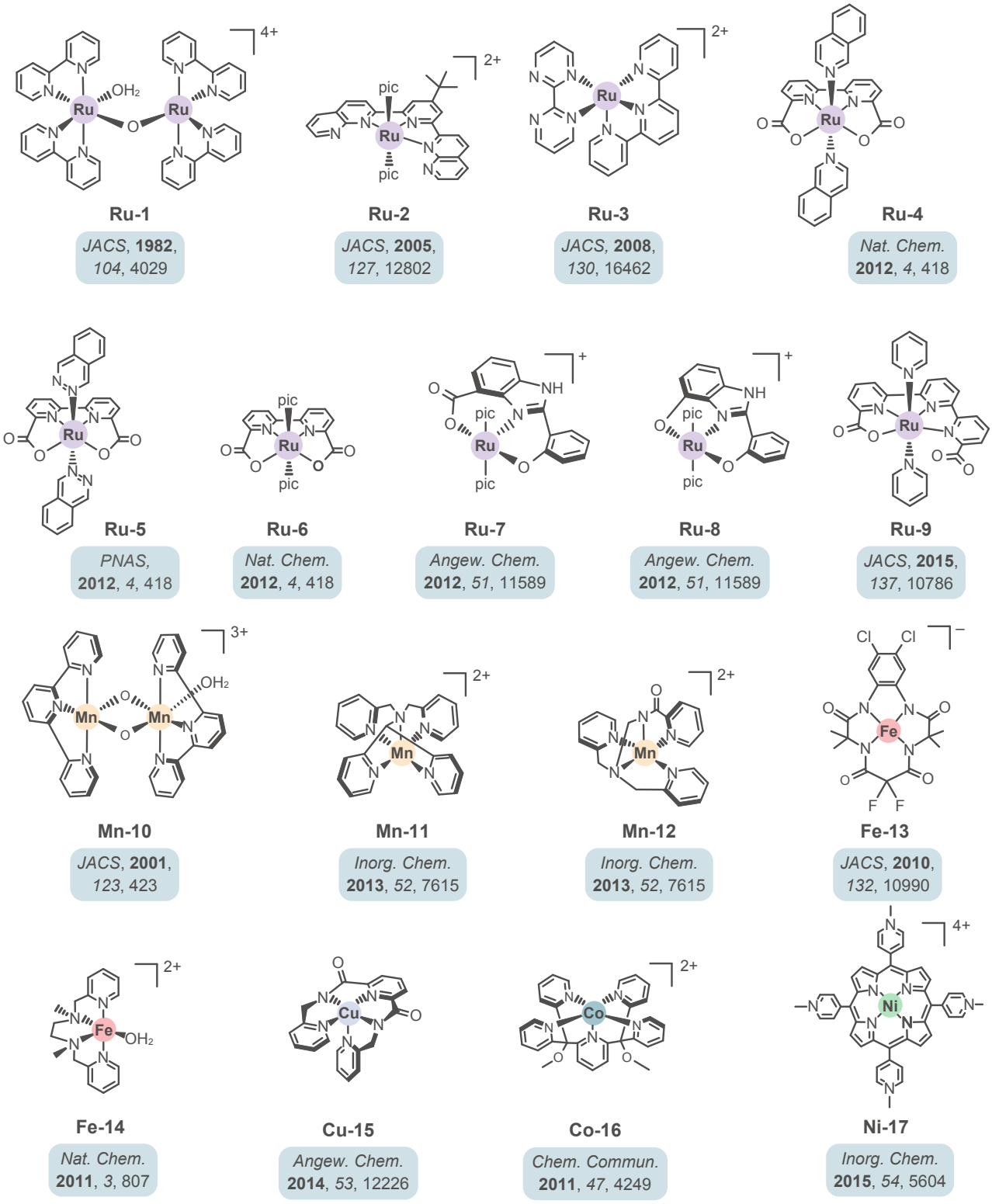

Figure 4.1. The set of molecular catalysts studied in this chapter, and the nomenclature and citation which is the first report of OER activity for the respective complex. The 4-picoline ligands in **Ru-2**, **Ru-6**, **Ru-**7and **Ru-8** have been replaced by "pic" for clarity.

molecular OER catalysts with tetradentate ligands and two active sites in a *cis* position,[163] seen as **Fe-14** in Figure 4.1. Although the initial TOF for these catalysts were low, being at most 0.1 s^{-1}, they had lifetimes on the order of hours. In any case, these represented the highest activity achieved for a homogeneous catalyst without Ir or Ru and spurred on the development of other earth abundant molecular OER catalysts. In the same year, Co housed within a pentadentate ligand was found to catalyse water oxidation,[164] denoted as **Co-16**. . More recently, multidentate Cu[165] and Ni[166] catalysts have been reported, labelled as **Cu-15** and **Ni-17**, respectively.

Mononuclear Mn-based catalysts bearing pentadentate anionic ligands were developed by Brudvig *et al.*[161] which could stabilize high valent Mn up to Mn(V); we refer to the two complexes reported in that work as **Mn-11** and **Mn-12**. Iron-based catalysts consisting of a single metal centre began to be discovered as a tetraamido macrocyclic ligand coordinating iron commonly referred to Fe-TAML and denoted as **Fe-13** in this chapter.[162] This catalyst exhibited a TOF of 1.3s^{-1}, although it degraded within minutes under relevant reaction conditions.[162] Lloret-Fillol, and co-workers then reported a family of Fe-based molecular OER catalysts with tetradentate ligands and two active sites in a *cis* position,[163] seen as **Fe-14** in Figure 4.1. Although the initial TOF for these catalysts were low, being at most 0.1 s^{-1}, they had lifetimes on the order of hours. In any case, these represented the highest activity achieved for a homogeneous catalyst without Ir or Ru and spurred on the development of other earth abundant molecular OER catalysts. In the same year, Co housed within a pentadentate ligand was found to catalyse water oxidation,[164] denoted as **Co-16**. . More recently, multidentate Cu[165] and Ni[166] catalysts have been reported, labelled as **Cu-15** and **Ni-17**, respectively.

In the case of the Ru and Mn dimer catalysts investigated in this thesis, we only considered one active site for simplicity and kept the investigation for specific molecules uniform in

that we only vary the intermediates at a single site. In addition, we did not consider Ir-based molecular catalysts since most of these systems featured pentamethylcyclopentadienyl (Cp*) ligands[167,168] and their integrity has been shown to be compromised under OER conditions,[168,169] despite some of them show considerable OER activity. More complex and unique systems with multi-metallic centres were also discarded due to the multiple distinct valence states and active sites which would have to be considered prior to oxygen evolution.[39]

Computational studies which focus on molecular OER have reported scaling relations for a few model molecular systems bearing a corrole, porphyrin ligands and functionalized graphitic materials,[170–172] but the generalization of these relations to catalysts featuring different metals and ligand scaffolds, as well as the applicability of the OER descriptor, is yet to be demonstrated. In this chapter we study the existence of universal scaling relations for the experimental catalysts depicted in Figure 4.1 and intends to rationalize this exceptional activity using methods from heterogeneous catalysis, while also investigating whether molecular catalysts can take advantage of the second coordination sphere to stabilize the HOO* intermediate, as has been proposed recently.[173]

To summarize the experimental activity of these complexes, we provide TON and TOF values for each catalyst, where possible, in Table 4.1. While we note that the results are very sensitive to reaction conditions (*e.g.* catalyst concentration, oxidant concentration, whether the catalyst is oxidized chemically or electrocatalytically, pH), we still feel it is instructive to note their relative differences and assume that these values represent some optimal performance across these conditions. We also note in Table 4.1 that there are empty values since in many cases experimental studies do not report the TON and TOF values, which precludes comparison between catalysts.

Table 4.1. Reported experimental TOF (in s^{-1}) and TON values for the set of catalysts shown in Figure 4.1. Unless states otherwise, each catalyst was oxidized using chemical oxidants. References were the reported values can be found are provided.

Catalyst	TON	TOF	Ref.
Ru-1	–	–	155
Ru-2	580	–	174
Ru-3	8	0.02	157
Ru-4	8360	303	25
Ru-5	4500	286	158
Ru-6	2010	32	25
Ru-7	800	1	159
Ru-8	4000	>7	159
Ru-9	27e6	8000	160
Mn-10	~5[a]	0.01	175
Mn-11	~5[a]	0.001	161
Mn-12	~5[a]	0.05	161
Fe-13	~5[a]	1.3	162
Fe-14	145	0.1	163
Cu-15	~5	–	165
Co-16	–	0.83–	164
Ni-17	–[b]	0.67	166

[a] Precise value not reported, but reference was made to the number of turnovers in terms such as ‘a few’ or ‘a number’.
[b] Reaction driven electrochemically.

While this data highlights the fact that results are so sensitive to conditions, to make comparisons to real world applications, we assume that the reported value is the optimum

for that catalyst, so that their utility can be compared. From this table we see that Ru-based catalysts show far higher activity and stability relative to any other metal, and that **Fe-14** catalysts stand out among the remaining catalysts in terms of TON.

4.2 Computational methods

DFT calculations were performed at the TPSSh level using the Gaussian09 software.[176] The choice of this functional was based on the satisfactory results obtained in a preliminary benchmark study of the redox potentials of four molecular OER catalysts investigated in this chapter using three different functionals with varying levels of HF exchange, namely B3LYP (20% HF),[106] TPSSh (10% HF),[100,103] and BP86 (0% HF).[177,178] The results and details of these calculations are presented in Table 4.2.

The binding energies of the different OER intermediates in the WNA mechanism were computed using the CHE model described in section 2.6.3 to arrive at Eqs. 4.1–3

$$\Delta G_{HO^*} = G_{HO^*} - G_* - G_{H_2O_{(l)}} + 0.5G_{H_{2(g)}} \quad (4.1)$$

$$\Delta G_{O^*} = G_{O^*} - G_* - G_{H_2O_{(l)}} + G_{H_{2(g)}} \quad (4.2)$$

$$\Delta G_{HOO^*} = G_{HOO(III)^*} - G_* - 2G_{H_2O_{(l)}} + 1.5G_{H_{2(g)}} \quad (4.3)$$

To describe the Ru, Mn, Fe, Cu, Co and Ni metals, the LANL2DZ effective core potential was used along with f-polarization functions with exponents 1.235, 2.195, 2.462, 3.525, 2.78 and 3.13, respectively.[116,117] The more electronegative O, N, F, and Cl atoms were described using the 6-31+G(d) basis set, while the 6-31g(d,p) basis set was employed for C and H atoms. To account for non-covalent interactions, Grimme-D3 dispersion corrections[179] Gibbs energy through single point calculations using the optimized geometries in solution. The primary conclusions of this chapter remain the same regardless of the addition of dispersion. Data calculated without dispersion corrections are included in Appendix A.

Molecular structures were optimized in solution using the implicit SMD solvation model with H_2O (ε = 78.3553) as a solvent.[131] Whenever high- and low-spin states (HS and LS, respectively) were accessible, both were considered in geometry optimizations and the lowest energy structure was selected.

Gibbs energies were calculated at the temperature of 298.15 K and pressure of 1 atm, except for the isolated H_2O molecule that was computed at the temperature and pressure at which both the liquid and gas phases are in equilibrium, *i.e.,* 298.15 K and 0.0035 bar. Relative Gibbs energies are referenced to H_2O and H_2 in solution, to avoid introducing the error associated with the modelling of O_2 with DFT methods, as discussed in the methods section. All the structures were verified to be real energy minima by means of vibrational frequency analysis.

4.3 Benchmarking

To justify our choice of DFT functional, we tested three separate functionals showing varying levels of HF exchange, with 0 % in BP86, 10 % for TPSSh and 20 % for B3LYP. The WNA mechanism consists in 4 PCETs which involve the oxidation of a transition metal, so our benchmark analysed standard reduction potentials for 4 of the 17 catalysts in Figure 4.1. Overall, the TPSSh functional provided the lowest MAE (MAE = 303 mV, max error = 470 mV) compared with the reported experimental values (see Table 4.2), and therefore, this functional was chosen for subsequent theoretical investigations throughout this thesis. This choice of functional, along with the chosen basis sets is further supported by results obtained in the computation of heats of formation of many different transition metal complexes.[2] The large discrepancy observed in using BP86 to predict the redox potential $[Mn(IV)Mn(IV)]^{4+}$ / $[Mn(III)Mn(IV)]^{3+}$ in **Mn-10** is thought to be a consequence of the inadequacy of applying GGA functionals to open-shell transition metal complexes.[180]

Table 4.2. Calculated and experimental reduction potentials ($E_{theor.}$ and $E_{exp.}$, respectively), in V_{RHE}, using different DFT functionals. The MAE for each modelled catalyst is provided. The lowest MAE value obtained for each catalyst is highlighted in bold.

Catalyst	Redox Pair	Functional	$E_{theor.}$	$E_{exp.}$	MAE
Ru-5	$[Ru(III)–H_2O]^+$ / $[Ru(II)–H_2O]$	B3LYP	0.63	0.43	**0.20**
		TPSSh	0.64		0.21
		BP86	0.80		0.37
Ru-2	$[Ru(III)–OOH]^{2+}$ / $[Ru(II)–OOH]^+$	B3LYP	–0.07	0.30	0.30
		TPSSh	–0.15		0.45
		BP86	0.02		**0.28**
Mn-10	$[Mn(IV)Mn(IV)]^{4+}$/ $[Mn(III)Mn(IV)]^{3+}$	B3LYP	1.87	1.24	0.63
		TPSSh	1.32		**0.08**
		BP86	6.43		5.19
Co-16	$[Co(III)–OH]^{2+}$ / $[Co(II)–H_2O]^{2+}$	B3LYP	1.53	0.75	0.78
		TPSSh	1.22		0.47
		BP86	0.32		**0.43**

4.4 Results

4.4.1 *Molecular OER scaling relations*

First, we demonstrate that there is a scaling relation between HO* and HOO* intermediates observed for heterogeneous systems using the molecular OER catalysts. As shown in

Figure 4.2, the binding energies of the HOO* species (ΔG_{HOO*}) against those obtained for the HO* species (ΔG_{HO*}) shows that the energetics of these two intermediates are strongly related, displaying a linear correlation ($R = 0.93$) with a slope of 1 – as expected based on the bond order conservation principle[181] – and an intercept of 3.26 eV. This confirms that the same linear scaling relation observed in metal and metal oxide systems can be applied to molecular OER catalysts, since this relation holds across complexes showcasing many distinct ligands and metal centres. In addition, the constraint imposed by the OER scaling implies that both homogeneous and heterogeneous catalysts – where intercepts of 3.2 eV are typically observed – are subject to a minimum overpotential of *ca.* 370 mV. This value is derived by calculating $\frac{3.2}{2} - 1.23 = 0.37$ where for the first term we divide the implied energy difference by the number of steps which is two (HO* to O*, then O* to HOO*) and we subtract the thermodynamic potential of 1.23.

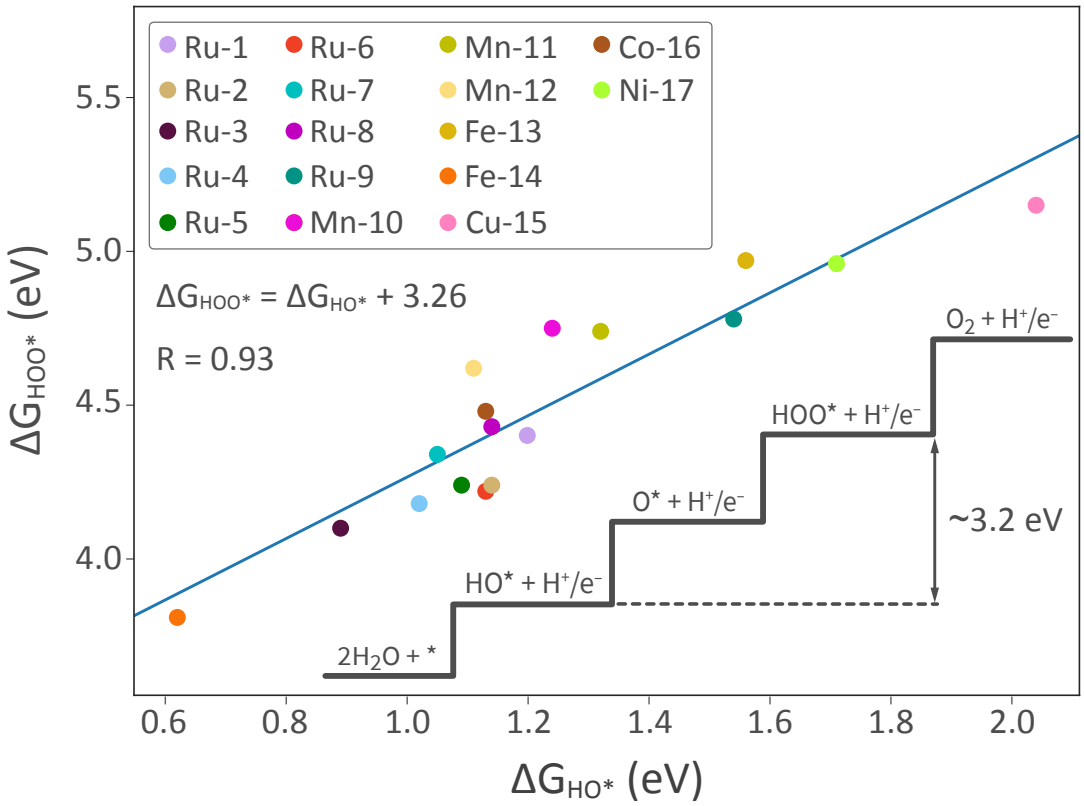

Figure 4.2. Linear scaling relation between the HO* and HOO* intermediates for the molecular OER catalysts investigated in this chapter and depicted in Figure 4.1.

Intramolecular hydrogen bonding has been proposed to lower ΔG_{HOO^*} independently of ΔG_{HO^*} given the innate rigidity of the HO* group (Figures 4.3b, c) in comparison to HOO*. This additional stabilization of the HOO* intermediate would shift down ΔG_{HOO*} with respect to ΔG_{HO*}, closing the energy gap between the two intermediates, and therefore, improving the OER scaling. To test this hypothesis, we classified data in Figure 4.2 as catalysts with or without a H-bond by measuring the minimum distance from the H atom in the HOO* group to the nearest N/O-ligand using different cut-off radii, chosen such that each split contained sufficiently different data points. As we anticipated, the ability of the HOO* intermediate to form intramolecular H-bonds decreases the value of ΔG_{HOO^*} and, consequently, reduces the energy difference $\Delta G_{HOO^*} - \Delta G_{HO^*}$. This effect is conveyed in Figure 4.3a, where distinct scaling relations are obtained depending on whether the HOO* intermediate exhibited a H-bond or not. Importantly, we note that all linear trends display slopes close to unity; however, those catalysts with an intramolecular H-bond present in the HOO* intermediate show a value of $\Delta G_{HOO^*} - \Delta G_{HO^*}$ that is *ca.* 0.1 eV lower than those without the H-bond. While this effect is not decisive – being within our reported MAE of the chosen functional – we conclude that H-bonding can be leveraged to improve the scaling, and therefore, it should be considered as an important feature in the design and fine-tuning of molecular OER catalysts. H-bonding can also be leveraged to boost the kinetics of the O* to HOO* step in the WNA mechanism, as recently shown by experiments,[160] while theoretical investigations have highlighted the possibility that the second coordination sphere can modulate the binding energy of the crucial O* intermediate.[182] A table including the binding energies of each intermediate for each complex, and whether the HOO* intermediate does or does not display a hydrogen bond at 2.2 Å, is shown in the Appendix Table A1.

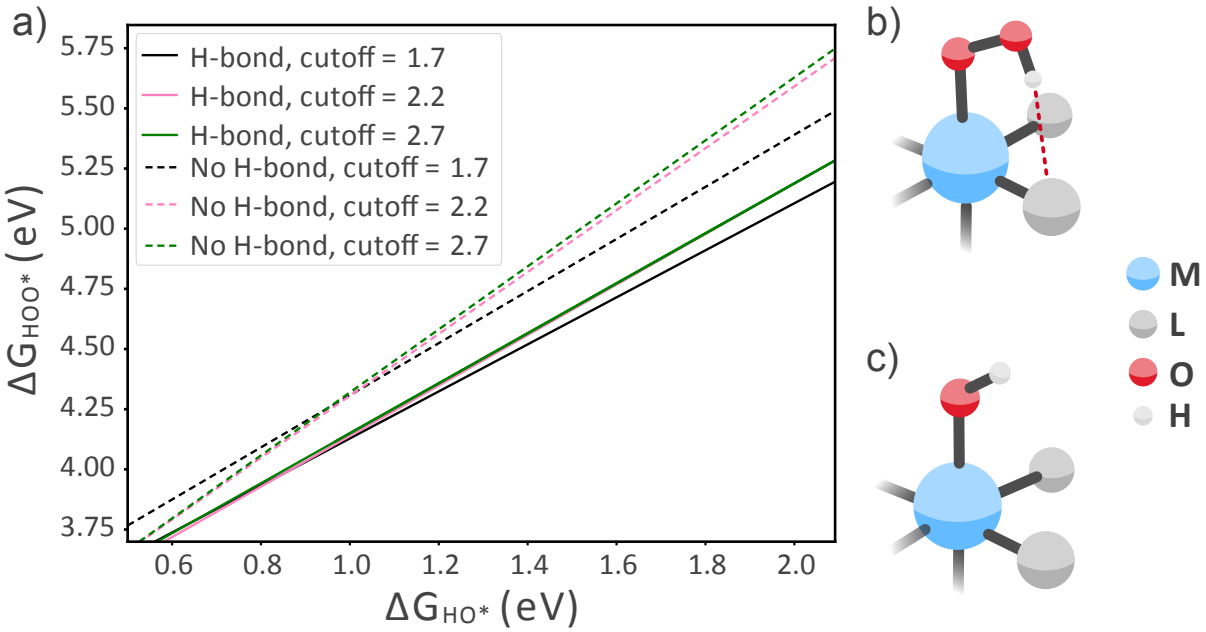

Figure 4.3. (a) Lines of best fit though points for catalysts with (solid lines) and without (dashed lines) hydrogen bonds within the OOH intermediates, for varying cut-offs specifying the maximum distance of a H-bond distance. Further illustrations of the intramolecular hydrogen bond which can occur from b) the HOO* fragment and c) HO* intermediate, where these bonds are less likely to form.

4.4.2 *Non-PCET OER mechanism*

After demonstrating that molecular catalysts exhibit a scaling relationship between the HO* and HOO* intermediates, we tested whether the OER descriptor proposed for heterogeneous catalysts, *ie.* $\Delta G_{O*} - \Delta G_{HO*}$, could also be applied to rationalize the experimental performance of the investigated complexes. By plotting this descriptor against the computed theoretical overpotential described in Section 2.6.3, a volcano representation is obtained, where the most active catalysts should lie at the top. This representation also allows us to categorize molecular catalysts based on the PLS, with catalysts lying on the left-hand side of the volcano displaying a small OER descriptor value, and therefore, the O* to HOO* transition becomes the PLS. On the other hand, catalysts found on the right leg of the volcano exhibit a high descriptor value, and we have that this descriptor value on the x-axis, $\Delta G_{O*} - \Delta G_{HO*}$, dictates the OER overpotential.

The volcano plot obtained for the 17 molecular catalysts is shown in Figure 4.4a where, surprisingly, none of the 17 are predicted to have an outstanding OER activity. This contrasts with the reported exceptional experimental activity of Ru-based catalysts as discussed in this chapter. In the following, we demonstrate that this unsuspected behaviour is caused by an oversimplification of the reaction mechanism typically assumed in most theoretical studies of heterogeneous OER catalysts.

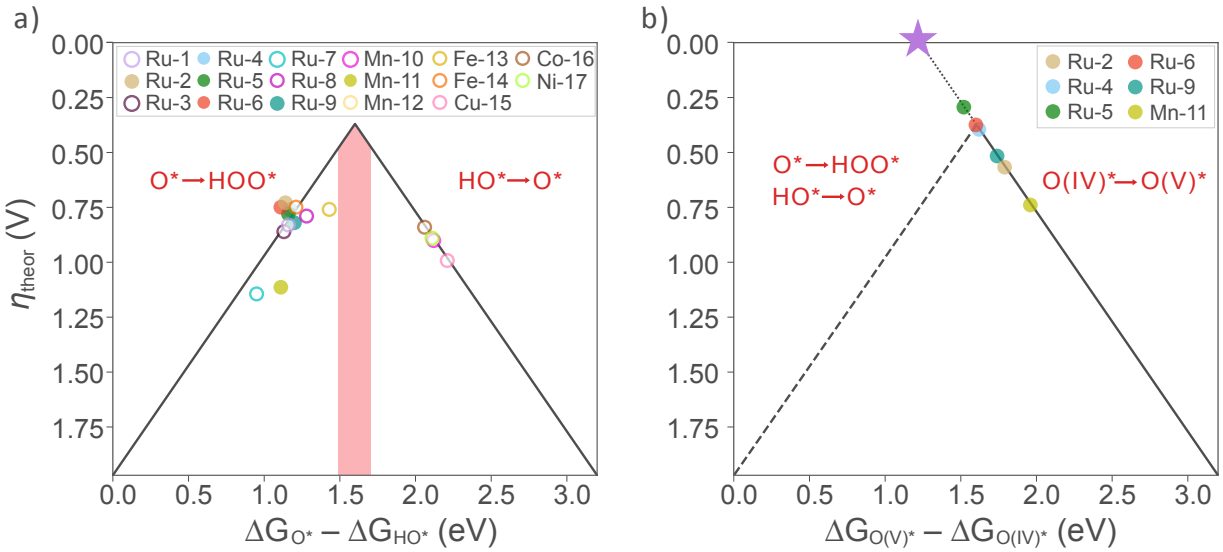

Figure 4.4. (a) Volcano representation using the conventional OER descriptor. Full markers denote catalysts which are theoretically predicted to undergo an additional ET step before O–O formation. The red shaded area indicates the optimal range for the conventional OER descriptor. (b) Volcano plot including only the molecular catalysts predicted to undergo an additional ET. In this volcano, the calculated Gibbs energy for the additional ET from the M(IV)-oxo to M(V)-oxo intermediate is represented in the *x*-axis as a new OER descriptor. Note, the same scale and the left leg of the volcano in a) has been used for comparability. The dotted line in b) is drawn to guide the eye towards an ideal OER catalyst. The PLS on each side of the two volcano plots is indicated in red text.

Notably, some metals, such as Ru, Mn or Fe, have been experimentally proven to undergo an additional one-electron transfer (ET) before O–O bond formation.[183–186] Bearing this in mind, we computed the Gibbs energies for the ET from the M(IV)-oxo to M(V)-oxo species with M = Ru, Mn, Fe, hereafter referred to as O(IV)* and O(V)*, respectively (see

Appendix A, Table A1 for details). We had modelled M(IV)–OH to M(V)–oxo for a subset of the complexes due to the mechanisms and charge balances reported in the manuscripts, so this extra oxidation was not tested for those complexes which were already found to be stable at M(V)–oxo. The Gibbs energy change associated with this step, and the subsequent O–O bond formation via a PCET event, given by:

$$\mathrm{O(IV)^*} \rightleftharpoons \mathrm{O(V)^*} + \mathrm{e^-}$$

$$\Delta G_{3'} = \Delta G_{O(V)^*} - \Delta G_{O(IV)^*} - eU \tag{4.4}$$

$$\mathrm{O(V)^*} + \mathrm{H_2O} \rightleftharpoons \mathrm{HOO^*} + \mathrm{H^+}$$

$$\Delta G_{4'} = \Delta G_{HOO^*} - \Delta G_{O(V)^*} + k_B T \ln a_{H^+} \tag{4.5}$$

After accounting for the additional ET in the M(IV)-oxo intermediates, we observed that catalysts which undergo this step exhibit an improved theoretical overpotential, deviating from the lines defined by the volcano in Figure 4.4a. This divergence from the scaling stems from the fact that those catalysts are neither limited by the HO* to O*, nor the O* to HOO* steps. Instead, the additional ET from the M(IV)-oxo species becomes the PLS, which demands less energy leading to a lower predicted overpotential. Based on this observation, we proceeded to apply the Gibbs energy change associated with the additional ET step, $\Delta G_{O(V)^*} - \Delta G_{O(IV)^*}$, as an alternative OER descriptor on the *x*-axis. The result of adopting this new descriptor can be appreciated in the volcano plot depicted in Figure 4.4b, where the relevant catalysts now lie on the right leg of the volcano and where the best Ru-based catalysts cluster together around the top. Notably, DFT calculations predict **Ru-4, Ru-5**, **Ru-6**, and **Ru-9** to exhibit the lowest theoretical overpotential amongst the 17 complexes investigated in this chapter, which agrees with the highest experimental TOF values reported for these complexes. It is important to note that the active species for **Ru-9** has come under scrutiny,[187] but our calculations predict that this catalyst would be a relatively active OER catalyst. We also note that when comparing energy differences

between the PCET and one-electron oxidation steps, it is important to consider whether this difference is within the inherent DFT error in the (Table 4.2), in which case neither of the two pathways can be entirely discarded.

Another important observation from Figure 4.4b is that **Ru-4**, **Ru-5** and **Ru-6** are predicted to display a theoretical overpotential below 370 mV, suggesting that molecular catalysts undergoing the O(IV)* to O(V)* transition might be able to hurdle the overpotential wall. We can demonstrate this concretely by examining the experimental Pourbaix diagram reported by Llobet *et al.* for **Ru-4**, shown in Figure 4.5, where the extra oxidation redox potential is depicted with the horizontal line separating Ru(IV)–O/(Ru(V)–O or Ru(IV)–O·) regions. Therefore, for this particular system, the mechanism of Ru(V)–O or Ru(IV)–O· formation is pH-dependent and can either form through the route typically considered in heterogeneous catalysis via PCET from Ru(IV)–OH or via ET from Ru(IV)–O. Note that the reaction occurs across the range of pHs, meaning the OER can occur via distinct mechanisms for the same catalyst, under different conditions, underscoring the necessity of considering mechanisms which are not composed solely of PCET steps.

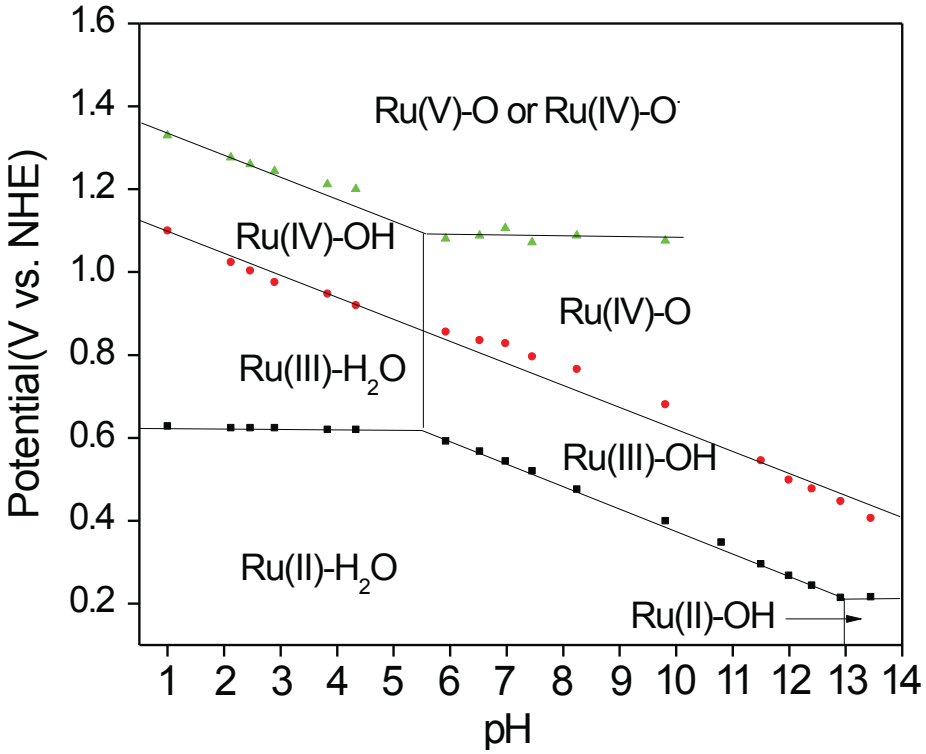

Figure 4.5. Pourbaix diagram adapted from Llobet *et al*. with permission.[25]

One blind spot of using this descriptor lies in the fact that it decouples proton and electron transfers into sequential steps. When using a descriptor such as $\Delta G_{O(IV)^*} - \Delta G_{OH(III)^*}$ there is a symmetry to arguing that it can map directly to overpotential because as you increase this descriptor, the barrier for the subsequent PCET comes down, and due to BEP arguments, it is posited that the kinetic barrier involved in going from O(IV)* to OOH(III)* intermediates reduces in tandem. In contrast, a change in $\Delta G_{O(V)^*} - \Delta G_{O(IV)^*}$ does not translate directly to a change in the barrier for the net proton transfer in forming, for example HOO(III)* via water nucleophilic attack on O(V)*. In either case, to get accurate kinetic barriers, *ab initio* molecular dynamics (AIMD) simulations are necessary, which were outside the scope of this thesis. These simulations are time consuming in heterogeneous catalyst surfaces, while they are even more demanding for molecular catalysts since the molecules need to be enclosed within a three-dimensional solvation shell.

4.5 Experimental TOF values

Comparing our DFT predicted overpotentials to the experimentally observed catalytic activity is challenging since the conditions applied to measure performance are not uniform across all investigations, as seen in Table 4.3. However, upon comparing our results with the reported experimental TOFs we feel confident that our calculations respect the right trend.

Table 4.3. Experimental conditions and TOF values reported for the most active Ru catalysts investigated in this chapter. In all the cases, cerium ammonium nitrate (CAN) was used as chemical oxidant.

Catalyst	TOF (s^{-1})	pH	[Catalyst] / M	[CAN] / M	Ref.	$\eta_{theor.}$
Ru-4	303	1	2.16×10^{-4}	0.48	25	0.39
Ru-5	286	1	2.22×10^{-4}	0.365	158	0.29
Ru-6	32	1	2.16×10^{-4}	0.48	25	0.38
Ru-9	8,000	7	1.7×10^{-3}	n.a.	160	0.51
Ru-9	50,000	10	1.7×10^{-3}	n.a.	160	0.51

Notably, the catalyst we predict to exhibit the lowest theoretical overpotential is **Ru-5**, followed by **Ru-4** and **Ru-6**. In experiments, this trend is respected also, with the **Ru-4** and **Ru-5** catalysts showing similar yet undoubtedly superior performance than **Ru-6**. The reason for the apparent difference between the experimental TOFs reported for **Ru-6** and **Ru-4-5** and our theoretical overpotentials may be ascribed to the fact that these Ru catalysts have been experimentally proposed to follow an I2M mechanism rather than the WNA assumed in our theoretical overpotentials. On the other hand, **Ru-9** shows remarkable activity at high pH (Table 4.3). This has been attributed the an intramolecular proton transfer which is facilitated by the dangling carboxylate arm[160,191] which betrays the fact that our model overlooks the potential for ligand involvement in O–O bond formation. In any case, to form the O–O bond, the preceding redox potentials still need to be low enough

to form a high-valent Ru(V)–oxo intermediate, and these redox potentials are considered here. This bond formation is likely a delicate function of the chemical oxidant used, the local environment and the nature of the catalyst ligands. Investigations into the effect of explicit solvent on the stabilization of OER intermediates have been undertaken in heterogeneous systems.[192] Due to the increased flexibility and asymmetric nature of molecular catalysts[193] compared to heterogeneous catalysts, such a study of solvent stabilization would require computationally taxing AIMD calculations with water molecules solvating the entire molecule as opposed to using layers of water molecules as in metal oxide systems. This level of theory would allow for the modelling of O–O bond barriers as a function of chemical oxidant and pH, but is not tackled in this thesis.

4.6 Discussion

This chapter sets the foundation for a fast and efficient screening of molecular OER catalysts in Chapter 6 and posits that catalysts which are close to the top of volcano, as seen in Figure 4.4b, have the potential to evolve oxygen through both the WNA mechanism as well as through more complex routes. This approach, yet to be exploited in homogeneous catalysis, could lead to the discovery of novel catalysts with improved performance. Therefore, we establish and discuss a series of catalyst design principles to accelerate the discovery of novel molecular systems based on earth-abundant elements which could exhibit low OER overpotential.

i. Any high-throughput search should focus on transition metal complexes which can stabilize high oxidation states such as Cr, Mn, and Fe.

ii. Although a complete characterization of activity would require the modelling of many more intermediates, our approach allows for the rapidly accelerated screening of molecular catalysts using thermodynamic OER descriptors. The activity of catalysts with a low conventional OER descriptor – those lying on the left leg of the volcano in

Figure 4.4a – can be underestimated if they undergo an extra one-electron oxidation. This can be prevented by considering our new proposed OER descriptor. In addition, the I2M mechanism could be leveraged by designing ligands which could facilitate dimer formation through π-π interactions.

iii. H-bonding with the metal ligands can be leveraged to improve the OER scaling between the HO* and HOO* intermediates, although ligands with different electronic properties may play a role in stabilizing other high-valent intermediates, or by acting as a proton shuttle to improve the overall reaction kinetics, as has been experimentally demonstrated recently.[160] Therefore, the electronic and steric effects of the ligand environment need to be systematically investigated to illuminate potential strategies for merging the desirable features of distinct ligands to identify highly active OER catalysts.

Owing to the vastness of chemical space, homogeneous catalysts are essentially infinitely tunable.[194] Highlighting the fruitful regions within this space is a demanding and exciting challenge which we can begin to address with these design principles. With enough data, which we will collect and utilize in Chapter 6, ML algorithms could become an integral part of such processes to greatly enhance the speed of catalyst discovery.

Finally, regardless of whether we use the conventional or novel OER descriptor, some of the experimental catalysts show significant overpotentials which would prohibit oxygen evolution for those complexes. Either the nature of some of the catalysts is not well described, or the representation we are using is wrong for reasons which may include the representativeness of the CHE model applied to chemically driven water splitting, inherent DFT error, as well as the instability of molecular catalysts in general, which may have led to erroneous reports of catalyst activity which were in fact obscured by metal oxide. This has been posited to occur for **Co-16**,[195,196] which could be rationalized by the high activity

of cobalt oxide in basic media, and this complex was reported to only evolve oxygen above pH 10. A similar rationalization could possibly be made for **Ni-17**, since this could be a precursor to the extremely active NiFe oxyhydroxide catalyst, which can be formed in situ in the presence of parts per billion impurities of Fe.[197] The ligands themselves can also behave as active sites or there may be two adsorbates and therefore two active sites, as is the case, for example, of **Fe-14**. In the next chapter, we consider this extra site to correctly identify promising Fe-based catalysts and justify the large OER descriptor found in Figure 4.4a for this complex.

4.7 Conclusions

In summary, in this chapter we began by demonstrating, for the first time, the universality of the linear relationship between the HO* and HOO* intermediates in the WNA mechanism by showing that this relationship holds for experimentally known molecular catalysts. The linear relationship is found to be very similar to that seen for metal oxides. In addition, we showed that molecular OER catalysts can circumvent the scaling between the HOO* and HO* intermediates by undergoing an additional one-electron oxidation prior to O–O bond formation. As a result, we predicted molecular catalysts which are able to carry out this extra oxidation could behave as efficient OER catalysts. Further, we demonstrated that the activity of such highly active systems is underestimated by the conventional OER descriptor. We also proposed a new descriptor to screen and narrow down the search of promising molecular catalysts and outlined design principles to realize this. In this chapter, we did not inspect the conventional OER descriptor at higher oxidation states since we focused on the novel mechanism, but a full characterization of activity will need to consider whether the O(IV)* or HO(IV)* intermediate is most stable, since this controls whether $\Delta G_{O(V)*} - \Delta G_{O(IV)*}$ or $\Delta G_{O(V)*} - \Delta G_{OH(IV)*}$ is responsible for setting the PLS. This will be determined by the pKa of this reaction, and thereby the pH of the solvent

or solution that the complex is in. In Chapter 6, we will tackle this and apply the extra oxidation descriptor, $\Delta G_{O(V)*} - \Delta G_{O(IV)*}$, to perform a search for low overpotential molecular OER catalysts.

Chapter 5 Activity and Inactivity Towards Water Splitting in Molecular Complexes

5.1 Introduction

Iron-based green technology solutions are especially appealing due to the abundance of iron in the Earth's crust, with Fe being found at rates which are orders of magnitude higher than for any other transition metal. The set of molecular OER catalysts investigated in this chapter is based on experimental studies,[163] one of which was denoted as **Fe-14** in the previous chapter. Lloret-Fillol *et al*. studied a wider family of iron complexes with tetradentate nitrogen-based ligands and two coordination sites in *cis* position that were identified to be OER active. The authors also reported the thwarted attempts to promote the OER using first-row transition metal complexes under identical experimental reaction conditions (*i.e.,* catalyst concentration, oxidant concentration, oxidant type, and pH). Subsequent experiments have shown that substituting electron withdrawing groups (EWG = NO_2, CO_2Et, Cl) in the *para* position of the pyridine ligand in one such catalyst, $[Fe(OTf)_2(Pytacn)]^{2+}$ (OTf denotes trifluoromethanesulfonate and Pytacn denotes 1-(2'-pyridyl-methyl)-4,7-dimethyl-1,4,7-triazacylononane), greatly improved the OER activity. In contrast, the substitution of a fluorine and methyl group in the ortho position led to reduced performance, which was posited to be due to increased catalytic degradation.[26] While the previous chapter focused on complexes which were reported to be highly active towards the OER, in this chapter, we will focus on both active Fe-based catalysts, as well as inactive Mn, Co and Ni complexes with two potential active sites in *cis* position.

Previous theoretical works investigating subsets of these catalysts have focused on exploring the mechanism of the O–O bond formation step, however, no reports gave an

account of the inactivity shown by the Co, Ni and Mn catalysts which were presented in the original paper, nor a direct comparison of the activities of the Fe-based active catalysts, nor a detailed rationalization of the effects of catalyst functionalization. In this chapter, we address these issues by modelling the intermediate steps – beginning from M^{II}–$(H_2O)(H_2O)$ – towards the $[M^{V}(O)(OH)]^{2+}$ intermediate of both active and inactive complexes. The form of this final intermediate has been chosen since experimental and computational studies strongly suggest that $[Fe(V)(O)(OH)]^{2+}$ is the only species which can promote O–O bond formation at room temperature, which we denote as the oxygen evolving intermediate (OEI).[198,199] PCET and electron transfer (ET) steps were modelled for every possible reaction intermediate starting from the metal oxidation state M^{II} to M^{V}. While our methodology does not include kinetic barriers, it provides essential insight into the redox potential at which electrochemical steps are expected to occur prior to the formation of the OEI. We also considered isomeric complexes where the catalyst geometry was asymmetric with respect to the position of the active site. Each of the catalysts examined, along with their associated experimental TOFs, are shown in Figure 5.1. Note that **4Fe** in Figure 5.1 is the same catalyst as was studied in the previous chapter as **Fe-14**, where we only considered a single active site instead of two. In that analysis, the predicted overpotential was 0.37 V higher than would be expected if we took the overpotential to be equal to the redox potential of CAN, (1.61 V_{NHE}) far higher than would be necessary for real world application. This suggests that the way we modelled the OER by considering only one active site was an oversimplification. Other Fe complexes reported by Lloret-Fillol *et al*. containing single active sites, or active sites *trans* to each other did not see any activity,[163] indicating that the redox flexibility afforded by having two sites to transfer electrons and protons, as well as the proximity of the sites, is key for molecular Fe-driven oxygen evolution, and we will study these factors in this chapter.

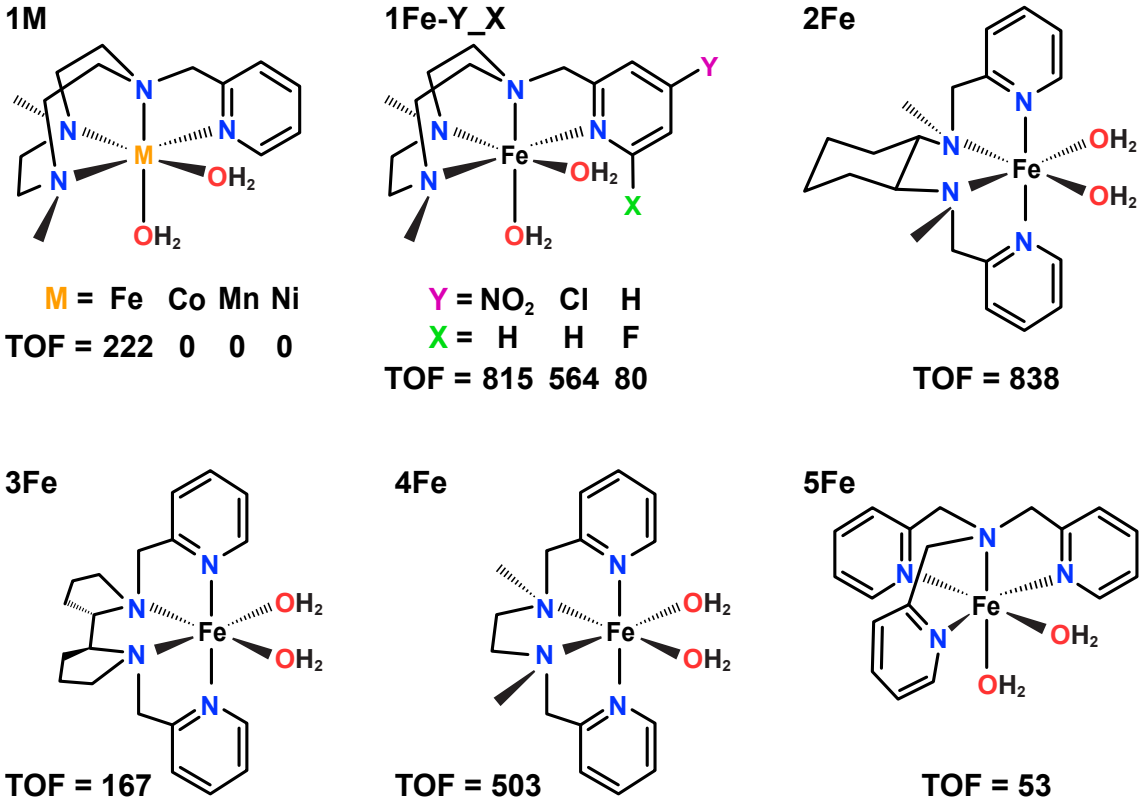

Figure 5.1. Complexes modelled in this chapter with accompanying labels and experimental initial TOF values (in h^{-1}) from Refs. 26,163.

5.2 Computational details

DFT calculations were carried out using the Gaussian 09 software[176] implementation of the hybrid meta-GGA TPSSh exchange-correlation functional.[100] C and H atoms were described using the 6-31g(d,p) split valence basis set while the same basis set including diffuse functions was used for O, N, Cl and F atoms. Fe, Mn, Co and Ni atoms were described using the LANL2DZ effective core potential[116] with additional *f*-polarization functions, with exponents of 2.462, 2.195, 2.780, 3.130, respectively, taken from work by Ehlers *et al.*[117] Geometry optimizations were performed without imposing any constraints and confirmation of the nature of stationary points was obtained through vibrational frequency analysis. In addition, for transition states, geometry relaxations along the reaction coordinate were carried out to confirm they connect the expected energy minima.

As in our previous study described in Chapter 4, the effect of the solvent was modelled using the SMD implicit solvation model (H_2O, ε = 78.3553) from Truhlar and co-workers.[131] High and low-spin states were modelled in each case and the lowest energy multiplicity was used. In cases where topological isomers were modelled, the multiplicity was assumed to be the lowest energy spin-state found for the previously modelled isomer. This level of theory was justified on the basis of the benchmarking results from the previous chapter.

The Gibbs energies of OER intermediates were calculated using the CHE model from Section 2.6.3 and the following equations:

$$\Delta G_{OH/H_2O(III)} = G_{OH/H_2O(III)} + \frac{1}{2}G_{H_{2(g)}} - G_{H_2O/H_2O(II)} \quad (5.1)$$

$$\Delta G_{O/H_2O(IV)} = G_{O/H_2O(IV)} + G_{H_{2(g)}} - G_{H_2O/H_2O(II)} \quad (5.2)$$

$$\Delta G_{O/OH(V)} = G_{O/OH(V)} + \frac{3}{2}G_{H_{2(g)}} - G_{H_2O/H_2O(II)} \quad (5.3)$$

$$\Delta G_{H_2O/H_2O(III)} = G_{H_2O/H_2O(III)} - G_{H_2O/H_2O(II)} + eE^*_{abs} \quad (5.4)$$

$$\Delta G_{OH/H_2O(IV)} = G_{OH/H_2O(IV)} + \frac{1}{2}G_{H_{2(g)}} - G_{H_2O/H_2O(II)} + eE^*_{abs} \quad (5.5)$$

$$\Delta G_{O/H_2O(V)} = G_{O/H_2O(V)} + G_{H_{2(g)}} - G_{H_2O/H_2O(II)} + eE^*_{abs}$$

(5.6)

Where the subscript denotes a specific arrangement of two distinct adsorbates on the *cis* active sites, shown in Figure 5.2, and E^*_{abs} is the value assigned to the NHE potential in water, previously calculated to be –4.28 V and described in Section 2.6.3. Each binding energy was calculated equivalently for distinct isomers.

To calculate transition state barriers for C–H hydroxylation reactions which can deactivate these catalysts, we performed a scan of the potential energy surface, restricted to the C–H distance, in steps of 0.2 Å, and performed a Berny transition state optimisation at the point along the reaction coordinate which had the lowest gradient. The geometry of one structure was then used as a starting point for the other complexes, where we would replace the metal

centre or functionalize the complex without altering the essential features of the transition state geometry.

5.3 Assessing OER reactivity

In Figure 5.2 we present the Gibbs energy profile of potential routes toward the OEI for the **1M** catalysts, calculated at ambient conditions and at U = 1.61 V_{NHE}. This potential corresponds to the redox potential of cerium ammonium nitrate (CAN),[200] the sacrificial oxidant used in the experiments. Each reaction intermediate in Figure 5.2 is labelled as **1M-A/B**, where *A* denotes the active site *trans* to the methyl-substituted amino group, and *B* denotes the active site co-planar with the pyridine ligand.

The calculated energies in Figure 5.2 illustrate clearly the well-documented large 'oxo-wall' for Co and Ni complexes,[201] showing no exergonic paths for **1Co** or **1Ni** in going from Co(III) to Co(IV), or from Ni(IV) to Ni(V). While we find that even though **1Mn** has exergonic paths between each oxidation state under reaction conditions, the most stable Mn(IV) intermediate, 1Mn(IV)-OH/OH, at –1.22 eV relative to the Mn(II) state, below all Mn(V) intermediates. Furthermore, –1.22 eV is more stable than the proposed OEI for **1Fe**, 1Fe(V)-O/OH or 1Fe(V)-OH/O which lie at –0.7 and –1.15 eV respectively indicating that this Mn(IV) intermediate is a thermodynamic sink. In addition, the 1Mn(IV)-OH/OH complex is calculated to be 0.35 eV lower in energy than the 1Mn(IV)-O/H_2O complex, which can also undergo a PCET to the OEI in oxidation state Mn(V).

UV-vis and Raman spectroscopy experiments indicated that 2Fe(IV)-O/H_2O complexes are the necessary precursors to an electrophilic oxygen evolving iron-oxo-cerium intermediate in **2Fe**.[163,202] Our results support this observation as we reproduce this iron species to be the resting state until an applied potential of *ca*. 1.5 V (Figure 5.3a). In the case of **1Mn**, however, these 1Mn(IV)-O/H_2O and 1Mn(IV)-H_2O/O intermediates are the least stable of the Mn(IV) complexes, so if CAN cannot perform the necessary PCET from 1Mn(IV)-

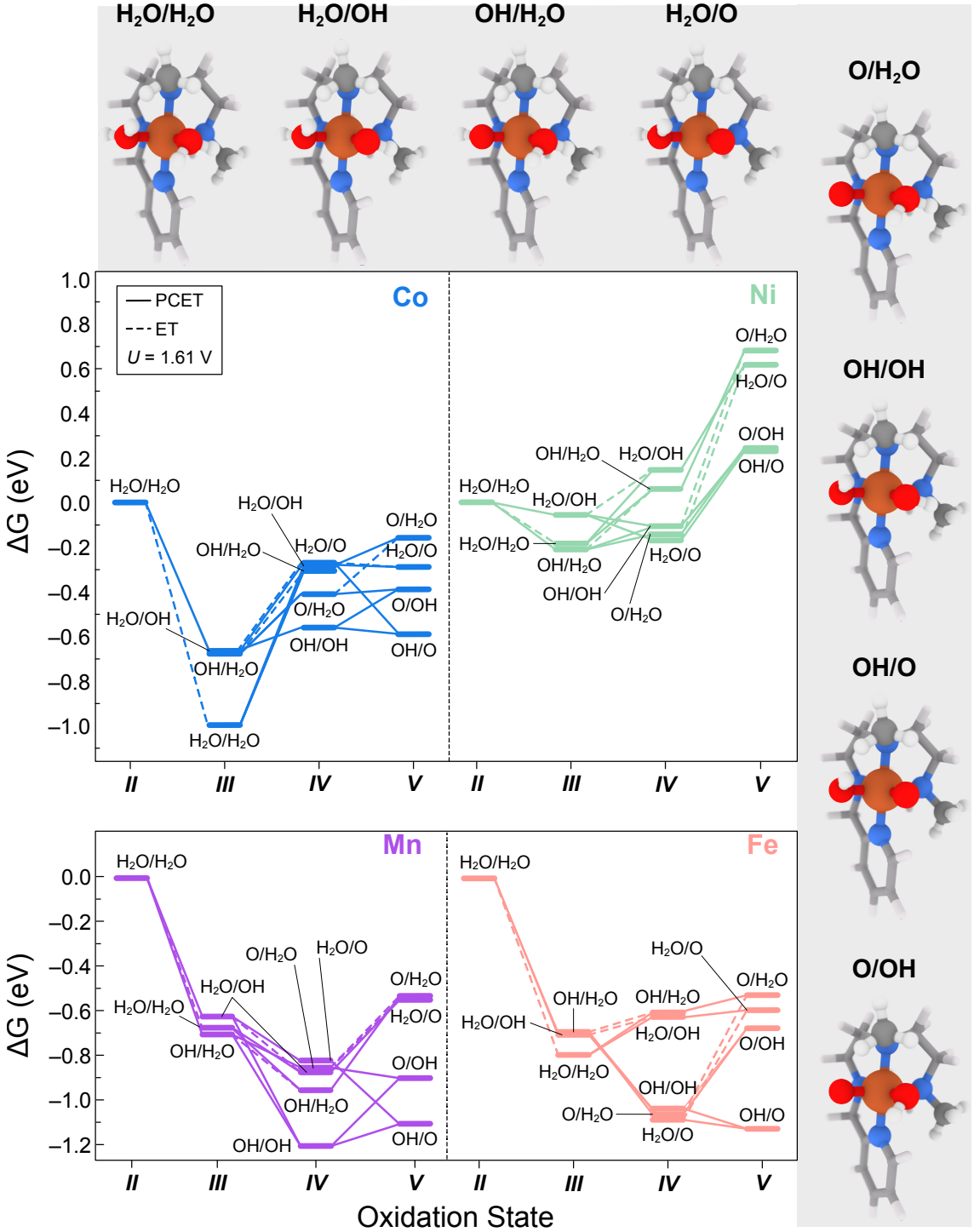

Figure 5.2. Calculated Gibbs energy diagrams at U = 1.61 V_{NHE} of potential OER pathways for **1M** complexes featuring different metals: Co (blue lines), Ni (green lines), Mn (yellow lines), and Fe (red lines). Solid lines between OER intermediates represent a PCET step, while dashed lines represent ETs. Accompanying oxidation states are shown along the x-axis. Each intermediate is labelled corresponding to one of the geometries indicated along the top of the energy diagrams. Colour code: metal centre (orange), O (red), N (blue), C (grey) and H (white).

OH/OH which it can for 2Fe(IV)-O/H_2O, then the OER may be blocked due to the stability of this *cis*-dihydroxo intermediate. Therefore, Lloret-Fillol and co-workers proposed a mechanism with Ce(III) or Ce(IV) atoms coordinating to the O fragment on the complex along with a solvent water molecule, which then facilitates the water nucleophilic attack.[196] To address the feasibility of a Ce-induced PCET, which has been reported for **2Fe**, we would need to model the reaction intermediate involving the chemical oxidant explicitly. This would be largely determined by the resting state of the complex prior to the addition of an excess of CAN, and we would assume that it would be more difficult to facilitate the Ce-enabled mechanism from the more hydrogenated resting state found for Mn (i.e., 1Mn(IV)-OH/OH). For the oxygen evolving **1Fe** catalyst, while there is no downhill path from 1Fe(III)-H_2O/H_2O, we note that the Gibbs energy difference between that intermediate and 1Fe(III)-H_2O/OH is only 0.08 eV, which can undergo an exothermic PCET step to the intermediates 1Fe(IV)-OH/OH, 1Fe(IV)-O/H_2O or 1Fe(IV)-H_2O/O. These latter intermediates are very close in energy (within *ca.* 0.08 eV), and all of them exhibit exergonic routes to the OEI. Using the same analysis, the activity of the remaining iron catalysts can be rationalized, as shown in Figures B1 and B2 in Appendix B. The plots were split in this way to group catalysts as symmetric and non-symmetric versions of **1M**. Having distinguished active and inactive catalysts in Figure 5.2, we now turn our attention to distinguishing the most active catalysts which are presented in the same fashion as in Figure 5.2 in Appendix B. The precursor species to oxygen evolution, the OEI, has been rigorously shown to be Fe(IV)-O/H_2O in **2Fe**.[202] Assuming each Fe catalyst shares the same essential oxidative intermediates, we have investigated the predicted potential for the PCET step from the lowest energy Fe(IV)-O/H_2O to the most stable topological Fe(V)-O/OH isomer for each active iron catalyst, hereafter referred to as the *predicted potential to OEI*. Interestingly, the representation of the experimental activity and that predicted potential,

shown in Figure 5.3, seems to be somewhat predictive of activity. Given that this analysis only considers the thermodynamic Gibbs energy change for one possible step in a complex reaction such as the OER, this is a noteworthy result, suggesting that oxidation to Fe(V)-O/OH is a common PLS. This finding ultimately indicates that O–O bond formation is not rate limiting for these complexes, which would not be without precedent, as this has been confirmed to be the case for **2Fe**,[4,22] as well as heterogeneous α-Fe_2O_3 OER catalysts.[203] We attribute this correlation to BEP relations between reaction and activation energies, which indirectly account for the kinetics and thereby TOF, to distinguish active from inactive catalysts. There are, however, a few deviations from the line of best fit (black line in Figure 5.3), which can be interpreted in different ways. For example, the relative difference between the predicted potentials are within previously reported inherent DFT errors for PCETs.[204] However, since the coordination environment of these complexes are all the same, one may expect qualitatively correct trends despite slight errors in the absolute values. Another possibility is that there are two sets of outliers to the linear model. This is illustrated in Figure 5.3, where we plot the linear fit after removing **1Fe-Cl_H**, with the remaining set of catalysts labelled Set A, or both **1Fe-NO_2_H** and **2Fe**, with the remaining catalysts denoted as Set B. Obviously, we would not expect this trend to continue indefinitely at continuously lower predicted potential to OEI, as the O–O bond formation may become limiting, for instance, which could also explain the deviation for **1Fe-Cl_H**. Additionally, because the 1Fe-Cl_H-OH/OH intermediate is more stable relative to the 1Fe-Cl_H-O/H_2O and 1Fe-Cl_H-H_2O/O intermediates in the oxidation state Fe(IV) (Figure 5.4), from which the OEI is proposed to form, we posit that the outlier is **1Fe-Cl_H** and stress that the linear relationship may cease below 1.5 V, or there may be a volcano-like relationship with **1Fe-NO_2_H** at the peak, since clearly if the complex is too readily oxidized it will not be reactive enough to perform the WNA. In all, we emphasize that

focusing only on O–O bond formation barriers may obscure the full picture for homogeneous OER catalysts. Therefore, we propose that the predicted potential to OEI descriptor is used along with an analysis of the relative stability of 1M(IV)-OH/OH against 1M(IV)-O/H_2O, or 1M-H_2O/O to garner a cursory prediction of activity. Of course, this descriptor cannot account for competing reactions which may deactivate the catalyst. In the following, we describe a primary route towards catalyst deactivation.

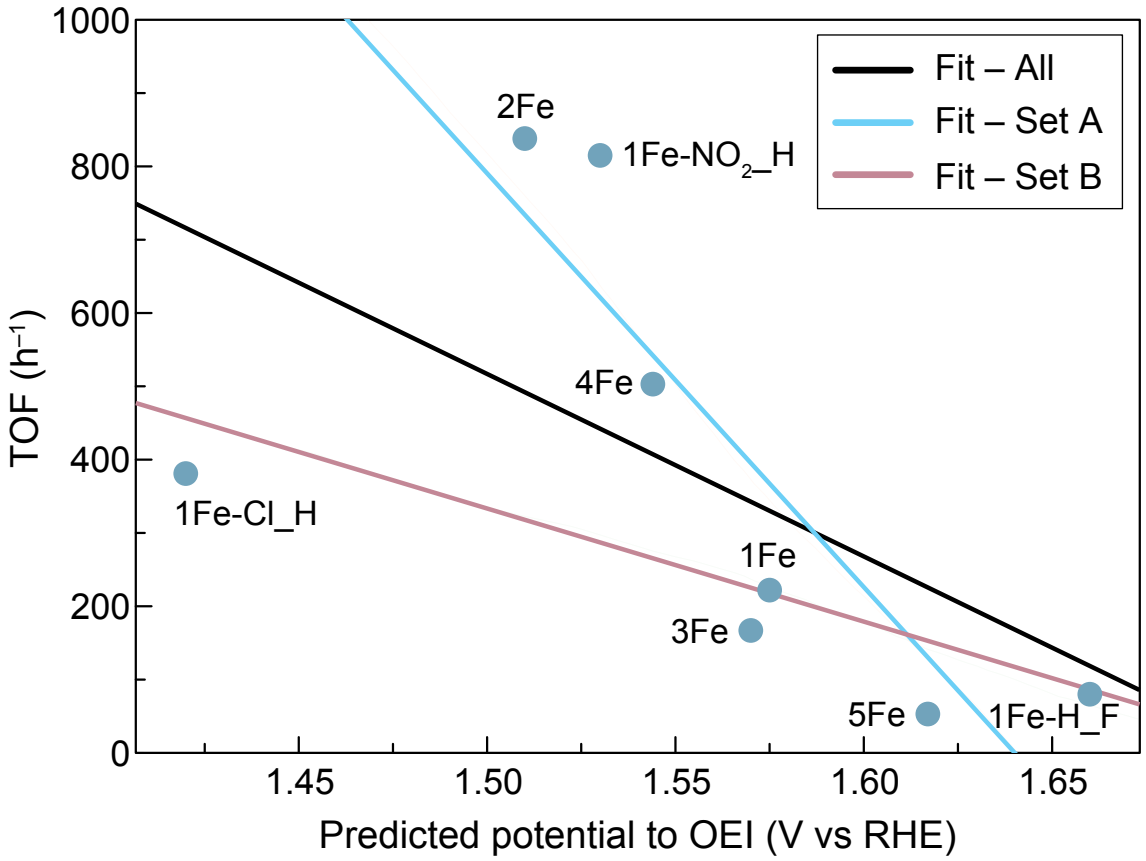

Figure 5.3. Plot illustrating the relationship between the reported experimental TOFs and the predicted potential to OEI in OER active Fe *cis*-labile catalysts.

5.4 Catalyst functionalisation

5.4.1 *Assessing reactivity*

In Figure 5.4, we present the data for functionalized **1Fe**, where again we see exergonic paths from at least one of 1Fe(IV)-H_2O/O or 1Fe(IV)-O/H_2O to 1Fe(V)-OH/O or 1Fe(V)-O/OH for the EWG functionalized catalysts, with an exception for the F-functionalized **1Fe**

in the α-position of pyridine (*i.e.*, **1Fe-H-F**). In that cases these two paths are endergonic by 0.05 eV, indicating a reason for the relatively low activity of this complex along with the differences in the predicted potential to OEI as presented in Figure 5.3.

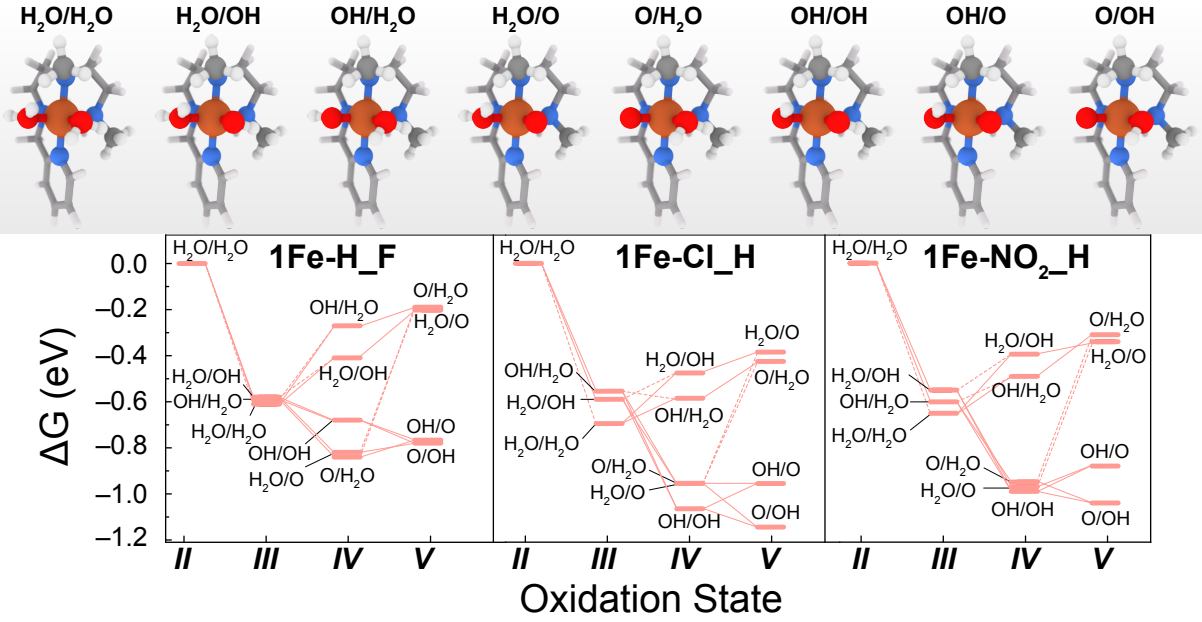

Figure 5.4. Gibbs energy profile at 1.61 V_{NHE} for functionalized **1Fe**. The information is presented as in Figure 5.2. The representative intermediates along the top of the figure corresponds to **1Fe** without functionalization, however, the labelling of intermediates in the case of the calculations for functionalized catalysts remains unchanged.

5.4.2 *Catalyst deactivation via C–H hydroxylation*

Costas *et al.* have recently reported that the deuteration of specific hydrogen atoms in the catalyst leads to striking effects on the OER activity.[205] In particular, the deuteration of the C atoms of the ethylene linker in **3Fe** caused a five-fold increase in the TON without improving the initial TOF, indicating that the bridging H atoms are deactivating the catalyst after a given number of cycles. For a separate Fe coordination complex, not studied in this chapter, the H-atoms of methyl groups were deuterated. This greatly increased the TOF with respect to the non-deuterated species from *ca*. 10 to 200 h^{-1}. The rationalisation for this was that deuteration helps prevent the hydroxylation of the methyl group at the equivalent OEI intermediate for this catalyst. This was confirmed by DFT studies, which

showed that the barrier heights involved for the C–H hydroxylation were accessible under experimental conditions, and that this deactivation was kinetically favoured for the methyl group. Due to the pronounced effect of deuterating the methyl group on the reported TOF, we sought to investigate this competing reaction leading to catalyst deactivation for some of the complexes studied in this Chapter. We present the results of this investigation for **1Mn**, **1Fe**, **1Fe-Cl_H** and **1Fe-NO$_2$_H** in Table 5.1, which includes the computed Gibbs energy barriers for the two hydroxylations possible from M(V)-OH/O, denoted as $\Delta G_A^{\ddagger}$ and $\Delta G_B^{\ddagger}$, and the one hydroxylation possible from 1M(V)-O/OH, reported as $\Delta G_C^{\ddagger}$. An illustration of these reactions is shown in Figure 5.5.

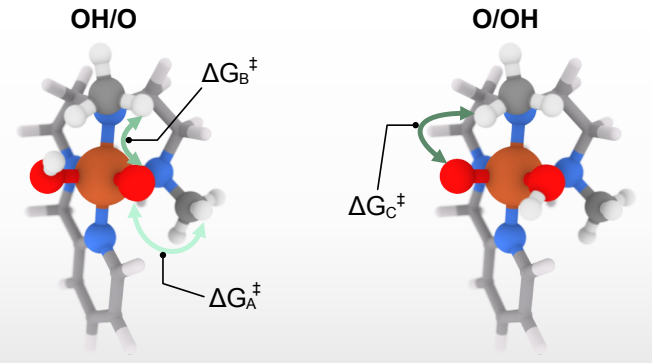

Figure 5.5. Possible competing C–H hydroxylation reactions from the two OEI isomers OH/O and O/OH. The associated calculated barriers are shown in Table 5.1.

Table 5.1. Calculated Gibbs energy barriers (in eV) for the hydroxylation reaction shown in Figure 5.5.

Catalyst	$\Delta G_A^{\ddagger}$	$\Delta G_B^{\ddagger}$	$\Delta G_C^{\ddagger}$
1Mn[a]	**0.53**	**0.71**	0.45
1Fe[a]	**0.72**	**0.85**	0.34
1Fe-Cl_H[b]	0.70	0.82	**0.98**
1Fe-NO$_2$_H [b]	0.72	0.83	**1.11**

[a] The most stable OEI is M(V)-OH/O. [b] The most stable OEI is M(V)-O/OH. The relevant barriers associated with the hydroxylations indicated in Figure 5.5 are highlighted in bold.

The results in Table 5.1 need to be interpreted with care, as the relevant barriers are the ones associated with the most stable isomer. Accounting for this, **1Mn** and **1Fe** both share the same isomeric stability (*i.e.* 1M(V)-OH/O is the most stable isomer). Here we can see that the Mn–O* moiety in the lowest energy intermediate 1Mn(V)-OH/O is the most easily deactivated of the studied complexes, with a $\Delta G_{A,B}^{\ddagger}$ of 0.53 and 0.71 eV respectively, which are accessible under the experimental conditions and below the previously reported barriers for O–O bond formation.[198] Furthermore, $\Delta G_{C}^{\ddagger}$ for **1Mn** exhibits an even lower barrier of 0.45 eV, although we expect this intermediate to be less easily accessible as the 1Mn(V)-O/OH isomer is less stable than 1Mn(V)-OH/O. All of this implies that **1Mn** could be rendered active by deuterating methyl groups, provided C–H hydroxylation is what prevents oxygen evolution instead of the thermodynamic sink at the 1Mn(IV)-OH/OH or 1Mn(IV)-OH/H_2O intermediates (Figure 5.2). The similarity between the oxygen evolving complex in Photosystem II and the iron-oxo-cerium OEI has been noted previously,[202] indicating that such *cis*-labile Mn catalysts could be possible. In the case of the Fe-based complexes, the calculated energy barriers increase by *ca.* 0.1-0.2 eV. While the barriers of the functionalized complexes from Fe(v)-OH/O ($\Delta G_{A,B}^{\ddagger}$) are almost identical, we see a marked difference in the values of the barrier for hydroxylation of the Fe(V)-O/OH isomer ($\Delta G_{C}^{\ddagger}$). Previous DFT studies of this hydroxylation found similarly distinct barriers for a specific catalyst,[205] although that analysis was less complex as it did not include a comparison of topological isomers or distinct catalysts.

Importantly, these results on modified **1Fe** catalysts also shed light on the improved activity of the catalysts functionalized with EWGs in *para*-position on the pyridine ligand (Figure

5.1). Calculations indicate that the Fe(V)-O/OH intermediates are more stable than Fe(V)-OH/O for **1Fe-Cl_H** and **1Fe-NO_2_H** (Figure 5.4), whereas the reverse trend is observed for **1Fe** (Figure 5.2). Hence, this functionalization swaps the stabilities of the topological isomers of the OEI as compared with **1Fe**, making the functionalized catalysts more resistant to deactivation via C–H hydroxylation. This is because by inspection that isomer has one less methyl group which can deactivate the catalyst from the OEI. This effect could be investigated experimentally by selectively deuterating specific methyl groups for functionalized and non-functionalized catalysts presented in this study. A potential explanation for the observed difference in $\Delta G_C^{\ddagger}$ between **1Fe** and the functionalized catalysts is a slight increased distance of the metal-oxo moiety in the Fe(V)-O/OH intermediate to the nearest H-atom of the single methyl group (from 2.561 to 2.625 Å), which is reflected in a larger hydroxylation barrier (Table 5.1). In general, this underscores that homogeneous OER catalysts should be designed to maximize the distance to methyl groups or any hydrogen atoms reactive enough to migrate from the ligand to an active site, while also demonstrating the tunability of molecular OER complexes. Furthermore, we propose that the slightly reduced $\Delta G_C^{\ddagger}$ value in **1Fe-Cl_H** may account for the observed deviation from the relationship shown in Figure 5.6.

5.5 Discussion

With all the knowledge acquired above, we formulate the following high-level blueprint for future efficient evaluation of OER complexes with two *cis*-active sites using only absolute Gibbs energies: i) Calculate the predicted potential to the OEI; ii) assess the relative stability of M(IV)-O/H_2O vs. M(IV)-OH/OH; and iii) note the proximity of the O atom in the most stable OEI to neighbouring methyl groups. If the predicted potential to OEI is less than 1.6 V, (all catalysts which satisfy this in Figure 5.6 exhibit a TOF greater than 100 h^{-1}), the M(IV)-O/H_2O intermediate is within 0.1 eV of M^{IV}-OH/OH (to avoid the

unfavourable thermodynamic sink), and the electrophilic O atom within the OEI is at least 3.0 Å away from the nearest H-atom of a dangling methyl group, then this complex is worthy of further study.

The importance of ligand oxidative stability has been experimentally shown by deuteration,[205] and our results emphasize this by indicating that ligand functionalization can bias certain topological isomers which would be more resistant to deactivation because they are not as close to flexible methyl groups. Future work to identify more stable and long-lasting Fe-based OER catalysts should focus on a broader set of ligands which are similarly neutral, non-equatorial and coordinate Fe as a tetradentate ligand, but crucially contain no H-atoms liable to oxidation. Finding the electronic effects governing the relative stability of different OH/O O/OH isomers should also be explored. Another important factor is the comparability of chemical and electrochemical oxidations of these molecular catalysts. In this context, a recent work on a set of molecular Ir OER catalysts have provided evidence that catalysts which showed the highest activity when using CAN do not continue to show the best activity under electrochemical conditions.[206]

5.6 Conclusions

In conclusion, in this chapter we presented a thorough investigation of experimentally reported active and inactive OER catalysts. We showed that straightforward considerations based on relative thermodynamic energies can be used to explain the inactivity of Co and Ni complexes, while also coarsely distinguishing active catalysts via a simple thermodynamic descriptor. This study also highlights the importance of experimental reports of inactive complexes which can then be benchmarked by computational chemistry. A primary advantage of molecular OER catalysts is their inherent tunability via functionalization, however, understanding the effects of such adaptations can be challenging. This chapter indicated that the site-selectivity of the OEI can be enforced by

functionalizing **1Fe** with EWGs in *para*-position, aiding the inhibition of the off-cycle hydroxylation of methyl groups. In all, we demonstrated that DFT-calculated PCET and ET energies are an effective means of screening hypothetical transition metal catalysts. This study extends on the work done in Chapter 4 by studying a specific subset of catalysts while considering two possible active sites as opposed to only one. As in the previous chapter, we presented a novel thermodynamic descriptor which could be used to screen this specific subset of catalysts, and which was directly correlated to experimental catalytic efficiencies. The system-specific approach that we outlined to screen Fe-based complexes considers the potential for catalyst deactivation, as well as our thermodynamic descriptor, and may allow for faster and more efficient evaluation of hypothetical Fe-based *cis*-active site OER complexes.

Chapter 6 Screening Molecular Water Splitting Catalysts

6.1 Introduction

In chapter 4, we described the importance of a one-electron oxidation occurring at the metal-oxo unit of certain molecular complexes, prior to O–O bond formation, which must be considered to explain the impressive activity of certain homogeneous OER catalysts. We showed that this additional step could allow for the circumvention of the restriction imposed by the OER scaling relation, leading to the possibility for catalysts to exhibit near-zero overpotentials provided the energy levels of redox intermediates are appropriately distributed.

With this insight, we proposed a series of catalyst design principles to allow for the discovery of molecular catalysts based on earth-abundant metals which can stabilize high oxidation states such as Mn and Fe. In this chapter, we test the design principles outlined in Chapter 4 by studying intermediates across metals and oxidation states among a uniform set of ligands. Traditional computational OER studies apply the conventional OER descriptor, $\Delta G_{O^*} - \Delta G_{HO^*}$ which is thought optimal when it is equal to half the value of the intercept found in the scaling relationship between ΔG_{HO^*} and ΔG_{HOO^*}. While this is effectively a pH-independent descriptor, OER catalyst performance is known to be pH-dependent, with activity varying significantly in alkaline or acidic conditions. This is especially relevant due to the exigency of developing catalysts which are active in acid.[154] Alterations in activity due to pH can be attributed to interwoven factors such as catalyst instability, ionic transport, switching mechanisms or a combination thereof. In this study, we examine distinct reaction mechanisms by modelling descriptors in differing oxidation states, which is typically not done in studies utilizing the OER descriptor. Since one can

expect more protonated intermediates in acidic conditions, one would expect the extra oxidation mechanism to be less favoured than in base. We believe such a simple consideration could allow for pH-dependence using simple descriptors.

To test our design principles, we set out to conduct a high-throughput computational screening of mononuclear complexes with the aim of accelerating the discovery of earth-abundant OER catalysts by focusing on non-critical elements which can stabilize high-valent M(V) intermediates and deepen our understanding of this reaction. In particular, in this chapter we present a fully-automated approach to create transition metal complexes with molSimplify[207] by permutating a selected set of ligands which have been previously seen in experimental OER catalysts.[24] As shown in Figure 6.1, five different geometries are generated from these ligands depending on their denticity, each of them containing one of six metal centres (*i.e.* Cr, Mn, Fe, Ru, Co, and Ni), leading to a total of 444 molecular catalysts which are octahedral upon the addition of the adsorbate. To more clearly explain how we constructed each of the complexes, we will detail how to interpret Figure 6.1. Each of the geometries except **32** contains either one (**41a**) or a combination of monodentate ligands, which we can see by inspection of Figure 6.1 since each of the **1a**, **1b** and **1c** ligands trace lines from their molecular representation to each of the five remaining geometry types. Five separate tridentate ligands are found in geometries **32**, **31t** and **31a** where the *t* and *c* denote active sites in *trans* and *cis*, respectively. We acknowledge that most coordinations of these complexes are derived from Ru-based catalysts, and that metals may not be exchanged with ease, although such freedom has been seen among first-row transition metal catalysts, specifically Mn, Fe, Co and Ni.[163] For each catalyst, $\Delta G_{HO(III)^*}$ and $\Delta G_{HOO(III)^*}$ are evaluated, with $\Delta G_{HO(IV)^*}$, $\Delta G_{HOO(IV)^*}$, $\Delta G_{O(IV)^*}$ and $\Delta G_{O(V)^*}$ calculated for a subset of these complexes which can access higher oxidation states.

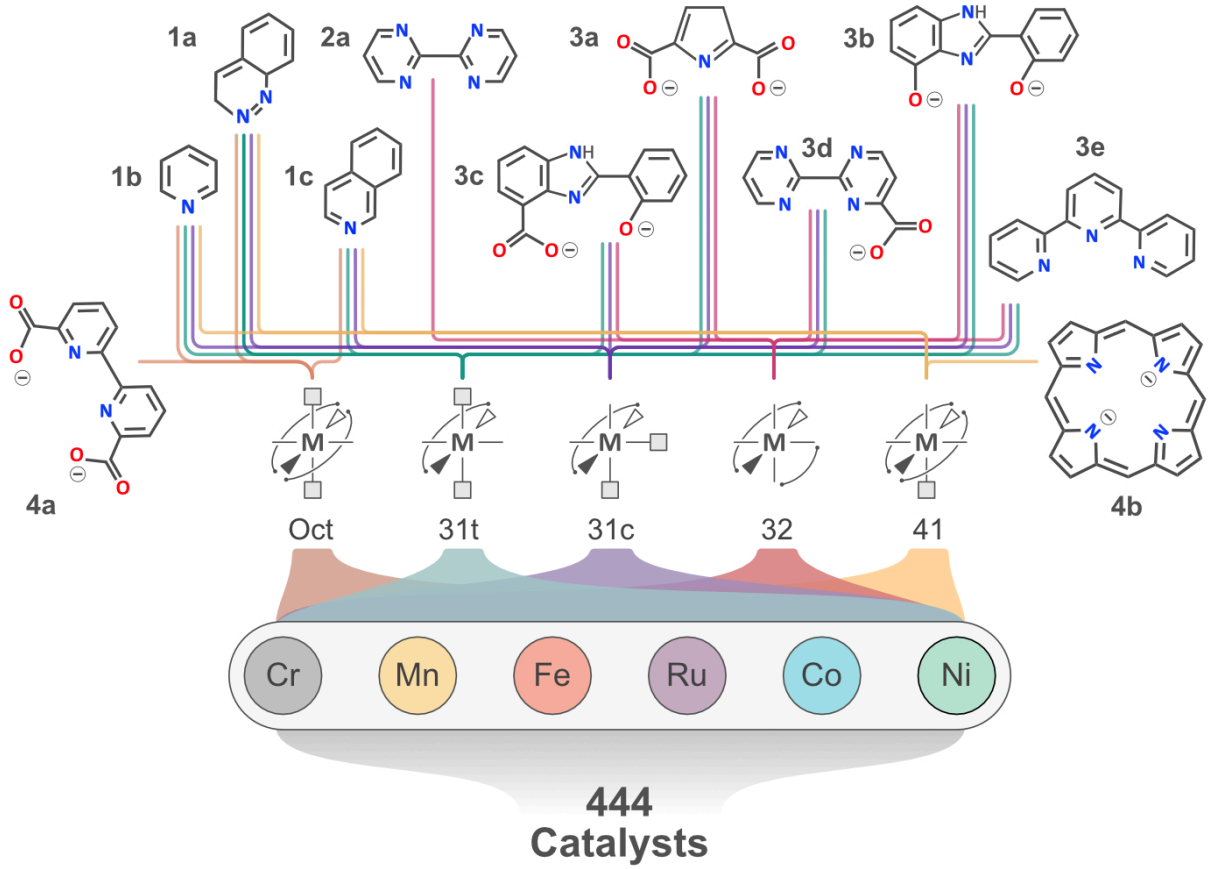

Figure 6.1. Depiction of the combination of ligands, geometries and transition metals used to automatically generate the OER complexes investigated in this chapter, with the label for each distinct geometry. Monodentate ligands in each of the geometries are represented by squares, while the adsorbate is placed at the end of the free lines protruding from the metal. Where there are two monodentate ligands, they can either be *cis* or *trans* to each other, leading to labels **31c** or **31t**, respectively.

In what follows we will describe the computational methodology applied, probe the existence of universal, OER scaling relations and re-examine fundamental assumptions of scaling relations between the HO* and O* intermediates. Our data also provides justifications for intriguing deviations from prototypical scaling relations that are a result of the spin states observed in the modelled open-shell systems. In addition, our automated high-throughput screening leads to 9 earth-abundant catalysts based on Cr, Mn and Fe exhibiting a predicted OER overpotential lower than 400 mV. In all, our high-throughput

analyses provide new insights on experimental findings and open new avenues for future research towards the discovery of low cost and efficient OER catalysts.

6.2 Computational details

DFT calculations were performed at the TPSSh, M06-L and B3LYP level using the Gaussian09 software, while BEEF-vdW calculations were performed using the VASP code, version 5.4.4.[208–211]

To describe the Ru, Mn, Fe, Cr, Co and Ni metals using Gaussian09, the Lanl2dz effective core potential was used along with *f*-polarization functions with exponents 1.235, 2.195, 2.462, 1.941, 2.78 and 3.13, respectively.[117] The more electronegative O, N, F, and Cl atoms were described using the 6-31+G(d) basis set, while the 6-31g(d,p) basis set was employed for C and H atoms. Molecular structures were optimized in water using the TPSSh functional and the implicit SMD solvation model (ε = 78.3553).[131] These geometries were used to generate the data with the B3LYP and M06-L functionals via single point calculations.

Gibbs energy corrections obtained from the TPSSh frequency calculations were then added to the potential energies computed with B3LYP and M06-L. Gibbs energies were calculated at the temperature of 298.15 K and pressure of 1 atm, except for the isolated H_2O molecule that was computed at the temperature and pressure at which both the liquid and gas phases are in equilibrium, *i.e.* 300 K and 0.035 atm. Relative Gibbs energies are referenced to H_2O and H_2 in solution, to avoid introducing the error associated with the modelling of O_2 with DFT methods, and the global reaction Gibbs energy was fixed to the experimental value of 4.92 eV. To ensure sound geometries, we inspect any intermediate if atoms coordinated to the metal change, or if a bond distance changes by 20% or more. Grimme D3 dispersion corrections[212] were added via single point calculations at the

optimized geometries, except for the results of M06-L calculations, as this Minnesota functional was partly fit to non-covalent interactions.

BEEF-vdW calculations in VASP-5.4.4 were performed using projector-augmented wave pseudopotentials[124] and plane waves with a kinetic energy cut-off of 500 eV. The valence configurations for each element is indicated in brackets beside their symbol: Cr ($3d^4 4s^2$), Mn($3d^5 4s^2$), Fe($3d^6 4s^2$), Co($3d^7 4s^2$), Ni($3d^8 4s^2$), Ru($4d^6 5s^2$), C($2s^2 2p^2$), N($2s^2 2p^3$), O($2s^2 2p^4$) and H(1s). Molecular catalysts were modelled in a unit cell with a vacuum spacing of at least 15 Å in each direction. A self-consistent evaluation of the wavefunction was stopped once the electronic energy changed by less than 1×10^{-6} eV, while geometry optimization completed when all forces on atoms were within 0.02 eV/Å with Gaussian smearing of 0.05 eV. Gibbs energy corrections – using the same conditions outlined in the previous paragraph – of 0.31 eV and 0.4 eV were added to ΔE_{HO^*} and ΔE_{HOO^*} to arrive at ΔG_{HO^*} and ΔG_{HOO^*}, respectively. These corrections were obtained by taking the average of the Gibbs corrections of a Ru and Fe catalyst, which only varied by at most 0.02 eV. These values were derived for individual adsorbates using the ideal gas approximation, comprising the zero-point energy, translational, rotational, vibrational and electronic inputs to the heat capacity at constant pressure of 1 atm and at 298.15 K, along with the entropic contributions via the Thermochemistry module provided by the Atomic Simulation Environment.[134]

The set of ligands seen in Figure 6.1 were chosen as they had seen application in experimentally realized catalysts, and the charges of these ligands were pre-assigned and used to define the total charge of the catalyst. The spin state of metals in each reaction intermediate was determined by investigating which multiplicity was the most stable for a representative set of molecules. If, for a given metal in a certain oxidation state, one multiplicity was consistently lower in energy by 0.3 eV, that spin state was assigned

throughout for all calculations. Following this criterion, all Mn oxidation states, Fe(II), Co(II), and Cr(II) were assigned to be high-spin, while all Ru oxidation states, Co(III), Ni(II), were assigned low-spin. For Fe(III) complexes, both high and low-spin structures were modelled as no prevalent spin-state was determined. The results of this investigation are shown in Appendix C, Table C1. The spin-states exhibiting the lowest energy were subsequently modelled using the M06-L and B3LYP exchange-correlation functionals.

The Gibbs binding energies of the different OER intermediates are defined using the computational hydrogen electrode model[1,2] described in Section 2.6.3, as in Eqs. 6.1–6

$$\Delta G_{HO(III)^*} = G_{HO(III)^*} - G_* - G_{H_2O_{(l)}} + \frac{1}{2} G_{H_{2(g)}} \tag{6.1}$$

$$\Delta G_{HO(IV)^*} = G_{HO(IV)^*} - G_* - G_{H_2O_{(l)}} + \frac{1}{2} G_{H_{2(g)}} + eE^*_{abs} \tag{6.2}$$

$$\Delta G_{O(IV)^*} = G_{O(IV)^*} - G_* - G_{H_2O_{(l)}} + G_{H_{2(g)}} \tag{6.3}$$

$$\Delta G_{O(V)^*} = G_{O(V)^*} - G_* - G_{H_2O_{(l)}} + G_{H_{2(g)}} + eE^*_{abs} \tag{6.4}$$

$$\Delta G_{HOO(III)^*} = G_{HOO(III)^*} - G_* - 2G_{H_2O_{(l)}} + \frac{3}{2} G_{H_{2(g)}} \tag{6.5}$$

$$\Delta G_{HOO(IV)^*} = G_{HOO(IV)^*} - G_* - 2G_{H_2O_{(l)}} + \frac{3}{2} G_{H_{2(g)}} + eE^*_{abs} \tag{6.6}$$

6.3 Method-agnostic scaling relations

With the 444 catalysts formed via the automatic structure generation outlined in Figure 6.1, we modelled the HO(III)* and HOO(III)* intermediates to investigate the universality and method-dependence of the OER scaling relation between ΔG_{HO^*} and ΔG_{HOO^*}. To confirm the robust nature of this relationship, we use a set of four different DFT methods, which include two widely used hybrid mGGA functionals exhibiting varying degrees of HF exchange (%), *i.e.* TPSSh[103] (10%) and B3LYP[106] (20%), as well as the m-GGA functional M06-L[97] and the pure GGA functional BEEF-vdW.[92] The latter functional also allows for the non-self-consistent evaluation of an ensemble of 2,000 separately parametrized GGA

functionals, which permits the estimation of errors.[92] Details outlining the application of these functionals is provided in the Computational Methods section. While this GGA functional is not appropriate for use in describing open-shell systems, we include it in our analysis to compare our results with prior OER scaling relation studies on heterogeneous catalysts which tend to employ GGA+U functionals.

In Figure 6.2a, the results of TPSSh calculations for individual catalysts are shown as data points, while the lines of best fit through each functional are also provided, showing each line to be essentially parallel, with the intercept of the lines being the only appreciable difference. Notably, we find that this data can be used to begin to rationalize past decades of experimental research into monometallic OER catalysts.[24] Ru complexes exhibit a tendency to shift below the line of best fit, meaning these complexes stabilize the HOO* intermediate to a greater extent than other metals, on average. This phenomenon, which reduces the minimum theoretical overpotential via the conventional WNA mechanism, was also noted in a computational study of IrO_2 and $SrIrO_3$ surfaces, and formed part of the rationalization for these materials' impressive activity in acidic media.[213] Similar to Ru, Ni catalysts are found to deviate from the line of best fit, which we will rationalize later.

Figure 6.2a also reveals that some octahedral Ru complexes bearing the **4a** ligand in the **Oct** geometry, shown as purple circles, exhibit a $\Delta G_{HO(III)^*}$ close to the ideal value of 1.23 eV, leading to a $\Delta G_{HOO(III)^*}$ of 4.5 eV. Notably, this particular family of Ru catalysts with the **4a** ligand are some of the best molecular catalysts known to date.[25,214] We propose that this is because they are not constrained to follow the conventional WNA pathway. Instead, these catalysts are known to undergo an extra oxidation step before forming the O–O bond via the I2M mechanism.[25,214] These complexes, therefore, avoid the constraints imposed by the scaling relationship by circumventing the formation of the HOO* intermediate.

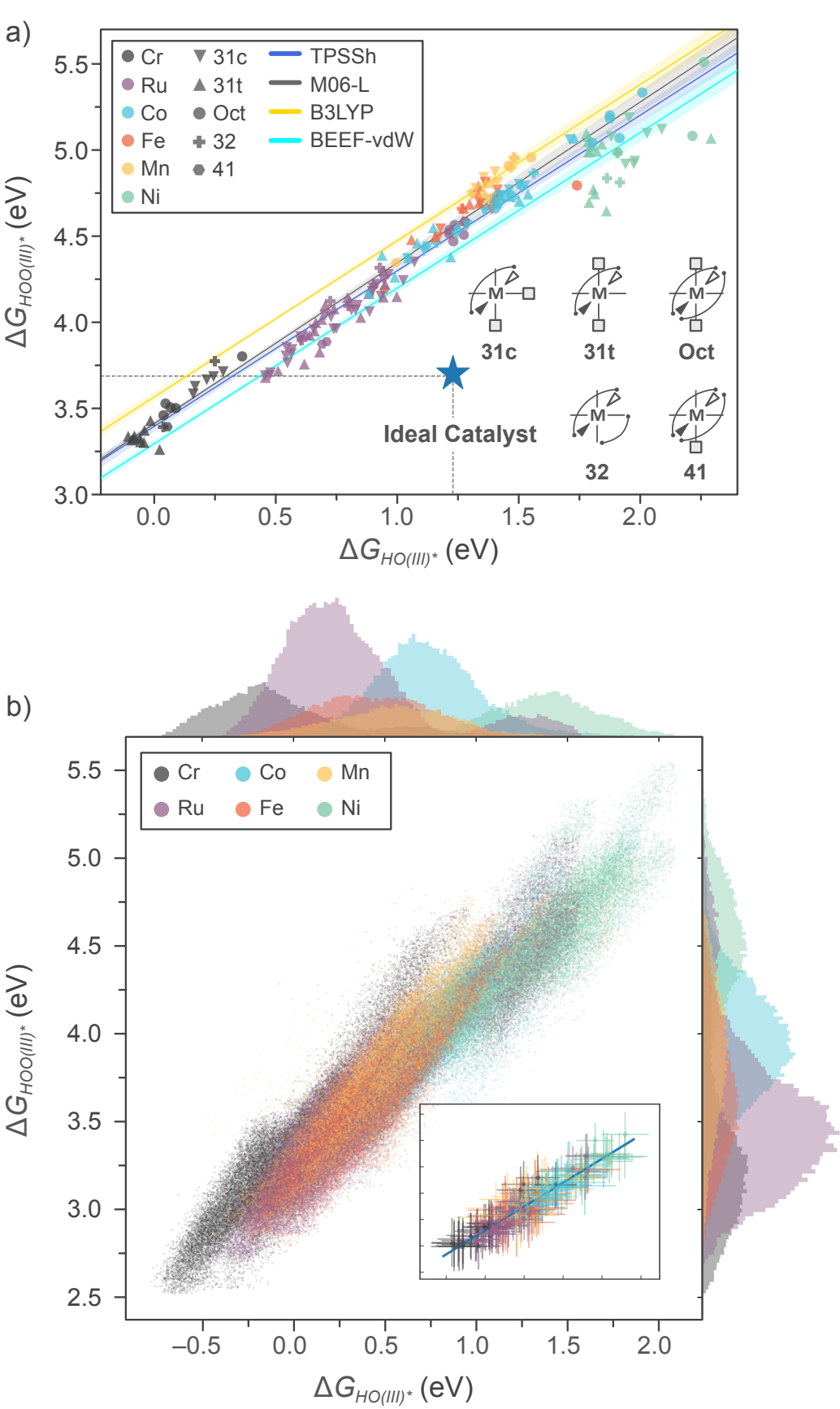

Figure 6.2. (a) Plot showing the OER scaling relationship between $\Delta G_{HO(III)^*}$ and $\Delta G_{HOO(III)^*}$ spanning different DFT methods with lines of best fit for the multiple methods and geometries. The line of best fit for TPSSh data was found to be $\Delta G_{HOO(III)^*} = 0.89\Delta G_{HO(III)^*} + 3.41$. Data points correspond to the calculated TPSSh data. The ideal binding energies are indicated with the star. Each marker represents a distinct geometry as depicted in Figure 6.1, with each colour denoting a distinct metal. (b) Plot showing the scaling plots across model space of BEEF-vdW and other GGA functionals. The distributions of values from these ensembles are shown in the secondary axes to illustrate the funtional-independent nature of the scaling relation using the BEEF ensemble. The inset shows the datapoints with the associated errorbars derived from the ensemble of the BEEF-vdW calculations.

To further confirm the robustness and insensitivity to method of the OER scaling, we applied the error estimation framework utility from BEEF-vdW to represent that relation for GGA functionals which are within one standard deviation of the mean value of this ensemble (Figure 6.2b). This was performed similarly in a study on the functional-dependence of scaling relations,[215] although to the best of our knowledge, this is the first time that the analysis in Figure 6.2b has been done for the OER. In the GGA space, we find that the distribution of the binding energies for each metal is the same, providing further evidence that the OER scaling relation is insensitive to method.

Implicit in the extra-oxidation mechanism is the assumption that the one-electron transfer occurs immediately prior to the formation of what we assume to be the site for the water nucleophilic attack, the M(V)–O intermediate. However, this M(IV)–O to M(V)–O oxidation could occur at any point before this, leading to the M(IV)–OH intermediate, which would be subject to the same constraints on the overpotential inherent in the scaling relation in Figure 6.2, as evidenced in the oxidation-state independent scaling in Figure C1 in Appendix C.

6.4 Spin-based scaling circumvention

Interestingly, Figure 6.2a also indicates that the $\Delta G_{HOO(III)^*}$ values for Ni(III) complexes deviate from the linear scaling relationship. We posit that this is because the HOO(III)* intermediate allows for these complexes to be stabilized in the Ni(II) oxidation state, while the HO(III)* intermediate cannot. To support this, we inspected the Ni spin densities in the HOO(III)* and HO(III)* intermediates to use them as a proxy for oxidation state, finding values of *ca.* 1.5 and 0.9, respectively. This makes a further connection to recent experimental findings, where it has been shown that orienting a magnet appropriately with electrocatalysts composed of mixed Ni, Fe and Zn oxides can significantly enhance the rate of the OER.[216] The authors proposed that this effect stems from the induced magnetic field

which facilitates the parallel spin alignment along the OER to yield the triplet oxygen product. In their case, they invoke the I2M mechanism, while we observe this phenomenon for a WNA intermediate, although the essential justification is the same; facilitating oxygen atoms to be spin-aligned, a rate enhancement can occur. Furthermore, a recent perspective has proposed that the magnetic enhancement effect could be related to a deviation from scaling relationships.[217]

This prompted us to investigate this hypothesis by inspecting the spin density in the HOO* intermediate and the deviation of the $\Delta G_{HOO(III)^*}$ values from the scaling shown in Figure 6.2a. To do this, we describe the collinearity of oxygen atoms, λ, using the Mulliken spin densities, μ, of the individual oxygens in the HOO* intermediate as:

$$\lambda = \mu_{O_1}\mu_{O_2} \tag{6.7}$$

The result of plotting λ along with the corresponding Mulliken spin density on the metal (μ_M) in the HOO* intermediate is shown in Figure 6.3, where we identify a distinct region defined by $\lambda > 0.1$ and $\mu_M > 1$ in which Ni catalysts deviating favourably from the OER scaling lie.

The remaining catalysts in Figure 6.3 are grouped into two regions. The upper left region denotes Fe(III), Mn(III) and Cr(III) complexes with HS d^5, d^4 and d^3 electronic configurations, respectively. These catalysts tend to lie above the line of best fit, except for an **Oct-Fe** complex which shows a seven-coordinated HOO* intermediate. This geometry has been shown to be important in Ru OER catalysts.[193] On the other hand, in the lower left region, we find Fe(III), Ru(III) and Co(III) catalysts with LS d^5, d^5 and d^6 configurations, respectively, which tend to lie below or close to the scaling line.

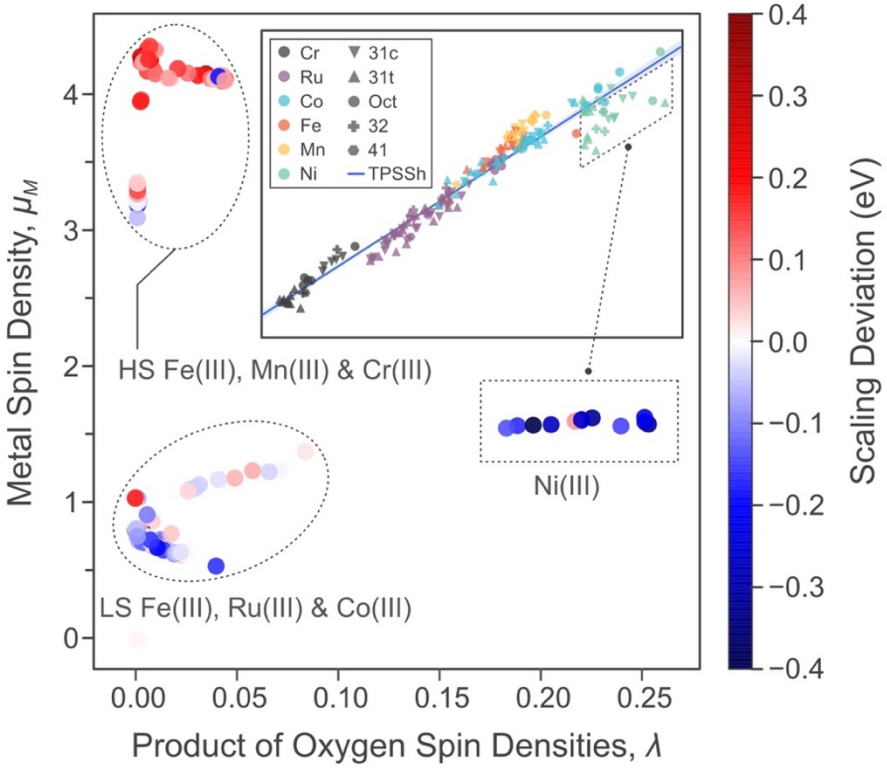

Figure 6.3. Graphical representation of the λ parameter defined in Eq. 6.7, against the metal spin density, μ_M, to rationalize the scaling deviation of the HOO* intermediate for Ni catalysts. The colourbar represents the deviation from the TPSSh line of best fit from Figure 6.2a (inset). The rectangle and parallelogram are used to illustrate the essence of the relationship found. We note there is not a one-to-one correspondence between the data points in each shape, that is, not all points in the rectangle are in the parallelogram.

Our calculations indicate that the ligand scaffold is not responsible for the deviation from the scaling, as H-bonding does not lead to the same decisive effect, as depicted in Figure 6.4. Hence, we conclude that the magnetic enhancement effect can also be leveraged in the WNA mechanism to facilitate O–O bond formation via the stabilization of the HOO* intermediate relative to the established scaling.

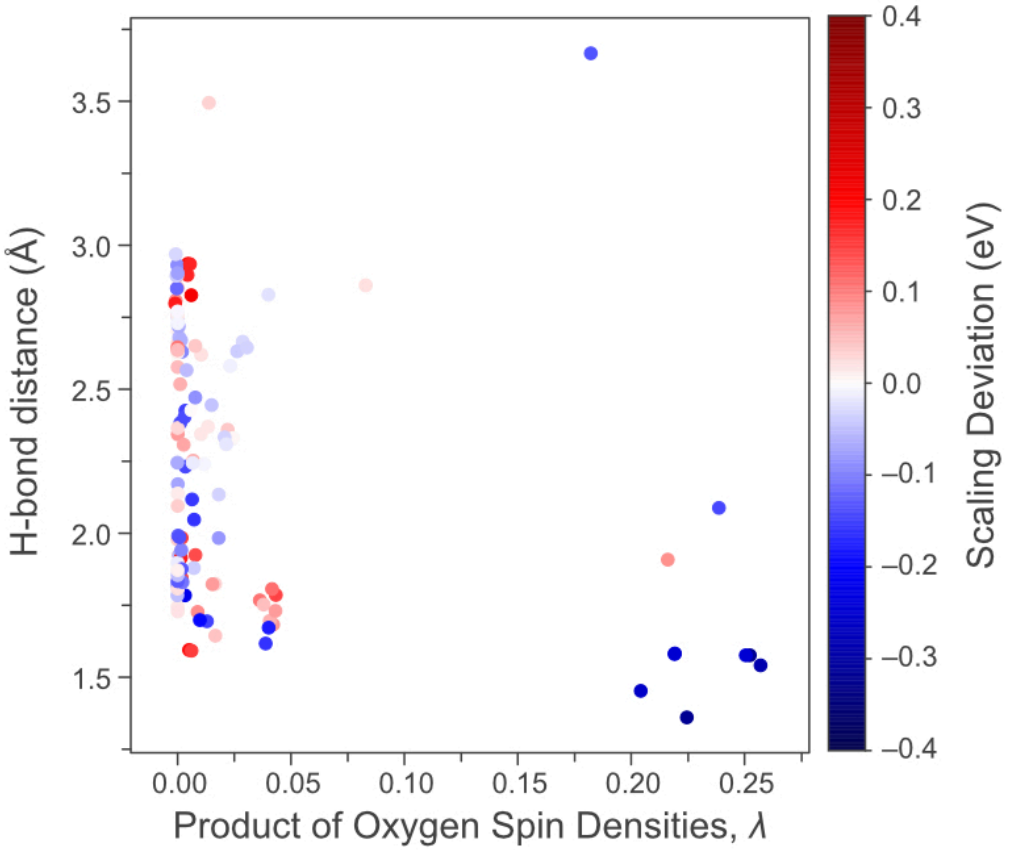

Figure 6.4. Graphical representation of the λ parameter against the H-bond distance to the nearest non-bonded O or N atom. This illustrates that H-bonding cannot be used to decisively explain the linear scaling deviations observed in Figure 6.2a.

The theoretical basis for spin-dependent oxygen electrochemistry has been developed and examined by Gracia and co-workers.[218–220] In those works, this effect was claimed to be exchange-mediated, which is borne out by our analysis as we only observe this effect when using DFT functionals which include HF exchange, as shown in Figure 6.5, where the effect is seen for B3LYP, but for M06-L, we only see one point decisively below the scaling relationship, as evidenced by the single dark blue point in the ellipse of Figure 6.5b. We note that B3LYP and M06-L are functionals with 20 and 0 % HF exchange, respectively. Our contribution indicates that there is a connection between spin conservation and circumventing well-established scaling relations, which to be of importance in identifying cost-effective OER materials.

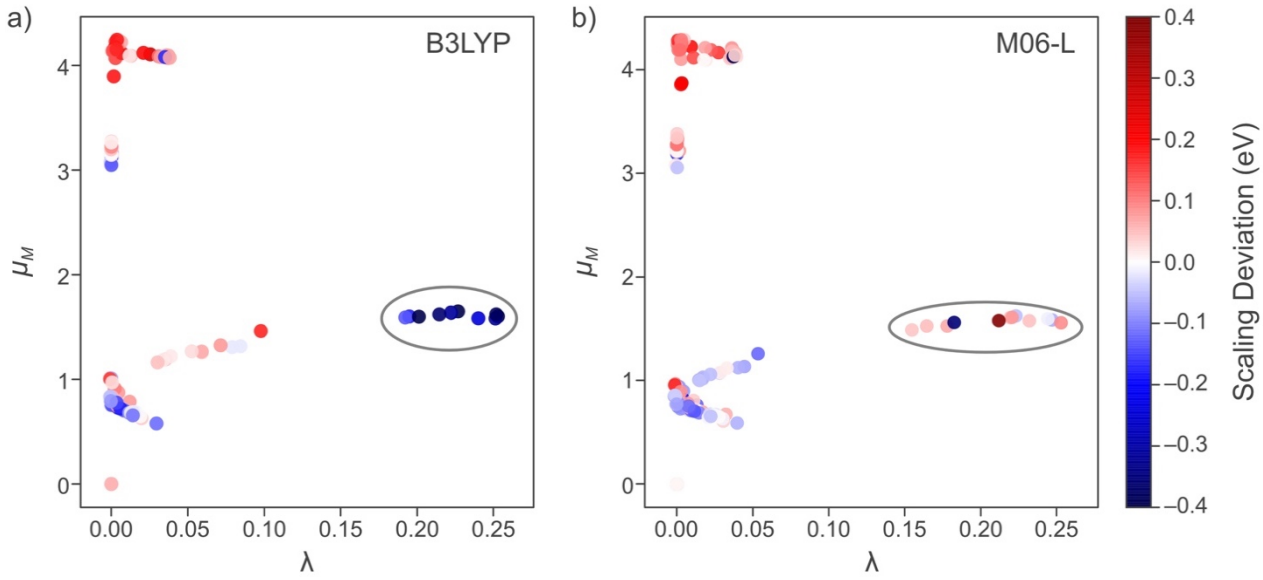

Figure 6.5. As in Figure 6.3, we show the scaling deviation as a function of metal multiplicity, μ_M, and the λ parameter for the B3LYP and M06-L functionals. This implies that HF exchange is required to observe a deviation from the scaling relation among the Ni catalysts, as a deviation is only manifest for the B3LYP and TPSSh functionals. The group of Ni points in question are highlighted within an ellipse.

6.5 Catalyst screening

We next sought to test the possibility of near-zero overpotential catalysts via an extra-oxidation mechanism.[204] With this aim, we computed the conventional OER descriptor, $\Delta G_{O(IV)^*} - \Delta G_{HO(III)^*}$, for catalysts in Figure 6.2a which exhibit a value of $\Delta G_{HO(III)^*} \leq 1.5$ eV, leading to the volcano plot presented in Figure 6.6a. Use of this volcano representation has found useful application across OER research.[11,221] This upper limit is chosen to place a lower limit on the overpotential due to $\Delta G_{HO(III)^*}$, where our aim is to find catalysts with overpotentials that circumvent the "overpotential wall". While catalysts which are close to the peak of the volcano in Figure 6.6a demand a considerable overpotential, they evolve oxygen via PCETs exclusively, thereby avoiding the building-up of positive charge.[222]

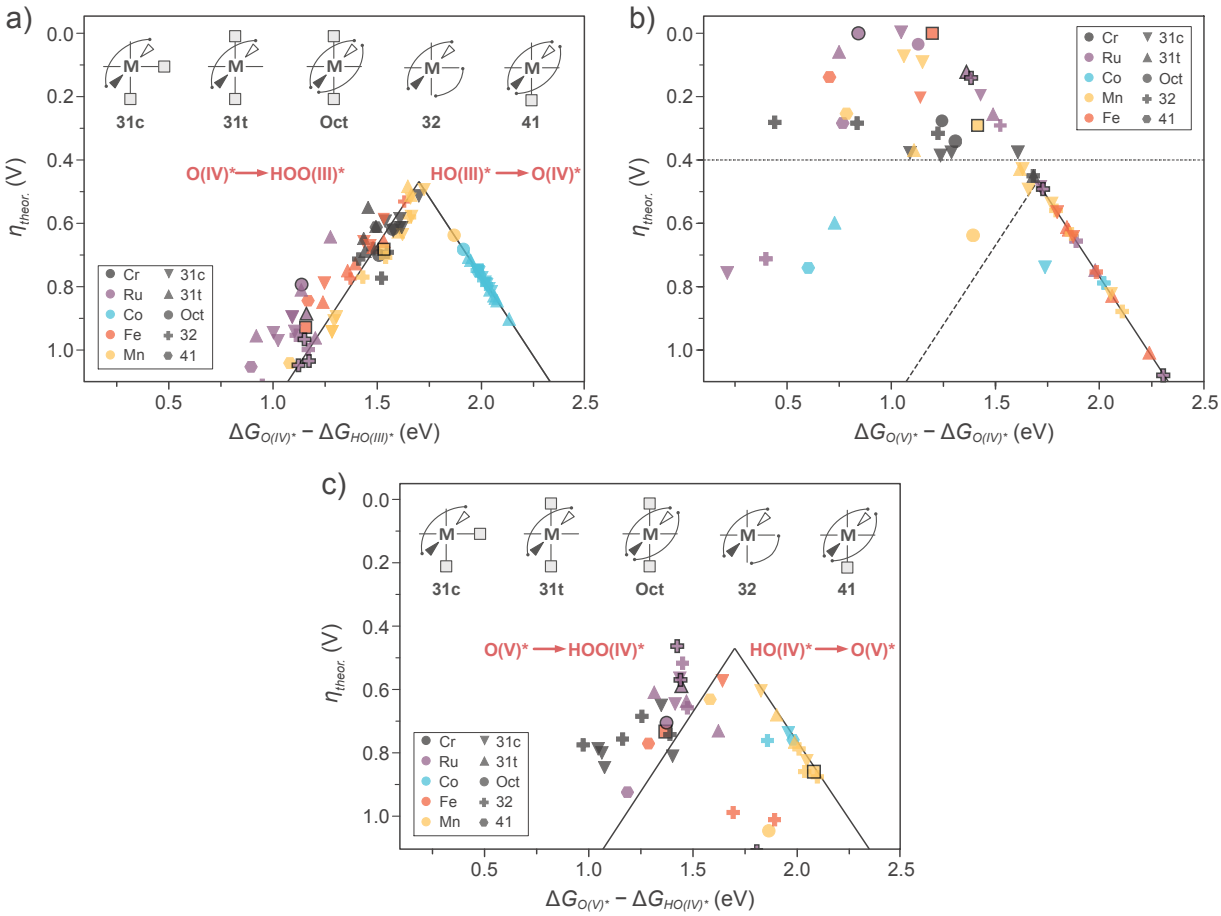

Figure 6.6. Two-dimensional volcano plots using (a) the conventional OER descriptor representing a PCET between oxidation states M(III) and M(IV), (b) the extra one-electron oxidation descriptor, in $\Delta G_{O(V)^*} - \Delta G_{O(IV)^*}$, with dashed line denoting the cutoff point of 400 mV overpotential and (c) the OER descriptor representing a PCET between oxidation states M(IV) and M(V). In a) and c) we present the presumed limiting step based on the scaling relations. The points with a black outline denote experimentally known OER catalysts, where we use a square to represent catalysts with pentadentate ligands, since this geometry is not represented in the set of catalysts generated as in Figure 6.1.

The best leads for future experiments which exhibit a PCET-only mechanism are chosen so that $\eta_{theor.} < 0.55$, (since this is close to the lower limit of 0.5 V imposed by the scaling relation depicted in the caption of Figure 6.2a and Figure C1); $\Delta G_{O(IV)^*} < \Delta G_{HO(IV)^*}$; and $\Delta G_{HOO(III)^*} < \Delta G_{O(V)^*}$, since we do not want to perform the extra oxidation in this case. This identifies a **32-Fe** catalyst composed of the **3a** tridentate and **2a** bidentate ligands, as seen in the labelled catalysts from Figure 6.1. The **32-Fe** catalyst is interesting as we expect

that the bipyrimidine ligand (labelled **2a** in Figure 6.1) could be used to immobilize the catalyst onto a solid support.[223] Also included in Figure 6.6 as black-outlined datapoints are catalysts which are experimentally known to catalyse the OER.

We next investigated whether the complexes with $\Delta G_{O(IV)^*} - \Delta G_{HO(III)^*} < 1.5$ eV can undergo the extra oxidation prior to O–O bond formation by inspecting the one-electron oxidation descriptor $\Delta G_{O(V)^*} - \Delta G_{O(IV)^*}$, leading to the volcano plot shown in Figure 6.6b. This step is reasoned to be crucial in finding low-overpotential earth-abundant catalysts for this reaction, and we note that it is required to justify the activity of the Fe and Mn mononuclear catalysts of the same geometry as the set of catalysts examined in this study. In particular, we correctly predict near-zero overpotential at pH = 0 for an amidate-ligated iron complex via the extra-oxidation mechanism, conferring with the experimental Pourbaix diagram which showed that this step occurred at *ca.* 1.25 V,[224] while correctly describing the Mn complex with an anionic N-donor ligand as low overpotential (< 0.4 V), and within the redox potential of the chemical oxidant used.[161] Importantly, this agreement with experiment is not possible without considering the extra oxidation, which affords greater confidence in our predictions of the OER activity. Also noteworthy is the fact that multiple earth-abundant catalysts lie within the region of low overpotential with $\eta < 0.4$ V, although we detail how to further filter catalysts before ultimately suggesting promising leads.

The volcano plot for this higher oxidation OER descriptor is shown in Figure 6.6c. Interestingly, we find that Ru and Cr catalysts predominate in the left leg of the volcano, implying a relative ease in the formation of the M(V) oxidation state, while Fe candidates lie on either side, and Mn and Co exclusively lying to the right leg of the volcano. In calculating the overpotential for Figure 6.6c, we calculated the Gibbs energy changes associated with going between the most stable intermediate for a given oxidation state, an

approach which we have applied to molecular OER catalysts with two active sites in Chapter 5. Note that in doing this, there are points which deviate significantly from the faces of the volcano, since the reaction intermediate we are considering does not necessarily determine the overpotential.

We note that the volcano peak at (1.7 eV, 0.47 V) in Figure 6.6a is larger than the overpotential wall reported in Chapter 4, which we attribute to the fact that individual metals have slightly different scaling relationships and intercepts, as seen in Figure 6.3, and this difference leads directly to a difference in overpotential walls. In Chapter 4, we reported a scaling relationship with an intercept of 3.26 eV, where the dataset of molecular catalysts contained 9 Ru catalysts out of a set of 17, which led to the scaling relation being overly representative of complexes with this metal.[204] As seen in Figure C2, fitting through the subset of Ru-containing data generated as a result of this screening led to an intercept of 3.25 eV, and a slope of essentially 1. The other catalysts with slopes close to 1 all have similar or higher values for their intercepts, leading to higher overpotential walls and therefore less room to identify a low overpotential catalyst.

With all the knowledge acquired above, and using the data from Figure 6.6, we can now propose catalysts for experimental realization based on predicted overpotentials less than 400 mV and consisting of earth-abundant metals. For this, we filter candidates by enforcing that $\Delta G_{O(V)^*} < \Delta G_{HOO(III)^*}$ so the extra oxidation is possible, and that the Gibbs energy change associated with the atom-proton transfer (APT), $\Delta G_{HOO(III)^*} - \Delta G_{O(V)^*}$, be less than 1eV, as this is the largest value exhibited by the set of transition metal complexes known experimentally to catalyse the OER (in particular, the red square in Figure 6.6b). Aside from the overpotential, we also need to determine what conditions the catalyst is predicted to evolve oxygen under. To properly determine which mechanism is expected to occur, the pK_a for the HO(IV)*/O(IV)* pair needs to be calculated. Doing this using only the Gibbs

energy differences of the transition metal species involved has proven challenging in protic environments such as water.[225] However, we use an OER-specific descriptor for the pK_a, created by reproducing Pourbaix diagrams and described.

We approximate the value of the pK_a for the M(IV)–O/OH pair using the following equation:

$$\mathrm{p}K_{a(O/OH)} \approx \frac{G_{O(IV)^*} - G_{HO(IV)^*} + \frac{1}{2}G_{H_2} + 4.28}{0.059e} \tag{6.8}$$

where each G value is in units of eV. We can understand this approach as a calculation of the intersection of the relevant redox species on a Pourbaix diagram for M(IV) to M(V) electron transfers using the 0.059 mV/pH unit. This is because the redox couple M(V)–O/M(IV)–OH is calculated as $\Delta G_{O(V)^*} - \Delta G_{HO(IV)^*}$ and varies with pH by 0.059 mV per pH unit. Then, the M(V)–O/M(IV)–O redox couple is calculated as $\Delta G_{O(V)^*} - \Delta G_{O(IV)^*}$ and does not vary with pH. Therefore, the intersection of the redox couples, which occurs at $\mathrm{pH} = \mathrm{p}K_{a(O/OH)}$ on a Pourbaix diagram, can be found by equating:

$$(\Delta G_{O(V)^*} - \Delta G_{HO(IV)^*}) - 0.059\mathrm{p}K_{a\left(\frac{O}{OH}\right)} = \Delta G_{O(V)^*} - \Delta G_{O(IV)^*} \tag{6.9}$$

If we solve for p$K_{a(O/OH)}$, and replace the binding energies with their individual components, we retrieve Eq. 6.9. This can be compared to the classic scheme to calculate pKa values:

$$\mathrm{p}K_{a(O/OH)} = -\log_{10} e^{\frac{-\left(G_{O(IV)^*} - G_{HO(IV)^*} + G_{(aq)}^{0H^+}\right)}{RT}} \tag{6.10}$$

where $G_{(aq)}^{0H^+}$ denotes the Gibbs energy of solvation of a proton in aqueous solution for which we take the value of –11.803 eV,[226] derived by Tissandier *et al.*

In doing this, we attempt to predict which mechanism can occur under certain conditions. Casting this value in terms of our OER mechanism; when Eqs. 6.8 and 6.10 are less than 0, the extra oxidation mechanism is predicted to occur for this catalyst above pH = 0. In Table 6.1 we see the results of the predicted pK_a values for experimentally known OER catalysts. Where possible, these values are compared with the experimental pK_a taken from Pourbaix diagrams for the given complex.

Table 6.1. Predicted p$K_{a(O/OH)}$ values for experimentally known catalysts with experimental values taken from Pourbaix diagrams provided in the references.

Catalyst	**p$K_{a,Eq\,(6.8)}$**	**p$K_{a,Eq\,(6.10)}$**	**p$K_{a,exp}$**	**Ref.**
[a][Ru(II)(bda)(isoq)$_2$]	9.1	7.7	5.5	25
[b][Ru(II)(bpc)(bpy)(H$_2$O)]$^+$	–4.9	–6.2	< 0	159
[c][Ru(II)(tpy)(bpm)(H$_2$O)]$^{2+}$	–8.6	–9.8	< 0	157
[d][Fe(III)(dpaq)(H$_2$O)]$^{2+}$	3.1	1.8	< 1	224

[a] (H$_2$bda = 2,2′-bipyridine6,6′ -dicarboxylic acid; isoq = isoquinoline)

[b] (bpc = 2,2′-bipyridine-6-carboxylate, bpy = 2,2′-bipyridine)

[c] (tpy = 2,2′:6′,2″-terpyridine; bpm = 2,2′-bipyrimidine)

[d] (dpaq = 2-[bis(pyridine-2-ylmethyl)]amino-N-quinolin-8-yl-acetamido)

While we acknowledge that Eq. 6.8 can lead to errors on the order of up to 3.6 pK_a units, one can determine whether a given mechanism should occur with reasonable certainty. We therefore use this to determine catalysts to suggest for experimental realization via the extra oxidation mechanism while also considering pH-dependence. With this, in concert with the data shown in Figure 6.6, we propose catalysts for experimental realization on the basis that predicted overpotentials which are less than 0.4 V and consist of earth-abundant metals. Correctly identifying catalysts undergoing the extra oxidation mechanism this mechanism is only possible if the OER descriptors are sampled at the correct oxidation states, leading to the ability to assess the resting state of the catalyst prior to the formation

of the high-valent M(V)–O species. Filtering based on the pK_a, such that the extra oxidation occurs, leads to 3 promising Cr-based catalysts, highlighted within the red rectangle in Figure 6.7.

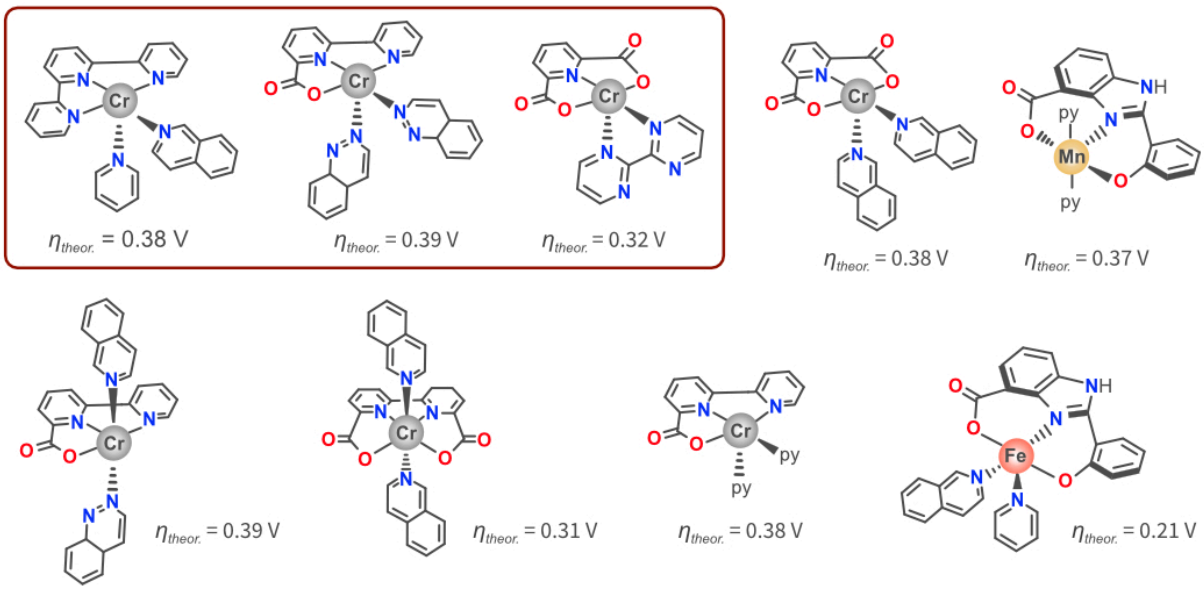

Figure 6.7. Catalysts found from the computational screening with overpotentials less than 400 mV, which have $\Delta G_{O(V)^*} < \Delta G_{HOO(III)^*}$ and $\Delta G_{HOO(III)^*} - \Delta G_{O(V)^*} < 1$ eV. The Cr catalysts highlighted in the red box are most promising having been further filtered on the basis that these catalysts can perform the extra oxidation at low pH. The theoretical overpotential for each catalyst at pH = 0 is provided alongside each structure. The monodentate pyridine ligand is represented as py for simplicity.

6.6 Metal-specific scaling relations

Taking the data presented in Figures 6.6a-c, we establish metal-specific scaling relations between $\Delta G_{HO(III,IV)^*}$ and $\Delta G_{O(IV,V)^*}$, shown in Figure 6.8. Notably, Co and Cr exhibit different slopes to the set of Mn, Fe and Ru catalysts, while two scaling relations are shown for Cr as the linear fit for oxidation-state specific scaling relations differ considerably for Cr, which is not the case for the other metals. Another interesting facet of these linear fits is the difference in the intercepts of the Mn, Fe and Ru set of metals, wherein the oxo-formation energy of Ru at a given binding energy, for either oxidation state, is *ca.* 0.2 eV

lower than for Fe and Mn for either oxidation state, thus indicating that forming high-valent intermediates is comparatively easier for Ru in complexes with the same $\Delta G_{HO(III,IV)^*}$.

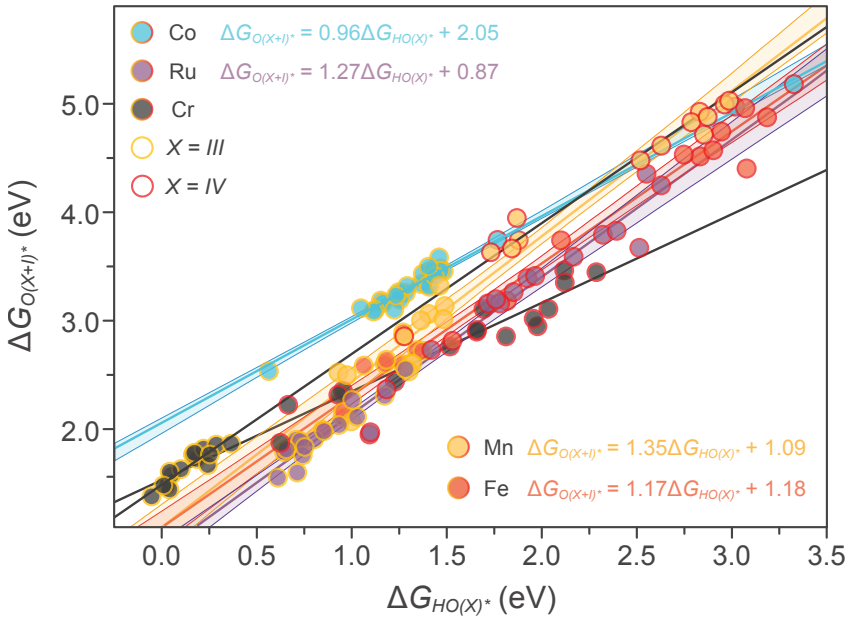

Figure 6.8. Metal-specific, cross-oxidation state scaling relations with lines of best fit for each set of metal-specific relations. Outlines of points denote the oxidation state of the HO*, O* pair. Two scaling relations are shown for Cr as the oxidation-state specific scaling relations differ considerably, which is not the case for the other metals.

The sensitivity of the slope to separating by metal in the scaling relations requires further discussion. On the basis of the d-band model,[227] which is the bedrock of scaling relations, these slopes should equal 2. However, there are often deviations from this behaviour in studies of both heterogeneous and homogeneous catalysts.[71,228] The justification for predicting a slope of 2 was predicated upon assumptions derived from effective medium theory that less electron density is required to stabilize metal active sites upon the addition of a hydrogen atom to an O adsorbate.[229] Yet, we note that this would not be the case in radical metal-oxyl (M–O•) fragments since the electron which forms the bond with H would not have been associated to the electron density of the complex, but only with the adsorbate. In fact, we observe this for Co, wherein the spin density on the metal centre remains the same in going from HO to O despite the d-electron count varying from d^4 to

d^6. This is enabled by the oxyl moiety (along with the organic ligand at Co(V)–O* and Co(IV)–OH) hosting spin density to allow for the reduction of cobalt to a LS-Co(III) with a d^6 electronic configuration. For this reason, the bonds between the Co–O(IV, V)* and Co(III, IV)–HO* species are of similar order, leading to a slope of *ca.* 1 in the scaling plot depicted in Figure 6.8. A similar effect is observed in Mn(IV)–O, Fe(IV, V)–O, Ru(IV, V)–O, with the metal only slightly oxidized in going from HO* to O* complexes. From these observations, we can approximate the expected slope for these metals as:

$$m_{pred.(\uparrow\uparrow)} = 2 - \frac{\Delta(spin\ on\ O)_{HO^*\rightarrow O^*}}{\Delta(spin\ on\ M-O)_{HO^*\rightarrow O^*}} \tag{6.11}$$

where the numerator denotes the average spin density change (for a given metal) occurring on the oxygen in the adsorbate in going from the HO* to O* intermediate, and the denominator denotes the average total spin density change in both the metal and the bound oxygen. However, we note that this equation falters in the case of Mn and Cr as the metal-oxygen spin pairing is antiferromagnetic in nature for Cr(V)–O and a mix of both ferromagnetic and antiferromagnetic for Mn(V)–O species. Indeed, spin-based non-linear d-band model refinements have been proposed for ammonia adsorption on heterogeneous catalysts.[230]

Creating lines of best fit through the antiferromagnetic complexes in Appendix C, we observe a slope less than 1. In these cases, the slope can be predicted by using Eq. 6.12.

$$m_{pred.(\uparrow\downarrow)} = 1 - \frac{\Delta(spin\ on\ O)_{HO^*\rightarrow O^*}}{\Delta(spin\ on\ M-O)_{HO^*\rightarrow O^*}} \tag{6.12}$$

The results of using Eq. 6.11 to predict the slopes of lines of best in Figure 6.8 are also outlined in Table 6.2, wherein we see an impressive agreement in predicting the slopes for Mn(V)–O and Cr(V)–O. We can now see that the slope of the combined Mn(IV, V)–O scaling relation is the combination of the ferromagnetically and antiferromagnetically coupled species, which leads to different slopes when separately fitted. We note that the

cluster of Cr(IV)–O points (black circles with yellow outlines in Figure 6.10) are the most closely-packed subset of data, which may obscure the true scaling relation due to the sensitivity of the lines of best fit to new points that lie outside the bounds of the considered points. Thus, altering adsorbates does not affect all metal active sites in a uniform way, an implicit assumption of cross-metal scaling relations. These results highlight the value of studying the effect of fitting subset-specific scaling relations and make a compelling case for revisiting scaling relations involving O* and HO* binding energies and using magnetism to guide deviations away from these relations towards optimum activity.

Table 6.2. Predicted slopes using the spin-based descriptors from Eqs. 6.11 and 6.12. The slope *m* was found by fitting the line of best fit to the relevant subset.

Catalyst Set	$\boldsymbol{m}$	$\boldsymbol{m_{pred.(\uparrow\uparrow)}}$	$\boldsymbol{m_{pred.(\uparrow\downarrow)}}$
Co(IV, V)	0.96	1.06	-
Ru(IV, V)	1.27	1.25	-
Fe(IV, V)	1.18	1.24	-
Mn(IV, V)[a]	1.66	1.43	-
Mn(V)[b]	0.92	-	0.76
Cr(IV)	1.33	1.96	0.96
Cr(V)	0.88	-	0.85

[a] Slope fitted by including only Mn(V) species which are ferromagnetically spin-coupled, of which there were four, shown in Appendix C.

[b] Mn(V)–O species with antiferromagnetic spin coupling, seen in Appendix C.

6.7 Convergence analyses

One may note that there are not actually 444 datapoints in every plot of the scaling relations, this is since not every calculation for every intermediate converged. The trade-off we made

was to only focus on those catalysts for which there were only a few intermediates to be completed to allow us to get all the binding energies that were required. In doing so, some catalysts are not plotted, simply because some intermediates did not converge, or had an associated imaginary frequency. In Figure 6.11, we plot the metal and intermediate for which the highest proportion of the calculations were not successful, for reasons which include convergence issues and imaginary frequencies. From this we note that the vacancy calculations tend to be problematic, as well as Fe and Mn calculations for other intermediates.

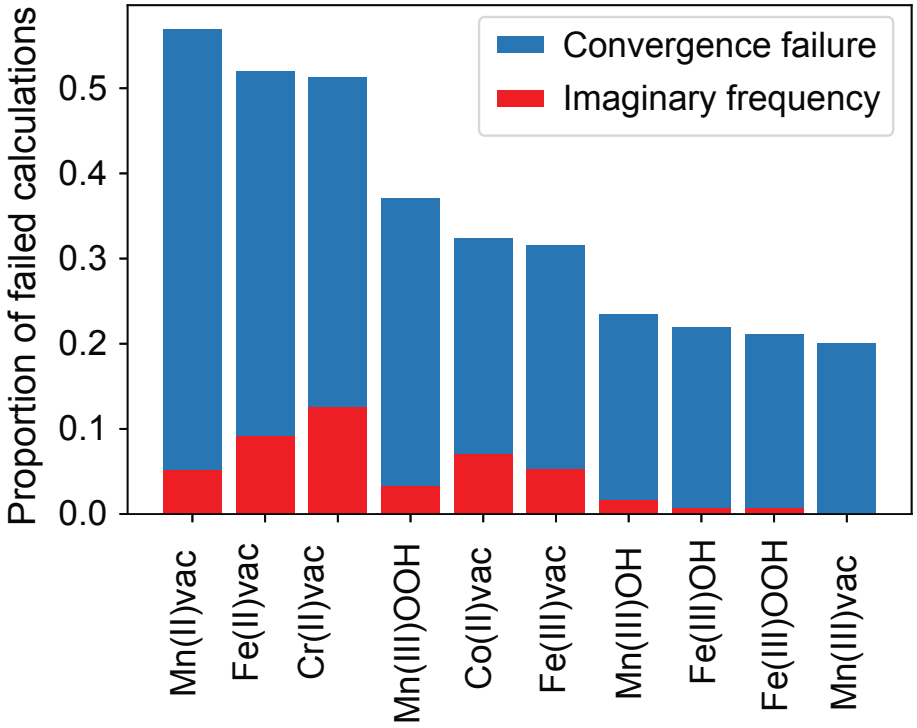

Figure 6.11. Most frequently failed combinations of intermediate, metal combinations, the remaining fraction in each case represents the proportion of successful calculations. We divide the failures into those that failed due to the geometry not resting within a stationary point, i.e., there is an imaginary frequency present in the frequency analysis of the PES, we colour those cases red and label them 'Imaginary frequency' and the calculations which failed for other reasons we label as 'convergence failure'.

Future studies could neglect the vacancy intermediate, since 5-coordinated molecules are rare in comparison to octahedral ones; the use of this vacancy intermediate is a result of

matching the typical modelling practice followed in computational studies on heterogeneous catalysts, where the vacancy intermediate is often a coordinatively unsaturated metal site. Since the formation of HO* does not typically limit OER, the choice of reference for the vacancy intermediate may not matter, and so we may suggest using a coordinating water so that the reference coordination is octahedral and thus may converge more reliably. We use this information in the following chapter by only calculating OH and O intermediates to arrive at a value for $\Delta G_{O(IV)^*} - \Delta G_{OH(III)^*}$ without considering the vacancy intermediate, since we are only interested in predicting the energy change for a single step in the following chapter.

6.8 Conclusions

In this chapter, we have tested our design principles from Chapter 4 to highlight potentially interesting candidate catalysts for the OER. To do this, we automated the generation of complexes from distinct combinations of ligand orientations around metal centres consisting of Cr, Mn, Fe, Co, Ni and Ru. In doing so, we confirmed a scaling relationship across methods, showing an increasing intercept in this linear relationship for increasing HF exchange, and showed that this increase in exchange also led to a favourable deviation in the scaling for Ni-based catalysts due to the alignment of spin densities on OOH fragments. We then set out to identify catalysts which have low overpotential and follow the extra oxidation mechanism laid out in Chapter 4. Further filtering these catalysts, so that only those which are predicted to be able to follow this mechanism in acid, led to the identification of three Cr-based complexes with promising activity. Finally, using this data, we showed the fundamental thermodynamic constraints on the binding energies for each of the metals by demonstrating each metal element had unique ΔG_{O^*} vs. ΔG_{HO^*} scaling relations, justifying the ascendency of Ru-based catalysts on the grounds that the energy

required to form higher valent intermediates is lower across oxidation states for this element.

In the following chapters, we shift focus towards heterogeneous catalyst stability, though the impetus behind this is driven by our understanding of the importance of oxidation states outlined by the data in this chapter.

Chapter 7 Oxidation State Analysis for Binary Oxide Stability Prediction

7.1 Introduction

The construction of phase diagrams is a time-consuming process experimentally, and while DFT has allowed for the calculation of phase diagrams from first principles,[146,231] populating these for the entire periodic table is too computationally demanding. An approach which saw widespread application in metallurgy was to simply calculate the formation energy of a ternary compound ABC from equal weights of AB, BC and AC formation energies.[232] More recent work extended this approach by correcting for the fact that taking weighted averages tends to underestimate formation energies systematically, leading to a MAE of 0.12 eV/atom across binary compositions of metals and demonstrating how simple heuristics can lead to impressive results.[233] Elucidating an approach to formation energy prediction with appropriately high fidelity holds great potential in materials discovery, since this quantity determines the ΔE_{hull}, described in Section 2.7, and thereby the stability of a given material with respect to phase segregation. Widely available databases of calculated crystal structure properties have naturally led to numerous predictive models of these properties.[234–237] A most impressive machine learning model applied to general stoichiometries, known as Roost[235] (Representation Learning from Stoichiometry), uses neural networks to form dense graph networks which can be used to learn the appropriate representations of general inorganic materials. This method can achieve 0.03 eV/atom accuracy when training over the lowest energy polymorphs in the OQMD[66] dataset. Another method is the crystal graph convolutional neural network approach from Xie and Grossman,[238] which is within the inherent error of GGA+U

formation energies for oxides.[239] Such methods could be ideal to use in addition to the approach described in this chapter, since the representations would not need to 'learn' about oxidation states. However, these methods tend to require on the order of tens of thousands of example calculations (*e.g.* Roost required over 200,000 training datapoints to achieve the quoted accuracy). Thus, these methods are highly data-intensive, very biased towards the pre-existing datapoints in computational materials databases and effectively uninterpretable in that there is no way to understand a specific prediction with respect to chemical or physical concept.

In this chapter, we begin by mining computational materials databases to analyse formation energies of unary and binary oxides, leading to an analysis of oxidation state changes for earth-abundant elements (*i.e.* Cr, Mn, Fe and Co) which would be ideal for use in commercial electrolysers. We restrict our analyses to oxides since these are the most technologically relevant for the OER,[240] while the impetus to study oxidation states specifically is a result of the analysis in Chapter 6 which demonstrated their influence on binding energies for this process. These results then lead to the development of a scheme to predict formation energies in binary oxides with a physics-based charge balancing scheme which can predict formation energies with errors of 0.09 eV/atom for $A_{1-z}B_zO_2$ stoichiometries (where z varies from 0–1) for elements across the periodic table. This scheme allows for the prediction of oxidation states within an oxide, the ideal concentration across a constrained convex hull diagram, and the oxide formation energy. Taking each of these capabilities in concert highlights the interpretability of the scheme while its generality is showcased in its application to elements across the periodic table.

7.2 Computational details

We begin by querying the Materials Project API using the python package `pymatgen` to gather data on binary and unary oxides. Our aim is to analyse the variation in the formation

energy of binary oxides with general formula $A_{1-z}B_zO_2$ by calculating their relative stability, $\delta_{A_{1-z}B_zO_2}$, with respect to their constituent unary oxides, AO_2 and BO_2. For this, we use the difference in formation energies between the observed Materials Project formation energy of a binary oxide, $\Delta E_{f(A_{1-z}B_zO_2)}$, and the weighted average of the unary formation energies

$$\delta_{A_{1-z}B_zO_2} = \Delta E_{f(A_{1-z}B_zO_2)} - (1-z)\Delta E_{f(AO_2)} - z\Delta E_{f(BO_2)} \quad (7.1)$$

We note that $\delta_{A_{1-z}B_zO_2}$ is calculated if each of the three oxides represented in the above equation have similar structures. To compare these, we have used a structure similarity metric defined by `pymatgen` which finds the nearest neighbour for every atom to define a site and then collect statistics about the nature of the site within a vector of length 61, where each value in the vector represents the likelihood that the site corresponds to a certain structural motif.[241] We include a detailed outline of one value contained in this vector in the subsequent paragraph, and this is one example of the values known as order parameters (OPs) to define equations which use rotationally invariant spherical coordinates to mathematically define likeness to a certain structure type. For a tetrahedral coordination, for instance, it is calculated via the OP shown in Eq. 7.2

$$q_{tet.} = \frac{1}{N_{ngh}(N_{ngh}-1)(N_{ngh}-2)} \sum_{j\neq k}^{N_{ngh}} \{\exp(\gamma_j) \sum_{m\neq j,k}^{N_{ngh}} cos^2(1.5\varphi)\exp(\gamma_m)\} \quad (7.2)$$

$$\gamma_i = \frac{-(\theta_i - 109.47)^2}{2\Delta\theta^2} \quad (7.3)$$

with N_{ngh} representing the number of neighbours bound to a central atom i, θ_j is the polar angle which j and k form with respect to the atom with which they are both bound, i, φ is the azimuthal angle between the $i-m$ bond and the plane formed by i, j, and k, and $\Delta\theta$ is set to the empirically-determined value of 12.[242] The Gaussian functions in the above

equation represents the notion that these polar angles should be close to the expected value of 109.47°.

Each of the 61 OPs vary from 0 to 1, with 1 representing exact match to a given structural motif and 0 meaning no resemblance. The other OPs represent the likelihood a motif is octahedral, body-centred cubic, face-centred cubic and hexagonal close packed. The product of these likelihoods is used to make up the 61-length vector for a given site. Over the entire structure, this vector is calculated for every site, leaving us with a matrix with the number of rows matching the number of atoms and the number of columns equal to 61. Then the minimum, maximum, mean, and standard deviation for each of the 61 values is taken as a structural fingerprint for a given structure, v_i^{struct}. To compare two structures, we calculate the distance between these vectors, as shown in Eq. 7.4

$$d = \| v_i^{struct} - v_j^{struct} \| \tag{7.4}$$

This value d is then used as a threshold where two structures are deemed similar if d is lower than this value.

The python scripts to carry out the analyses presented in this chapter are available on the open-source repository GitHub at: github.com/michaelcraiger/oxide_formation_energy.

7.3 Materials project data analysis

7.3.1 *Structure similarity*

We wish to understand how changes in oxidation states of individual elements in binary oxides influence their stability. There are of course other sources of stabilization separate to charge balancing via oxidation state changes which we do not wish to consider as we can loosely capture them under the umbrella of morphology-related stabilization. Thus, there is a need to minimize the influence of structure on $\delta_{A_{1-z}B_zO_2}$. To do this we vary d, defined above, from 0.1 to 1.5 in intervals of 0.1 and plot $\delta_{A_{1-z}B_zO_2}$ as a function of this parameter. In Figure 7.1, we note that for $d = 0.1$ we have $\delta_{A_{1-z}B_zO_2} \approx 0$, which means

that the binary formation energy could be calculated directly from the unary oxide formation energies. This is useful in itself since it indicates that taking the weighted average of the formation energies of oxides is predictive of binary oxide formation energy in the restrictive case where each of the three oxides share near-identical morphologies. As we increase from $d = 0.1$, we see a mostly monotonic increase in the mean value of $\delta_{A_{1-z}B_zO_2}$, and from this analysis we took a threshold of $d = 0.5$ since this balances allowing the most comparisons while minimising the introduction of noise into $\delta_{A_{1-z}B_zO_2}$, which could be attributable to structural variations.

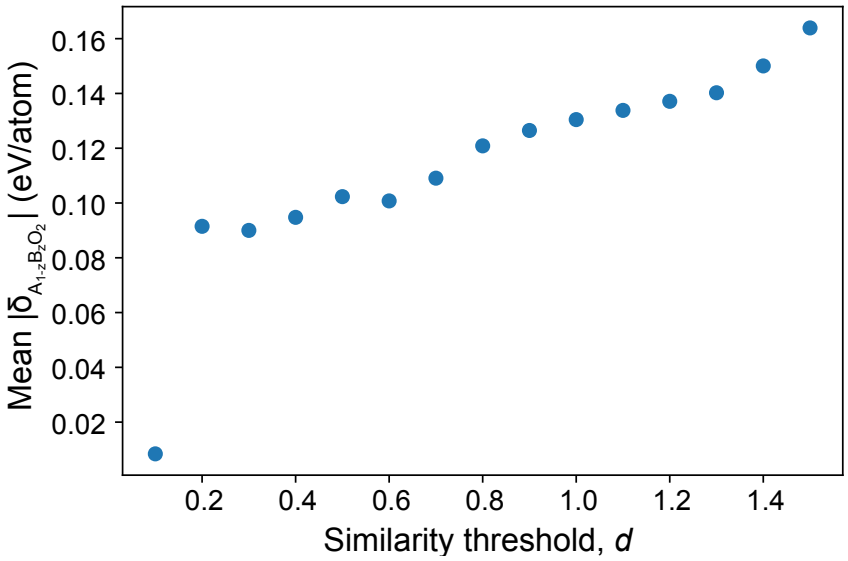

Figure 7.1. Calculated mean value of binary oxide stabilisation in $A_{1-z}B_zO_2$, $\delta_{A_{1-z}B_zO_2}$, as defined in Eq. 7.1 against the similarity threshold, *d*, defined in Eq. 7.4. We allow for measurements of this value in cases where the structures to be compared, $A_{1-z}B_zO_2$, AO_2 and BO_2 are deemed similar since, when each oxide is compared, their structures lie within a given similarity threshold *d*, which is the Euclidean norm between two structure fingerprint vectors.

7.4 Oxidation state analysis

To track changes in oxidation state in unary and binary oxides, we calculate the weighted change in bond length for a given material. Namely, given $A_{1-z}B_zO_2$ where $z = [0-1]$, we calculate the mean bond distances between $A-O$ and $B-O$ ($\mu_{A-O,A_{1-z}B_zO_2}$, $\mu_{B-O,A_{1-z}B_zO_2}$,

respectively) and compare each of these averages to the mean bond distance for A and B in AO_2 and BO_2 ($\mu_{A\text{-}O,AO_2}$ and $\mu_{B\text{-}O,BO_2}$), where we count bonds when the interatomic distances are within a cut-off radius of 2.5 Å. Then we calculate the weighted bond length change over the oxide for each element according to

$$\left(\mu_{A\text{-}O,AO_2} - \mu_{A\text{-}O,A_{1-z}B_zO_2}\right)(1-z) \tag{7.5}$$

$$\left(\mu_{B\text{-}O,BO_2} - \mu_{B\text{-}O,A_{1-z}B_zO_2}\right)(z) \tag{7.6}$$

and compare bond length shifts whenever each of the three oxides, AO_2, BO_2, $A_{1-z}B_zO_2$ lie within the threshold for the similarity metric of $d = 0.5$ for each of the three pairings of materials so that $AO_2 \sim BO_2 \sim A_{1-z}B_zO_2$. A negative value in the Eqs 7.5 and 7.6 indicates that the bond length in the binary oxide is lengthened with respect to the unary oxide, meaning that the element is more reduced in the binary material, whereas positive values indicate that the element is more oxidized. We perform this calculation for the subset of Cr, Mn, Fe and Co-containing binary oxides in the Materials Project database, with the result of this analysis shown in Figure 7.2. Here note that for each of the metals, the largest stabilisation, *i.e.* lowest $\delta_{A_{1-z}B_zO_2}$, is seen when the metal is reduced, and that in each of these cases there is a seemingly complementary shift in the bond length shift of the other element. In the Materials Project, each of these first-row transition elements are unstable as AO_2 relative to their most stable phases, with Cr and Fe preferring corundum phases A_2O_3 with oxidation state 3+, Mn the spinel Mn_3O_4, and Co the rock salt CoO with oxidation state 2+. We nevertheless study these oxides to gain an understanding for how to construct a method which can forecast formation energies for oxides of any stoichiometry based on the stabilisations which are a result of changes in oxidation state.

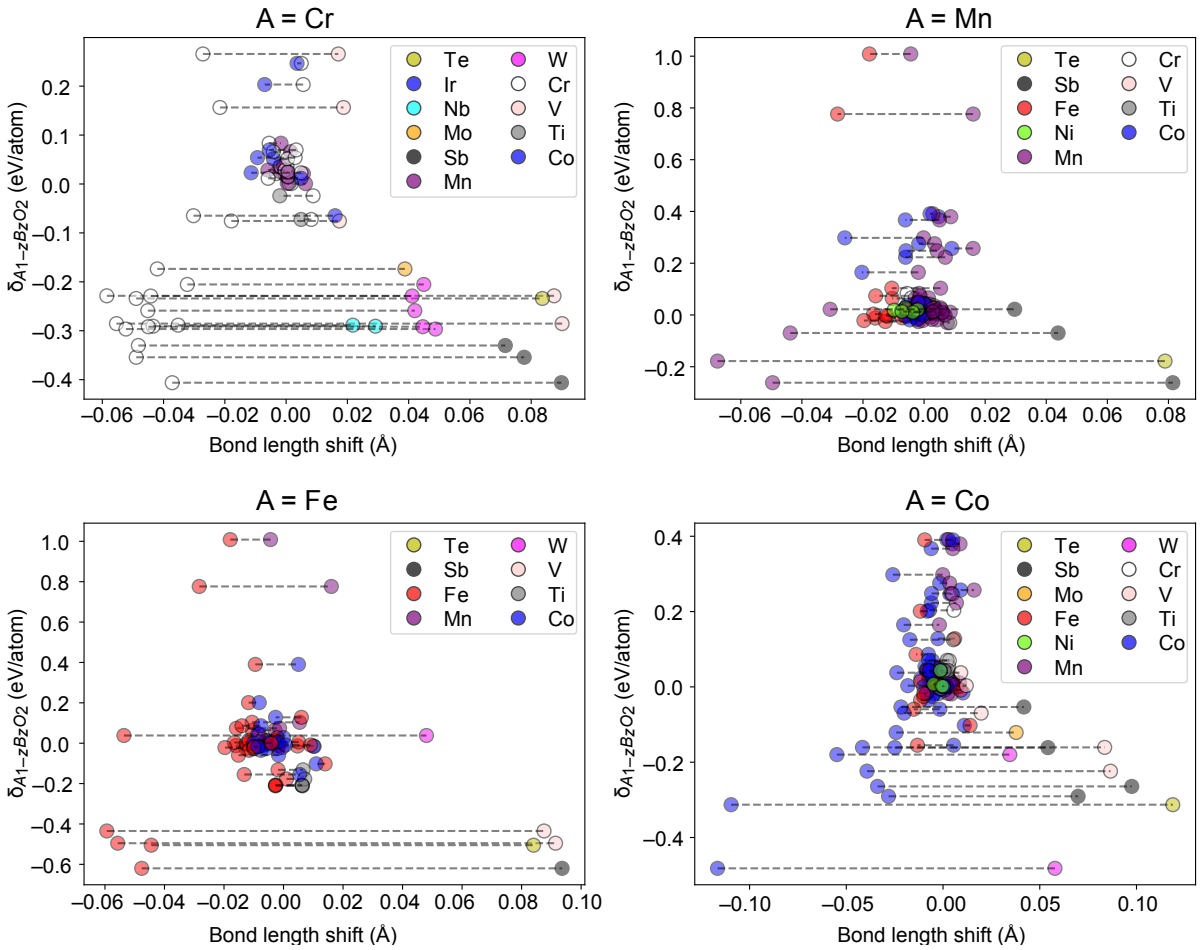

Figure 7.2. Weighted change in bond lengths for Cr, Mn, Fe and Co-containing binary oxides with respect to the MO_2 bond lengths, with negative values denoting that the given bond length is shorter in MO_2 than in the binary oxide. These shifts are plotted against the stabilization $\delta_{A_{1-z}B_zO_2}$ energy from Eq. 7.1 for that oxide, and the shift in bond length for both elements –calculated as in Eqs. 7.5 and 7.6 – within the binary oxide are plotted, where the dashed line is drawn to illustrate that the two elements *A* and *B* are contained in a certain binary oxide.

Having shown that oxidation state disproportionation could be a common source of stabilisation across oxides, we focused specifically on the effect of doping rutile CrO_2. The effect of calculating δ, where only MO_2 rutile morphologies are compared, is shown in Figure 7.3, where we note that disproportionation in oxides again appears to drive stability within this subset of oxides. Using this approach, we again observe that Cr reduction, represented by a lengthening of Cr–O bond lengths, appears to belie stability in chromium-

based binary oxides, and one can see a rough correlation between the Cr–O bond length shift and stabilisation.

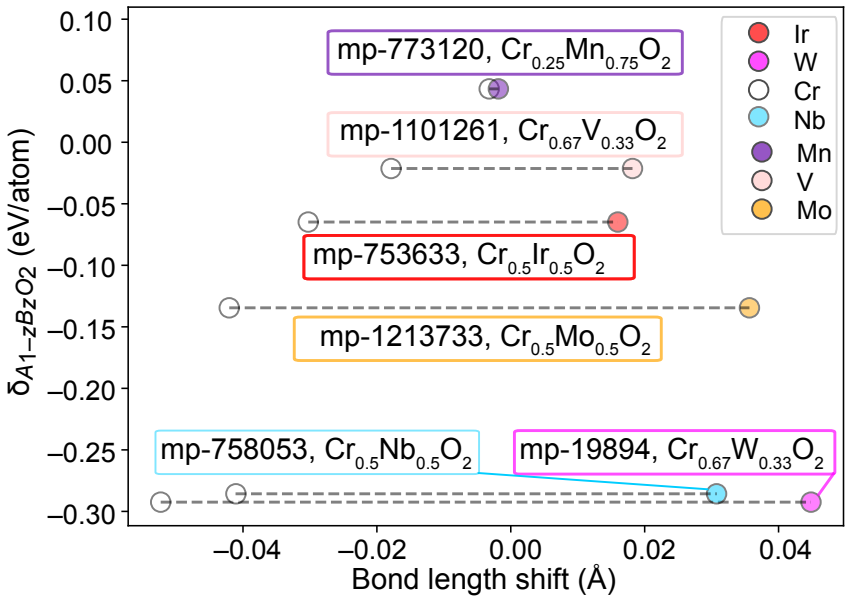

Figure 7.3. Stabilisation against bond length changes in binary oxides with respect to their pure unary rutile counterparts, with the y-axis representing the deviation from weighted formation energies described in Eqs. 7.4 and 7.5. Dashed lines connecting the elements which make up the binary oxide are drawn to demonstrate that the shifts are centred roughly around 0, to anchor the labels of Materials Project ids and associated stoichiometries are found along each line.

Next, we set out to determine quantitative measures for the propensity of each element towards a given oxidation state. To do this, we simply take the difference in Materials Project-calculated formation energies between CrO_2 and Cr_2O_3, and the difference between MO_2 and that MO_x which would exhibit an appropriate oxidation state to make the average oxidation state of the material 4+; given Cr is assumed to be 3+, *i.e.* for mp-19894 ($Cr_{0.67}W_{0.33}O_2$) we require W^{6+} oxidation state (since $4 = 3(\frac{2}{3}) + 6(\frac{1}{3})$) so we take the difference in formation energy between WO_2 and WO_3. To represent points which do not exist in the Materials Project, we calculate the formation energy at the convex hull of the M–O phase diagram, *i.e.* the projected formation energy of hypothetical Ir_2O_5, Mo_2O_5,

V_4O_9, Mn_6O_{13} materials, which are chosen so that their assumed oxidation state, $\frac{2b}{a}$ for oxide A_aO_b, and the assumed oxidation state of Cr in 3+ make the overall oxidation state of the binary oxide 4+. The projected formation energy and required oxidation states for each of the six cases in Figure 7.3 are shown in Table 7.1.

Table 7.1. Formation energies (in eV/atom) for reference MO_2 compared to that MO_x presumed to represent the oxidation state of the material if the binary oxide in Figure 7.3 contains Cr^{3+}.

$Cr_{1-z}M_zO_2$	$\Delta E_{f(MO_2)}$	$Cr^{3+}, M^{ox.+}$	$\Delta E_{f(MO_x)}$	$\Delta E_{f(MO_x)} - \Delta E_{f(MO_2)}$	$\delta_{Cr_{1-z}M_zO_2}$
–	–2.05	–	–2.37	–0.32	–
$Cr_{0.67}W_{0.33}O_2$	–1.94	Cr^{3+}, W^{6+}	–2.19	–0.25	–0.29
$Cr_{0.5}Nb_{0.5}O_2$	–2.90	Cr^{3+}, Nb^{5+}	–3.03	–0.13	–0.29
$Cr_{0.5}Mo_{0.5}O_2$	–2.02	Cr^{3+}, Mo^{5+}	–1.97†	0.05	–0.13
$Cr_{0.5}Ir_{0.5}O_2$	–1.26	Cr^{3+}, Ir^{5+}	–1.12†	0.14	–0.06
$Cr_{0.33}V_{0.67}O_2$	–2.29	$Cr^{3+}, V^{4.5+}$	–2.39†	0.10	–0.02
$Cr_{0.25}Mn_{0.75}O_2$	–1.79	$Cr^{3+}, Mn^{4.3}$	–1.94†	0.07	–0.04

† The formation energy for this value is calculated by projecting between points on the convex hull as opposed to using values in the Materials Project.

Using the data from Table 7.1, we can define proxies for the gain in stability of elements in being oxidized or reduced by taking the difference between the preferred MO_x and MO_2. To account for cases such as Mn-doping, where no bond length changes, and therefore no oxidation state appears altered, we need a way to represent the relative amount that Cr is reduced. To do this we set a hypothetical percentage of Cr reduction, χ_{Cr}, which we set to

be 1 in the Cr-W case since this structure has the longest Cr–O bond in Figure 7.3. Then, the fraction of Cr reduction in each other case is set to the fraction of the bond lengthening that is seen, and the oxidation fraction for the other element is the same. We then multiply the resulting product by the fractional metal concentration of that element in the oxide relative, *i.e.* z in $Cr_{1-z}M_zO_2$, leaving us with a predicted stabilisation, which we denote $\sigma_{Cr_{1-z}M_zO_2}$, for a given $Cr_{1-z}M_zO_2$ of

$$\sigma_{Cr_{1-z}M_zO_2} = (1-z)\left(\Delta H_{f(Cr_2O_3)} - \Delta H_{f(CrO_2)}\right)\chi_{Cr} + (z)\left(\Delta H_{f(MO_x)} - \Delta H_{f(MO_2)}\right)\chi_M \quad (7.7)$$

We plot this heuristic energy defined in Eq. 7.7 against $\delta_{A_{1-z}B_zO_2}$, revealing a slight correlation in Figure 7.4. The reduction and oxidation of similar pairs of elements appears to occur in Figure 7.2 across Cr, Mn, Fe and Co-based oxides; for instance, Sb, W and Te are alloyed elements which show lower values of $\delta_{(Cr,Mn,Fe,Co)_{1-z}M_zO_2}$. This is promising when taken in tandem with the data shown in Figure 7.4 which indicates that the formation energies of unary oxides could be used to predict binary oxide formation energies. This simple scheme appears as though it could be applicable to a wide class of materials which has inspired the development of a methodology which extends this scheme. Effectively we need to construct measures of the propensity of elements to be certain oxidation states based on their unary formation energies, and test whether this can be used to predict binary oxide stability.

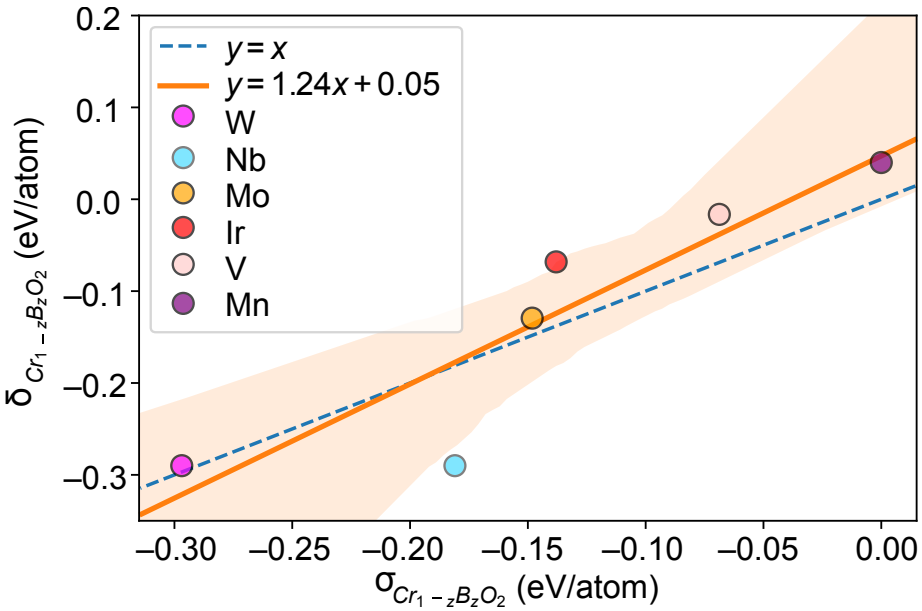

Figure 7.4. Result of plotting the $\sigma_{Cr_{1-z}M_zO_2}$ value as shown in Eq. 7.7 against the observed $\delta_{Cr_{1-z}M_zO_2}$ (Eq. 7.1) values from MP. The line $y = x$ is drawn as a dashed to show the decent parity between the two variables as well as an equation of best fit through the datapoints ($R = 0.9$).

7.5 Formation energy prediction via oxidation state

The insights drawn from the previous section impelled a study across the periodic table, with the specific goal of highlighting potentially interesting acid stable catalysts or supports for the OER. Clearly, the method applied above is not predictive since it can only be applied *a posteriori* by measuring bond lengths in optimized structures. Instead, to more generally describe the propensity of a given element to be oxidized or reduced when mixed, we fit quadratic equations through formation energies of the most stable entries in computational materials databases across M:O ratios. For each element, M, we have quadratic equations, $f_{ox,MO_2}(x)$ and $f_{red,MO_2}(x)$, which take the general form

$$f_{ox/red,MO_2}(x) = a_1x^2 + a_2x \tag{7.8}$$

where a_1 and a_2 are determined by ordinary least square fitting over the formation energies at the standard state, with formation energies calculated by MP outlined in Section 2.8. We provide further details on fitting these equations in the subsequent section, and in what

follows focus on the mathematical details of our model. Then, x is used to represent the way unary oxide formation energies change in response to oxidation and reduction and it is applied as a dimension along a phase diagram. We set the origin at the stoichiometry we wish to represent, for example MO_2, and we fit two quadratic equations from that origin, where given an oxide A_aO_c, $x = \frac{2c}{a}$ or for $A_aB_bO_c$, $x = \frac{2c}{a+b}$.

In Figure 7.5a we fit quadratic equations over the standard formation energies for the oxidation of Ir, $f_{ox,IrO_2}(x) = 0.11x$, and the reduction of Cr, $f_{red,CrO_2}(x) = 0.43x^2 - 0.82x$, where we use CrO_2 and IrO_2 as our (0, 0) point, and fit through the points which form the convex hull in the direction of oxidation or reduction. Given Cr_2O_3 is the chromium-based oxide with the lowest formation energy at standard state, this curve is a mathematical representation of the fact that Cr's preferred oxidation state is 3+. The $f_{ox,IrO_2}(x)$ is shaped linearly, with IrO_3 just piercing the hull formed by IrO_2 and O_2.

To maintain charge balance, we constrain the average oxidation state of the material $A_aB_bO_c$ to the oxidation state $\frac{2c}{a+b}$. We then enforce that the mixed compositions have the same fixed average oxidation state as the unmixed oxides, in this case 4+. If we use o and r to represent the oxidation and reduction of a material $A_{1-z}B_zO_y$, then to keep the oxidation state constant when mixing we need:

$$o(1-z) - r(z) = 0 \tag{7.9}$$

And use a change of variables in x to balance the equation, setting $o = x(z)$ and $r = x(1-z)$. This allows us to take appropriately weighted averages of the parabolic equations from Eq. 7.8 to represent the propensity to mix. For instance, a $Cr_{0.5}Ir_{0.5}O_2$ stoichiometry could observe Cr^{3+}, Ir^{5+} oxidation states, while $Sb_{0.67}Ni_{0.33}O_2$ could exhibit oxidation states Sb^{5+}, and Ni^{2+} under this scheme, such that the overall oxidation state remains 4. In real systems,

however, such ideal oxidation mixing eventually breaks down, and further compensation occurs via oxygen or metal vacancies, or interstitials.

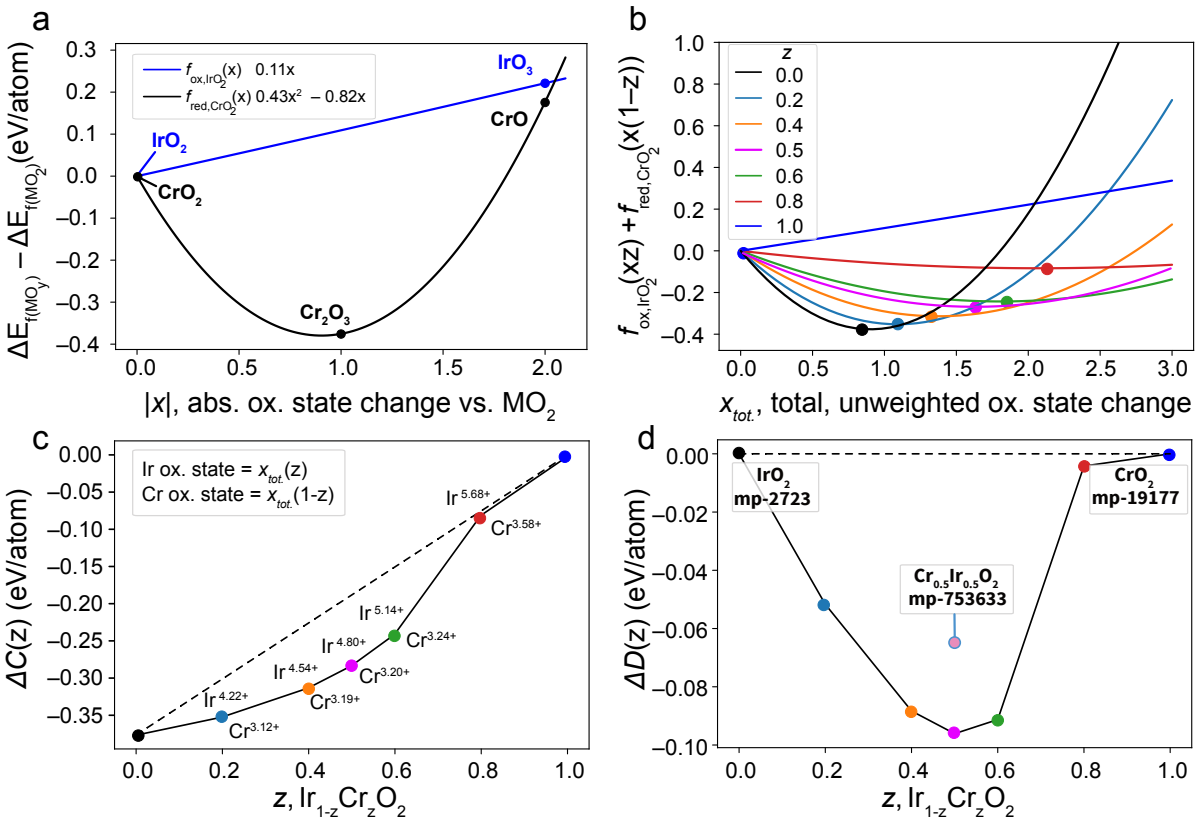

Figure 7.5. a) Fitted parabolic equations for Cr and Ir, with fitted datapoints indicated by the stoichiometry of the material, and with x-axis for an oxide A_aO_c, given by $x = \frac{2c}{a}$. b) Weighted averages of the equations in a), dependent on the concentrations of Cr and Ir, z, the minima of those curves are used to denote $\Delta C_{(Ir_{1-z}Cr_zO_2)}$ as in Eq. 7.10. The x-axis here represents $x_{tot.}$ the overall oxidation state change, without being weighted by concentration with the points representing the minimum of the curve. c) The minima of the curves plotted in b), plotted as a function of z, with the predicted oxidation states of each element shown, and derived by taking the product of $x_{tot.}$ and the relevant concentration. The dashed line is to guide the eye connecting the values for z = 0, 1. d) Convex hull phase diagram constructed using $\Delta D_{(A_{1-z}B_zO_2)}$ from Eq. 7.12 compared against a calculation in MP.

To mathematically define a combination energy, ΔC, we use the parabolic equations $f_{ox,AO_2}(x)$, $f_{red,AO_2}(x)$, $f_{ox,BO_2}(x)$, and $f_{red,BO_2}(x)$ for a hypothetical material $A_{1-z}B_zO_2$

and test both combinations of oxidizing and reducing either of the constituent elements, which leads to:

$$\Delta C = min_x(f_{ox,AO_2}(xz) + f_{red,BO_2}(x(1-z)), f_{red,AO_2}(xz) + f_{ox,BO_2}(x(1-z))) \quad (7.10)$$

In Figure 7.5b we show Eq. 7.10 for varying values of z for the specific case of Ir oxidizing and Cr reducing, where the minimum is shown as a point along the weighted average curves. Taking that minimum from the weighted parabolic equation, with respect to x, where possible, represents the stabilization driving force that can be induced by mixing these elements, and can be performed for an arbitrary concentration z, as shown in Figure 7.5c. Then, to represent a mixing formation energy with respect to segregation against CrO_2 and IrO_2, which represents a deviation in weighted formation energies of CrO_2 and IrO_2, we define $\Delta D_{(A_{1-z}B_zO_y)}$ with:

$$\Delta D_{(A_{1-z}B_zO_2)} = 0 \quad \text{for} \quad z = \{0,1\} \quad (7.11)$$

To enforce this, we calculate the formation energy of mixing using the endpoint calculations of Eq. 7.10, that is:

$$\Delta D_{(A_{1-z}B_zO_2)} = \Delta C_{(A_{1-z}B_zO_2)} - (1-z)\Delta C_{(A_1B_0O_2)} - z\Delta C_{(A_0B_1O_2)} \quad (7.12)$$

To ensure the condition in Eq. 7.11 is met, set $z = 0$ then we note the third term is zero and the first and second term cancel, set $z = 1$ and the second term is zero and the first and third terms cancel. This ΔD value can then be thought of as a deviation from the weighted average in formation energies of the respective endmembers, thereby allowing for a predicted formation energy:

$$\Delta E_{f(A_{1-z}B_zO_2)} = \Delta D_{(A_{1-z}B_zO_2)} + (1-z)\Delta E_{f(AO_2)} + z\Delta E_{f(BO_2)} \quad (7.13)$$

This general method can be used to predict formation energies given any relative concentration z, and we can compare our predicted $\Delta D_{(A_{1-z}B_zO_y)}$ values with those which have been observed by previous calculations in the MP by setting values of $\Delta E_{f((A,B)O_2)}$ by

choosing the most stable unary oxides in MP and comparing their weighted average to $\Delta E_{f(A_{1-z}B_zO_2)}$. We demonstrate the application of this method to predict $\Delta D_{(A_{1-z}B_zO_y)}$ for mixing Cr and Ir in the MO_2 stoichiometry, as seen in the convex hull phase diagram constrained to the $Ir_{1-z}Cr_zO_2$ phase space in Figure 7.5d, where we observe a deviation of 0.03 eV/atom between our prediction and the observed $Ir_{0.5}Cr_{0.5}O_2$ material in the MP (ID mp-753633). This scheme therefore holds promise as a rapid means of garnering a prediction for the minimum energy over a span of concentrations for a given stoichiometry as well as the oxidation states of the respective elements. In the case outlined in Figure 7.5, we can read off the predicted oxidation states of Cr and Ir by noting the value of x which minimizes the curves in Figure 7.5b and multiplying that value by the concentration of the other element. We see that for $z = 0.5$ the minimum is for $x \approx 1.5$, multiplying this change by z so that the change in oxidation state should be 0.75 relative to the MO_2 unary oxide. So, Cr and Ir should have oxidation numbers of 3.25 and 4.75 respectively.

This methodology can, in principle, be applied to any combination of elements provided formation energy data about the M:O stoichiometry attempting to be mixed, and preferably data for other stoichiometries to construct appropriate parabolic equations for use in the outlined scheme, is available. In the next section, we detail the protocol for fitting these parabolic equations.

7.6 Parabolic equation fitting

To gather data for the fitted parabolic equations we use the computational materials databases MP[65] and OQMD.[66] Our stipulations for the form of the parabolic equations are:

1. The resultant parabolic equation should pass as close as possible through the material with the lowest formation energy for a given element. This respects the preference of a given element to be in a certain oxidation state.

2. The curve should avoid linearity where possible and must avoid being concave up. This is enforced by setting the second order coefficient to zero if it is negative.

The way we decide which points to fit to a parabolic equation is element-specific, and to some degree arbitrary, since constraining the ordinary least squares regression analytically severely restricts the possible space of parabolic equations. If we were to assert that the slope of the parabolic equation is zero at the lowest energy material, then the form of the parabolic equation is forced to be symmetric about that point, regardless of the presence of other materials of different oxygen concentration. Instead, we prune points which are not at the apex of the convex hull until we satisfy condition 1.

To choose between OQMD- or MP-fitted quadratic equations, the parabolic equation which most closely satisfies condition 1 is taken. While the oxides may not correspond to the same materials in each database, the fitted equation should represent something inherent for that element. If this is not enough data, to satisfy condition 2, we use a linear equation:

$$f_{red,AO_2} = \frac{\Delta E_{f(AO_2)} x}{4}; \quad f_{ox,AO_2} = \frac{\Delta E_{f(AO_2)} x}{8-4} \tag{7.14}$$

The definition of f_{ox,AO_2} assumes the creation of a more oxidized hypothetical AO_4 material with oxidation state 8+, which is poorly defined so systems using these linear equations should be treated with relatively more suspicion. This choice is somewhat arbitrary, and effectively comes down to choosing at what oxidation state do we set the formation energy to 0, normally we use the energy of O_2 as the end member, but this would have an 'infinite' oxidation number as per our oxidation state scheme. Thus we choose 8+ since it is close to the highest observed oxidation number of 9+,[243] and since it means the denominator of the Eqs. 7.14 are the same, affording a symmetry to the equations formed. Future work could focus on tuning this value. A table of the coefficients for the parabolic equations which

satisfy the rules outlined in this subsection, and will be in use throughout both this and the following chapter, is shown in Table D1 in Appendix D.

We will attempt to predict ΔE_f using ΔD as in Eq. 7.13 for $A_{1-z}B_zO_2$ oxides where $z = [0-1]$ so we will need 2 parabolic equations per element, representing both oxidation and reduction from AO_2 oxides.

7.7 Model performance

7.7.1 *Formation energy prediction*

We now gather parabolic equations for any element which has a binary oxide with an M:O ratio of 2:1, without restricting ourselves to any part of the periodic table, and test the model for its ability to predict the formation energy deviations as in Figure 7.5d. This leads to the following elements being considered: Mo, W, Nb, Ni, V, Ir, Cr, Fe, Mn, Co, Sb, Sn, Bi, Ti, Ta, In, Pt, Re, Ge, Rh, Cu, Te, Li, Na, Mg, Y, Ca, Sc and Zn. All the coefficients for these equations are tabulated in Table D1, and the reference MP ids required to calculate ΔD in Eq. 7.13 are provided in Table D2. Our model was constructed with the notion of a constant average oxidation state across the composition of a binary oxide, so we use a filtering condition which requires: i) A and B are within 2.5 Å to 6 oxygen atoms, ii) oxygen atoms are taken to be O^{2-} anions which are within 2.5 Å to 3 metal atoms, and iii) no oxygen atom is within 1.5 Å of another oxygen atom. This way we attempt to constrain the overall oxidation state across the elements A and B is respected to be 4, where both are elements that exhibit a unique oxidation state for every site in the oxide. We also gather only those Materials Project datapoints with the lowest derived ΔD values across all A: B ratios so that only the ground state for that concentration is taken; this mitigates the noise which could be introduced by taking unrealistic structures with unrealistic formation energies.

A parity plot of these predictions against the observed MP is shown in Figure 7.6, where we can see a remarkable correlation between predicted and observed points despite the

simplicity of our model. MAE values of predicted and observed ΔD values of 0.09 and 0.16 eV/atom are shown for the case where we do and do not filter by coordination, respectively.

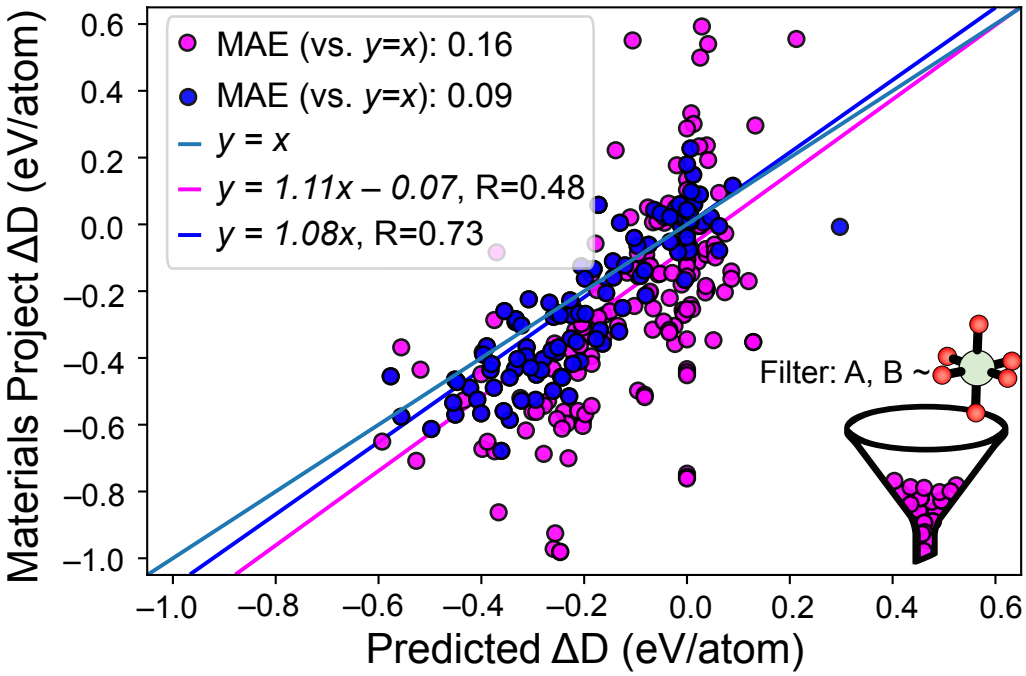

Figure 7.6. Parity plot showing the correlation between the ΔD derived from our formation energy prediction scheme (defined in Eq. 7.10) against the observed ΔD from Materials Project for different sets of filtered and unfiltered data contained. The blue and pink colours represent filtered and unfiltered structures of the $A_{1-z}B_zO_2$ stoichiometry for which we predict ΔD, with the MAE in units of eV/atom. The inset is shown to highlight that blue points contain only those oxides which are composed solely of A and B elements coordinated by oxygen atoms in an octahedral geometry, which leads to a filtering out of the pink datapoints. Lines of best fit and correlation coefficients are shown in the legend, with the line representing $y = x$ is shown to compare the predictions.

This prediction of ΔD can be used to predict the formation energy of a binary oxide by inspection of Eq. 7.13, so our MAEs can be compared with other machine learning models trained on tens of thousands of datapoints which attempt to predict this quantity. To highlight the need to filter by coordination, we include the unfiltered cases as pink points, where we observe a higher error than if we restrict our comparisons to specific co-ordinations. This is expected, since controlling for co-ordinations should reduce the

possibility for each element to have distinct oxidation states, which our model does not represent, it only considers that A and B have constant oxidation states. The distinctly influential character of specific co-ordinations has been demonstrated in the case of the tetrahedral d^0 VO_4 structural motif, which has been found to be a common feature of oxide photoanodes with favourable bandgaps.[244]

In general, our model seems to underestimate stability, as we see with the line of best fit exhibiting a slope greater than 1 in Figure 7.6. Even when separating by individual elements, parity plots where each prediction shares a common element in the target material are included in Figures D1 and D2 of the Appendix D, where this underestimation tends to be observed for each element. This systematic bias could be reduced by calibrating the predictions per element, or by understanding potential sources for the deviation which simply cannot be captured by this method.

We call the above method to derive formation energies from oxidation states (FEFOS) and now compare this error to the state-of-the-art deep learning method to predict formation energies, which reported a test set of 25,663 OQMD entries with a MAE of 0.03 eV/atom when trained with 230,959 datapoints.[235] This test set contains materials of any composition, whereas our test set from Figure 7.6 only compares formation energies in binary oxides. Goodall *et al.* thankfully accompanied their report with a spreadsheet of values including the composition, target variable and prediction for each of the 25,663 test datapoints, and therefore we can condition the composition so that we only compare values for $A_{1-z}B_zO_2$ type calculations. Their algorithm does not use any information about the structure and uses a neural network to create feature vectors for each element and for pairs of elements. While the Roost model ignores structural features, our method does account for structure through coordination numbers. They also provided what is known as a learning curve, where they report the error in their test set when the deep learning algorithm has

been trained on progressively more datapoints. We compare both their MAE across all datapoints to ensure we reproduce their value, and also the MAE for the $A_{1-z}B_zO_2$ oxides in the test set and show these values as a function of the number of training datapoints in Figure 7.7.

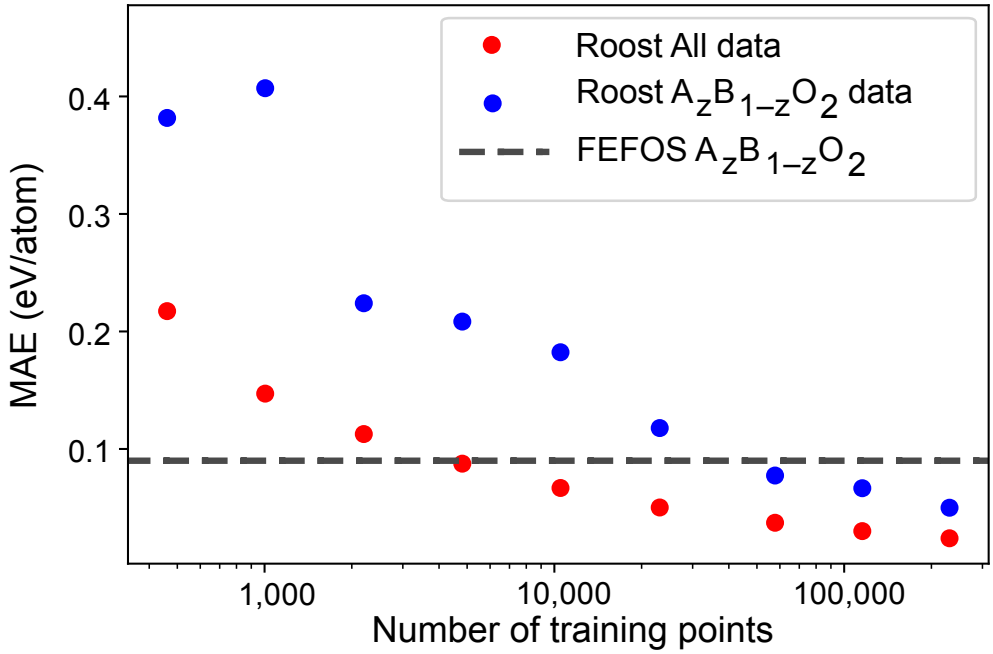

Figure 7.7. Learning curves of the state-of-the-art deep learning method[235] to for both the as-reported red datapoints which includes the entire OQMD formation energy test set, and only the OQMD entries which have the form $A_{1-z}B_zO_2$ shown as blue points. The MAE from our FEFOS method from Figure 7.6 is shown as a horizontal dashed line.

Our MAE in Figure 7.6 is shown as a dashed horizontal line and can be directly compared to the learning curve from the blue datapoints by Goodall *et al.* In comparing these values, we see that this state-of-the-art methodology requires a training set size of approximately 30,000 to surpass the MAE achieved by our FEFOS method.

To further demonstrate the appeal of this method, in the next section we test the model by alloying specific oxides (*i.e.* SnO_2, NbO_2) with 3d metals (*i.e.* Mo, Nb, W) demonstrating distinct cases on opposite sides of the periodic table where $\Delta D_{(A_{1-z}B_zO_2)}$ is either predominantly negative, or positive. Where possible, we compare these values to MP

calculations of $A_{1-z}B_zO_2$ which are only octahedrally coordinated A and B sites and three-coordinated oxygen sites, as in Figure 7.6. These calculated values are considered as the ground truth which our model is attempting to capture.

7.7.2 SnO_2

We see the results of alloying SnO_2 in Figure 7.8a, where the model agrees with MP-calculated energies for first-row transition metals in predicting they are unstable with respect to their respective native SnO_2 and BO_2 phases. The difficulty in alloying SnO_2 is that it has a low formation energy and is at the apex of the convex hull for the Sn–O composition, which can be noted for the purposes of our model from the equations for $f_{ox,SnO_2}(x) = 0.40x$ and $f_{red,SnO_2}(x) = 0.16x^2 + 0.03x$ in Table D1, which are positive for all $x > 0$. The only dopants which show a negative $\Delta D_{(Sn_{1-z}B_zO_2)}$ are Nb and W, which are predicted to be oxidized to 5+, 5+ and 6+, respectively, as Sn is reduced. We attribute this to the fact that all of the tested 3d elements except Ti are most stable at lower oxygen concentration than is seen in rutile structures (M:O = 1:2), so their $f_{red,MO_2}(x)$ equation must out-compete $f_{ox,SnO_2}(x) = 0.40x$. On the other hand, for Nb and W the relevant Sn equation is $f_{red,SnO_2}(x) = 0.16x^2 + 0.03x$ which exhibits a shallower slope. In fact, Sn is known to form oxygen vacancies more readily than tin vacancies,[245] and work in transparent conducting oxides (TCOs) from Scanlon and Watson studied formation energies to point towards the infeasibility of efficient p-type doping in SnO_2.[246] Notably, recent work has reported the doping of SnO_2 with Nb, W and Ta for application as a TCO.[247,248]As an aside, we highlight that if $\Delta D_{(Sn_{1-z}B_zO_2)} < 0$ it implies that the material is stable with respect to segregation to SnO_2 and BO_2 but not necessarily against segregation to other competing phases.

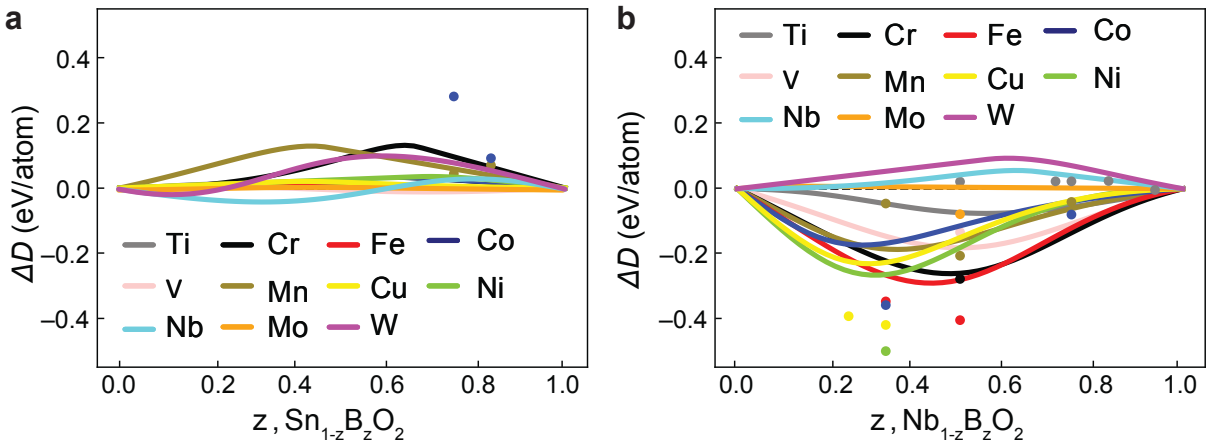

Figure 7.8. Constrained convex hull diagrams showing the predicted ΔD from Eq. 7.10 across the compositions spaces a) $Sn_{1-z}B_zO_2$ and b) $Nb_{1-z}B_zO_2$ after alloying them with earth-abundant elements, B. The datapoints denote MP-calculated values which our model attempts to capture. Here we plot our prediction across composition space, not only comparing our prediction with MP data as in Figure 7.6.

7.7.3 NbO_2

When doping niobium with first-row transition metals, (Figure 7.8b) all have negative $\Delta D_{(Sn_{1-z}B_zO_2)}$ due to their preference for reduction with respect to MO_2 (except Ti). Except for Mn, which we discuss later in this subsection, the positions of the minima of our curves appear to align with the calculated values from the MP, which we could reasonably assume are close to the true minima, for example the Cu, Co, and Ni points are clustered around the Nb($z = 0.33$) area, attributable to these metal's affinity for oxidation state 2+, while Fe and Cr have minima closer to Nb($z = 0.5$) due to their preference for oxidation state 3+. For $MnNb_2O_6$ with Materials Project id mp-22100, an older calculation, not indexed by MP is lower in energy. Through enquiry with Materials Project developers, this appears to be due to a process by which the program automatically deprecates prior calculations based on deprecated input sets which do not agree with updated revised calculations. In this case the initialized magnetic moments for Mn were less than 1 in the newer calculations, and 5 in the old, deprecated calculations, despite the expected high-spin states

of Mn in this material. When the old energy is used, the minima align more closely with those expected by our method, indicating that this tool is useful in detecting outliers within materials databases, and demonstrating its predictive power. Note, also, that this calculated material matches an ICSD entry despite Materials Project giving it an energy above hull of 0.25 eV/atom, if we take the older calculation as the ground truth, the formation energy is lowered by 0.29 eV/atom, such that it is below the hull.

7.8 Discussion

The spate of data in computational materials databases have led to the creation of machine learning-based techniques to predict formation energies, which have seen some success. However, these methods suffer severe limitations, such models require lots of data to become useful, their predictions may be biased towards previously discovered classes of materials and understanding the outputs of machine learning models is challenging. In contrast, our model only requires information about unary oxides, thereby allowing for the automatic screening of any potential combination of elements in each oxygen concentration, and the source of stabilisation or destabilisation is easily interpreted with respect to an element's propensity to be oxidized or reduced.

On a related note, the prediction of the stability of perovskites (with general formula ABX_3) has relied on the use of the Goldschmidt tolerance factor,[249] t, defined as:

$$t = \frac{r_A + r_X}{\sqrt{2}(r_B + r_X)} \tag{7.15}$$

where r_i denote atomic radii of the constituent elements, and the perovskite is predicted to be stable if t is within the range 0.9–1.05. The justification for the ratio is formed from the lattice parameters for an ideal cubic structure, as the ratio of the two lengths expressed in different radii is Eq. 7.15. More recently, another metric has been developed[250] which

extends upon this by including the oxidation state of A, n_A, as well as ionic radii by defining a new variable, τ:

$$\tau = \frac{r_X}{r_B} - n_A\left(n_A - \frac{r_A/r_B}{ln(r_A/r_B)}\right) \tag{7.16}$$

For a fixed perovskite stoichiometry, n_A determines n_B to maintain charge balance, so the fact that this descriptor makes an improvement over considerations Eq. 7.15 forms an interesting connection with the results presented in this chapter, while the importance of ionic radii points towards a promising route to improve our model.

We also note that our current model only handles 2-component systems within oxides, although the same methodology could be applied to more than two elements. Here we outline how a 3-component system could be tackled. Taking $A_aB_bC_cO_y$, with $a + b + c = 1$, we need to check the response of $\Delta C_{(A_aB_bC_cO_y)}$ to six possible combinations of oxidations and reductions over A, B, and C. We can illustrate one example combination, where A is oxidized by an amount x_A and B and C are reduced by x_B and x_C respectively, Then, to keep the overall oxidation state constant we need

$$x_A a = x_B b + x_C c \tag{7.17}$$

In the 2-component system, we could directly form the weighted sum of the parabolic equations since there was a direct relationship between the amount each element was oxidized, whereas in this case we can vary two variables freely, which then determines the third variable. Therefore, given that we know the concentrations a, b, and c, we can perform a grid search over possible combinations of $f_{ox,AO_x}(x_A)$, $f_{red,BO_x}(x_B)$ and $f_{red,BO_x}(x_C)$ to find the minimum of the sum of parabolic equations for each element. Performing this for each of the six combinations would then provide us with our final value $\Delta C_{(A_aB_bC_cO_y)}$ from which we subtract the respective unary oxide formation energies that have the same overall stoichiometry.

$$\Delta E_{f(A_aB_bC_cO_y)} = \Delta D_{(A_aB_bC_cO_y)} - a\Delta E_{f(AO_x)} - b\Delta E_{f(BO_x)} - c\Delta E_{f(CO_x)} \quad (7.18)$$

Spinel oxides can exhibit multiple oxidation states given the co-existence of different co-ordinations. These systems could be studied using this method by fitting coordination-specific parabolic equations to represent these types of systems, so that the relative affinities for certain oxidation states in both octahedral and tetrahedral sites could be considered in tandem by applying the grid search approach that we have detailed above.

The applicability of this approach relies on the notion that phase diagram surfaces can be drawn as parabolic equations, but the shape of these surfaces could conceivably be more appropriate as a piecewise linear function, or step functions in the case of p-block elements like Sn, which are only known to exist either as Sn(II) or Sn(IV). At low concentrations of dopant, the oxidation state of the host material is only slightly shifted, meaning that the resolution of the phase diagram close to the apex of the convex hull determines the accuracy of predictions. Performing vacancy formation energy calculations to resolve this could be the subject of future work, although such calculations would detract from the appeal of this high-throughput scheme. Interestingly, a recent work has proposed using the convex hull to predict differing defect formation energies directly,[251] again forming an interesting connection with the work described in this chapter. Our model predicts non-integral oxidation states due to the concave curvature of the separable quadratic equations for each element stabilises points at arbitrary positions of oxidation states. Interestingly, the motivation behind work in DFT+U, which was due in part to address the fact that simulations often do not predict a clear oxidation state with integer charge.

Our reported MAE of 0.09 eV/atom is on par with state-of-the-art methods reported by Wolverton *et al.* which uses feature vectors of length 145 to generally describe any crystalline compound.[237] The method presented in this chapter is distinct in that it focuses on oxides and oxidation states specifically and is more interpretable than methods which

rely solely on machine learning, since a prime source of stability can be explained with respect to which elements are changing their oxidation states in what direction and by what amount. While we do not study as wide an array of structures, our FEFOS method can be extended to other M:O ratios by fitting more sets of parabolic equations and is far more interpretable than a black box machine learning method using a vast set of features, and our model is not biased like ML algorithms trained on whichever set of structures happen to be available in materials databases. Extending our simple scheme across other stoichiometries and applying machine learning models to learn how to correct for the systematic biases in the model appear to be the most logical next steps in improving this methodology.

7.9 Conclusions

In this chapter we have presented an analysis of the source of stability in earth-abundant binary oxides with reference to their structure in their respective unary oxides. Tracking the changes in bond length as a proxy for alteration in oxidation number with respect to unary oxides, we observed that Cr, Mn, Fe and Co alloyed in a $A_{1-z}B_zO_2$ stabilize most when their bond lengths are lengthened, indicating a tendency to reduce their oxidation state from 4+, and this was satisfied when alloyed with another element which has a propensity to be oxidized. The common elements which were oxidized in concert with the first-row transition metals included Sb, W, Ta, and Te. This qualitative observation was made concretely into a linear relationship between binary oxide stabilisation and a measure of the relative propensity for elements to be in a certain oxidation state. That linear relationship motivated the creation of a model allowing for the pre-screening of elemental compositions requiring only appropriately fitted parabolic equations of formation energies, where these were taken from the MP and OQMD databases and the oxidation number was assumed to be a function of oxygen concentration across M–O compositions. The intuitive

representation of these equations, which simply relates to the thermodynamic affinity that an element has for a certain relative concentration of oxygen, means the approach is easily interpretable. We then develop the mathematical methodology to predict binary oxide $A_{1-z}B_zO_2$ formation energies and compare these predictions to 118 pre-existing calculations in MP. Our model's performance leads to a MAE of 0.09 eV/atom, which is comparable to state-of-the-art models which are trained on tens of thousands of datapoints. In addition, we demonstrated the interpretability of our method by inspecting its behaviour across composition space for $Sn_{1-z}B_zO_2$ and $Nb_{1-z}B_zO_2$ showing two distinct cases for Sn and Nb, where they behave as an element which prefers to be reduced and oxidized from 4+, respectively. From this, we conclude that only certain earth-abundant elements can be alloyed into Sn, namely those with a preference to be oxidized with respect to 4+, *i.e.* Mo, Nb and W, with Nb and W having been previously doped into SnO_2 for application in a transparent conducting oxide.[247] Conversely, Nb cannot be alloyed with these elements, but it can with first-row transition metals. The ability to predict which of the pairs of elements tend to be oxidized and reduced provides an added benefit of our method which we could be used to tailor the activities of individual elements based on their position on the OER volcano plots with respect to a reference oxidation state. From our studies of OER catalysts in Chapter 6, we know that higher oxidation states exhibit weaker binding energies, so we could use this methodology to attempt to bring elements closer to the peak of the volcano in cases which allowed for one element with weak binding to be reduced and the other element with strong binding to be oxidized. Finally, we stress that this model is generalisable to any relative concentration of oxygen, and so we need only to create reasonable references at that concentration and construct appropriate equations. In the next chapter, we will apply this method to screen for oxides which are predicted to be stable in acidic OER conditions.

Chapter 8 High-throughput Screening of Binary oxides for Acid Stable Water Splitting

8.1 Introduction

Green hydrogen production is much more efficient in acid owing to the selective permeability of PEM electrolysers which allow for higher current densities with respect to AEM electrolysers. However, such harsh conditions inhibit the space of possible materials due to the highly oxidising, acidic environment. By screening oxides using the method presented in Chapter 7, this chapter attempts to outline the limits imposed by thermodynamics on the feasibility of low-cost materials for the OER in PEM electrolysers, *i.e.* operating conditions of *ca.* 1.6 V_{SHE}.

IrO_2 and RuO_2 are state-of-the-art catalysts for PEM electrolysis, with IrO_2 showing better stability than RuO_2, but worse activity.[252] The scarcity of these elements has driven researchers to seek out acid-stable catalysts which contain less or no precious metals. Cr-doping these oxides has led to interesting results, with $Ru_{0.4}Cr_{0.6}O_2$ solid solutions showing a record low overpotential,[253] while IrCr films deposited through electron beam co-evaporation exhibiting a two-fold increase in specific activity over the deposited Ir films.[254] Lyons *et al.* and others have also shown that Mn-doped RuO_2 exhibits improved activity and stability over RuO_2.[255,256] Research efforts in precious metal-free acid stable catalysts have led to the discovery of nickel, manganese and cobalt antimonate systems. First noted by Lewis *et al.*, antimonates such as $MnSb_2O_x$, $CoSb_2O_x$, $NiSb_2O_x$ have exhibited stability yet poor activity for the OER.[36] These materials were set upon by the OER and ORR research communities once their stability and activity were tested for the chlorine evolution reaction in acidic media, a reaction which necessitates similar conditions

to the OER (*ca.* 1.6 V_{SHE}).[257,258] Taylor and Choi also synthesised, $CoSb_2O_6$ and, $MnSb_2O_x$ samples by electrodepositing (Co,Mn)$(OH)_2$ and Sb amorphous films which were subsequently crystallized into rutile structures by annealing at 700 °C for 3 hours in air.[259] Subsequent electrochemical testing demonstrated that both structures exhibit similar activity towards the OER at pH = 0.3, although post-electrochemical analyses demonstrated that Mn had dissolved in solution over the course of the OER.[259]

Nocera and co-workers outlined a promising strategy towards enabling earth-abundant PEM electrolysis by improving both stability and activity in tandem.[37] In this fundamental study, the activity and stability of first-row transition metals, MO_x and, PbO_x were compared and extensively characterized. PbO_x was shown to be a stable unary oxide under the necessarily harsh conditions, though its Tafel slope was near infinite. However, the Tafel slope was made comparable to first-row transition metal catalysts by doping, while avoiding the instability inherent to the respective dopants, with the optimum found for $Co_{0.14}Fe_{0.03}Pb_{0.85}O_x$. Their justification for using Pb derived from the fact that it could be easily electrodeposited, it is a cheap element, and it is highly acid stable as a unary oxide, although the authors noted that this template strategy could be applied to other acid stable unary materials. Lastly, recent work in spinel Co_2MnO_4 represents the state-of-the-art in precious metal-free acidic OER catalysis, having pushed the preceding Pareto frontier from previously reported acid stable catalysts on the axes of current density and time running with values of 1,000 mA/cm^2 operating for 10 hours and 200 mA/cm^2 operating for 1,000 hours.[260]

Computational research into the activity of OER catalyst has derived fundamental insights into the origins of the overpotential, as well as the fundamental constraints imposed on the reaction by thermodynamics,[46,47,261] as we have outlined in previous chapters. However, these OER descriptors described and applied in previous chapters do not account for pH,

and so are not discriminative in distinguishing potential acid stable catalysts. Stability descriptors, such as the Pourbaix energy (ΔG_{pbx}) developed by Persson *et al*.[59,61] represents the difference in Gibbs energy between a bulk phase and the most stable phases under a given set of conditions (*i.e.* pH, applied potential) and the concentrations of the respective elements. This descriptor has allowed for quantitative estimations of oxide stability under varying conditions of pH and voltage, which has seen widespread adoption[61,71,262] as a means to justify acid stability. Singh *et al.* studied this descriptor to create empirically-derived thresholds above which a material should not be considered stable.[61] To do this, they evaluated ΔG_{pbx} for a number of photoanode materials whose corrosion behaviour is well-known, and found this value can be as high as 0.5 eV/atom, in which case the material in question, a triclinic-$FeVO_4$, forms a self-passivating layer to protect against corrosion under the conditions used to predict ΔG_{pbx}. The highest value for a material which is reportedly stable and does not self-passivate was found for $BiFeO_3$ at 0.19 eV/atom. Stability measures are a more discriminative descriptor than activity for PEM electrolysis, and a recent study of materials which exist as entries in the MP as well as in CatalysisHub,[77] a catalysis-focused computational materials database, has shown this quantitatively.[78] This matches experiments since chronoamperometry studies held at 0.1 A/cm^2 and pH = 2 show no unary first-row transition metal oxides lasting longer than three hours.[37]

Efforts to screen for catalysts that are acid-stable computationally have begun applying the ΔG_{pbx} descriptor to identify novel materials. Some efforts have used a tandem approach of querying a materials database such as the MP for ΔG_{pbx} and then calculating bandgaps at a higher level of theory than the GGA+*U* framework from Materials Project,[263] or going beyond this and further calculating surface reactivity among the subset of entries predicted to be stable.[71] Such efforts all share the same inherent bias towards entries which already exist in the computational materials databases. Hence, some studies have focused on

computing ΔG_{pbx} for a tailored dataset of materials which are not contained in the MP but are presumed to have potential to contain some acid stable entries such as transition metal-doped equimolar IrO_2 and IrO_3 oxides;[76] however, this is very computationally demanding and the study was restricted to a narrow space of concentrations. Therefore, we have focused on applying our scheme from Chapter 7 to predict formation energies in mixed oxides, focusing on binary oxides with $A_{1-z}B_zO_2$ stoichiometries. We use our scheme to forecast the stability induced by doping host materials with earth-abundant transition metals. This affords the advantage of considering oxidation state changes in constituent elements, which has shown to be a key consideration in a very recent study reporting this discovery of a state-of-the-art PEM electrolysis. For instance, a Ir: WO_3 catalyst (Ir concentration 6%), with superior mass activity as compared to any other previously synthesized acid stable catalyst, was justified from *ab initio* calculations based on the variation of OER descriptors at different oxidation states. These results indicated that OER descriptors for $Ir^{5+/6+}$ sites are more favourable than for Ir^{4+} sites found in commercially used IrO_2, further emphasizing the importance of considering OER descriptors for multiple oxidation states which we highlighted in Chapter 6. A broad discussion of the high-level implications of the existence of how oxidation state specific OER descriptors relate to this oxide screening method is included towards the end of this chapter. Finally, previous acid-stable screening attempts tend to condition materials based on a ΔG_{pbx} value at some fixed electrochemical conditions which tend to have a range pH = 0–1 and U = 1–2 V_{SHE}. In this chapter we will study the validity of choosing such a threshold in more detail.

8.2 Computational details

Throughout this screening, we use the python package `pymatgen` to interface our predicted formation energies developed using the method outlined in the preceding chapter to insert hypothetical calculated bulk energetics as entries into the MP database. This allows for

ΔE_{hull} calculations at fixed oxygen chemical potential (described in Section 2.7.1) via the `GrandPotentialPhaseDiagram` module and the ΔG_{pbx} (described in Section 2.7.2) using the `PourbaixDiagram` module. All the code associated with the results in this chapter is available in the open source repository GitHub under: github.com/michaelcraiger/oxide_formation_energy and the coefficients and reference oxides required for the application of the method described in the previous chapter can be found in Table D1 and D2.

8.3 Oxide screening for acid stability

8.3.1 *Protocol definition*

Given a formation energy correction as outlined in the previous chapter, we can create synthetic entries into the MP using `pymatgen` to add hypothetically-calculated energies for Pourbaix[59] and phase diagram analyses.[146,264] We use known catalysts to construct a filter which can discriminate between stable and unstable candidate catalysts. To do this, we will analyse both the distance to the hull in grand chemical potential phase diagrams and the Pourbaix energy described by Persson *et al*.[59] The threshold past which a material is thought to be safely considered unstable has been reported to depend on the predicted stable phases, where, if the material is thought to phase segregate into solid materials, this phase segregation process can be kinetically-limited and thus can have a larger threshold of 0.5 eV/atom.[61] In this high-throughput search we want to identify the true phase of material under OER conditions, and as such, we should apply a stronger filter which we will determine empirically so that it distinguishes catalysts which are and are not stable in acid. The family of catalysts we test are doped IrO_2 with Li,[265] Cr,[266,267] Mn,[267] Fe,[267] Co,[267] Ni,[267] Cu[268] and Nd.[269] We choose these elements doped into Ir to first construct grand chemical phase diagrams. Note that the values derived from grand chemical phase diagrams are dependent on the existence of other entries to calculate this hull distance, so our values

are inherently functions of the resolution with which we scan the composition space with our synthetically generated materials.

In Figure 8.1, we see the position of our synthetically-generated MP points plotted on grand chemical potential phase diagrams for $\mu_{O_2} = -5.3$ eV, (where μ_{O_2} is defined in Eq. 2.49) this chemical potential of oxygen is chosen to correspond roughly to match 1.23 V_{RHE}. This was done by inspecting Ir oxide stability with varying oxygen chemical potential and finding that for $\mu_{O_2} > -5.3$ eV IrO_3 is more stable than IrO_2 and this also occurs from 1.23 V_{RHE} and higher potentials. If we wanted to find out whether a given mixture is ever on the hull, we would set μ_O to the value which minimises the distance to the hull and the line connecting mixtures of AO_2 and BO_2. However, we are here interested in discovering materials which can sustain oxidising conditions, so we set $\mu_{O_2} = -5.3$ eV. In doing so, we observe that only Cu and Co are not found on the hull of the grand chemical potential phase diagram at some concentration, and they are both within 0.09 eV/atom, while each of the other dopants for IrO_2 catalysts are predicted to be on the hull at some concentration for $\mu_{O_2} = -5.3$ eV. Of the transition metals, Fe, Ni, and Mn are on the hull up to ca. $z = 0.3$, while Cr exists on the hull at higher concentrations. Our predictions also seem to corroborate experimental observations where Cr concentrations up to 0.5 have been seen,[254,267] while the other transition metals have only seen reports of z up to 0.05.[267] Meanwhile, the molar ratio of Li:Ir in an amorphous Li- IrO_x system was reported to be 0.5:1,[265] which, if we map to the z value in our systems would leave $z = 0.33$, while the Nd-doped acid stable system was reported to be $Ir_{0.8}Nd_{0.2}O_x$, thus, $z = 0.2$.[269] Both of these points can be seen on the hull in Figure 8.1, demonstrating our model's ability to represent the stabilising effect of dopants which span the periodic table. The fact that Nd-doped systems appear to be on the hull up to $z = 0.7$ will be handled when we consider ΔG_{pbx}. While each of these systems are presumably not exactly of the form $Ir_zB_{1-z}O_2$, as

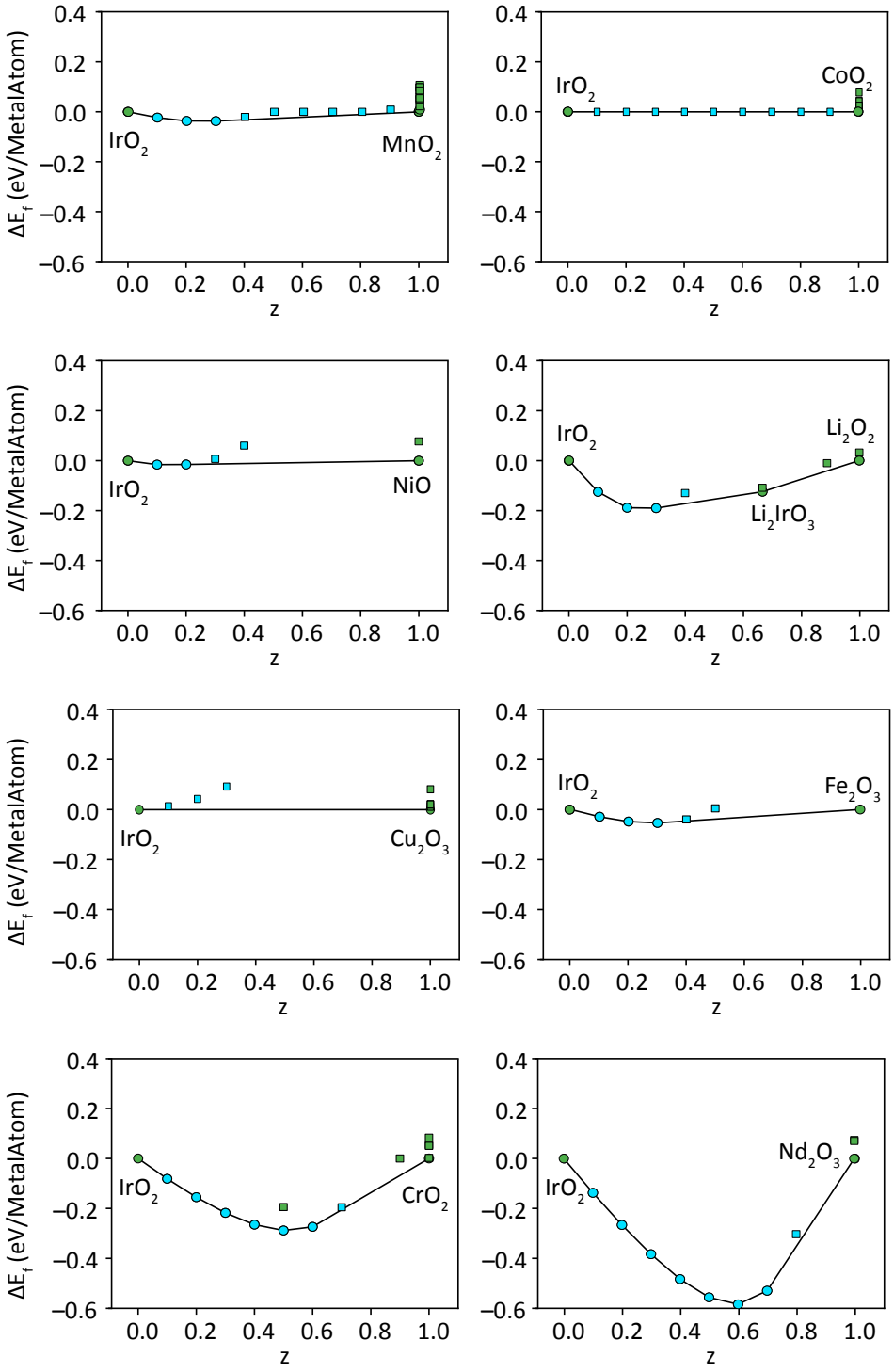

Figure 8.1. Grand chemical potential phase diagrams with $\mu_{O_2} = -5.3$ eV for Ir-based oxides doped with Mn, Co, Ni, Li, Cu, Fe, Cr and Nd. Green points denote Materials Project entries, while blue points represent our synthetic entries using the scheme described in Chapter 7. A datapoint is a circle if it lies on the hull formed by the black line connecting the endpoints, and a square if it does not. Only points within 0.05 eV/ Metal atom (*i.e.* 0.15 eV/atom) away from the hull were included for each of the plots.

our model from Chapter 7 assumes, computational studies accompanying the experimental works assume that they are.[254,265,266,269] Further, experimental reports of the true catalyst surface are absent from each of these reports, and for IrO_2 many studies report that IrO_3 is in fact the active surface.[270] Note that our predicted distance from the hull is a function of the pre-existing data in the MP, and only Cr, W and Mo exist as $Ir_zB_{1-z}O_3$ entries in such database, so whether our points are more stable than some doped $Ir_zB_{1-z}O_3$ entry at $\mu_{O_2} = -5.3$ eV is not considered. We argue that it is still noteworthy if our model highlights that a given mixture is stable with respect to competing phases in the MP.

As has been mentioned, the Pourbaix distance to hull, ΔG_{pbx}, has been used for recent screening studies for acid stable OER catalysts. To define a condition to apply when screening for acid stability we use a set of materials whose behaviour in acidic media is well-known. Rutile RuO_2, IrO_2, and MnO_2 compounds have been found to be active and stable within a narrow window of applied potential of 1.6–1.75 V_{SHE} at pH = 2,[270] while PbO_2 is an acid stable material used in the anodic end of lead-acid batteries. By studying ΔG_{pbx} for these materials we will rationally derive a criterion on ΔG_{pbx} to use in predicting acid stable binary oxides. Note that we would not expect PbO_2 to be an active OER catalyst, but its stability at *ca.* 2 V_{RHE} in acid is on a strong footing given its widespread use in lead-acid batteries at this applied potential. Furthermore, catalytic activity and stability have been argued to be inextricably linked, so assuming a stable catalyst could even be active may be misguided and we may be left instead to make conditions for application-specific use cases such as active within a specific potential window, or extremely stable yet inactive, as PbO_2 is.[37] The values for ΔG_{pbx} over the range 1–2 V_{SHE} at pH = 0 are shown in Figure 8.2, where we take the rutile MO_2 entries in the MP. Here we see that each of the materials have $\Delta G_{pbx} = 0$ eV/atom at some point in the range of applied potentials, with Ru seeing an increase in ΔG_{pbx} at 1 V_{RHE} and Ir seeing an increase

from 0 at 1.2 V_{RHE}, respecting the known trend that Ru is less stable than Ir for the OER.[16] MnO_2 has $\Delta G_{pbx} = 0$ at 1.5 V_{RHE}, with the range 1.4–1.6 V_{RHE} seeing $\Delta G_{pbx} < 0.02$ eV/atom, while past this potential we see an increase as permanganate becomes the most stable species. Interestingly, the active, stable windows for oxygen evolution in γ- MnO_2 – which is close in energy to rutile MnO_2 at 0.03 eV/atom – are in the range 1.6 to 1.75 V_{RHE}, and at this upper potential we have $\Delta G_{pbx} = 0.15$ eV/atom. Finally, PbO_2 only sees $\Delta G_{pbx} = 0$ eV/atom from *ca.* 1.7 V_{RHE} with a negative slope prior to having $\Delta G_{pbx} = 0$ eV/atom because PbO is more stable up to that point. This ΔG_{pbx} descriptor does respect well-known trends in OER catalysis regarding stability, and it appears sensible to set a voltage at which you require the material to be stable, and then couple that with conditions on min (ΔG_{pbx}). Previously-used screening protocols for acid stable catalysts, such as $\Delta G_{pbx} < 0.1$ eV/atom at pH = 0, U = 1.23 V_{SHE},[76] would not have identified RuO_2, PbO_2 or MnO_2 as potential candidates, or requiring max (ΔG_{pbx}) < 0.5 eV/atom at pH = 0 and U = 1–2 V_{SHE}[71] would not identify RuO_2 or IrO_2. While these are not ideal catalysts, we believe screening studies should justify their choice of method with respect to what types of known catalysts either are or are not identified by conditioning on ΔG_{pbx}. If we want our screening protocol to identify these four materials as acid stable, which are themselves known to be acid stable, we would need to condition min (ΔG_{pbx}) over the span of applied potentials.

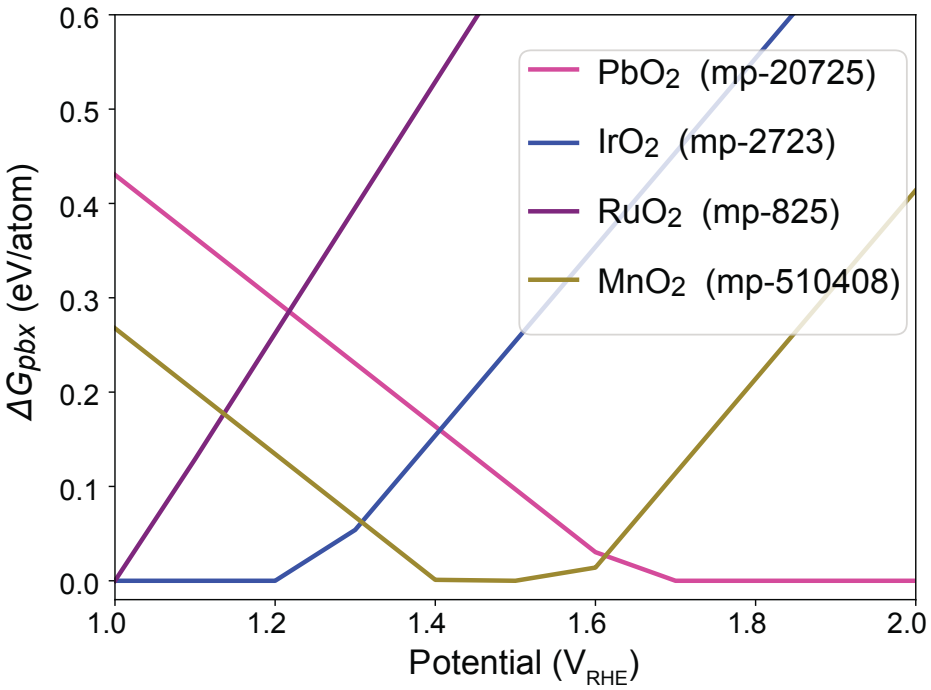

Figure 8.2. Pourbaix energies, ΔG_{pbx}, at pH = 0 over a range of applied potentials relevant for the OER in single metal oxides which are reported to be acid stable. The accompanying Materials Project entry IDs are included in the legend.

In the following, we determine what threshold to take by continuing to study the doped IrO_x systems presented in Figure 8.1, and define a reasonable cut-off paired with the hull energy from the grand chemical phase diagram which is that the material is on the hull $E_{hull} = 0$ and min $(\Delta G_{pbx.}) < 0.2$ eV/atom over the range of 1–2 V_{SHE} at pH = 0. To arrive at this condition, we use the synthetically generated datapoints, calculate their distance to the hull on the grand chemical potential phase diagram and plot their minimum and maximum $\Delta G_{pbx.}$ over 1–2 V_{SHE} at pH = 0, as seen in Figure 8.3. Here, we note there is an averaging of respective ΔG_{pbx} values at either endpoint, where at concentrations $z = 0.1$ and 0.9 the minimum and maximum closely reflect the values found for the unmixed oxide. Again, we compare filtering conditions previously used to identify acid stable catalysts, for instance, conditioning max $(\Delta G_{pbx}) < 0.5$ eV/atom over the considered applied potentials would miss all systems which have been doped $(z < 0.2)$ into IrO_x. In contrast,

conditioning on $\min(\Delta G_{pbx})$ is more sensible, but appears to be insufficient on its own, since if, for example, we only require $\min(\Delta G_{pbx.}) < 0.2$ eV/atom, then Co, Fe, Cr and Mn dopants into IrO_2 would be predicted across almost all concentrations, which has not been reported experimentally. Conversely, setting a more stringent condition such as $\min(\Delta G_{pbx.}) < 0.05$ eV/atom would neglect concentrations of Nd, Cu and Li which have been observed in IrO_x.[265,268,269] It appears more sensible to set a voltage at which you require the material to be stable, and then couple that with conditions on $\max(\Delta G_{pbx})$, and that it is important to know where $\Delta G_{pbx} = 0$ and where ΔG_{pbx} is increasing, as this could to indicate where OER begins occur or where a phase transformation towards the truly OER active surface begins. Therefore, the filter we apply is that the material be on the hull for $\mu_{O_2} = -5.3$ eV – since, as outlined earlier, this correctly predicts the stability of most of the doped systems – and that $\min(\Delta G_{pbx.}) < 0.2\ e$V/atom over the range of 1–2 V_{SHE} at pH = 0, this combined filter is subsequently used to screen for novel catalysts or novel supports in the MO_2 stoichiometry.

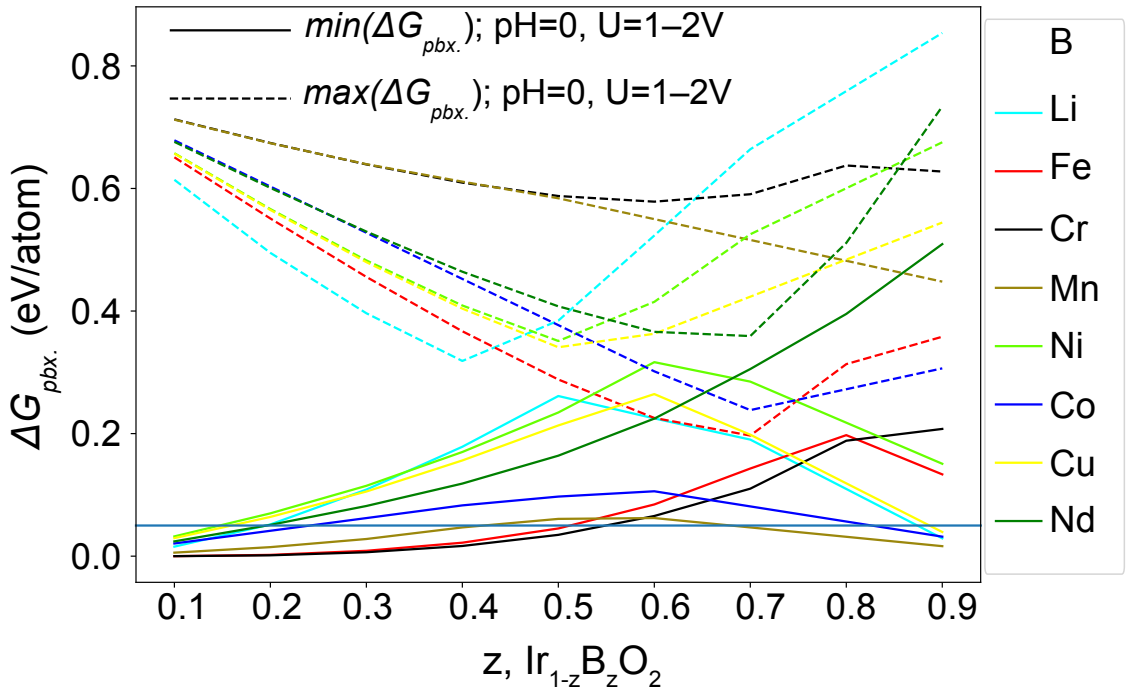

Figure 8.3. Pourbaix energies across composition space for dopants which are known to have been added to IrO_2 while being stable in acidic OER conditions for certain values of z. Colours of each line represents which dopant is being represented, with dopant concentration varying from $z = 0.1$–0.9. The minimum and maximum $\Delta G_{pbx.}$ across the range of applied potentials 1–2 V_{SHE} at pH = 0 is shown as solid and dashed lines, respectively.

8.3.2 *Search space definition*

Our method allows for pre-screening of mixtures which could be of interest for acid-stable water splitting catalysts with built-in interpretability as to the source of stabilisation. With this in mind, we applied our analysis using a set of elements which are stable in acid, that is, they have $\Delta G_{pbx} = 0$ at some point for some oxide for U = 1–2 V_{SHE} H (H = Bi, Co, Ir, Nb, Pb, Pd, Pt, Rh, Ru, Sb, Si, Sn, Ta, Te, Ti, Tl, W, Mo). The MP has some blind spots, as such we want to test combinations of these host materials for application in an acid stable OER catalyst by alloying each H element with a set of earth-abundant elements E (E = Ti, V, Cr, Mn, Fe, Co, Ni, Cu, Mo, Nb, W) which could be catalyst active sites for the OER. Lastly, we also alloy them with a separate set of potential stabilising elements S (S = Li,

Na, K, Rb, Cs, Mg, Ca, Sr, Sc, Y, Zr, La, Ce, Pr, Nd, Sm, Eu, Nd, Er, Tm, Yb) which could be co-doped with earth-abundant elements to reduce the content of precious metals.[265,269,271] We model across the composition space of $A_zB_{1-z}O_2$ where we only combine elements from H with elements from either E or S, and vary z from 0.05 to 0.95 in increments of 0.05. It is important to note this increment since the variables that we screen over are a function of the existing entries, given that the distance to the hull is a function of all considered phases in a system of ternary oxides.

8.4 Screening results

8.4.1 *Candidates for OER application*

Of the sets E and S, we only consider the elements in E as exhibiting the potential ability to perform OER, since the elements in S have not been seen to catalyse the OER as an unmixed oxide. From Table 8.1, we note that the predominant elements from the host set are precious metals such as Ir, Pd, Pt, Rh, and Ru, although there are 8 combinations (of the 195 considered) which are not composed of precious metals. We can inspect the MP for any similar entries which these predictions match to interpret the veracity of our model. The prediction of $Co_{1-z}Cr_zO_2$, $z = 0.05 - 0.25$ matches two entries, mp-756960 is a layered structure labelled as $CrCo_5O_{12}$ with $\Delta E_{hull} = 0.10$ eV/atom and $\Delta G_{pbx} < 0.2$ eV/atom for ca. 1.5–2 V and MP entry $CrCo_3O_8$ mp-837636 with a hexagonal structure with interlocking layers of Co and Cr exhibits $\Delta E_{hull} = 0.06$ eV/atom and $\Delta G_{pbx} < 0.2$ eV/atom for ca. 1.2–2 V at pH = 0. For $Sb_{1-z}Cr_zO_2$, $z = 0.40 - 0.45$ we note the presence of mp-33857 $CrSbO_4$ which is on the hull and has $\Delta G_{pbx} < 0.2$ eV/atom for ca. 0.4–1.9 V at pH = 0. Finally, we can match our prediction of acid stability for the composition space $W_{1-z}Cr_zO_2$, $z = 0.75 - 0.90$ to an entry with similar composition, Cr_2WO_6, mp-19894 which is on the hull with $\Delta G_{pbx} < 0.2$ eV/atom for ca. 0.1–1.5 V at pH = 0. This correspondence between our predictions and the entries in the Materials Project validates

the model while providing exciting avenues to inspect the stability and activity of these proposed composition spaces. It is also encouraging that the predicted acid stable chromium-doped into Ir and Ru systems matches experiment.[253,254] These predictions are of great interest, though they remain to be verified by DFT calculations and this screening protocol does not consider the activity of the proposed materials.

Table 8.1. Candidate acid stable mixed oxides predicted by our screening which satisfy $\Delta E_{hull} = 0$ for $\mu_{O_2} = -5.3$ eV and $\min(\Delta G_{pbx}) < 0.2$ at the specified concentration for a certain voltage between U = 1–2 V_{SHE} at pH = 0. Mixed oxides based only on earth-abundant elements are highlighted in bold.

$A,B:A_{1-z}B_zO_2$	z	$A,B:A_{1-z}B_zO_2$	z
Ir,Cr	0.05–0.65	Pd,Cr	0.05–0.45
Ir,Mn	0.05–0.30	Pd,Fe	0.05
Ir,Fe	0.05–0.30	Pt,Cr	0.35
Ir,Co	0.05–0.85	Rh,Cr	0.05–0.20
Ir,Ni	0.05–0.15	Rh,Mn	0.05–0.85
$\boldsymbol{Co,Cr}$	0.05–0.25	Rh,Co	0.10–0.45
$\boldsymbol{Pb,Cr}$	0.05–0.25	Ru,Cr	0.65–0.70
$\boldsymbol{Pb,Mn}$	0.5–0.95	$\boldsymbol{Sb,Cr}$	0.40–0.45
$\boldsymbol{Pb,Co}$	0.90–0.95	$\boldsymbol{Sn,Mn}$	0.95
$\boldsymbol{Pb,W}$	0.15–0.20	$\boldsymbol{W,Cr}$	0.75–0.90

Having performed a screening for a set of elements doped into another set of elements, we can collect high-level statistics about the descriptors we are screening over. In particular, we calculate the mean value of $\overline{\Delta E}_{hull}$ and $\overline{\Delta G}_{pbx}$ at 50% concentration for every element when combined with elements from the other sets. We wish to get a characteristic stability curve for each element and calculating these averages at lower concentrations would see curves which average out to the same shape, while higher concentrations would simply morph towards the stability curve of the unary oxide. To calculate these values for an element in the host set H, we calculate $\overline{\Delta E}_{hull}$ and $\overline{\Delta G}_{pbx}$ over the set of elements in $E \bigcup S$ at 50% concentrations, while for elements in $E \bigcup S$, we would calculate their average at 50% concentration with elements in H, where the sets H, E and S defined above in the search space definition, Section 8.3.2. We calculate this metric at equimolar concentrations so that we get a high level view of each elements behaviour across 1–2 V_{SHE} of applied potential, allowing for general trends to be appreciated and to highlight specific elements to target as potential sources of stabilisation. We use set notation to denote the union of two sets and the symbol ∈ to denote that a given element is in said set.

$$\overline{\Delta G}_{pbx}(A) = \begin{cases} \frac{1}{N} \sum_{B \in E \bigcup S, A \neq B} \Delta G_{pbx}(A_{0.5}B_{0.5}O_2), & A \in H \\ \frac{1}{N} \sum_{B \in H, A \neq B} \Delta G_{pbx}(A_{0.5}B_{0.5}O_2), & A \in E \bigcup S \end{cases} \tag{8.1}$$

Each element in the sets E or S combined with the same set of elements from the host set H, so we can consider the measurement as some uniform function which tells us, generally, how close a given element is to being acid stable. So, the average is calculated differently depending on whether you want the average for a host element, or an element alloyed into the host. In the case of ΔG_{pbx}, we can also observe where each element affords the most stability at a given potential. In Figure 8.4a we see the set of elements which were considered as possible active sites for the OER.

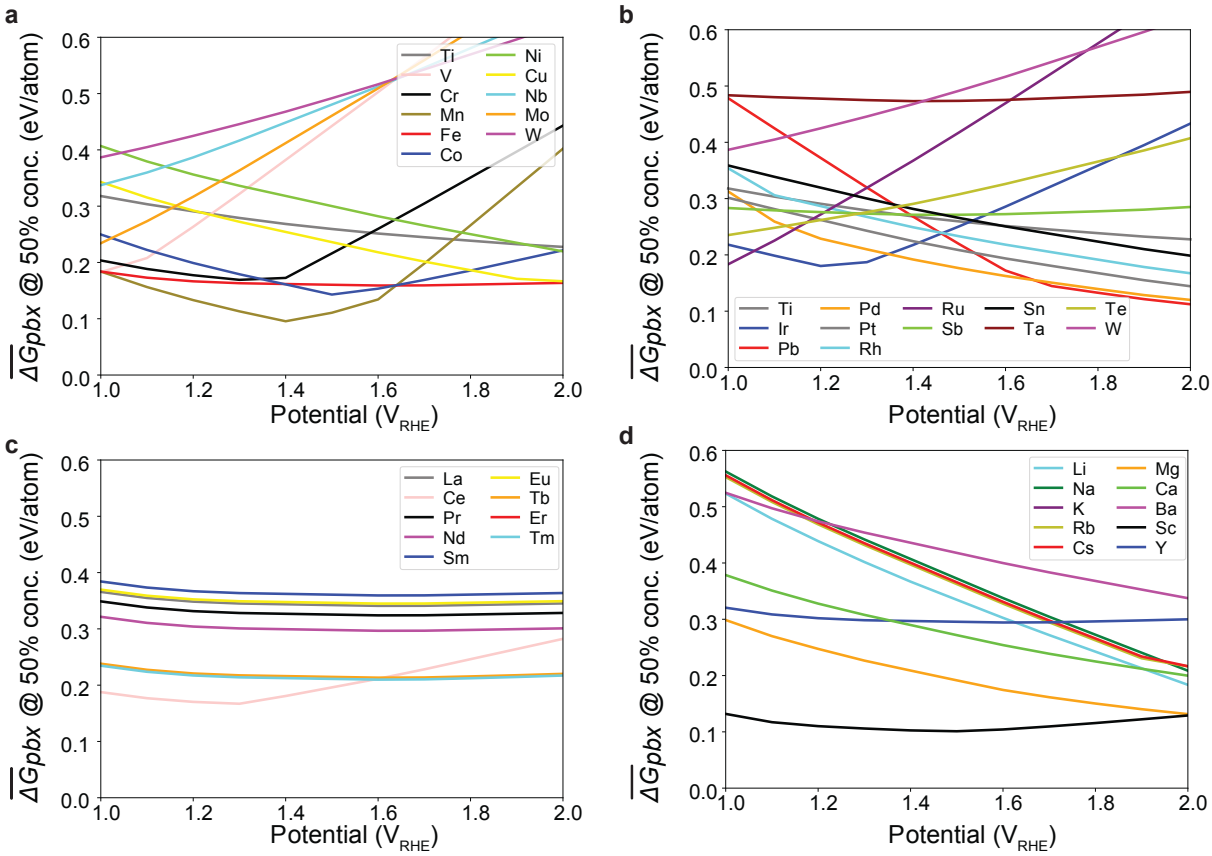

Figure 8.4. $\overline{\Delta G_{pbx}}$ defined as in Eq. 8.1 found by averaging $\Delta G_{pbx}(A_{0.5}B_{0.5}O_2)$ for a specific element A paired each of the appropriate sets of elements B, at pH = 0 for a range of applied potential 1–2 V_{SHE}. For a) earth-abundant transition metals, $A = E$ and $B = H$ b) host elements, $A = H$ *and* $B = E \bigcup S$ c) lanthanides and d) alkali, alkali-earth, and early transition metals. The elements plotted in a), c), and d) make up the set $E \bigcup S$.

In Figure 8.4 we see Mn is the element with the lowest ΔG_{pbx} until 1.65 V_{RHE} at which point the average Fe hull distance is the lowest. In general, the shape of these curves for a given element at 50% concentration mirrors the curve for the binary, unmixed reference oxide associated with that element. This can be seen directly by comparing the Mn, Ru, Ir and Pb data in Figure 8.4 with the data presented in Figure 8.2 for the same elements. In each case, the line is qualitatively the same, while being *ca.* 0.1–0.2 eV/atom higher, as expected when mixed with other elements in the set which are unstable over different potentials. If we take heed of the stability-activity relationship, we discussed earlier, in that instability may in fact bestow activity, then perhaps the more sensible approach is to

attempt to mimic the behaviour of the precious metals Ru and Ir which are known to be performant. In this case, by inspection Cr seems to match the behaviour of Ir and V appears to match that of Ru. We must note here that the ΔG_{pbx} values for rutile IrO_2 and RuO_2 have an important difference between those for rutile CrO_2 and VO_2 in that the precious metal-based oxides have $\Delta G_{pbx} = 0$ at some point over the range considered in Figure 8.4a, which cannot be said for CrO_2 and VO_2, where the minimum value is at least 0.2 eV/atom. In Figure 8.4b we note the distinct character of those Ir and Ru elements with respect to the other considered host materials, which are either unstable throughout (Te, Sb, W, Ta), with $\Delta G_{pbx} > 0.25$ eV/atom or become stable at potentials greater than 1.5 V_{RHE} (Ti, Pd, Pt, Rh, Sn). The lanthanides in Figure 8.4c show a high degree of similarity except for Ce, with this element seeing the lowest ΔG_{pbx} up to about 1.6 V at which point Tm and Tb exhibit lower values. Finally, alkali, alkali earth and early transition metals have qualitatively similar ΔG_{pbx} values within those three subgroups, as shown in Figure 8.4d with Li, Mg and Sc affording the most stability of the elements. Of course, this analysis neglects the fact that certain elements may be particularly well-suited to alloying with certain other elements based on lattice constants or other factors, but this picture allows for a first order thermodynamic assessment of how feasible it may be for a given element to be alloyed in an acid stable OER catalyst.

We also used ΔE_{hull} as a condition to determine whether an entry is considered as potentially acid stable in Table 8.1, so we have also gathered the average $\overline{\Delta E}_{hull}$ for $\mu_{O_2} = -5.3$ eV, at 50% concentration, defined analogously to Eq. 8.1, and shown below, where the sets H, E and S defined in the search space definition, Section 8.3.2.

$$\overline{\Delta E}_{hull}(A) = \begin{cases} \frac{1}{N} \sum_{B \in E \cup S, B \neq A} E_{hull}(A_{0.5}B_{0.5}O_2), & A \in H \\ \frac{1}{N} \sum_{B \in H, B \neq A} E_{hull}(A_{0.5}B_{0.5}O_2), & A \in E \bigcup S \end{cases} \tag{8.2}$$

We plot the results of calculating Eq. 8.2 in Figure 8.5 – this is distinct from the data in Figure 8.4 in that this is restricted to the distance to the hull formed only by solid phase materials, so the effect of pH and voltage is not considered. To be clear, the voltage is only considered tangentially from the use of the oxygen chemical potential.

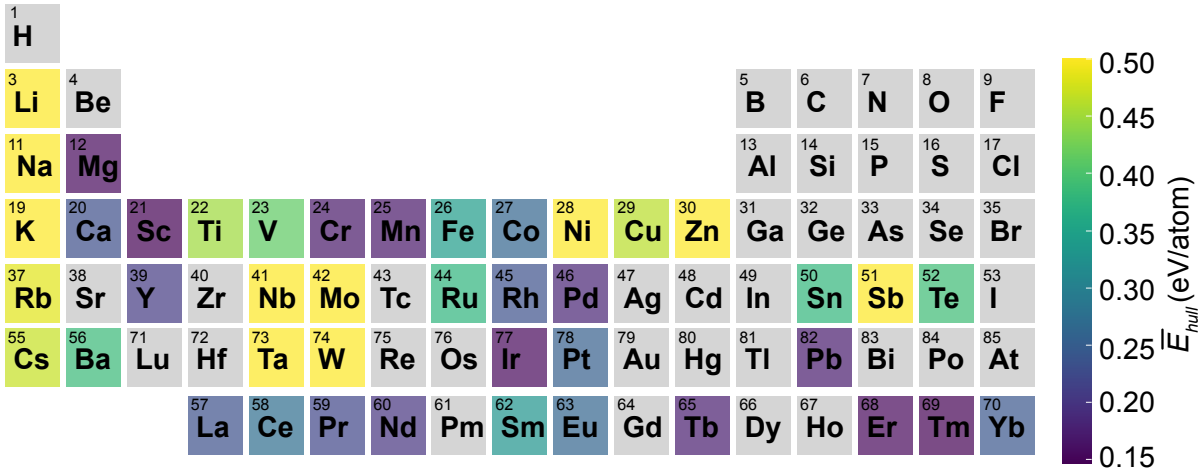

Figure 8.5. Mean value of $\overline{\Delta E}_{hull}$, defined in Eq. 8.2, for $\mu_{O_2} = -5.3$ eV across the periodic table. More stable average values are displayed as more violet, and the maximum average eV/atom to display was set at 0.5 eV/atom to enable better comparability of values by eye.

From this, we see that of the earth-abundant transition metal elements, Cr and Mn have the lowest average distance to the hull, while Ir displays the lowest value of all elements. Despite RuO_2 being one of the most active materials for OER, its $\overline{\Delta E}_{hull}$ value at $\mu_{O_2} = -5.3$ eV is *ca.* 0.3 eV/atom. This explains the fact that it is shown as one of the relatively unstable elements in the image of the periodic table, since at this oxygen chemical potential, RuO_4 is more stable than RuO_2. Also of note is the stabilising effect that lanthanides appear to afford, as this group appears to be the only one consistently low, so exploring their use as an element to reduce precious metal content is a promising avenue.

8.5 Discussion

The method presented in this chapter is extremely fast, with the ability to predict over the 572 combinations in a matter of minutes. Its interpretability also allows us to make broad statements about oxidation state shifting analysis with implications across OER catalysis.

In Chapter 6, we showed that the OER descriptor for hypothetical molecular complexes is oxidation state-dependent, element-specific and that this quantity was not correlated. Each of these factors are important in thinking about mixing elements at a given M:O ratio with OER catalysis in mind. As shown in Figure 8.6a, an ideal scenario for OER would be one whereby A and B elements in AO_x and BO_x are non-ideal catalysts, but their reduced and oxidised counterparts, respectively, are. This is illustrated in Figure 8.6a where A is reduced and B is oxidised by some unspecified degree, and in Figure 8.6 b we depict a scenario where this leads their OER descriptors to comes closer to the ideal value. This picture could explain why doping Ir and Ru oxides with elements which have an affinity for oxidation states 3+ or lower improves OER activity,[272–274] since the oxidation state of Ir and Ru atoms increases. Computational results have shown that IrO_2 and RuO_2 have lower OER descriptors than the ideal value,[52,275] and that when these metals are in higher oxidation states, which can be stabilised by low valent dopants, it approaches the ideal value. Indeed, precisely this explanation from first principles calculation was used to justify the activity of the Ir:WO_3 system mentioned in the introduction.[272] Conversely, Sargent *et al.* have observed an increase in activity of NiFe and CoFe oxyhydroxides can be improved by doping them with high-valent elements Mo^{5+}, Ta^{5+}, Nb^{5+}, Re^{6+} or W^{6+},[11,13] and this enhancement in catalytic rate was justified on the basis that the Fe atoms were reduced relative to the undoped catalysts. This does not contradict the argument we have made that adding low valent dopants improves IrO_2 and RuO_2 catalysts because we assume that the variation of the OER descriptor as a function of oxidation state is not uniform across elements. Time-resolved spectroelectrochemical analyses coupled with *ab initio* calculations have provided detailed insight into the relative effects of Mn-doped, Fe-, Co-, and Zn-doped NiO on the proportion of oxidized species to understand why Fe doping shows the most optimal performance.[276] This was achieved by deriving a rate law which

showed Fe doping to exhibit an optimal balance between binding oxygen too strongly or too weakly, our FEFOS model could provide a means to forecast this given the built-in consideration of oxidation states.

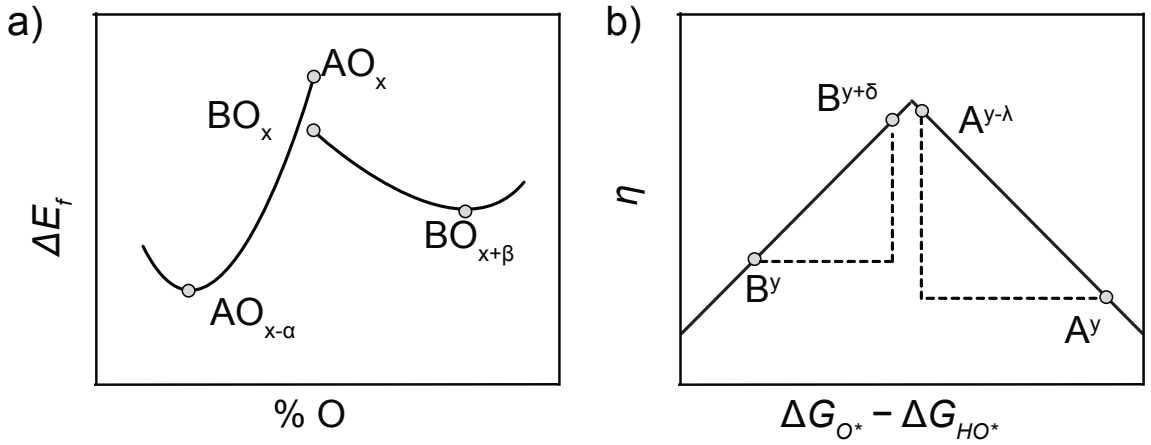

Figure 8.6. Scheme illustrating a scenario where two hypothetical elements A and B are reduced and oxidised, respectively, due to their unmixed oxides affinity for lower or higher oxidation states with respect to that seen in MO_x. In the ideal scenario shown here, where in a) we see the stability shifts and simultaneous improvements in the OER activities in b) of both A and B within the $A_zB_{1-z}O_x$ mixture relative to the unmixed case due to the behaviour of the oxidation state-dependence of the unmixed OER descriptors.

8.5.1 *False positives*

Our predictions for acid stable binary oxides could also produce false positives, and here we will outline potential reasons based on the limitations of our model. The reliability of our method for low concentrations is less trustworthy since MP points tend to include entries with z = 0.25–0.75, and our predictions have predominantly been tested within this concentration range. Also, the most stable phase for the MO_2 composition tends to be rutile, but that is not always the case. For instance, NiO_2 is most stable as a layered structure, so it is unclear how we should interpolate between that end member and an end member composed of a rutile structure, for example. Another potential source of false positives is the inherent error of our model of 0.09 eV/atom shown in the previous chapter. Finally,

our model does not consider the relative expansion or contractions which would be expected by swapping out elements with different atomic radii.

8.5.2 *False negatives*

We now outline instances of known acid stable materials which our method did not highlight, such as Sb-containing oxides. From the analyses in the preceding chapter, where we compared our predictions directly to MP calculations, we noted a systemic underestimation of stability. This is especially pronounced for when we restrict the analysis to any Sb-containing oxide, which we show in Figure 8.7 where the MAE is 0.15 eV/atom. This is a concrete example of the limitations of our model, which could be tackled by increasing the threshold of stability, but this is bound to lead to more false positives also. However, the fact that it is easily interpretable in this way is an advantage since such shortcomings can be identified in a straightforward way in this high-throughput screen.

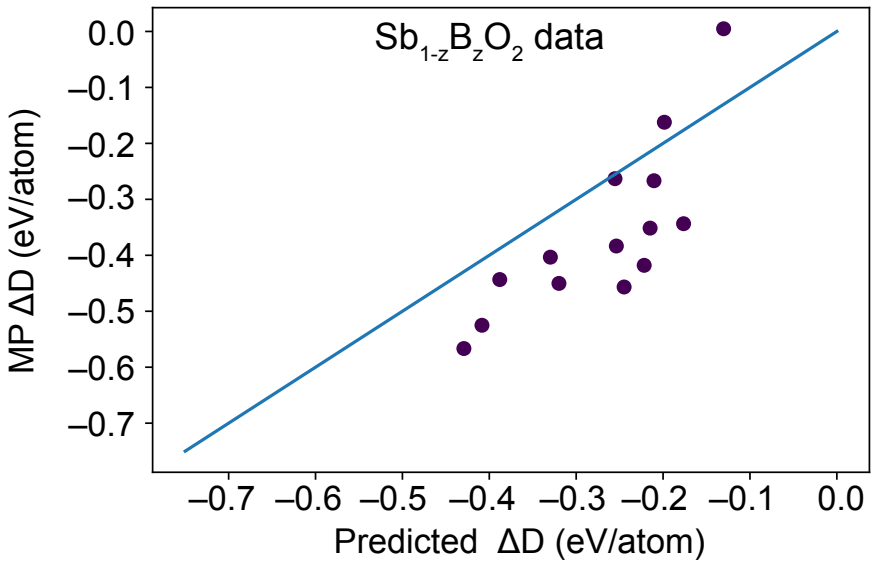

Figure 8.7. Parity plot of our schemes predicted deviation from the weighted average formation energy against that observed for Materials Project entries containing Sb at M:O ratios of 1:2. The line $y = x$ is shown to emphasise the systematic underestimation of stability within this subset of oxides.

Our scheme also does not consider the formation of vacancies which are inevitable at low concentrations whenever an element is swapped out for an element with a different valence.

At low concentrations, the oxidation state of the host material is only slightly shifted, meaning that the resolution of the phase diagram close to the apex of the convex hull determines the accuracy of predictions. Another way to tackle this would be to calculate the necessary parabolic equations at MO_x stoichiometries across the ranges of, say, x = 1–3 in intervals of 0.01. This could be performed by doing vacancy formation energy calculations, which could be the subject of future work, although such calculations would detract from the appeal of this high-throughput, interpretable scheme.

8.6 Conclusions

In this chapter we showcase the potential of the method described in Chapter 7 to allow for the screening of oxides on the order of seconds per composition space. To apply our methodology, which predicts formation energies, to the prediction of acid stable OER catalysts, we began by investigating how best to correctly identify a set of known catalysts which had been doped into IrO_2. This led to the development of a filtering condition which correctly identifies 9/10 of these known compounds when applying our formation energy prediction. With this protocol we then tested 100s of combinations with dopants consisting of alkali and transition metal elements for acid stability, with only 10% of the tested combinations coming back as potentially candidates, underscoring the difficulty there is in finding cheap catalysts for this reaction in acid. We also gathered cross-periodic table statistics about the stability of each of the elements being contained within an acid stable oxide in the MO_2 composition at 50% concentration. Here we found that we could make comparisons across applied potential for elements, and that some groups such as the alkali metals, alkaline earth-metals and lanthanides all exhibited similar curves of stability, indicating a uniformity to stabilization effects which can be afforded by adding elements of specific groups. This analysis also found that Li, Ce, and Mg show the lowest average $\overline{\Delta G}_{pbx}$, indicating that these elements have the most potential to alloy with the host elements

considered in this study. Cr appeared to be the most promising earth-abundant element to further consider for application in future screening methods based on the average distance to the convex hull with respect to solid phases, $\overline{\Delta E}_{hull}$, as well as the $\overline{\Delta G}_{pbx}$ across 1–2 V_{RHE} which mimicked the behaviour of $\overline{\Delta G}_{pbx}$ for active, though precious, Ir.. We then discussed the high-level implications of OER descriptors varying with oxidation state and relate them to results from our investigations of molecular catalysts in Chapter 6 and to previous experimental work describing how doping Ir and Ru oxides affords stability and activity. We then finish by providing potential reasons for false positives and false negatives in our screening, thereby providing clear directions for future work.

Future work should focus on refining the model so that stability predictions are not biased towards underestimating stability and understand the sources of errors shown in Chapter 7. The implication of this methodology is that there are fundamental thermodynamic constraints on our ability to discover first-row transition metal-based, acid stable catalysts, and that these constraints can be represented simply by the formation energies of oxides based on these elements. Ultimately, this chapter shows how we are constrained by thermodynamics in the search for acid stable catalysis and indicates that these constraints imply that without going to different coordination environments other than octahedral, it will be difficult to surpass or approach the stabilities and activities shown by Ru or Ir-containing oxides.

Chapter 9 Conclusions and Future Work

9.1 Conclusions

The primary aim of this thesis was to describe and develop methods which would enable for faster evaluation times and deeper understanding of OER catalysts in both homogenous and heterogeneous phases.

In Chapter 4 we used DFT methods to analyse a set of molecular OER catalysts which chart the course of catalyst discovery within homogeneous water splitting. Using the hybrid meta-GGA functional TPSSh, we showed that these catalysts exhibit a similar relationship between intermediate binding energies as do heterogeneous catalysts. We then described how the typical descriptor for activity used in heterogeneous catalysis could not explain the activity of Ru-based complexes, leading to a descriptor derived from the redox potential of one-electron oxidations, and outlined principles for general molecular OER catalyst discovery.

Through analysing a specific subset of Fe-based molecular catalysts with tetradentate, non-equatorial ligands, and two active sites in *cis*, we noted another descriptor based on redox potentials and correlated our calculated values for this descriptor to experimental TOFs across active catalysts. This relates nicely with experimental work which indicates that the O–O bond formation is not rate limiting,[202] but instead the rate limiting step involves an oxidation of the Fe centre.

In Chapter 6 we applied our design principles outlined in Chapter 4 to identify catalysts which undergo the extra oxidation mechanism at low overpotential. This led to the prediction of 9 Cr-based complexes as interesting experimental leads. Analyses generated secondary to this included the demonstration of oxidation state independent scaling relations, a spin-based justification for circumvention of established scaling relations, and

a means to explain why different metals follow different scaling relations by analysing changes in metal-oxygen spin densities.

In Chapters 7 and 8, we turned our attention to binary oxides – the typical OER catalysts found in acidic medium. Specifically, we focused on predicting materials stability as a function of competing changes in oxidation states. As a result, we established a method to create binary oxide phase diagrams which have MAE values of 0.09 eV/atom over $A_{1-z}B_zO_2$ stoichiometries, using physics-based models and just four parameters. This relates nicely with the work in preceding chapters which outlined the influence of oxidation state on the energetics of OER intermediates. We then applied this scheme in Chapter 8 to screen across the periodic table for potential binary oxides for application as catalysts or supports in acidic OER, highlighting Cr as the most promising earth-abundant dopant for acidic OER, as well as, surprisingly, lanthanides and alkaline-earth elements.

Although the scheme developed an interesting approach to predict formation energies in mixed oxides, it cannot yet handle mixed coordinations, which may be of interest for attempts to discover novel materials. For instance, high entropy oxides have garnered interest recently for the OER,[277] with activity maps as a function of varying composition: we could envisage an extended version of the method presented in Chapter 7 could feasibly generate similar maps of stability among a high dimensional composition space.

9.2 Future work

9.2.1 *Homogeneous oxygen evolution*

We posit that metal ligands must be multidentate to handle the lability of first-row transition metal complexes – multiple monodentate ligands are likely to become hydrolysed, so that the appropriate catalyst to model in this case would be some MO_xH_y-type catalyst. While utilising predominantly monodentate or bidentate ligands allows for greater combinatorial flexibility and much larger dataset construction, since we can permute through a set of

ligands in different positions, their inclusion is not realistic for labile first-row transition metals (with which we want to design active catalysts). Secondly, any organic ligand framework proposed for water oxidation must also be oxidatively stable. An inspiring and insightful overview of these considerations was recently outlined in a perspective by Nocera and Thorarinsdottir.[278] Two of the useful instructions that the authors summarized from seminal works from Collins,[279] outlining an instructive ruleset for making oxidatively stable organic ligands: "(1) elimination of β-H atoms, especially if the α atom can support an increase in bond order with β-H elimination; (2) elimination of heteroatoms that can stabilize the cationic character that remains on atoms from which oxidative bond cleavage has occurred." We have highlighted these considerations specifically since ligands could be filtered computationally on this basis by creating code that can distinguish types of H atoms. Concrete demonstrations of the first rule for molecular OER was provided by Lloret-Fillol and co-workers reporting a 5-fold improvement in TON values after deuterating β-H atoms.[205] Furthermore, the same authors also showed that deuteration of methyl groups can lead up to a *ca.* 10-fold improvement in TOFs. This was proposed to be due to C–H hydroxylation whereby the H atom is transferred to the Fe(V)=O site. In this context, the insights derived from Chapter 5 suggested the importance of having at least a 3.0 Å distance between the WNA active site and the most proximal methyl group. In any case, tight collaboration between computational and experimental chemists is required to realize the potential of any endeavour to create a useful and applicable search space of OER catalysts. Further research into homogeneous oxygen evolution reaction catalysts should investigate a larger set of hypothetical materials. These could be generated either through mining databases for ligands of specific denticity, or potentially by novel generative models which create structures after training a machine learning model to be able to distinguish between real and "fake" molecules.[1] The cost of the constituent ligands must also be accounted for,

since complicated organic ligand synthesis can make ligand costs per unit of catalyst comparable to the cost of an atom from the platinum group metals. Thus, the goal must be to find the cheapest set of ligands which can both catalyse OER and remain stable against demetallation. The central appeal in studying molecular catalysts lies in their potential to be anchored onto heterogeneous supports to improve the stability[40] of those complexes, although fundamental experimental research into what methods are most feasible to accomplish this are lacking.

9.2.2 *Heterogeneous oxygen evolution*

To continue the work of screening for acid stable OER catalysts, our scheme should be extended so that it can handle mixed coordinations, or multicomponent oxides. Future work should also focus on reducing errors and reproducing the known acid stable catalysts which are composed of cheap elements such as antimonates. We noted in Chapter 8 the underestimation of Sb-containing oxide stability by our model, the source of which should be analysed in concert with others. One avenue to consider further would be the co-compatibility of effective lattice radii in the predicted oxidation state with the observed lattice lengths of the binary oxide for which we are predicting the stability. For instance, if it were found that an $A_{0.5}B_{0.5}O_2$ oxide had a cubic structure and our model predicted a spurious non-integral cationic charges of $A^{3.75+}$ and $B^{4.25+}$. hen perhaps an ideal scenario would be observed when a pair of prescribed effective ionic radii are equal, since the structure is cubic. One potential way to ascribe effective ionic radii would be to take A^{3+} and A^{4+} and say: $A^{3.75+} = 0.75A^{4+} + 0.25A^{3+}$, and similarly $B^{4.25+} = 0.75B^{4+} + 0.25B^{5+}$. Another approach would be to attempt to simply predict the deviations between our model and the observed formation energy in the MP using some machine learning model such as linear regression, passing in features of the elements in the binary oxide as

vectors. The ease with which predictions can be made using this scheme is very appealing, allowing for quick suggestions of promising materials.

References

1. Things We Can't Live Without: The List Has Grown in the Past Decade. *Pew Research Center* (2006).
2. Wei, P.-S. *et al.* Absorption coefficient of carbon dioxide across atmospheric troposphere layer. *Heliyon* **4**, 10 (2018).
3. Ritchie, H., Roser, M. CO_2 and Greenhouse Gas Emissions. *Our World in Data* (2019).
4. van der Spek, M. *et al.* Perspective on the hydrogen economy as a pathway to reach net-zero CO_2 emissions in Europe. *Energy & Environmental Science.* **15**, 1034–1077 (2022).
5. EirGrid. *Annual Renewable Energy Constraint and Curtailment Report 2018*. 20 (2019).
6. Pellow, M. A., Emmott, C. J. M., Barnhart, C. J. & Benson, S. M. Hydrogen or batteries for grid storage? A net energy analysis. *Energy & Environmental Science* **8**, 1938–1952 (2015).
7. Pan, S.-Y., He, K.-H., Lin, K.-T., Fan, C. & Chang, C.-T. Addressing nitrogenous gases from croplands toward low-emission agriculture. *npj Climate and Atmospheric Science* **5**, 43 (2022).
8. Wang, R. R., Zhao, Y. Q., Babich, A., Senk, D. & Fan, X. Y. Hydrogen direct reduction (H-DR) in steel industry—An overview of challenges and opportunities. *Journal of Cleaner Production* **329**, 129797 (2021).
9. Hansen, J. N. *et al.* Is There Anything Better than Pt for HER? *ACS Energy Letters* **6**, 1175–1180 (2021).
10. Li, W. *et al.* Low-temperature water electrolysis: fundamentals, progress, and new strategies. *Materials Advances* **3**, 5598–5644 (2022).
11. Zhang, B. *et al.* Homogeneously dispersed multimetal oxygen-evolving catalysts. *Science* **352**, 333–337 (2016).
12. Etzi Coller Pascuzzi, M., Man, A. J. W., Goryachev, A., Hofmann, J. P. & Hensen, E. J. M. Investigation of the stability of NiFe-(oxy)hydroxide anodes in alkaline water electrolysis under industrially relevant conditions. *Catalysis Science & Technology* **10**, 5593–5601 (2020).
13. Zhang, B. *et al.* High-valence metals improve oxygen evolution reaction performance by modulating 3d metal oxidation cycle energetics. *Nature Catalysis* **3**, 985–992 (2020).
14. Holladay, J. D., Hu, J., King, D. L. & Wang, Y. An overview of hydrogen production technologies. *Catalysis Today* **139**, 244–260 (2009).
15. Shaner, M. R., Atwater, H. A., Lewis, N. S. & McFarland, E. W. A comparative technoeconomic analysis of renewable hydrogen production using solar energy. *Energy & Environmental Science* **9**, 2354–2371 (2016).
16. McCrory, C. C. L. *et al.* Benchmarking Hydrogen Evolving Reaction and Oxygen Evolving Reaction Electrocatalysts for Solar Water Splitting Devices. *Journal of the American Chemical Society* **137**, 4347–4357 (2015).
17. Arges, C. G., Wang, L., Parrondo, J. & Ramani, V. Best Practices for Investigating Anion Exchange Membrane Suitability for Alkaline Electrochemical Devices: Case Study Using Quaternary Ammonium Poly(2,6-dimethyl 1,4-phenylene)oxide Anion Exchange Membranes. *Journal of the Electrochemical Society.* **160**, 11 (2013).
18. Wu, X., Scott, K., Xie, F. & Alford, N. A reversible water electrolyser with porous PTFE based OH^- conductive membrane as energy storage cells. *Journal of Power Sources* **246**, 225–231 (2014).
19. Cho, M. K. *et al.* Factors in electrode fabrication for performance enhancement of anion exchange membrane water electrolysis. *Journal of Power Sources* **347**, 283–290 (2017).
20. Leng, Y. *et al.* Solid-State Water Electrolysis with an Alkaline Membrane. *Journal of the American Chemical Society* **134**, 9054–9057 (2012).
21. Grimaud, A. *et al.* Activating lattice oxygen redox reactions in metal oxides to catalyse oxygen evolution. *Nature Chemistry* **9**, 457–465 (2017).
22. Schweinar, K., Gault, B., Mouton, I. & Kasian, O. Lattice Oxygen Exchange in Rutile IrO_2 during the Oxygen Evolution Reaction. *Journal of Physical Chemistry Letters* **11**, 5008–5014 (2020).
23. Detz, R. J., Abiri, Z., Kluwer, A. M. & Reek, J. N. H. A Fluorescence-Based Screening Protocol for the Identification of Water Oxidation Catalysts. *ChemSusChem* **8**, 3057–3061 (2015).
24. Kärkäs, M. D., Verho, O., Johnston, E. V. & Åkermark, B. Artificial Photosynthesis: Molecular Systems for Catalytic Water Oxidation. *Chemical Reviews* **114**, 11863–12001 (2014).
25. Duan, L. *et al.* A molecular ruthenium catalyst with water-oxidation activity comparable to that of photosystem II. *Nature Chemistry* **4**, 418–423 (2012).
26. Codolà, Z. *et al.* Electronic Effects on Single-Site Iron Catalysts for Water Oxidation. *Chemistry - A European Journal* **19**, 8042–8047 (2013).

27. Watabe, S. *et al.* Critical Hammett Electron-Donating Ability of Substituent Groups for Efficient Water Oxidation Catalysis by Mononuclear Ruthenium Aquo Complexes. *Inorganic Chemistry* **58**, 12716–12723 (2019).
28. Bullock, R. M. *et al.* Using nature's blueprint to expand catalysis with Earth-abundant metals. *Science* **369**, eabc3183 (2020).
29. Corrigan, D. A. The Catalysis of the Oxygen Evolution Reaction by Iron Impurities in Thin Film Nickel Oxide Electrodes. *Journal of the Electrochemical Society* **134**, 377–384 (1987).
30. Browne, M. P. *et al.* Oxygen evolution catalysts under proton exchange membrane conditions in a conventional three electrode cell *vs.* electrolyser device: a comparison study and a 3D-printed electrolyser for academic labs. *Journal of Materials Chemistry A* **9**, 9113–9123 (2021).
31. Weber, M. F. & Dignam, M. J. Efficiency of Splitting Water with Semiconducting Photoelectrodes. *Journal of the Electrochemical Society* **131**, 1258–1265 (1984).
32. Walter, M. G. *et al.* Solar Water Splitting Cells. *Chemical Reviews* **110**, 6446–6473 (2010).
33. Gorlin, Y. & Jaramillo, T. F. A Bifunctional Nonprecious Metal Catalyst for Oxygen Reduction and Water Oxidation. *Journal of the American Chemical Society* **132**, 13612–13614 (2010).
34. Li, D. *et al.* Highly quaternized polystyrene ionomers for high performance anion exchange membrane water electrolysers. *Nature Energy* **5**, 378–385 (2020).
35. Minke, C., Suermann, M., Bensmann, B. & Hanke-Rauschenbach, R. Is iridium demand a potential bottleneck in the realization of large-scale PEM water electrolysis? *International Journal of Hydrogen Energy* **46**, 23581–23590 (2021).
36. Moreno-Hernandez, I. A. *et al.* Crystalline nickel manganese antimonate as a stable water-oxidation catalyst in aqueous 1.0 M H_2SO_4. *Energy & Environmental Science* **10**, 2103–2108 (2017).
37. Huynh, M., Ozel, T., Liu, C., Lau, E. C. & Nocera, D. G. Design of template-stabilized active and earth-abundant oxygen evolution catalysts in acid. *Chemical Science* **8**, 4779–4794 (2017).
38. Li, N. *et al.* Template-stabilized oxidic nickel oxygen evolution catalysts. *Proceedings of the National Academy of Sciences of the United States of America* **117**, 16187–16192 (2020).
39. Okamura, M. *et al.* A pentanuclear iron catalyst designed for water oxidation. *Nature* **530**, 465–468 (2016).
40. Jackson, M. N. & Surendranath, Y. Molecular Control of Heterogeneous Electrocatalysis through Graphite Conjugation. *Accounts of Chemical Research* **52**, 3432–3441 (2019).
41. Hoque, M. A. *et al.* Water oxidation electrocatalysis using ruthenium coordination oligomers adsorbed on multiwalled carbon nanotubes. *Nature Chemistry* **12**, 1060–1066 (2020).
42. Trasatti, S. Electrocatalysis by oxides — Attempt at a unifying approach. *Journal of Electroanalytical Chemistry and Interfacial Electrochemistry* **111**, 125–131 (1980).
43. Trasatti, S. Electrocatalysis in the anodic evolution of oxygen and chlorine. *Electrochimica Acta* **29**, 1503–1512 (1984).
44. Rossmeisl, J., Logadottir, A. & Nørskov, J. K. Electrolysis of water on (oxidized) metal surfaces. *Chemical Physics* **319**, 178–184 (2005).
45. Nørskov, J. K. *et al.* Origin of the Overpotential for Oxygen Reduction at a Fuel-Cell Cathode. *Journal of Physical Chemistry B* **108**, 17886–17892 (2004).
46. Man, I. C. *et al.* Universality in Oxygen Evolution Electrocatalysis on Oxide Surfaces. *ChemCatChem* **3**, 1159–1165 (2011).
47. Koper, M. T. M. Thermodynamic theory of multi-electron transfer reactions: Implications for electrocatalysis. *Journal of Electroanalytical Chemistry* **660**, 254–260 (2011).
48. Huang, J. *et al.* Modifying redox properties and local bonding of Co_3O_4 by CeO_2 enhances oxygen evolution catalysis in acid. *Nature Communications* **12**, 3036 (2021).
49. Bajdich, M., García-Mota, M., Vojvodic, A., Nørskov, J. K. & Bell, A. T. Theoretical Investigation of the Activity of Cobalt Oxides for the Electrochemical Oxidation of Water. *Journal of the American Chemical Society* **135**, 13521–13530 (2013).
50. Friebel, D. *et al.* Identification of Highly Active Fe Sites in (Ni,Fe)OOH for Electrocatalytic Water Splitting. *Journal of the American Chemical Society* **137**, 1305–1313 (2015).
51. Huang, X., Wang, J., Tao, H. B., Tian, H. & Xu, H. An essential descriptor for the oxygen evolution reaction on reducible metal oxide surfaces. *Chemical Science.* **10**, 3340–3345 (2019).
52. Flores, R. A. *et al.* Active Learning Accelerated Discovery of Stable Iridium Oxide Polymorphs for the Oxygen Evolution Reaction. *Chemistry of Materials* **32**, 5854–5863 (2020).
53. Rossmeisl, J., Qu, Z.-W., Zhu, H., Kroes, G.-J. & Nørskov, J. K. Electrolysis of water on oxide surfaces. *Journal of Electroanalytical Chemistry* **607**, 83–89 (2007).
54. Evans, M. G. & Polanyi, M. Further considerations on the thermodynamics of chemical equilibria and reaction rates. *Transactions of the Faraday Society* **32**, 1333 (1936).

55. Koper, M. T. M. Analysis of electrocatalytic reaction schemes: distinction between rate-determining and potential-determining steps. *Journal of Solid State Electrochemistry* **17**, 339–344 (2013).
56. Govindarajan, N., García-Lastra, J. M., Meijer, E. J. & Calle-Vallejo, F. Does the breaking of adsorption-energy scaling relations guarantee enhanced electrocatalysis? *Current Opinion in Electrochemistry* **8**, 110–117 (2018).
57. Cherevko, S. *et al.* Oxygen and hydrogen evolution reactions on Ru, RuO_2, Ir, and IrO_2 thin film electrodes in acidic and alkaline electrolytes: A comparative study on activity and stability. *Catalysis Today* **262**, 170–180 (2016).
58. Kim, Y.-T. *et al.* Balancing activity, stability and conductivity of nanoporous core-shell iridium/iridium oxide oxygen evolution catalysts. *Nature Communications* **8**, 1449 (2017).
59. Persson, K. A., Waldwick, B., Lazic, P. & Ceder, G. Prediction of solid-aqueous equilibria: Scheme to combine first-principles calculations of solids with experimental aqueous states. *Physical Review B* **85**, 235438 (2012).
60. Zhou, L. *et al.* Rutile Alloys in the Mn–Sb–O System Stabilize Mn^{3+} To Enable Oxygen Evolution in Strong Acid. *ACS Catalysis* **8**, 10938–10948 (2018).
61. Singh, A. K. *et al.* Electrochemical Stability of Metastable Materials. *Chemistry of Materials* **29**, 10159–10167 (2017).
62. Rong, X., Parolin, J. & Kolpak, A. M. A Fundamental Relationship between Reaction Mechanism and Stability in Metal Oxide Catalysts for Oxygen Evolution. *ACS Catalysis* **6**, 1153–1158 (2016).
63. de Pablo, J. J., Jones, B., Kovacs, C. L., Ozolins, V. & Ramirez, A. P. The Materials Genome Initiative, the interplay of experiment, theory and computation. *Current Opinion in Solid State and Materials Science* **18**, 99–117 (2014).
64. de Pablo, J. J. *et al.* New frontiers for the materials genome initiative. *npj Computational Materials* **5**, 41 (2019).
65. Jain, A. *et al.* Commentary: The Materials Project: A materials genome approach to accelerating materials innovation. *APL Materials* **1**, 011002 (2013).
66. Kirklin, S. *et al.* The Open Quantum Materials Database (OQMD): assessing the accuracy of DFT formation energies. *npj Computational Materials* **1**, 15010 (2015).
67. Curtarolo, S. *et al.* AFLOW: An automatic framework for high-throughput materials discovery. *Computational Materials Science* **58**, 218–226 (2012).
68. Jain, A., Shin, Y. & Persson, K. A. Computational predictions of energy materials using density functional theory. *Nature Reviews Materials* **1**, 15004 (2016).
69. Bornmann, L., Haunschild, R. & Mutz, R. Growth rates of modern science: a latent piecewise growth curve approach to model publication numbers from established and new literature databases. *Humanities and Social Sciences Communications* **8**, 224 (2021).
70. National Science and Technology Council, USA (2011). Materials genome initiative for global competitiveness.
71. Gunasooriya, G. T. K. K. & Nørskov, J. K. Analysis of Acid-Stable and Active Oxides for the Oxygen Evolution Reaction. *ACS Energy Letters* **5**, 3778–3787 (2020).
72. Haastrup, S. *et al.* The Computational 2D Materials Database: high-throughput modeling and discovery of atomically thin crystals. *2D Materials* **5**, 042002 (2018).
73. Mounet, N. *et al.* Two-dimensional materials from high-throughput computational exfoliation of experimentally known compounds. *Nature Nanotechnology* **13**, 246–252 (2018).
74. Zhou, J. *et al.* 2DMatPedia, an open computational database of two-dimensional materials from top-down and bottom-up approaches. *Scientific Data* **6**, 86 (2019).
75. Jain, A., Wang, Z. & Nørskov, J. K. Stable Two-Dimensional Materials for Oxygen Reduction and Oxygen Evolution Reactions. *ACS Energy Letters* **4**, 1410–1411 (2019).
76. Back, S., Tran, K. & Ulissi, Z. W. Discovery of Acid-Stable Oxygen Evolution Catalysts: High-Throughput Computational Screening of Equimolar Bimetallic Oxides. *ACS Applied Materials & Interfaces* **12**, 38256–38265 (2020).
77. Winther, K. T. *et al.* Catalysis-Hub.org, an open electronic structure database for surface reactions. *Scientific Data* **6**, 75 (2019).
78. Rao, K. K. *et al.* Overcoming Hurdles in Oxygen Evolution Catalyst Discovery via Codesign. *Chemistry of Materials* **34**, 899–910 (2022).
79. Born, M. & Oppenheimer, R. Zur Quantentheorie der Molekeln. *Annalen der Physik* **389**, 457–484 (1927).
80. Mardirossian, N. & Head-Gordon, M. Thirty years of density functional theory in computational chemistry: an overview and extensive assessment of 200 density functionals. *Molecular Physics* **115**, 2315–2372 (2017).

81. Cramer, C. J. & Truhlar, D. G. Density functional theory for transition metals and transition metal chemistry. *Physical Chemistry Chemical Physics* **11**, 10757 (2009).
82. Thomas, L. H. The calculation of atomic fields. *Mathematical Proceedings of the Cambridge Philosophical Society* **23**, 542–548 (1927).
83. Dirac, P. A. M. Note on Exchange Phenomena in the Thomas Atom. *Mathematical Proceedings of the Cambridge Philosophical Society* **26**, 376–385 (1930).
84. Slater, J. C. A Simplification of the Hartree-Fock Method. *Physical Review* **81**, 385–390 (1951).
85. Hohenberg, P. & Kohn, W. Inhomogeneous Electron Gas. *Physical Review* **136**, B864–B871 (1964).
86. Kohn, W. & Sham, L. J. Self-Consistent Equations Including Exchange and Correlation Effects. *Physical Review* **140**, A1133–A1138 (1965).
87. Hartree, D. R. The Wave Mechanics of an Atom with a Non-Coulomb Central Field. Part II. Some Results and Discussion. *Mathematical Proceedings of the Cambridge Philosophical Society* **24**, 111–132 (1928).
88. Johnson, B. G., Gill, P. M. W. & Pople, J. A. The performance of a family of density functional methods. *Journal of Chemical Physics* **98**, 5612–5626 (1993).
89. Curtiss, L. A., Raghavachari, K., Trucks, G. W. & Pople, J. A. Gaussian-2 theory for molecular energies of first- and second-row compounds. *Journal of Chemical Physics* **94**, 7221–7230 (1991).
90. Curtiss, L. A., Raghavachari, K., Redfern, P. C. & Pople, J. A. Assessment of Gaussian-2 and density functional theories for the computation of enthalpies of formation. *Journal of Chemical Physics* **106**, 1063–1079 (1997).
91. Perdew, J. P., Burke, K. & Ernzerhof, M. Generalized Gradient Approximation Made Simple. *Physical Review Letters* **77**, 3865–3868 (1996).
92. Wellendorff, J. *et al.* Density functionals for surface science: Exchange-correlation model development with Bayesian error estimation. *Physical Review B* **85**, 235149 (2012).
93. Wellendorff, J. *et al.* A benchmark database for adsorption bond energies to transition metal surfaces and comparison to selected DFT functionals. *Surface Science* **640**, 36–44 (2015).
94. Mallikarjun Sharada, S., Bligaard, T., Luntz, A. C., Kroes, G.-J. & Nørskov, J. K. SBH10: A Benchmark Database of Barrier Heights on Transition Metal Surfaces. *Journal of Physical Chemistry C* **121**, 19807–19815 (2017).
95. Lee, K., Murray, É. D., Kong, L., Lundqvist, B. I. & Langreth, D. C. Higher-accuracy van der Waals density functional. *Physical Review B* **82**, 081101 (2010).
96. Perdew, J. P. & Constantin, L. A. Laplacian-level density functionals for the kinetic energy density and exchange-correlation energy. *Physical Review B* **75**, 155109 (2007).
97. Zhao, Y. & Truhlar, D. G. A new local density functional for main-group thermochemistry, transition metal bonding, thermochemical kinetics, and noncovalent interactions. *Journal of Chemical Physics* **125**, 194101 (2006).
98. Gusev, D. G. Assessing the Accuracy of M06-L Organometallic Thermochemistry. *Organometallics* **32**, 4239–4243 (2013).
99. Husch, T., Freitag, L. & Reiher, M. Calculation of Ligand Dissociation Energies in Large Transition-Metal Complexes. *Journal of Chemical Theory and Computation* **14**, 2456–2468 (2018).
100. Tao, J., Perdew, J. P., Staroverov, V. N. & Scuseria, G. E. Climbing the density functional ladder: nonempirical meta-generalized gradient approximation designed for molecules and solids. *Physical Review Letters* **91**, 146401 (2003).
101. Slater, J. C. The Self Consistent Field and the Structure of Atoms. *Physical Review* **32**, 339–348 (1928).
102. Fock, V. "Selfconsistent field" mit Austausch für Natrium. *Zeitschrift für Physik* **62**, 795–805 (1930).
103. Staroverov, V. N., Scuseria, G. E., Tao, J. & Perdew, J. P. Comparative assessment of a new nonempirical density functional: Molecules and hydrogen-bonded complexes. *Journal of Chemical Physics* **119**, 12129–12137 (2003).
104. Kossmann, S., Kirchner, B. & Neese, F. Performance of modern density functional theory for the prediction of hyperfine structure: meta-GGA and double hybrid functionals. *Molecular Physics* **105**, 2049–2071 (2007).
105. Jensen, K. P. Bioinorganic Chemistry Modeled with the TPSSh Density Functional. *Inorganic Chemistry* **47**, 10357–10365 (2008).
106. Becke, A. D. Density-functional thermochemistry. III. The role of exact exchange. *Journal of Chemical Physics* **98**, 5648–5652 (1993).
107. Dudarev, S. L., Botton, G. A., Savrasov, S. Y., Humphreys, C. J. & Sutton, A. P. Electron-energy-loss spectra and the structural stability of nickel oxide: An LSDA+U study. *Physical Review B* **57**, 1505–1509 (1998).
108. Wang, L., Maxisch, T. & Ceder, G. Oxidation energies of transition metal oxides within the GGA+U framework. *Physical Review B* **73**, 195107 (2006).

109. Grimme, S., Antony, J., Ehrlich, S. & Krieg, H. A consistent and accurate *ab initio* parametrization of density functional dispersion correction (DFT-D) for the 94 elements H-Pu. *Journal of Chemical Physics* **132**, 154104 (2010).
110. Boys, S. F. Electronic wave functions - I. A general method of calculation for the stationary states of any molecular system. *Proceedings of the Royal Society of London A* **200**, 542–554 (1950).
111. Hehre, W. J., Stewart, R. F. & Pople, J. A. Self-Consistent Molecular-Orbital Methods. I. Use of Gaussian Expansions of Slater-Type Atomic Orbitals. *Journal of Chemical Physics* **51**, 2657–2664 (1969).
112. Ditchfield, R., Hehre, W. J. & Pople, J. A. Self-Consistent Molecular-Orbital Methods. IX. An Extended Gaussian-Type Basis for Molecular-Orbital Studies of Organic Molecules. *Journal of Chemical Physics* **54**, 724–728 (1971).
113. Gordon, M. S., Binkley, J. S., Pople, J. A., Pietro, W. J. & Hehre, W. J. Self-consistent molecular-orbital methods. 22. Small split-valence basis sets for second-row elements. *Journal of the American Chemical Society* **104**, 2797–2803 (1982).
114. Park, Y. J. *et al.* Secondary Coordination Sphere Influences the Formation of Fe(III)-O or Fe(III)-OH in Nitrite Reduction: A Synthetic and Computational Study. *Inorganic Chemistry* **61**, 8182–8192 (2022).
115. Maddock, L. C. H., Mu, M., Kennedy, A. R., García-Melchor, M. & Hevia, E. Facilitating the Ferration of Aromatic Substrates through Intramolecular Sodium Mediation. *Angewandte Chemie International Edition* **60**, 15296–15301 (2021).
116. Hay, P. J. & Wadt, W. R. *Ab initio* effective core potentials for molecular calculations. Potentials for the transition metal atoms Sc to Hg. *Journal of Chemical Physics* **82**, 270–283 (1985).
117. Ehlers, A. W. *et al.* A set of f-polarization functions for pseudo-potential basis sets of the transition metals Sc-Cu, Y-Ag and La-Au. *Chemical Physics Letters* **208**, 111–114 (1993).
118. Mulliken, R. S. Electronic Population Analysis on LCAO–MO Molecular Wave Functions. I. *Journal of Chemical Physics* **23**, 1833–1840 (1955).
119. Mulliken, R. S. Electronic Population Analysis on LCAO–MO Molecular Wave Functions. II. Overlap Populations, Bond Orders, and Covalent Bond Energies. *Journal of Chemical Physics* **23**, 1841–1846 (1955).
120. Mulliken, R. S. Electronic Population Analysis on LCAO-MO Molecular Wave Functions. III. Effects of Hybridization on Overlap and Gross AO Populations. *Journal of Chemical Physics* **23**, 2338–2342 (1955).
121. Mulliken, R. S. Electronic Population Analysis on LCAO-MO Molecular Wave Functions. IV. Bonding and Antibonding in LCAO and Valence-Bond Theories. *Journal of Chemical Physics* **23**, 2343–2346 (1955).
122. Philips, J. J., Hudspeth, M. A., Browne, P. M. & Peralta, J. E. Basis set dependence of atomic spin populations. *Chemical Physics Letters* **495**, 146–150 (2010).
123. Bloch, F. Über die Quantenmechanik der Elektronen in Kristallgittern. *Zeitschrift für Physik* **52**, 555–600 (1929).
124. Blöchl, P. E. Projector augmented-wave method. *Physical Review B* **50**, 17953–17979 (1994).
125. Kresse, G. & Joubert, D. From ultrasoft pseudopotentials to the projector augmented-wave method. *Physical Review B* **59**, 1758–1775 (1999).
126. Beak, P. Energies and alkylations of tautomeric heterocyclic compounds: old problems - new answers. *Accounts of Chemical Research* **10**, 186–192 (1977).
127. Fester, J. *et al.* Edge reactivity and water-assisted dissociation on cobalt oxide nanoislands. *Nature Communications* **8**, 14169 (2017).
128. Wangsness, R. K. *Electromagnetic Fields*. (Wiley: New York, 1979).
129. Miertuš, S., Scrocco, E. & Tomasi, J. Electrostatic interaction of a solute with a continuum. A direct utilizaion of AB initio molecular potentials for the prevision of solvent effects. *Chemical Physics* **55**, 117–129 (1981).
130. Cossi, M., Scalmani, G., Rega, N. & Barone, V. New developments in the polarizable continuum model for quantum mechanical and classical calculations on molecules in solution. *Journal of Chemical Physics* **117**, 43–54 (2002).
131. Marenich, A. V., Cramer, C. J. & Truhlar, D. G. Universal Solvation Model Based on Solute Electron Density and on a Continuum Model of the Solvent Defined by the Bulk Dielectric Constant and Atomic Surface Tensions. *Journal of Physical Chemistry B* **113**, 6378–6396 (2009).
132. Giesen, D. J., Cramer, C. J. & Truhlar, D. G. Entropic Contributions to Free Energies of Solvation. *Journal of Physical Chemistry* **98**, 4141–4147 (1994).
133. Ochterski, J. W. Thermochemistry in Gaussian. *Gaussian, Inc.* (2000).

134. Hjorth Larsen, A. *et al.* The atomic simulation environment—a Python library for working with atoms. *Journal of Physics: Condensed Matter* **29**, 273002 (2017).
135. Nørskov, J. K. *et al.* Origin of the Overpotential for Oxygen Reduction at a Fuel-Cell Cathode. *Journal of Physical Chemistry B* **108**, 17886–17892 (2004).
136. Liu, P., Logadottir, A. & Nørskov, J. K. Modeling the electro-oxidation of CO and H_2/CO on Pt, Ru, PtRu and Pt_3Sn. *Electrochimica Acta* **48**, 3731–3742 (2003).
137. Soriano-López, J., Schmitt, W. & García-Melchor, M. Computational modelling of water oxidation catalysts. *Current Opinion in Electrochemistry* **7**, 22–30 (2018).
138. Kurth, Stefan, Perdew, John P., & Blaha, Peter. Molecular and Solid-State Tests of Density Functional Approximations: LSD, GGAs, and Meta-GGAs. *International Journal of Quantum Chemistry* **75**, 889–909 (1999).
139. Kelly, C. P., Cramer, C. J. & Truhlar, D. G. Single-Ion Solvation Free Energies and the Normal Hydrogen Electrode Potential in Methanol, Acetonitrile, and Dimethyl Sulfoxide. *Journal of Physical Chemistry B* **111**, 408–422 (2007).
140. Bartmess, J. E. Thermodynamics of the Electron and the Proton. *Journal of Physical Chemistry* **98**, 6420–6424 (1994).
141. Ertem, M. Z., Gagliardi, L. & Cramer, C. J. Quantum chemical characterization of the mechanism of an iron-based water oxidation catalyst. *Chemical Science* **3**, 1293 (2012).
142. Wang, S. *et al.* Universal transition state scaling relations for (de)hydrogenation over transition metals. *Physical Chemistry Chemical Physics* **13**, 20760 (2011).
143. Tripković, V., Skúlason, E., Siahrostami, S., Nørskov, J. K. & Rossmeisl, J. The oxygen reduction reaction mechanism on Pt(111) from density functional theory calculations. *Electrochimica Acta* **55**, 7975–7981 (2010).
144. Sun, W. *et al.* The thermodynamic scale of inorganic crystalline metastability. *Science Advances* **2**, 11 (2016).
145. Fultz, B. Vibrational thermodynamics of materials. *Progress in Materials Science* **55**, 247–352 (2010).
146. Ong, S. P., Wang, L., Kang, B. & Ceder, G. Li−Fe−P−O_2 Phase Diagram from First Principles Calculations. *Chemistry of Materials* **20**, 1798–1807 (2008).
147. Richards, W. D., Miara, L. J., Wang, Y., Kim, J. C. & Ceder, G. Interface Stability in Solid-State Batteries. *Chemistry of Materials* **28**, 266–273 (2016).
148. Xiao, Y., Miara, L. J., Wang, Y. & Ceder, G. Computational Screening of Cathode Coatings for Solid-State Batteries. *Joule* **3**, 1252–1275 (2019).
149. Pourbaix, M. *Atlas of electrochemical equilibria in aqueous solutions*. (National Association of Corrosion Engineers, 1974).
150. Yan, Q. *et al.* $Mn_2V_2O_7$: An Earth Abundant Light Absorber for Solar Water Splitting. *Advanced Energy Materials* **5**, 1401840 (2015).
151. Morgan, B. J. & Watson, G. W. A DFT+U description of oxygen vacancies at the TiO_2 rutile (110) surface. *Surface Science* **601**, 5034–5041 (2007).
152. Jain, A. *et al.* Formation enthalpies by mixing GGA and GGA+U calculations. *Physical Review B* **84**, 045115 (2011).
153. Kibsgaard, J. & Chorkendorff, I. Considerations for the scaling-up of water splitting catalysts. *Nature Energy* **4**, 430–433 (2019).
154. Craig, M. J. & García-Melchor, M. Faster hydrogen production in alkaline media. *Nature Catalysis* **3**, 967–968 (2020).
155. Gersten, S. W., Samuels, G. J. & Meyer, T. J. Catalytic oxidation of water by an oxo-bridged ruthenium dimer. *Journal of the American Chemical Society* **104**, 4029–4030 (1982).
156. Limburg, J. *et al.* Characterization of the O $_2$ -Evolving Reaction Catalyzed by $[(terpy)(H_2O)Mn^{III}(O)_2Mn^{IV}(OH_2)(terpy)](NO_3)_3$(terpy = 2,2‘:6,2‘ ‘-Terpyridine). *Journal of the American Chemical Society* **123**, 423–430 (2001).
157. Concepcion, J. J., Jurss, J. W., Templeton, J. L. & Meyer, T. J. One Site is Enough. Catalytic Water Oxidation by $[Ru(tpy)(bpm)(OH_2)]^{2+}$ and $[Ru(tpy)(bpz)(OH_2)]^{2+}$. *Journal of the American Chemical Society* **130**, 16462–16463 (2008).
158. Duan, L., Araujo, C. M., Ahlquist, M. S. G. & Sun, L. Highly efficient and robust molecular ruthenium catalysts for water oxidation. *Proceedings of the National Academy of Sciences of the United States of America* **109**, 15584–15588 (2012).
159. Kärkäs, M. D. *et al.* Water Oxidation by Single-Site Ruthenium Complexes: Using Ligands as Redox and Proton Transfer Mediators. *Angewandte Chemie Internatinal Edition* **51**, 11589–11593 (2012).
160. Matheu, R. *et al.* Intramolecular Proton Transfer Boosts Water Oxidation Catalyzed by a Ru Complex. *Journal of the American Chemical Society* **137**, 10786–10795 (2015).

161. Young, K. J., Takase, M. K. & Brudvig, G. W. An Anionic N-Donor Ligand Promotes Manganese-Catalyzed Water Oxidation. *Inorganic Chemistry* **52**, 7615–7622 (2013).
162. Ellis, W. C., McDaniel, N. D., Bernhard, S. & Collins, T. J. Fast Water Oxidation Using Iron. *Journal of the American Chemical Society* **132**, 10990–10991 (2010).
163. Fillol, J. L. *et al.* Efficient water oxidation catalysts based on readily available iron coordination complexes. *Nature Chemistry* **3**, 807–813 (2011).
164. Wasylenko, D. J., Ganesamoorthy, C., Borau-Garcia, J. & Berlinguette, C. P. Electrochemical evidence for catalytic water oxidation mediated by a high-valent cobalt complex. *Chemical Communications* **47**, 4249 (2011).
165. Coggins, M. K., Zhang, M.-T., Chen, Z., Song, N. & Meyer, T. J. Single-Site Copper(II) Water Oxidation Electrocatalysis: Rate Enhancements with HPO_4^{2-} as a Proton Acceptor at pH 8. *Angewandte Chemie International Edition* **53**, 12226–12230 (2014).
166. Han, Y., Wu, Y., Lai, W. & Cao, R. Electrocatalytic Water Oxidation by a Water-Soluble Nickel Porphyrin Complex at Neutral pH with Low Overpotential. *Inorganic Chemistry* **54**, 5604–5613 (2015).
167. Thomsen, J. M., Huang, D. L., Crabtree, R. H. & Brudvig, G. W. Iridium-based complexes for water oxidation. *Dalton Transactions* **44**, 12452–12472 (2015).
168. Blakemore, J. D., Crabtree, R. H. & Brudvig, G. W. Molecular Catalysts for Water Oxidation. *Chemical Reviews* **115**, 12974–13005 (2015).
169. Sackville, E. V., Marken, F. & Hintermair, U. Electrochemical and Kinetic Insights into Molecular Water Oxidation Catalysts Derived from Cp*Ir(pyridine-alkoxide) Complexes. *ChemCatChem* **10**, 4280–4291 (2018).
170. Govindarajan, N., Koper, M. T. M., Meijer, E. J. & Calle-Vallejo, F. Outlining the Scaling-based and Scaling-free Optimization of Electrocatalysts. *ACS Catalysis* **9**, 4218–4225 (2019).
171. Busch, M., Fabrizio, A., Luber, S., Hutter, J. & Corminboeuf, C. Exploring the Limitation of Molecular Water Oxidation Catalysts. *Journal of Physical Chemistry C* **122**, 12404–12412 (2018).
172. Calle-Vallejo, F., Martínez, J. I., García-Lastra, J. M., Abad, E. & Koper, M. T. M. Oxygen reduction and evolution at single-metal active sites: Comparison between functionalized graphitic materials and protoporphyrins. *Surface Science* **607**, 47–53 (2013).
173. Ghosh, A., Dasgupta, S., Kundu, A. & Mandal, S. The impact of secondary coordination sphere engineering on water oxidation reactivity catalysed by molecular ruthenium complexes: a next-generation approach to develop advanced catalysts. *Dalton Transactions* **51**, 10320–10337 (2022).
174. Zong, R. & Thummel, R. P. A New Family of Ru Complexes for Water Oxidation. *Journal of the American Chemical Society* **127**, 12802–12803 (2005).
175. Limburg, J. *et al.* Characterization of the O_2-Evolving Reaction Catalyzed by $[(terpy)(H_2O)Mn^{III}(O)_2Mn^{IV}(OH_2)(terpy)](NO_3)_3$(terpy = 2,2‘:6,2‘ ‘-Terpyridine). *Journal of the American Chemical Society* **123**, 423–430 (2001).
176. Frisch, M. J. Gaussian 09, Revision A.02. *Gaussian 09, Revision A.02* (2009).
177. Perdew, J. P. Density-functional approximation for the correlation energy of the inhomogeneous electron gas. *Physical Review B* **33**, 8822–8824 (1986).
178. Becke, A. D. Density-functional exchange-energy approximation with correct asymptotic behavior. *Physical Review A* **38**, 3098–3100 (1988).
179. Grimme, S., Ehrlich, S. & Goerigk, L. Effect of the damping function in dispersion corrected density functional theory. *Journal of Computational Chemistry* **32**, 1456–1465 (2011).
180. Nandy, A. *et al.* Computational Discovery of Transition-metal Complexes: From High-throughput Screening to Machine Learning. *Chemical Reviews* **121**, 9927–10000 (2021).
181. Abild-Pedersen, F. *et al.* Scaling Properties of Adsorption Energies for Hydrogen-Containing Molecules on Transition-Metal Surfaces. *Physical Review Letters* **99**, 016105 (2007).
182. Baran, J. D., Grönbeck, H. & Hellman, A. Analysis of Porphyrines as Catalysts for Electrochemical Reduction of O_2 and Oxidation of H_2O. *Journal of the American Chemical Society* **136**, 1320–1326 (2014).
183. Angeles-Boza, A. M. *et al.* Competitive oxygen-18 kinetic isotope effects expose O–O bond formation in water oxidation catalysis by monomeric and dimeric ruthenium complexes. *Chemical Science* **5**, 1141–1152 (2014).
184. Matheu, R. *et al.* Hydrogen Bonding Rescues Overpotential in Seven-Coordinated Ru Water Oxidation Catalysts. *ACS Catalysis* **7**, 6525–6532 (2017).
185. Taguchi, T. *et al.* Preparation and Properties of a Monomeric High-Spin Mn^{V}–Oxo Complex. *Journal of the American Chemical Society* **134**, 1996–1999 (2012).

186. Miró, P., Ertem, M. Z., Gagliardi, L. & Cramer, C. J. Quantum Chemical Characterization of Water Oxidation Catalysts. in *Molecular Water Oxidation Catalysis* 233–255 (John Wiley & Sons, Ltd, 2014).
187. Moonshiram, D. *et al.* Uncovering the Role of Oxygen Atom Transfer in Ru-Based Catalytic Water Oxidation. *Journal of the American Chemical Society* **138**, 15605–15616 (2016).
188. Hessels, J., Detz, R. J., Koper, M. T. M. & Reek, J. N. H. Rational Design Rules for Molecular Water Oxidation Catalysts based on Scaling Relationships. *Chemistry - A European Journal* **23**, 16413–16418 (2017).
189. Lang, C. *et al.* Observation of a potential-dependent switch of water-oxidation mechanism on Co-oxide-based catalysts. *Chem* **7**, 2101–2117 (2021).
190. Govindarajan, N., Koper, M. T. M., Meijer, E. J. & Calle-Vallejo, F. Outlining the Scaling-Based and Scaling-Free Optimization of Electrocatalysts. *ACS Catalysis* **9**, 4218–4225 (2019).
191. Govindarajan, N., Tiwari, A., Ensing, B. & Meijer, E. J. Impact of the Ligand Flexibility and Solvent on the O–O Bond Formation Step in a Highly Active Ruthenium Water Oxidation Catalyst. *Inorganic Chemistry* **57**, 13063–13066 (2018).
192. Gauthier, J. A., Dickens, C. F., Chen, L. D., Doyle, A. D. & Nørskov, J. K. Solvation Effects for Oxygen Evolution Reaction Catalysis on IrO_2(110). *Journal of Physical Chemistry C* **121**, 11455–11463 (2017).
193. Matheu, R., Ertem, M. Z., Gimbert-Suriñach, C., Sala, X. & Llobet, A. Seven Coordinated Molecular Ruthenium–Water Oxidation Catalysts: A Coordination Chemistry Journey: Focus Review. *Chemical Reviews* **119**, 3453–3471 (2019).
194. Ramakrishnan, R., Dral, P. O., Rupp, M. & von Lilienfeld, O. A. Quantum chemistry structures and properties of 134 kilo molecules. *Scientific Data* **1**, 140022 (2014).
195. Folkman, S. J., Soriano-Lopez, J., Galán-Mascarós, J. R. & Finke, R. G. Electrochemically Driven Water-Oxidation Catalysis Beginning with Six Exemplary Cobalt Polyoxometalates: Is It Molecular, Homogeneous Catalysis or Electrode-Bound, Heterogeneous CoO_x Catalysis? *Journal of the American Chemical Society* **140**, 12040–12055 (2018).
196. Safdari, R. *et al.* A mononuclear cobalt complex for water oxidation: new controversies and puzzles. *Dalton Transactions* **47**, 16668–16673 (2018).
197. Trotochaud, L., Young, S. L., Ranney, J. K. & Boettcher, S. W. Nickel–Iron Oxyhydroxide Oxygen-Evolution Electrocatalysts: The Role of Intentional and Incidental Iron Incorporation. *Journal of the American Chemical Society* **136**, 6744–6753 (2014).
198. Acuña-Parés, F., Codolà, Z., Costas, M., Luis, J. M. & Lloret-Fillol, J. Unraveling the Mechanism of Water Oxidation Catalyzed by Nonheme Iron Complexes. *Chemistry - A European Journal* **20**, 5696–5707 (2014).
199. Acuña-Parés, F., Costas, M., Luis, J. M. & Lloret-Fillol, J. Theoretical Study of the Water Oxidation Mechanism with Non-heme Fe(Pytacn) Iron Complexes. Evidence That the Fe^{IV}(O)(Pytacn) Species Cannot React with the Water Molecule To Form the O–O Bond. *Inorganic Chemistry* **53**, 5474–5485 (2014).
200. Nair, V. & Deepthi, A. Cerium(IV) Ammonium NitrateA Versatile Single-Electron Oxidant. *Chemical Reviews* **107**, 1862–1891 (2007).
201. O'Halloran, K. P. *et al.* Revisiting the Polyoxometalate-Based Late-Transition-Metal-Oxo Complexes: The "Oxo Wall" Stands. *Inorganic Chemistry* **51**, 7025–7031 (2012).
202. Codolà, Z. *et al.* Evidence for an oxygen evolving iron–oxo–cerium intermediate in iron-catalysed water oxidation. *Nature Communications* **6**, 5865 (2015).
203. Takashima, T., Ishikawa, K. & Irie, H. Detection of Intermediate Species in Oxygen Evolution on Hematite Electrodes Using Spectroelectrochemical Measurements. *Journal of Physical Chemistry C* **120**, 24827–24834 (2016).
204. Craig, M. J. *et al.* Universal scaling relations for the rational design of molecular water oxidation catalysts with near-zero overpotential. *Nature Communications* **10**, 4993 (2019).
205. Codolà, Z. *et al.* Design of Iron Coordination Complexes as Highly Active Homogenous Water Oxidation Catalysts by Deuteration of Oxidation-Sensitive Sites. *Journal of the American Chemical Society* **141**, 323–333 (2019).
206. Olivares, M. *et al.* Relevance of Chemical vs. Electrochemical Oxidation of Tunable Carbene Iridium Complexes for Catalytic Water Oxidation. *European Journal of Inorganic Chemistry* **2020**, 801–812 (2020).
207. Ioannidis, E. I., Gani, T. Z. H. & Kulik, H. J. molSimplify: A toolkit for automating discovery in inorganic chemistry. *Journal of Computational Chemistry* **37**, 2106–2117 (2016).
208. Kresse, G. & Hafner, J. *Ab initio* molecular dynamics for liquid metals. *Physical Review B* **47**, 558–561 (1993).

209. Kresse, G. & Hafner, J. *Ab initio* molecular-dynamics simulation of the liquid-metal–amorphous-semiconductor transition in germanium. *Physical Review B* **49**, 14251–14269 (1994).
210. Kresse, G. & Furthmüller, J. Efficient iterative schemes for *ab initio* total-energy calculations using a plane-wave basis set. *Physical Review B* **54**, 11169–11186 (1996).
211. Kresse, G. & Furthmüller, J. Efficiency of ab-initio total energy calculations for metals and semiconductors using a plane-wave basis set. *Computational Materials Science* **6**, 15–50 (1996).
212. Grimme, S., Antony, J., Ehrlich, S. & Krieg, H. A consistent and accurate *ab initio* parametrization of density functional dispersion correction (DFT-D) for the 94 elements H-Pu. *Journal of Chemical Physics* **132**, 154104 (2010).
213. Seitz, L. C. *et al.* A highly active and stable IrO_x/$SrIrO_3$ catalyst for the oxygen evolution reaction. *Science* **353**, 1011–1014 (2016).
214. Duan, L., Araujo, C. M., Ahlquist, M. S. G. & Sun, L. Highly efficient and robust molecular ruthenium catalysts for water oxidation. *Proceedings of the National Academy of Science of the United States of America* **109**, 15584–15588 (2012).
215. Christensen, R., Hansen, H. A., Dickens, C. F., Nørskov, J. K. & Vegge, T. Functional Independent Scaling Relation for ORR/OER Catalysts. *Journal of Physical Chemistry C* **120**, 24910–24916 (2016).
216. Garcés-Pineda, F. A., Blasco-Ahicart, M., Nieto-Castro, D., López, N. & Galán-Mascarós, J. R. Direct magnetic enhancement of electrocatalytic water oxidation in alkaline media. *Nature Energy* **4**, 519–525 (2019).
217. Pérez-Ramírez, J. & López, N. Strategies to break linear scaling relationships. *Nature Catalysis* **2**, 971–976 (2019).
218. Gracia, J. Spin dependent interactions catalyse the oxygen electrochemistry. *Physical Chemistry Chemical Physics* **19**, 20451–20456 (2017).
219. Jiao, Y., Sharpe, R., Lim, T., Niemantsverdriet, J. W. H. & Gracia, J. Photosystem II Acts as a Spin-Controlled Electron Gate during Oxygen Formation and Evolution. *Journal of the American Chemical Society* **139**, 16604–16608 (2017).
220. Gracia, J., Sharpe, R. & Munarriz, J. Principles determining the activity of magnetic oxides for electron transfer reactions. *Journal of Catalysis* **361**, 331–338 (2018).
221. Ng, J. W. D. *et al.* Gold-supported cerium-doped NiOx catalysts for water oxidation. *Nature Energy* **1**, 16053 (2016).
222. Huynh, M. H. V. & Meyer, T. J. Proton-Coupled Electron Transfer. *Chemical Reviews* **107**, 5004–5064 (2007).
223. García-Melchor, M., Vilella, L., López, N. & Vojvodic, A. Computationally Probing the Performance of Hybrid, Heterogeneous, and Homogeneous Iridium-Based Catalysts for Water Oxidation. *ChemCatChem* **8**, 1792–1798 (2016).
224. Coggins, M. K., Zhang, M.-T., Vannucci, A. K., Dares, C. J. & Meyer, T. J. Electrocatalytic Water Oxidation by a Monomeric Amidate-Ligated Fe(III)–Aqua Complex. *Journal of the American Chemical Society* **136**, 5531–5534 (2014).
225. Sinha, V., Laan, J. J. & Pidko, E. A. Accurate and rapid prediction of pK_a of transition metal complexes: semiempirical quantum chemistry with a data-augmented approach. *Physical Chemistry Chemical Physics* **23**, 2557–2567 (2021).
226. Tissandier, M. D. *et al.* The Proton's Absolute Aqueous Enthalpy and Gibbs Free Energy of Solvation from Cluster-Ion Solvation Data. *Journal of Physical Chemistry A* **102**, 7787–7794 (1998).
227. Hammer, B. & Norskov, J. K. Why gold is the noblest of all the metals. *Nature* **376**, 238–240 (1995).
228. Craig, M. J., Barda-Chatain, R. & García-Melchor, M. Fundamental insights and rational design of low-cost polyoxometalates for the oxygen evolution reaction. *Journal of Catalysis* **393**, 202–206 (2021).
229. Abild-Pedersen, F. *et al.* Scaling Properties of Adsorption Energies for Hydrogen-Containing Molecules on Transition-Metal Surfaces. *Physical Review Letters* **99**, (2007).
230. Bhattacharjee, S., Waghmare, U. V. & Lee, S.-C. An improved d-band model of the catalytic activity of magnetic transition metal surfaces. *Scientific Reports* **6**, 35916 (2016).
231. Ulissi, Z. W., Singh, A. R., Tsai, C. & Nørskov, J. K. Automated Discovery and Construction of Surface Phase Diagrams Using Machine Learning. *Journal of Physical Chemistry Letters* **7**, 3931–3935 (2016).
232. Muggianu, Y.-M., Gambino, M. & Bros, J.-P. Enthalpies de formation des alliages liquides bismuth-étain-gallium à 723 k. Choix d'une représentation analytique des grandeurs d'excès intégrales et partielles de mélange. *Journal de Chimie Physique et de Physico-Chimie Biologique* **72**, 83–88 (1975).
233. Meredig, B. *et al.* Combinatorial screening for new materials in unconstrained composition space with machine learning. *Physical Review B* **89**, 094104 (2014).

234. Jha, D. *et al.* ElemNet: Deep Learning the Chemistry of Materials From Only Elemental Composition. *Scientific Reports* **8**, 17593 (2018).
235. Goodall, R. E. A. & Lee, A. A. Predicting materials properties without crystal structure: deep representation learning from stoichiometry. *Nature Communications* **11**, 6280 (2020).
236. Dunn, A., Wang, Q., Ganose, A., Dopp, D. & Jain, A. Benchmarking materials property prediction methods: the Matbench test set and Automatminer reference algorithm. *npj Computationl Materials* **6**, 138 (2020).
237. Ward, L., Agrawal, A., Choudhary, A. & Wolverton, C. A general-purpose machine learning framework for predicting properties of inorganic materials. *npj Computational Materials* **2**, 16028 (2016).
238. Xie, T. & Grossman, J. C. Crystal Graph Convolutional Neural Networks for an Accurate and Interpretable Prediction of Material Properties. *Physical Review Letters* **120**, 145301 (2018).
239. Friedrich, R. *et al.* Coordination corrected ab initio formation enthalpies. *npj Computational Materials* **5**, 59 (2019).
240. Song, F. *et al.* Transition Metal Oxides as Electrocatalysts for the Oxygen Evolution Reaction in Alkaline Solutions: An Application-Inspired Renaissance. *Journal of the American Chemical Society* **140**, 7748–7759 (2018).
241. Zimmermann, N. E. R., Horton, M. K., Jain, A. & Haranczyk, M. Assessing Local Structure Motifs Using Order Parameters for Motif Recognition, Interstitial Identification, and Diffusion Path Characterization. *Frontiers in Materials* **4**, 34 (2017).
242. Zimmermann, N. E. R., Vorselaars, B., Quigley, D. & Peters, B. Nucleation of NaCl from Aqueous Solution: Critical Sizes, Ion-Attachment Kinetics, and Rates. *Journal of the American Chemical Society* **137**, 13352–13361 (2015).
243. Wang, G. *et al.* Identification of an iridium-containing compound with a formal oxidation state of IX. *Nature* **514**, 475–477 (2014).
244. Yan, Q. *et al.* Solar fuels photoanode materials discovery by integrating high-throughput theory and experiment. *Proceedings of the National Academy of Sciences of the United States of America* **114**, 3040–3043 (2017).
245. Kılıç, Ç. & Zunger, A. Origins of Coexistence of Conductivity and Transparency in SnO_2. *Physical Review Letters* **88**, 095501 (2002).
246. Scanlon, D. O. & Watson, G. W. On the possibility of p-type SnO_2. *Journal of Materials Chemistry* **22**, 25236 (2012).
247. Stöwe, K. & Weber, M. Niobium, Tantalum, and Tungsten Doped Tin Dioxides as Potential Support Materials for Fuel Cell Catalyst Applications. *Zeitschrift für Anorganische und Allgemeine Chemie* **646**, 1470–1480 (2020).
248. Williamson, B. A. D. *et al.* Resonant Ta Doping for Enhanced Mobility in Transparent Conducting SnO_2. *Chemistry of Materials* **32**, 1964–1973 (2020).
249. Goldschmidt, V. M. Die Gesetze der Krystallochemie. *Naturwissenschaften* **14**, 477–485 (1926).
250. Bartel, C. J. *et al.* New tolerance factor to predict the stability of perovskite oxides and halides. *Science Advances* **5**, eaav0693 (2019).
251. Anand, S., Male, J. P., Wolverton, C. & Snyder, G. J. Visualizing defect energetics. *Materials Horizons.* **8**, 1966–1975 (2021).
252. Reier, T., Oezaslan, M. & Strasser, P. Electrocatalytic Oxygen Evolution Reaction (OER) on Ru, Ir, and Pt Catalysts: A Comparative Study of Nanoparticles and Bulk Materials. *ACS Catalysis* **2**, 1765–1772 (2012).
253. Lin, Y. *et al.* Chromium-ruthenium oxide solid solution electrocatalyst for highly efficient oxygen evolution reaction in acidic media. *Nature Communications* **10**, 162 (2019).
254. Strickler, A. L. *et al.* Systematic Investigation of Iridium-Based Bimetallic Thin Film Catalysts for the Oxygen Evolution Reaction in Acidic Media. *ACS Applied Materials & Interfaces* **11**, 34059–34066 (2019).
255. Browne, M. P. *et al.* Thermally Prepared Mn_2O_3/RuO_2/Ru Thin Films as Highly Active Catalysts for the Oxygen Evolution Reaction in Alkaline Media. *ChemElectroChem* **3**, 1847–1855 (2016).
256. Chen, S. *et al.* Mn-Doped RuO_2 Nanocrystals as Highly Active Electrocatalysts for Enhanced Oxygen Evolution in Acidic Media. *ACS Catalysis* **10**, 1152–1160 (2020).
257. Ham, K., Hong, S., Kang, S., Cho, K. & Lee, J. Extensive Active-Site Formation in Trirutile $CoSb_2O_6$ by Oxygen Vacancy for Oxygen Evolution Reaction in Anion Exchange Membrane Water Splitting. *ACS Energy Letters* **6**, 364–370 (2021).
258. Gunasooriya, G. T. K. K. *et al.* First-Row Transition Metal Antimonates for the Oxygen Reduction Reaction. *ACS Nano* **16**, 6334–6348 (2022).

259. Evans, T. A. & Choi, K.-S. Electrochemical Synthesis and Investigation of Stoichiometric, Phase - Pure $CoSb_2O_6$ and $MnSb_2O_6$ Electrodes for the Oxygen Evolution Reaction in Acidic Media. *ACS Applied Energy Materials* **3**, 5563–5571 (2020).
260. Li, A. *et al.* Enhancing the stability of cobalt spinel oxide towards sustainable oxygen evolution in acid. *Nature Catalysis* **5**, 109–118 (2022).
261. Koper, M. T. M. Theory of multiple proton–electron transfer reactions and its implications for electrocatalysis. *Chemical Science* **4**, 2710 (2013).
262. Hubert, M. A. *et al.* Acidic Oxygen Evolution Reaction Activity–Stability Relationships in Ru-Based Pyrochlores. *ACS Catalysis* **10**, 12182–12196 (2020).
263. Wang, Z., Zheng, Y.-R., Chorkendorff, I. & Nørskov, J. K. Acid-Stable Oxides for Oxygen Electrocatalysis. *ACS Energy Letters* **5**, 2905–2908 (2020).
264. Ong, S. P., Jain, A., Hautier, G., Kang, B. & Ceder, G. Thermal stabilities of delithiated olivine MPO_4 (M=Fe, Mn) cathodes investigated using first principles calculations. *Electrochemistry Communications* **12**, 427–430 (2010).
265. Gao, J. *et al.* Breaking Long-Range Order in Iridium Oxide by Alkali Ion for Efficient Water Oxidation. *Journal of the American Chemical Society* **141**, 3014–3023 (2019).
266. Gou, W., Zhang, M., Zou, Y., Zhou, X. & Qu, Y. Iridium-Chromium Oxide Nanowires as Highly Performed OER Catalysts in Acidic Media. *ChemCatChem* **11**, 6008–6014 (2019).
267. Lee, H. *et al.* Comparative study of catalytic activities among transition metal-doped IrO_2 nanoparticles. *Scientific Reports* **8**, 16777 (2018).
268. Sun, W., Song, Y., Gong, X.-Q., Cao, L. & Yang, J. An efficiently tuned d-orbital occupation of IrO_2 by doping with Cu for enhancing the oxygen evolution reaction activity. *Chemical Science* **6**, 4993–4999 (2015).
269. Hu, J. *et al.* Neodymium-Doped IrO_2 Electrocatalysts Supported on Titanium Plates for Enhanced Chlorine Evolution Reaction Performance. *ChemElectroChem* **8**, 1204–1210 (2021).
270. Li, A. *et al.* Stable Potential Windows for Long-Term Electrocatalysis by Manganese Oxides Under Acidic Conditions. *Angewandte Chemie International Edition* **58**, 5054–5058 (2019).
271. Pittkowski, R. K. *et al.* Synergistic effects in oxygen evolution activity of mixed iridium-ruthenium pyrochlores. *Electrochimica Acta* **366**, 137327 (2021).
272. Shi, X. *et al.* Efficient and Stable Acidic Water Oxidation Enabled by Low-Concentration, High-Valence Iridium Sites. *ACS Energy Letters* 2228–2235 **7**, 2228–2235 (2022).
273. Wang, Y. *et al.* Nanoporous Iridium-Based Alloy Nanowires as Highly Efficient Electrocatalysts Toward Acidic Oxygen Evolution Reaction. *ACS Applied Materials & Interfaces* **11**, 39728–39736 (2019).
274. Lin, C. *et al.* In-situ reconstructed Ru atom array on α-MnO_2 with enhanced performance for acidic water oxidation. *Nature Catalysis* **4**, 1012–1023 (2021).
275. Dickens, C. F. & Nørskov, J. K. A Theoretical Investigation into the Role of Surface Defects for Oxygen Evolution on RuO_2. *Journal of Physical Chemistry C* **121**, 18516–18524 (2017).
276. Rao, R. R. *et al.* Spectroelectrochemical Analysis of the Water Oxidation Mechanism on Doped Nickel Oxides. *Journal of the American Chemical Society* **144**, 7622–7633 (2022).
277. Svane, K. L. & Rossmeisl, J. Theoretical Optimization of Compositions of High-Entropy Oxides for the Oxygen Evolution Reaction. *Angewandte Chemie International Edition* **61**, e202201146 (2022).
278. Thorarinsdottir, A. E. & Nocera, D. G. Energy catalysis needs ligands with high oxidative stability. *Chem Catalysis* **1**, 32–43 (2021).
279. Collins, T. J. Designing Ligands for Oxidizing Complexes. *Accounts of Chemical Research* **27**, 279–285 (1994).
280. Sanchez-Lengeling, B. & Aspuru-Guzik, A. Inverse molecular design using machine learning: Generative models for matter engineering. *Science* **361**, 360–365 (2018).

Appendix A

Scaling relations without Grimme D3 dispersion corrections

Here we present our data for calculations without dispersion corrections to show that the main conclusions of our Chapter 4 are robust regardless of this subtle choice of method.

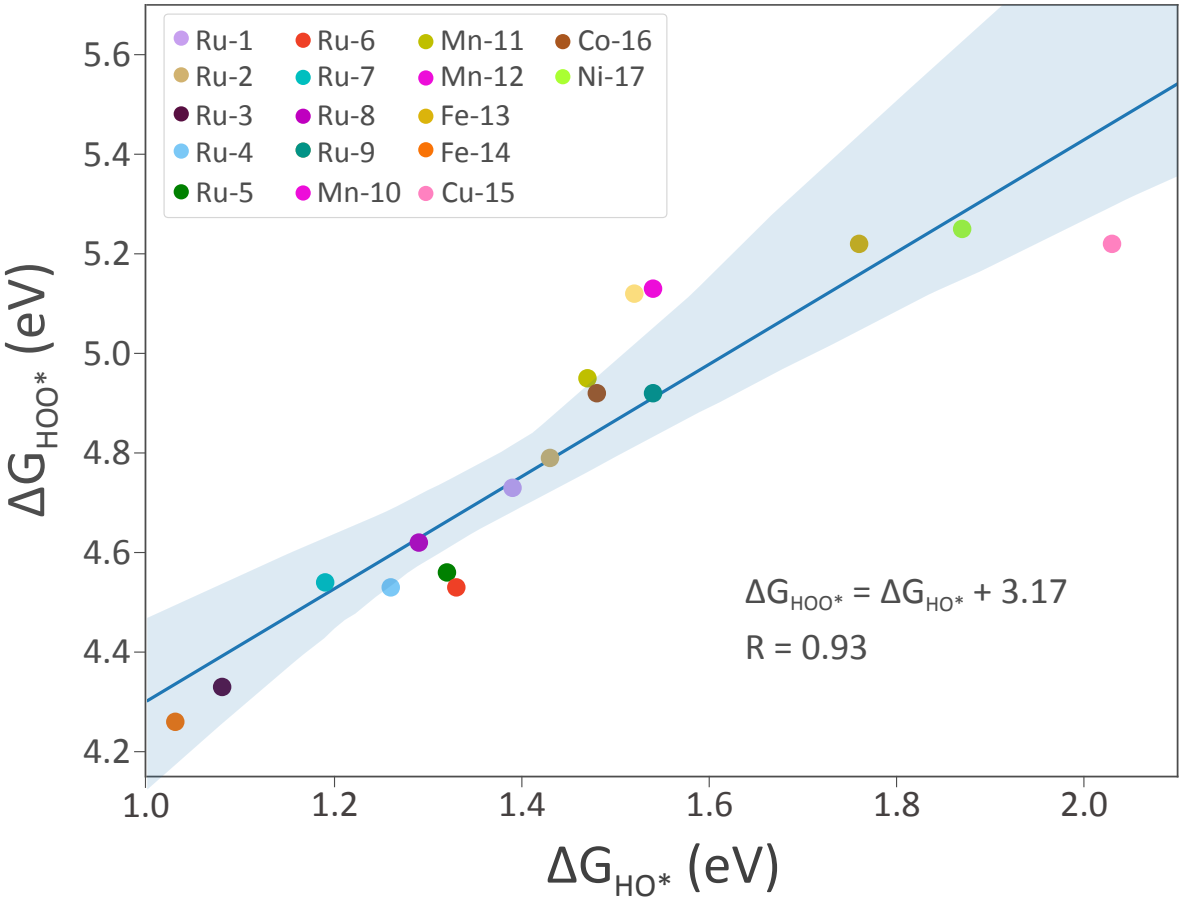

Figure A1: OER scaling plot without dispersion corrections.

The overall effect of adding dispersion corrections is to stabilize the HO* and HOO* intermediates relative to the intermediate with a vacancy.

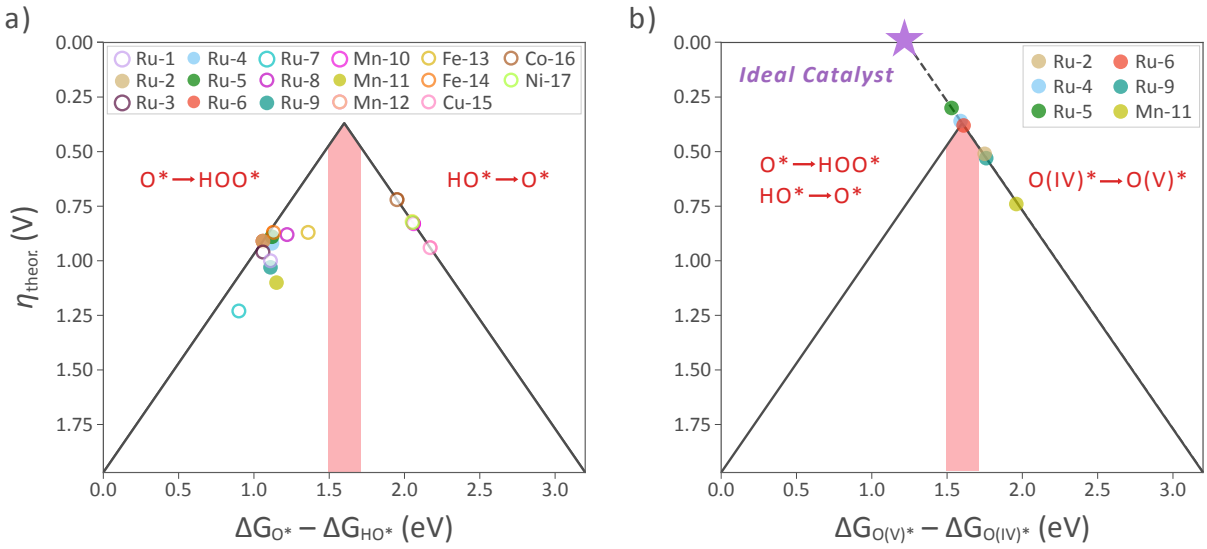

Figure A2: Volcano plots without dispersion correction corrections for (a) the conventional OER descriptor and (b) the one-electron oxidation descriptor.

With Figure S4, we note a general stabilization of the HO* with respect to the O* intermediate, when compared to Figure 3, the data with dispersion. The leads to a reduction or increase in the predicted overpotential for catalysts on the left or right of the volcano in Figure S4, respectively. In any case, the most active catalysts remain some distance away from the top of the volcano irrespective of the addition of dispersion corrections.

Reported electronic and Gibbs energies

Table A1. Computed absolute and relative (i.e. binding energies, BE) electronic and Gibbs energies of all the intermediates for each modelled catalyst.

Catalyst	Species	Multiplicity	E (Ha)	ΔE_{BE} (eV)	G (Ha)	ΔG_{BE} (eV)
Ru-4	Ru(II–*	1	–1769.461435	–	–1769.085071	–
	Ru(III)–OH	2	–1845.285084	0.77	–1844.898797	1.02
	Ru(IV)=O	3	–1844.642247	2.28	–1844.267613	2.20
	Ru(V)=O	4	–1844.427527	3.84	–1844.050900	3.81
	Ru(III)–OOH[a]	2	–1920.436978	3.83	–1920.046188	4.18

	Ru(IV)–dimer	5	– 3688.917407	–1.70[c]	– 3688.136025	–0.93[c]
Ru-5	Ru(II)–*	1	– 1801.484622	–	– 1801.131987	–
	Ru(III)–OH	2	– 1877.306099	0.83	– 1876.943318	1.09
	Ru(IV)=O	3	– 1876.665632	2.27	– 1876.312676	2.25
	Ru(V)=O	4	– 1876.451563	3.82	– 1876.099556	3.77
	Ru(III)–OOH[a]	2	– 1952.456158	3.94	– 1952.090619	4.24
	Ru(IV)–dimer[c]	5	- 3752.950094	-1.28	-3752.219888	-0.57
Ru-6	Ru(II)–*	1	– 1540.781359	–	– 1540.443174	–
	Ru(III)–OH	2	– 1616.602794	0.83	– 1616.252867	1.13
	Ru(IV)=O	3	– 1615.961807	2.29	– 1615.623775	2.25
	Ru(V)=O	4	– 1615.745473	3.89	– 1615.407574	3.85
	Ru(III)–OOH[a]	2	– 1691.755202	3.88	– 1691.402521	4.22
	Ru(IV)–dimer[c]	5	- 3231.533954	-1.17	-3230.825323	-0.28
Ru-7	Ru(III)–*	2	– 1429.417374	–	– 1429.057701	–
	Ru(IV)–OH	3	– 1505.241689	0.75	– 1504.871147	1.03
	Ru(V)=O	4	– 1504.606285	2.06	– 1504.248235	1.98
	Ru(IV)–OOH[b]	3	– 1580.386629	4.01	– 1580.012891	4.34
Ru-8	Ru(III)–*	2	– 1542.817136	–	– 1542.447151	–
	Ru(IV)–OH	3	– 1618.637760	0.85	– 1618.256518	1.14
	Ru(V)=O	4	– 1617.991907	2.44	– 1617.621468	2.42
	Ru(IV)–OOH[b]	3	– 1693.781349	4.14	– 1693.399046	4.43
Ru-3	Ru(II)–*	1	– 1363.863714	–	– 1363.548697	–
	Ru(III)–OH	2	– 1439.693636	0.60	– 1439.367219	0.89
	Ru(IV)=O	3	– 1439.053015	2.05	– 1438.737518	2.02

	Ru(V)=O	4	−1438.810387	4.37	−1438.494919	4.35
	Ru(III)–OOH[b]	2	−1514.840162	3.81	−1514.512764	4.10
Ru-9	Ru(II)–*	1	−1709.277448	–	−1708.925402	–
	Ru(III)–OH	2	−1785.082706	1.27	−1784.720222	1.54
	Ru(IV)=O	3	−1784.438723	2.81	−1784.088075	2.74
	Ru(V)=O	4	−1784.218715	4.52	−1783.866870	4.48
	Ru(III)–OOH[a]	2	−1860.231358	4.42	−1859.864521	4.78
Ru-1	Ru(III)–*	3	−2320.960846	–	−2320.362349	–
	Ru(IV)–OH	4	−2396.780644	0.88	−2396.169509	1.20
	Ru(V)=O	5	−2396.138572	2.36	−2395.538655	2.37
	Ru(IV)–OOH[a]	4	−2471.928043	4.06	−2471.314760	4.41
Ru-2	Ru(II)–*	1	−1908.379427	–	−1907.803352	–
	Ru(III)–OH	2	−1984.200355	0.85	−1983.612678	1.14
	Ru(IV)=O	3	−1983.557116	2.36	−1982.982577	2.29
	Ru(V)=O	4	−1983.333219	4.17	−1982.759453	4.08
	Ru(III)–OOH[a]	2	−2059.351050	3.94	−2058.762007	4.24
Mn-11	Mn(II)–*	6	−1266.810381	–	−1266.463762	–
	Mn(III)–OH	5	−1342.626660	0.97	−1342.266550	1.32
	Mn(IV)=O	4	−1341.992859	2.23	−1341.637630	2.43
	Mn(V)=O	3	−1341.763936	4.18	−1341.408605	4.38
	Mn(III)–OOH[b]	5	−1417.767263	4.34	−1417.404290	4.74
Mn-12	Mn(III)–*	5	−1227.081183	–	−1226.754556	–
	Mn(IV)–OH	4	−1302.906290	0.73	−1302.565160	1.11
	Mn(V)=O	3	−1302.230586	3.13	−1301.899382	3.22

	Mn(IV)–OOH[b]	4	−1378.042881	4.21	−1377.699278	4.62
Mn-10	Mn(III)–*	8	−1919.706849	–	−1919.278593	–
	Mn(IV)–OH	1	−1995.528760	0.82	−1995.084332	1.24
	Mn(V)=O	6	−1994.849611	3.31	−1994.418420	3.36
	Mn(IV)–OOH[b]	7	−2070.664133	4.33	−2070.218666	4.75
Fe-13	Fe(III)–*	4	−2420.099130	–	−2419.858797	–
	Fe(IV)–OH	3	−2495.905602	1.24	−2495.652945	1.56
	Fe(V)=O	4	−2495.251392	3.05	−2495.012270	2.99
	Fe(IV)–OOH[b]	3	−2571.044661	4.65	−2570.790935	4.97
Fe-14	Fe(II)–*	3	−1041.772009	–	−1041.428137	–
	Fe(III)–OH	2	−1117.619785	0.11	−1117.256564	0.62
	Fe(IV)=O	3	−1116.976084	1.64	−1116.623900	1.84
	Fe(V)=O	4	−1116.737215	3.86	−1116.385804	4.03
	Fe(III)–OOH[a]	2	−1192.766970	3.31	−1192.402658	3.81
Cu-15	Cu(II)–*	2	−1353.609050	–	−1353.348108	–
	Cu(III)–OH	1	−1429.398080	1.71	−1429.124425	2.04
	Cu(IV)=O	2	−1428.714801	4.32	−1428.454907	4.26
	Cu(III)–OOH[a]	1	−1504.549031	4.80	−1504.273294	5.15
Co-16	Co(II)–*	4	−1689.425377	–	−1688.989311	–
	Co(III)–OH	1	−1765.250084	0.74	−1764.799248	1.13
	Co(IV)=O	2	−1764.572417	3.20	−1764.135313	3.19
	Co(III)–OOH[b]	1	−1840.392146	4.07	−1839.939301	4.48
Ni-17	Ni(II)–*	1	−2305.501674	–	−2304.861453	–

	Ni(III)–OH	2	–2381.290337	1.72	–2380.650122	1.71
	Ni(IV)=O	3	–2380.614802	4.12	–2379.984367	3.82
	Ni(III)–OOH[a]	2	–2456.443085	4.76	–2455.793706	4.96

[a] Intramolecular H–bond present.
[b] Intramolecular H–bond not present.
[c] Energy change calculated with respect to the Ru(V)=O energy.

Relative energies and theoretical overpotentials

Table A2. Computed relative Gibbs energies (in eV) and theoretical overpotentials (in V) for catalysts which do and do not undergo an extra oxidation step. Catalysts which have a value of ΔG_3, and positive accompanying ΔG_4, undergo this extra oxidation step.

Catalyst	ΔG_1	ΔG_2	ΔG_3,	$\Delta G_{3/4}$,	$\Delta G_{4/5}$,	**η**
Ru-4	1.02	1.17	1.62	0.36	0.74	0.39
Ru-5	1.09	1.16	1.52	0.48	0.67	0.29
Ru-6	1.13	1.11	1.60	0.37	0.71	0.38
Ru-7	1.03	0.95	–	2.36	0.58	1.13
Ru-8	1.14	1.28	–	2.01	0.49	0.78
Ru-3	0.89	1.13	2.32	–0.25	0.83	0.84
Ru-9	1.54	1.20	1.74	0.30	0.14	0.51
Ru-1	1.20	1.16	–	2.05	0.51	0.82
Ru-2	1.14	1.14	1.79	0.16	0.69	0.56
Mn-11	1.32	1.11	1.96	0.37	0.16	0.73
Mn-12	1.11	2.11	–	1.40	0.30	0.88
Mn-10	1.24	2.12	–	1.39	0.17	0.89
Fe-13	1.56	1.43	–	1.98	-0.05	0.75
Fe-14	0.62	1.21	2.20	–0.22	1.11	0.75
Cu-15	2.04	2.21	–	0.90	–0.23	0.98
Co-16	1.13	2.06	–	1.29	0.44	0.83
Ni-17	1.71	2.11	–	1.14	-0.04	0.88

Appendix B

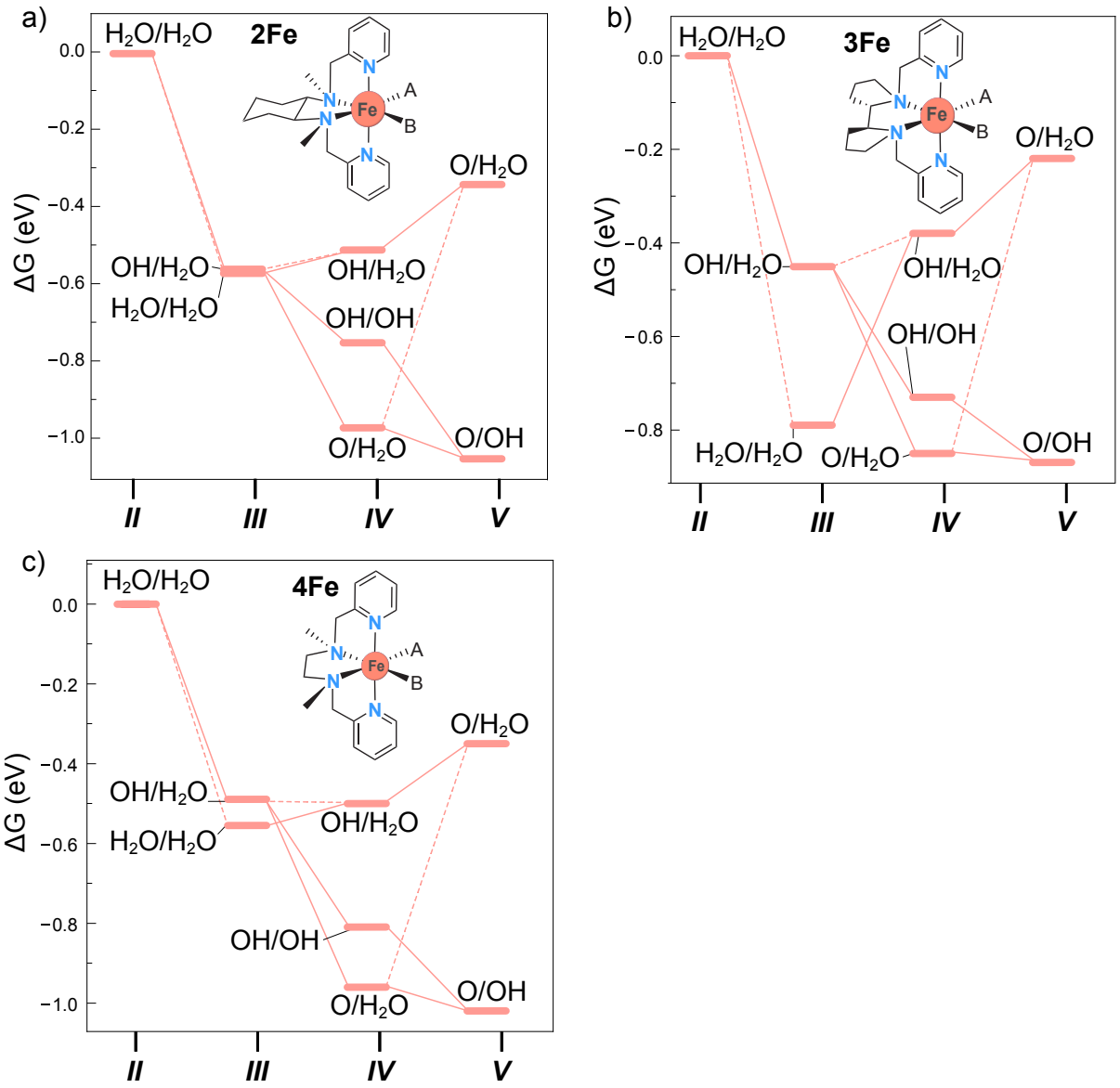

Figure B1. Gibbs energy profiles at 1.61 V vs. NHE for symmetric catalysts: a) **2Fe**, b) **3Fe** and c) **4Fe**, with the x-axis representing the oxidation state of a given intermediate. Topological isomers are not relevant for these catalysts; therefore, each intermediate is labelled based on the pair of constituents present in the interchangeable A, B positions shown in each catalyst representation, where A appears first and B second in the A/B labelling for each intermediate. The lines connecting intermediates are solid where a PCET is the reaction implied, and dashed lines where an electron transfer reaction is implied.

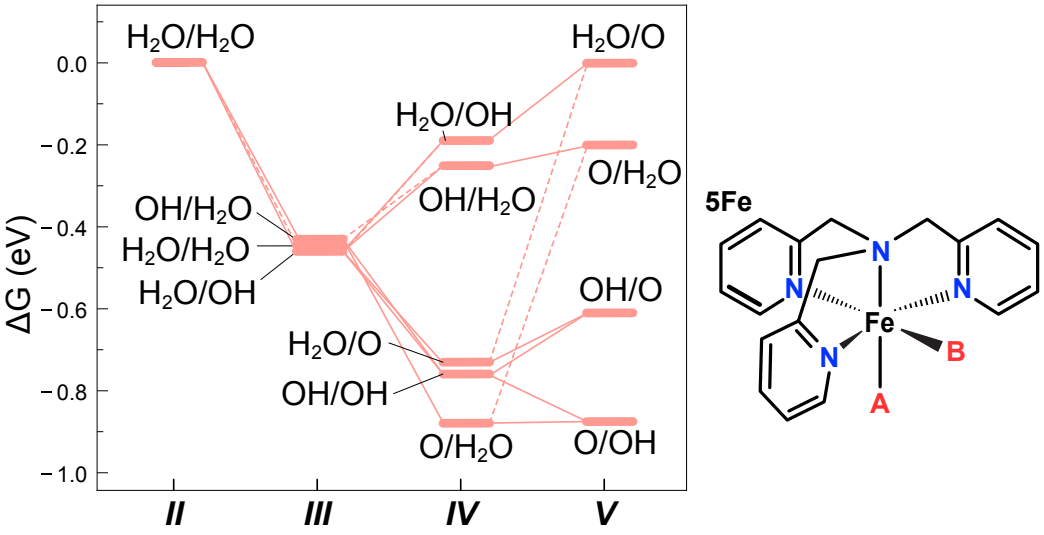

Figure B2. Gibbs energy profiles at 1.61 V vs. NHE for the asymmetric **5Fe** catalyst (inset, right) with the x-axis representing the oxidation state of a given intermediate. Intermediates are described as A/B as indicated in the depiction of the catalyst. For example, the lowest energy intermediate in oxidation state M(V) exhibits O at position A and OH at position B, therefore O/OH. The lines connecting intermediates are solid where a PCECT is the reaction implied, and dashed lines where an electron transfer reaction is implied.

Appendix C

Table C1. Multiplicity analysis for each metal and each oxidation state by computing the energy difference (in eV) between low- (LS) and high-spin (HS) states. The second column is positive when the high-spin complex is more stable, and negative in the converse case.

Catalyst and Intermediate	$E_{LS} - E_{HS}$
Ru_oct_4a_1a_1a_VAC	–1.84
Ru_31t_3a_1b_1b_OH	–4.25
Cr_32_3e_2a_VAC	1.79
Cr_31c_3b_1c_1c_VAC	2.39
Cr_31t_3e_1b_1c_VAC	2.17
Cr_31c_3d_1b_1c_VAC	2.43
Co_oct_4a_1a_1a_VAC	0.70
Co_32_3e_2a_OH	–0.91
Co_32_3e_2a_VAC	0.14
Co_31t_3e_1a_1a_VAC	0.23
Co_31t_3e_1a_1a_OH	–0.74
Fe_31t_3e_1a_1a_VAC	0.42
Fe_oct_4a_1a_1a_VAC	1.07
Mn_oct_4a_1a_1a_OH	0.59
Mn_oct_4a_1a_1a_VAC	1.40
Mn_31c_3a_1b_1c_VAC	1.94
Mn_31c_3a_1b_1c_OH	0.67
Ni_32_3e_2a_OH	–0.47
Ni_32_3d_2a_VAC	0.51
Ni_32_3d_2a_OOH	0.06
Ni_32_3a_2a_OOH	0.05

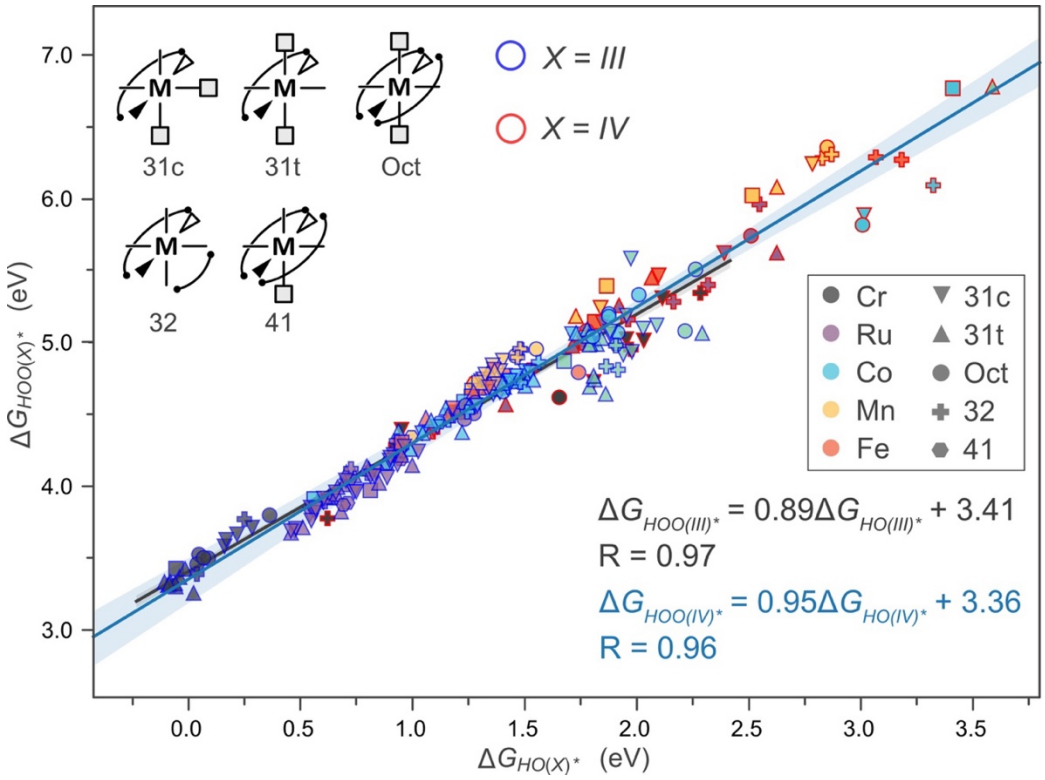

Figure C1. Scaling plot as in Figure 6.2a of the main text including the intermediates with higher oxidation states to demonstrate the independence of the scaling relation. The outline of the points denote which oxidation state is shown and the linear relationship for each plot is shown. The Pearson R coefficients are shown beneath the lines of best fit.

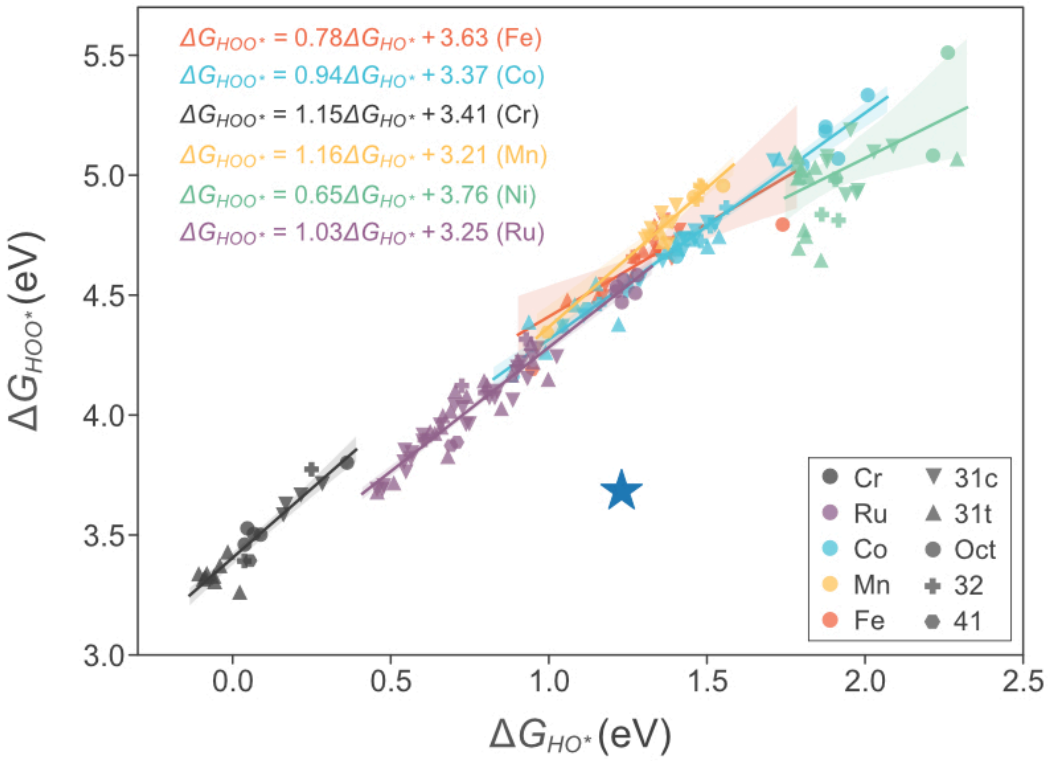

Figure C2. Metal-specific scaling relations obtained with TPSSh. The blue star represents the 'ideal' value of each binding energy for a catalyst undergoing the water nucleophilic attack mechanism of (x = 1.23, y = 3.69) eV.

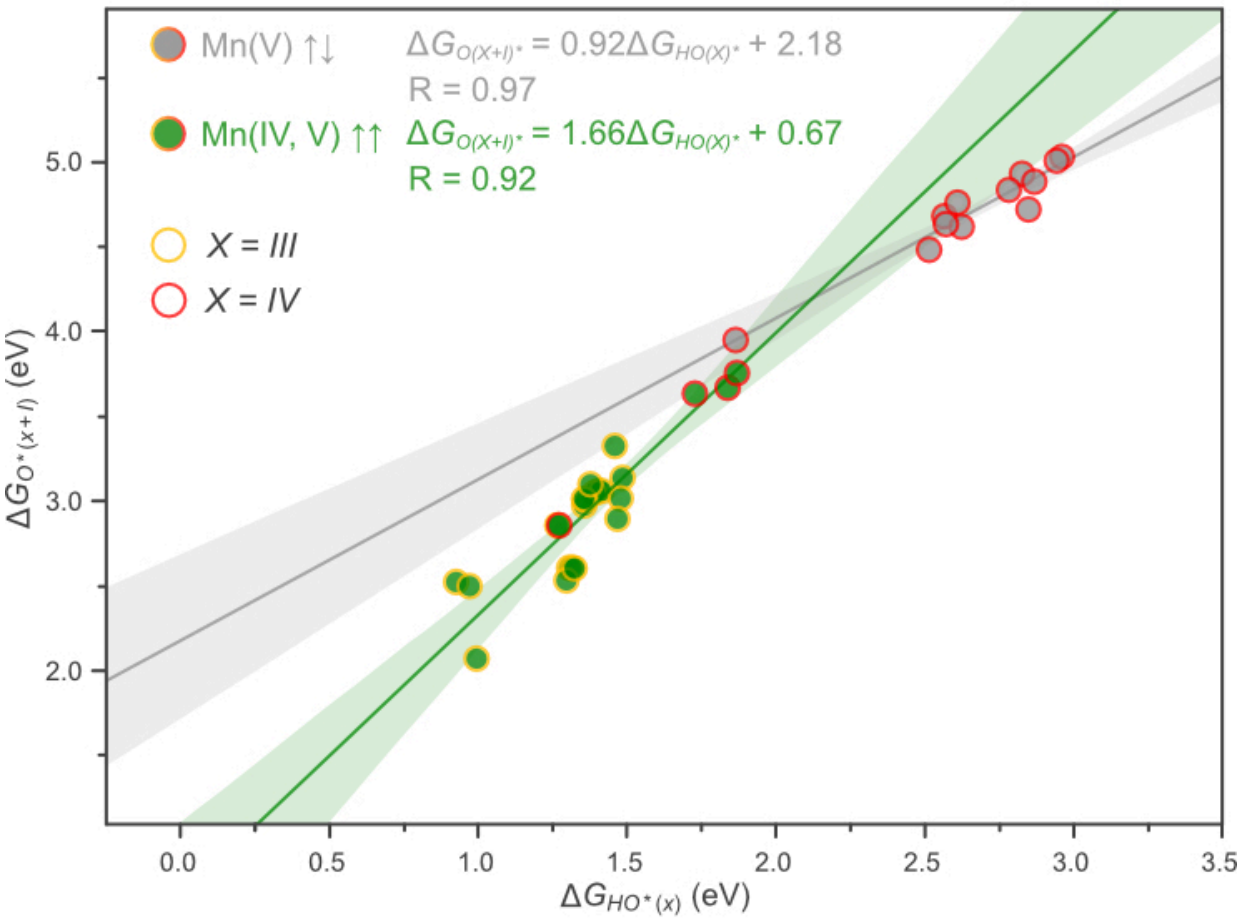

Figure C3. Fitting for the antiferromagnetic scaling relations in Mn(V)–O referenced in Table 6.2 of Chapter 6 as well as the Mn(IV, V)–O ferromagnetic scaling relation.

Appendix D

Table D1. Parabolic equations, formulated as outlined in Chapter 7, for each considered element, with the oxidation and reduction equations presented as o_{MO_2} and r_{MO_2} respectivley.

M	$o_{MO_2}(x)$	$r_{MO_2}(x)$	M	$o_{MO_2}(x)$	$r_{MO_2}(x)$
Mo	$0.05x^2 - 0.04x$	$0.32x^2 + 0.20x$	Cu	$0.13x$	$0.10x^2 - 0.41x$
W	$0.07x^2 - 0.26x$	$0.21x^2 + 0.60x$	Te	$0.02x^2 + 0.04x$	$0.00x^2 + 0.37x$
Nb	$0.34x^2 - 0.47x$	$0.04x^2 + 0.23x$	Li	$0.26x$	$0.11x^2 - 0.68x$
Ni	$0.07x^2 + 0.44x$	$0.13x^2 - 0.53x$	Na	$0.23x$	$0.06x^2 - 0.35x$
V	$0.21x^2 - 0.02x$	$0.38x^2 - 0.56x$	Ca	$0.55x$	$0.28x^2 - 1.10x$
Ir	$0.11x^{\dagger}$	$0.31x$	K	$0.25x$	$0.07x^2 - 0.29x$
Ru	$0.01x^2 + 0.05x^{\dagger}$	$0.36x$	Rb	$0.24x$	$0.07x^2 - 0.26x$
Cr	$0.03x^2 + 0.26x^{\dagger}$	$0.43x^2 - 0.82x$	Cs	$0.24x$	$0.06x^2 - 0.26x$
Fe	$0.02x^2 + 0.08x^{\dagger}$	$0.35x^2 - 0.82x$	Mg	$0.51x$	$0.26x^2 - 1.03x$
Mn	$0.02x^2 + 0.10x^{\dagger}$	$0.13x^2 - 0.35x$	Y	$0.78x$	$0.86x^2 - 1.70x$
Co	$0.27x$	$0.06x^2 - 0.22x$	Sc	$0.76x$	$0.79x^2 - 1.71x$
Pb	$0.20x^{\dagger}$	$0.29x^2 - 0.64x^{\dagger}$	Ba	$0.54x$	$0.16x^2 - 0.65x$
Sb	$0.70x^2 - 0.77x^{\dagger}$	$0.42x$	Zn	$0.16x$	$0.29x^2 - 1.17x$
Sn	$0.40x^{\dagger}$	$0.16x^2 - 0.03x^{\dagger}$	La	$0.77x$	$0.73x^2 - 1.51x$
Bi	$0.18x^2 + 0.18x$	$0.21x^2 - 0.39x$	Ce	$0.98x$	$0.21x^2 - 0.06x$
Ti	$0.30x^2 + 0.40x$	$0.23x^2 - 0.14x$	Pr	$0.76x$	$0.70x^2 - 1.41x$
Ta	$0.38x^2 - 0.62x$	$0.09x^2 + 0.36x$	Nd	$0.06x^2 + 0.42x$	$0.67x^2 - 1.29x$
In	$0.36x$	$0.60x^2 - 1.17x$	Sm	$0.77x$	$0.57x^2 - 1.21x$
Pt	$0.22x$	$0.00x$	Eu	$0.62x$	$0.36x^2 - 1.03x$

Pd	0.18x	$0.02x^2 – 0.06x$	Tb	$0.00x^2 + 0.80x$	$0.80x^2 – 1.59x$
Re	$0.07x^2 – 0.30x$	0.44x	Dy	$0.00x^2 + 0.79x$	$0.84x^2 – 1.68x$
Os	0.34x	$0.04x^2 + 0.17x$	Er	$0.00x^2 + 0.80x$	$0.89x^2 – 1.75x$
Ge	$0.30x^2 + 0.17x$	$0.09x^2 + 0.27x$	Tm	$0.00x^2 + 0.81x$	$0.87x^2 – 1.73x$
Tc	0.46x	0.46x	Yb	$0.08x^2 + 0.16x$	$0.41x^2 – 1.63x$
Rh	0.31x	0.31x			

† Highlights cases where the parabolic equation in use is derived from OQMD-fitted formation energies.

Table D2. Reference Materials Project ids and formation energies for each element MO_2 which is used to generate the ΔD values from Eq. 7.13 and thus used to generate the results shown in Chapters 7 and 8.

M	MP id	$\Delta E_{f(MO_2)}\ (eV)$	M	MP id	$\Delta E_{f(MO_2)}\ (eV)$
Mo	mp-510536	–2.016	Cu	mp-25378	–0.528
W	mp-19372	–1.942	Te	mp-2125	–1.493
Nb	mp-557057	–2.896	Li	mp-1018789	–1.126
Ni	mp-35925	–0.685	Na	mp-1901	–0.916
V	mp-19094	–2.479	Ca	mp-634859	–2.209
Ir	mp-2723	–1.26	K	mp-1866	–0.986
Ru	mp-825	–1.456	Rb	mp-12105	–0.971
Cr	mp-19177	–2.046	Cs	mp-1441	–0.978
Fe	mp-1205429	–1.235	Mg	mp-2589	–2.039
Mn	mp-19395	–1.805	Y	mp-1206610	–3.305
Co	mvc-14149	–1.079	Sc	mp-1179114	–3.303
Pb	mp-20725	–1.298	Ba	mp-1105	–2.169
Sb	mvc-5581	–1.664	Zn	mp-1094003	–1.188
Sn	mp-856	–2.112	La	mp-1206559	–3.225
Bi	mp-557993	–1.46	Ce	mp-20194	–3.927
Ti	mp-390	–3.494	Pr	mp-1302	–3.109
Ta	mp-510	–3.056	Nd	mp-31049	–3.158
In	mp-1181008	–1.433	Sm	mp-1077235	–3.215
Pt	mp-1077716	–0.883	Eu	mp-1018700	–2.638
Pd	mp-1018886	–0.727	Tb	mp-2458	–3.316

Re	mp-12875	–1.774	Dy	mp-1206731	–3.167
Os	mp-996	–1.342	Er	mp-1206338	–3.377
Ge	mp-2633	–1.853	Tm	mp-1206313	–3.407
Tc	mp-1205302	–1.833	Yb	mp-1178667	–2.413
Rh	mp-725	–1.226			

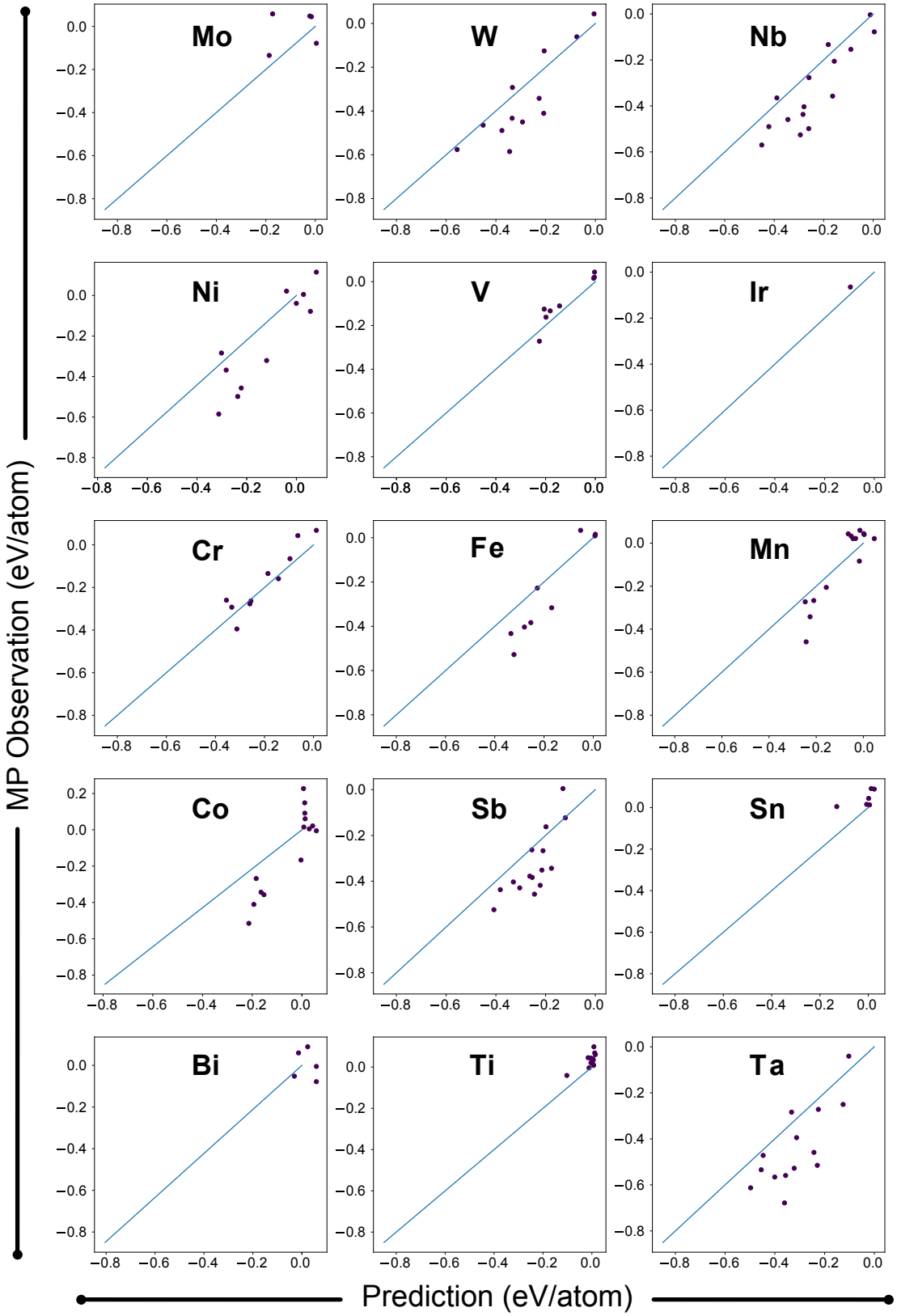

Figure D1. Parity plots for subsets of the data shown in Figure 7.6, where each subset is defined as all entries in Materials Project which have the filtered coordinations and contain the indicated element.

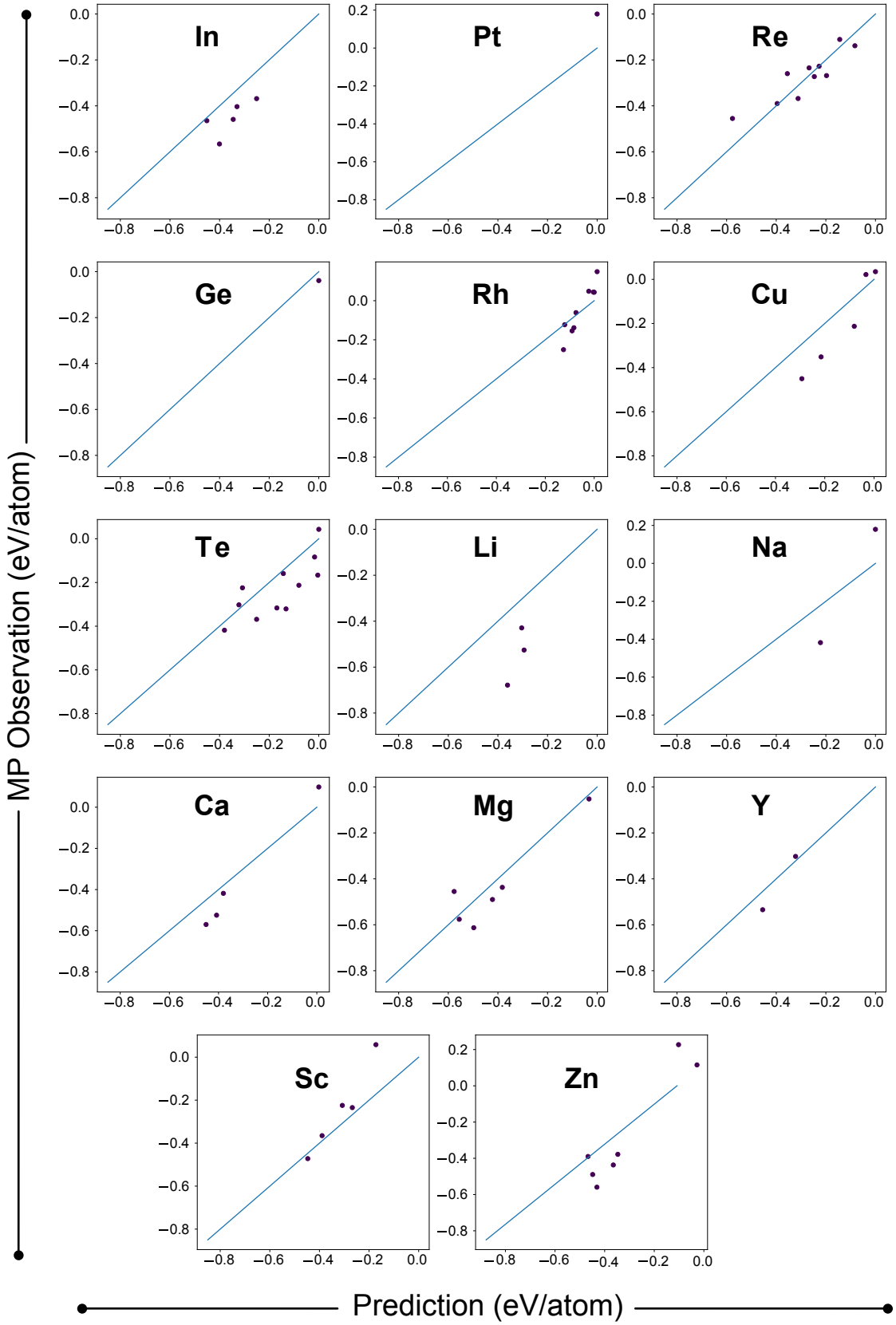

Figure D2. Parity plots for subsets of the data shown in Figure 7.6, where each subset is defined as all entries in Materials Project which have the filtered coordinations and contain the indicated element.